Dissertation

submitted to the
Combined Faculties for the Natural Sciences and for Mathematics
of the Ruperto-Carola University of Heidelberg, Germany
for the degree of
Doctor of Natural Sciences

put forward by

Dipl.-Phys. Johanna Katharina Kerch

born in Mainz, Germany

Oral examination: November 2016

Crystal-orientation fabric variations on the cm-scale in cold Alpine ice: Interaction with paleo-climate proxies under deformation and implications for the interpretation of seismic velocities

"Mir brennt der Kittel!"
In Erinnerung an Dietmar Wagenbach.

Abstract

The macroscopic flow of a glacier is substantially influenced by the plastic anisotropy of individual ice crystals on the microscale. A preferred crystal orientation develops with depth in a glacier and is subjected to the influence of the temperature, deformation and recrystallisation regime as well as the climate-dependent impurity load in the ice. Detailed knowledge about the crystal anisotropy in a glacier is thus required to better constrain the response of ice sheets in a changing climate. While the gradual change in anisotropy on a large scale of tens to hundreds of metres can mostly be explained, this is not the case for changes in anisotropic fabric on a shorter scale of centimetres to decimetres. This work aims to improve the understanding of how and why the anisotropic crystal-orientation fabric (COF) changes on a short scale in a glacier. Fabric data from an ice core, drilled at the high-altitude Alpine site Colle Gnifetti, were measured in continuously sampled sections, covering $10\,\%$ of the entire core length. The distribution of crystal axes was analysed in high-resolution together with impurity data from meltwater analysis. It is found that the fabric anisotropy exhibits a strong variability on the short scale in all depths of the ice core with extreme eigenvalue differences within one metre of ~ 0.2, often associated with small- or large-grained layers. The clear connection between the grain size variation and the impurity content leads to the conclusion that the influence of impurities on short-scale fabric variations is partially conveyed by the impurity-controlled grain size in combination with the local deformation regime. To further connect ice-core fabric data and COF measurements using seismics, a framework for the exact calculation of seismic phase velocities based on the asymmetric fabric distributions obtained from ice cores is developed and evaluated in two case studies.

Zusammenfassung

Das Fließverhalten eines Gletschers wird maßgeblich durch die plastische Anisotropie der einzelnen Eiskristalle bestimmt. Mit zunehmender Tiefe in einem Gletscher richten sich die anisotropen Kristalle in Abhängigkeit von Temperatur-, Deformations- und Rekristallisationsregime sowie den klimaabhängigen Verunreinigungen, die ins Eis eingetragen werden, aus. Um die Reaktion der Eisschilde auf ein sich veränderndes Klima besser verstehen zu können, bedarf es daher genauer Kenntnisse über die Kristallanisotropie. Die graduelle Veränderung der Anisotropie, wenn man sie in großen Abständen betrachtet, kann weitgehend erklärt werden, aber auf kurzen Distanzen ist dies nicht der Fall. Diese Arbeit soll dazu beitragen, zu verstehen, wie und warum die Anisotropie im Gletscher auf kurzen Distanzen variiert. An einem Eiskern vom hochalpinen Gletscher Colle Gnifetti wurden COF-Daten entlang kontinuierlicher Bereiche erhoben, insgesamt über $10\,\%$ der Kernlänge. Die Verteilung der Kristallachsen wurde hochaufgelöst und im Vergleich mit Spurenstoffdaten aus der Schmelzanalyse analysiert. Die Ergebnisse zeigen eine starke Variabilität der Anisotropie auf kurzen Distanzen mit Eigenwertdifferenzen von etwa 0.2 innerhalb eines Meters, oftmals im Einklang mit fein- oder grobkörnigen Schichten. Der eindeutige Zusammenhang zwischen der Korngröße und der Spurenstoffkonzentration führt zu dem Schluss, dass die kurzskaligen COF-Variationen indirekt über die Korngröße durch die Verunreinigungen beeinflusst sein können, bei gleichzeitiger Abhängigkeit von der lokalen Deformation. Für die Verknüpfung von COF-Daten aus Eiskern- und seismischen Messungen wurde eine Methode zur exakten Berechnung von seismischen Phasengeschwindigkeiten anhand von asymmetrischen Kristallachsenverteilungen aus Eiskernmessungen entwickelt und in zwei Fallstudien angewendet.

Contents

1 Introduction

The Intergovernmental Panel on Climate Change (IPCC) has acknowledged that, despite of significant advances in the understanding and modelling of contributing factors to sea level change, the largest uncertainties arise from the need to further constrain the contribution from ice sheets under changing climate conditions (IPCC AR5, Church et al., 2013). A key point is the improvement of the understanding of the ice flow by internal deformation. The internal deformation of an ice sheet is largely governed by its mass distribution, the topography conditions, the temperature field and the characteristics of the smallest compounds of a glacier: the ice crystals. The inherent plastic anisotropy of the individual crystals leads to their alignment in preferred orientations, referred to as *crystal-orientation fabric* (COF), thus changing the viscous behaviour of the bulk material (e.g. Schulson and Duval, 2009). A complex feedback arises from the fact that the deformation in return influences the development of preferred orientations. The importance of including the crystal anisotropy into ice flow models has repeatedly been demonstrated (e.g. Pettit et al., 2007; Martin et al., 2009). However, the large-scale behaviour can only be truly understood as a function of the microscopic behaviour, the study of which poses a big challenge. Ice sheets are large, complex systems, that react only slowly under changing boundary conditions. For the study of ice-physical properties in a more dynamic system, smaller and warmer (but still cold, frozen to bedrock) glaciers are favorable. They can serve as in situ laboratories, i.e. with temperature and deformation conditions that are not feasible in laboratory experiments and several orders closer to polar ice sheet conditions.

The strength of anisotropy is changing on different scales, from the macro-scale, i.e. hundreds of metres, to the micro-scale, i.e. the grain- and subgrain-scale. Different competing causes might be responsible for this scale-dependent evolution, including the initial surface conditions, the glacio-dynamical setting, and the influence of climate-dependent impurities incorporated in the glacier ice. The principal processes that drive the development of crystal-orientation fabric have been investigated for a long time and are largely understood (e.g. Gow and Williamson, 1976; Azuma and Higashi, 1985; Alley, 1992; Faria et al., 2014), often advanced by laboratory experiments (e.g. Jacka, 1984; Jacka and Jun, 2000; Treverrow et al., 2012) and fabric modelling on micro- and macro-scales (e.g. Faria et al., 2002; Thorsteinsson, 2002; Montagnat et al., 2013; Llorens et al., 2016b). However, under controlled laboratory or computing conditions these processes can be studied separately, while, in situ, a multitude of partially unconstrained variables, that may vary in dependence of each other, contribute to the resulting fabric. To predict the crystal-orientation fabric of a specific glacier system by only knowing the physical boundary conditions remains thus a distant objective (Treverrow et al., 2015). Meanwhile, in order to provide reliable estimates of the heterogeneous distribution of anisotropy strength for improving ice flow models that take anisotropy into account (e.g. Azuma, 1994; Gillet-Chaulet et al., 2005; Seddik et al., 2008; Martin et al., 2009; Gagliardini et al., 2009), there are currently three options for the assessment of the anisotropy at specific sites: a) By studying crystal-orientation fabric on ice core samples or b) by applying a fabric measuring borehole device or c) by inferring crystal-orientation fabric from the application of geophysical

1

1. Introduction

methods on the glacier surface, i.e. ground-penetrating radar (GPR) and seismic surveys.

The measurement of crystal-orientation fabric on thin section samples from polar ice cores by polarisation microscopy is an established method and provides a means to infer the deformation and recrystallisation regime for different depths, i.e. on the large scale, in a glacier (e.g. Gow and Williamson, 1976; Thorsteinsson et al., 1997; Azuma et al., 1999; Svensson et al., 2003; Wang et al., 2003; DiPrinzio et al., 2005; Gow and Meese, 2007; Durand et al., 2009; Montagnat et al., 2012; Montagnat et al., 2014; Fitzpatrick et al., 2014; Treverrow et al., 2016; Weikusat et al., in press). On the contrary, for non-polar glaciated regions only few studies of crystal-orientation fabric are known, most of which are not recent (Allen et al., 1960; Vallon et al., 1976; Hambrey and Müller, 1978; Hambrey et al., 1980; Tison and Hubbard, 2000). The polar ice core samples for the study of fabric on thin sections are typically spaced in intervals of the order of 10–50 m. Continuous measurements are not feasible with this time consuming method. While they provide an exact information on the local fabric, it should not a priori be assumed that it is representative for the laterally extended fabric in a larger region. The recently described technique of sonic logging for the continuous measurement of fabric in a borehole (Gusmeroli et al., 2012) suffers from the same limitation but overcomes the low sampling restriction, however, at the expense of detailed microstructure information, that is usually obtained together with the fabric information from ice core samples. The only means to obtain crystal-orientation fabric information on a lateral scale is by radar or seismics, which are applied to investigate the englacial structure and map the bedrock beneath the ice. Both methods are sensitive to changes in COF, among other properties. The attribution of recorded reflections to changes in COF is not straightforward and rarely unambiguous, but can provide strong evidence for some laterally extended COF changes (Eisen et al., 2007; Drews et al., 2012; Horgan et al., 2008; Horgan et al., 2011; Diez et al., 2013). However, the recognition of such fabric-induced reflections does not provide sufficient information to feed to anisotropic flow models. Only the combination of the above-mentioned methods will promote the progressive understanding of two- and possibly three-dimensional fabric structures in a glacier. A recent advance has been the linking of fabric data from ice core thin sections to seismic velocities via the elastic properties of polycrystalline ice (Diez and Eisen, 2015; Diez et al., 2015) based on early studies on the influence of anisotropy on the propagation of seismic waves (Bennett, 1968; Blankenship and Bentley, 1987).

Crystal-orientation fabric is not only an indicator for the glacio-dynamic regime but has been observed to be sensitive to a large change in dust load associated with a climatic transition, volcanic ash or basal microparticles (DiPrinzio et al., 2005; Samyn et al., 2005; Durand et al., 2007; Gow and Meese, 2007). The connection can be understood as a consequence of the softening effect of the impurities and microparticles on the ice polycrystal (Paterson, 1991; Thorsteinsson, 1996) and the resulting strong shear deformation. This dependency is often mentioned and investigated with regard to the pinning of grain boundaries by microparticles (e.g. Weiss et al., 2002; Song et al., 2008). The question arises if short-scale variations in dust, or more general, impurity content, which is governed by seasonal or annual deposition cycles, cause corresponding short-scale variations in crystal-orientation fabric.

From the above elaboration following questions can be identified:

- How variable is crystal-orientation fabric on a scale shorter than the typical sampling interval of 10–50 m and can this sampling be considered as representative?

2

- How variable is crystal-orientation fabric on a sub-sample scale that is not associated with a major climate transition (glacial/interglacial)?

- If there is a fabric variability on the short scale, can it be associated with an impurity content that varies on a seasonal, annual or multi-annual time scale, which would allow the development of crystal-orientation fabric as a climate proxy?

- If there is a fabric variability on the short scale, how would it influence the propagation of seismic waves?

- Principally, if the anisotropy can be assessed on different scales, which scale is the most revealing for the glacio-dynamic understanding of the entire glacier?

Therefore, to address these questions, it is essentiell to investigate crystal-orientation fabric on a short scale, of the order of centimetres, in the context of impurities and deformation processes on the microscale to improve the ice-dynamic understanding on all scales and provide refined input for the modelling of ice flow and the interpretation of seismic studies.

For a comprehensive study that is feasible within a limited time frame a site with polar-comparable conditions and processes but on a different, smaller scale is required. Thus, the focus is shifted to mid-latitude high mountain glaciers, as already discussed above. A unique site in the European Alps which meets these criteria is Colle Gnifetti (CG) at 4450 m above sea level (a.s.l.) in the summit region of the Monte Rosa massif in Switzerland/Italy (Wagenbach et al., 2012). At this small glacier saddle, the firn and ice are cold, i.e. below the pressure melting point, throughout the year and the net snow accumulation is low which leads to ice ages in the basal region in the range of 4000–10000 years before present (Bohleber, 2008; Jenk et al., 2009; Hoffmann, 2016), allowing for the establishment of long-time ice-physical processes as described for polar ice. Ice cores recovered from Colle Gnifetti enable the retrieval of unique environmental records of mid-latitude European climate and, although the ice is relatively pure due to the high altitude, its dust content is larger than in Holocene ice of polar cores by a factor of about 10 (Wagenbach and Geis, 1989), increasing the probability of observing a connection between fabric and dust load. Furthermore, Colle Gnifetti is an eligible site for the detailed study of fabric as the existence of anisotropic COF was inferred from seismic studies (Polom et al., 2014; Diez et al., 2014). Additionally, a small pilot study on crystal-orientation fabric in a CG ice core (pers. comm. Ilka Weikusat and Jan Eichler, 2013) provided indications of a high short-scale fabric variability, prompting an in-depth investigation.

The present thesis shows the results of the first extensive study of crystal orientation and microstructure along a cold Alpine ice core in an unprecedented coverage and resolution. The main objectives are to:

1. Sample an Alpine ice core in continuous ranges, i.e. several successive thin sections between intervals, instead of the typically applied sampling of only one thin section per interval. This will provide the necessary data for short-scale investigations.

2. Characterise the evolution of crystal-orientation fabric based on thin section data obtained with polarisation microscopy and microstructure scanning.

3. Determine the anisotropy variability of the polycrystal on the scale of centimetres to decimetres.

4. Identify the likely mechanisms responsible for short-scale anisotropy variability by comparing the fabric data with complementary ice core data. Specifically, the impurity data from melt analysis is considered as a potential driver for short-scale fabric variations.

5. Assess the relevance of short-scale anisotropy variations for the interpretation of seismic studies of the glacier structure.

The fabric and microstructure of ice samples from other non-polar sites (Grenzgletscher and Chli Titlis, Switzerland; Kilimanjaro, Tanzania) were measured during the course of this study; however, the results are not included in the present thesis.

The thesis is organised as follows:

- Chapter 2 provides the theoretical background of crystal-orientation fabric development considering the physical properties and processes in ice including the influence of deformation, recrystallisation and impurity content, concluding with an introduction to the parameters used in this thesis.

- The study sites and methods of data acquisition are described in chapter 3 with a comprehensive section on data processing.

- Chapter 4 concentrates on the fabric analysis of a cold Alpine ice core, including a stratigraphical description and classification approach to the entire ice core. A classical assessment of the fabric evolution with depth in the glacier is followed by the high-resolution analysis of the fabric data. The microstructure, i.e. pores and grains, is analysed to provide supplementary information for the interpretation of the fabric results. The observations of distinct cm-scale variations in crystal-orientation fabric in the Alpine fabric data are reported.

- Their origin is investigated in chapter 5 through the comparison with climate proxy data from continuous-flow analysis, addressing the hypothesis of short-scale fabric variability conveying information on local climatic conditions. A pilot study demonstrating the potential of laser ablation-inductively coupled plasma-mass spectrometry for the investigation of the spatial distribution of impurities in relation to the ice microstructure is included.

- Chapter 6 is dedicated to the derivation of seismic velocities in arbitrarily anisotropic ice using the information from fabric data. By applying an exact calculation of seismic velocities from COF data to the fabric data of an Alpine core and a polar core from Antarctica an earlier calculation framework by Diez and Eisen (2015) is revisited and implications for the future combination of seismic measurements and fabric data are discussed.

Each result chapter concludes with a discussion of the particular findings. Chapter 7 reflects the results and provides an outlook on future work following the perceptions of this thesis.

2 Theory of crystal orientation fabric evolution

Section 2.1 explains the optical and mechanical anisotropy of hexagonal ice crystals and section 2.2 introduces the metamorphosis of snow to ice. The process of how crystal-orientation fabric evolves with depth in a stratified ice body depends on time, impurity content, and temperature and deformation regime. The respective contributions of these influences according to current knowledge are summarised in sections 2.3 and 2.4. An overview on the parameters used in this thesis to describe crystal-orientation fabric and ice microstructure is given in 2.5.

2.1 The anisotropy of ice I$_h$

Under natural conditions on the Earth's surface, as in a glacier, water molecules crystallise in a hexagonal lattice to the so-called ice I$_h$. In this lattice the oxygen molecules are organised in layers of hexagonal rings that form the basal planes of the crystal (Fig. 2.1) that lie perpendicular to the crystal lattice unit cell's c-axis. Extensive information on the crystal structure can be found in, e.g., Petrenko and Whitworth (1999). The c-axis is the crystallographic symmetry
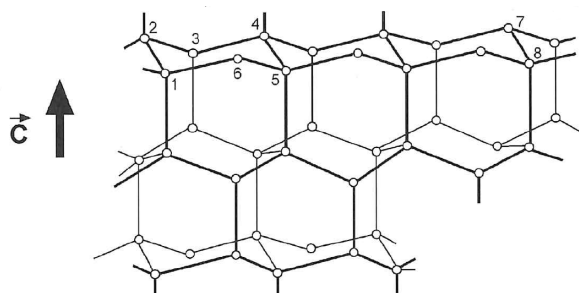
Fig. 2.1: Crystal structure of Ice I$_h$: Oxygen molecules forming layers of hexagonal rings (Cuffey and Paterson, 2010).

axis of the hexagonal crystal and defines the direction of the mechanical and optical anisotropy of the crystal. The basal planes provide a ready mechanism for easy deformation by sliping past each other, depending on the direction of an applied stress with respect to the c-axis (section 2.3). The deformation perpendicular to the basal planes is much harder, by two orders of magnitude (Duval et al., 1983). This mechanical anisotropy plays a center role in the creep of glacier masses and it is crucial to study how the anisotropy changes in a glacier and under various conditions to improve the understanding of ice dynamics on every scale.

For a polycrystal, the ensemble of c-axes of the individual crystals is referred to as crystal-orientation fabric[1] (COF). If the c-axes of an ensemble are uniformly distributed, the net effect is that of an isotropic polycrystal. Else, the polycrystal has a preferred orientation. If all c-axes are oriented parallel, the fabric exhibits a single maximum and has its maximum strength. Preferred orientations in ice polycrystals result from the fact that c-axes tend to

---

[1]This term is used in this thesis. Alternative terms as described in appendix A. are commonly used by some authors.

rotate towards compressional axes and away from extensional axes to minimise the local stress (Gow and Williamson, 1976), e.g. the vertical compression axis in a stratified glacier. This is achieved by a combination of deformation and recrystallisation, depending on the stress field and temperature regime (Faria et al., 2014). Different patterns of crystal-orientation fabric are observed (Alley, 1992; Cuffey and Paterson, 2010), e.g. single maximum or girdle fabric, and can be interpreted to infer the deformation and recrystallisation regime (e.g. Azuma et al., 1999; DiPrinzio et al., 2005; Fitzpatrick et al., 2014).

For the study of crystal-orientation fabric the optical anisotropy inherent to an ice crystal is exploited. Ice I_h can be classified as a positive uniaxial birefringent mineral, i.e. its refractive index depends on the polarisation and propagation direction of light. For light that travels parallel to the c-axis with an arbitrary polarisation and light that travels perpendicular to the c-axis with a polarisation perpendicular to the c-axis the refractive index n_o is smaller than for light that travels in the basal plane but with a polarisation parallel to the c-axis with refractive index n_e (e.g. Petrenko and Whitworth, 1999). The value of both extreme indices depends on the wavelength of the light source, i.e. the shorter wavelengths have larger indices. For a wavelength of 589 nm the refractive indices are $n_o = 1.3091$ and $n_e = 1.3105$ at -3.6 °C. Ice is only weakly birefingent with a birefringence of $\delta n(589\,\text{nm}) = n_e - n_o = 0.0014$, which is two orders smaller than the birefringence of calcite.

Polarised light microscopy

The optical anisotropy of ice is used in polarised light microscopy to determine the orientation of the c-axis in a thin section. The thin section is placed between crossed polarisers. The incident polarised wave is split in two wave trains with different speeds according to the refractive indices of ordinary and extraordinary ray. Upon emergence from the thin section they recombine with a phase difference $\Delta\phi = 2\pi\,\delta n\,d/\lambda_0$ which depends on the birefringence, the wavelength λ in free space and the thickness d of the section. As some wavelengths might be eliminated from the analyser, the crystals will appear colored. If the c-axis of a grain lies parallel to either polariser or analyser, the light will not be transmitted and the grain appears dark. To find the direction of the c-axis in a grain the section and the crossed polarisers need to be rotated with respect to each other. The finer details of the procedure can be found in, e.g., Wilson et al. (2003); Peternell et al. (2009).

2.2 From snow to ice

Snow accumulates in polar or high-altitude regions and under suitable conditions the densification process begins to turn the snow into firn. This process is driven thermodynamically by the reduction of the free energy of the system and involves the rounding of ice particles, the formation of necks between them and redistribution of material by sublimation. The firn grows less porous as the load pressure of the snow cover increases. At a density of $830\,\text{m/kg}^3$ the previously connected pores close off and become bubbles, this defines the firn-ice-transition (FIT). The density is further increased by the compression of these bubbles and reaches $917\,\text{m/kg}^3$ for bubble-free ice. High firn temperatures and the presence of melt is a strongly contributing factor in the snow consolidation process, also influencing the deeper stages of densification, and particularly relevant in high-altitude regions in the mid-latitudes where the insolation is stronger and the firn temperature is higher than in polar regions. Freitag et al. (2013) provide

strong evidence that the densification in deep firn is substantially influenced by stratified impurity content, apparently independent of the mean impurity concentration. Fujita et al. (2009) observe a clustering of c-axes in the firn in changing dependence of the density.

The growth of ice crystals in snow is governed by the temperature and vapour pressure regime during snow formation and accumulation (Petrenko and Whitworth, 1999), as well as the temperature gradient in the snow (Pinzer et al., 2012). This controls, e.g., if crystals grow faster along the a-axis (plates) or the c-axis (prisms), introducing a preferential orientation in the snow cover (Adams and Miller, 2003). Riche et al. (2013) observe an initially anisotropic crystal orientation in the snowpack which changed under a temperature gradient and in dependence of the density. These initial conditions may well determine the subsequent processes in the firn, including deformation and recrystallisation, to a certain degree, but no complete understanding of the evolution of crystal-orientation fabric in firn, considering the multitude of connected processes, has emerged. However, Kennedy et al. (2013) model the evolution of crystal-orientation fabric, taking into account dynamic recrystallisation (section 2.3), and claim that the initial variations in fabric induced by a climatic perturbation will be preserved in the depth of an ice sheet.

2.3 Deformation mechanisms and recrystallisation processes

The internal deformation of an ice body largely determines its dynamical behaviour. While the flow (or creep) of a glacier is described using bulk properties, they depend on the various processes on the microscale, most notably on recrystallisation. Abundant literature, e.g. Cuffey and Paterson (2010); Petrenko and Whitworth (1999); Schulson and Duval (2009), summarise in detail the state of scientific knowledge on this complex topic that has grown for many decades and is under constant development. Only a short summary of the most important aspects is outlined here, with links to current advances (Faria et al., 2014; Llorens et al., 2016a; Llorens et al., 2016b).

The most important mechanism for plastic deformation of an ice crystal is, on the intragranular scale, basal slip (or basal glide), i.e. the motion of dislocations along the basal plane, if there is a resolved shear stress component on the basal plane (e.g. Duval et al., 1983; Hondoh, 2000, etc.). The rate of shear deformation increases with stress according to a power law (Glen, 1955). Slip on the combined slip systems leads to a rotation of the grain, thus contributing to a preferred crystal orientation. According to the von Mises criterion (Von Mises, 1928), basal slip needs to be accommodated by additional slip systems (prismatic and pyramidal slip) or by other deformation mechanisms. Goldsby and Kohlstedt (2001) proposed that grain-boundary sliding (GBS) is an alternative mechanism, which is activated at low stress. In this case, grains slide past each other along their boundaries. GBS is grain size-sensitive, and may also depend on the orientation and curvature of grain boundaries (GB), as well as the impurity content ("micro shear", Faria et al., 2014). GBS cannot occur independently as geometric incompatibilities between the crystals would arise.

Recrystallisation refers to the reordering of the crystal lattice and the associated shifts and reorganisation of grain boundaries, driven by the reduction of free energy. It is reflected in changes of fabric and, particularly, the microstructure of the polycrystal. Irrespective of a driving stress,

normal grain growth (NGG) is a process in which the grain size of some grains increases on the expense of other, smaller grains, governed by the curvature of the grain boundaries (Alley et al., 1986). As a result, the mean cross-sectional area is expected to increase linearly with the age of the ice and in dependence of the temperature, but also influenced by impurities (section 2.4). In polar firn with high temperature ($> -20\,°\text{C}$) growth rates of $0.02\,\text{mm}^2/\text{year}$ have been observed (Cuffey and Paterson, 2010). Dynamic recrystallisation (DRX) occurs as a response to the deformation. Bending of grains can lead to the alignment of dislocations to form new grain boundaries and the subdivision of a grain, this is termed polygonisation or rotation recrystallisation (RRX) and deemed the "most fundamental mechanism to [...] accommodate strain in ice" (Faria et al., 2014). It decreases the mean grain size and, thus, counteracts normal grain growth, but the orientation of the new grain will not differ much from the original grain. The recrystallisation by migrating GBs into grains with higher stored energy, i.e. a higher dislocation density due to deformation, has an effect on the crystal-orientation fabric of the polycrystal (strain-induced boundary migration (SIBM-O), Faria et al., 2014). Similarly, new grains can nucleate with orientations that are in favor of basal slip (SIBM-N). At high stresses this leads to a reduction of average grain size. The different mechanism were understood to be active in different depths of a glacier, but this view has been challenged by more recent studies (e.g. Kipfstuhl et al., 2009; Weikusat et al., 2009) and a new approach for the allocation of recrystallisation processes based on strain rate, temperature and mean grain size was proposed by Faria et al. (2014). However, numerical modelling of ice deformation suggests that dynamic recrystallisation has a much larger effect on the microstructure than on the fabric (Llorens et al., 2016a). Complementary, Llorens et al. (2016b) observe in their simulations that a single maximum will develop quickly under simple shear, which is the expected dominant stress regime in the deeper part of mountain glaciers (Cuffey and Paterson, 2010), but largely independently of recrystallisation. Further, first numerical simulations additionally including air inclusions reveal an enhanced localisation of strain between bubbles and hint at a heterogeneous deformation in the firn which is only secondarily controlled by crystallographic orientations (Steinbach et al., in review).

2.4 Influence of impurities in polycrystalline ice

Impurities in ice are commonly differentiated in soluble impurities, i.e. ions, and particulate impurities, e.g. terrestial mineral dust and other microparticles. They originate from aerosols that are transported in the atmosphere to be deposited on the glacier surface. The different species are indicators for seasonal environmental cycles in, e.g., ocean and biosphere, and, more recently, for human activity. The stratified impurity content in ice cores is crucial for the dating by annual-layer counting and allows for a reconstruction of past climate conditions. However, when impurities are incorporated into the snow, they become an agent in the various processes described above. Many studies investigate the interaction of different species with the crystal lattice and the influence on deformation and recrystallisation processes. Of particular interest is the spatial distribution of impurities with respect to the microstructure in order to reveal their contribution to specific processes. The magnitude of impurity concentration, the stress regime, temperature and depth in the ice column are all contributing factors and complicate the disclosure of direct dependencies.

Alley et al. (1986) suggested that normal grain growth is impeded by the pinning of GBs by

impurities and bubbles, slowing down the motion of GBs. Paterson (1991) build on that, reporting that chloride and sulphate ions reduce the grain growth at high concentrations. Alley and Woods (1996) further observe that high ammonium concentrations will especially correlate with slowed down grain growth. An associated softening effect (Paterson, 1991) of impurity-enriched ice is attributed to an increase in dislocation mobility (Schulson and Duval, 2009). Several studies on polar ice state that impurities can be found throughout the ice (e.g. Baker et al., 2003), while specific species were found to preferentially accumulate heterogeneously. A study from Mulvaney et al. (1988) revealed that sulphuric acid in polar ice almost entirely accumulates in triple junctions, whereas it was concluded that sodium must be distributed in the grain interior. Contrarily, filaments along GBs, largely consisting of concentrated sodium and chloride, were described by Cullen and Baker (2000). Dust particles were found to consist of magnesium, aluminium, silicate, chloride, potassium, calcium and iron, and were also found in grain boundaries (Baker et al., 2003; Barnes et al., 2002). A comprehensive study by Barnes and Wolff (2004) provides an overview over several impurity localisations in different polar ice samples. As mechanism for the accumulation in GBs, Iliescu and Baker (2008) propose that during strain-induced boundary migration impurities are driven from the recrystallised lattice. They remark that the influence of soluble impurities on GB mobility is dependent on the concentration. Song et al. (2008) found in experiments that the nucleation of new grains under stress is enhanced by a particle load. Weiss et al. (2002) find evidence that the pinning of GBs is realised by dust particles and able to explain the changing microstructure at glacial-interglacial climatic transitions, while a high concentration of solubles will not necessarily affect the grain growth. This is confirmed by Durand et al. (2006a) by modeling the grain size evolution taking into account normal grain growth, rotation recrystallisation and pinning of microparticles. However, Faria et al. (2010) inspect the interaction between visible microparticles and GBs and cannot find evidence of much interaction in glacial ice.

From the collected results of the multitude of studies, from which only a few were introduced here, no comprehensive theory on impurity-microstructure interaction has emerged yet, but the most general observation is that of average grain size reduction at high impurity concentrations. Specifically, in Holocene, mid-latitude glacier ice, where impurity concentrations are higher, but variability is much smaller than the change in impurity load during a climatic transition, the perceptions from impurity interaction with polar ice microstructure on large scales might be questionable.

2.5 Fabric and microstructure parameters

The parameters used in this thesis to quantify and describe the fabric and microstructure of thin section samples largely follow the review by Durand et al. (2006b). Further, definitions from Eichler (2013) apply as are described for the programme `cAxes`. The parameters are briefly introduced here.

- The **c-axis** of a crystal is expressed as a vector in spherical coordinates with unit length:

$$\boldsymbol{c} = \begin{pmatrix} \sin(\varphi)\cos(\vartheta) \\ \sin(\varphi)\sin(\vartheta) \\ \cos(\varphi) \end{pmatrix} \tag{2.1}$$

with colatitude angle $\varphi \in [0, \pi/2]$ and azimuth angle $\vartheta \in [0, 2\pi]$ (Fig. 2.2).

Fig. 2.2: The global coordinate system $\{x, y, z\}$ used for the description of a c-axis (purple) with unit length: Spherical coordinates ϑ and φ (green) specify the orientation of the c-axis. For each grain the c-axis can be expressed in its local coordinate system $\{p, q, r\}$ by $(0, 0, 1)$; p,q are not shown here. The equatorial plane (grey) corresponds to the thin section plane.
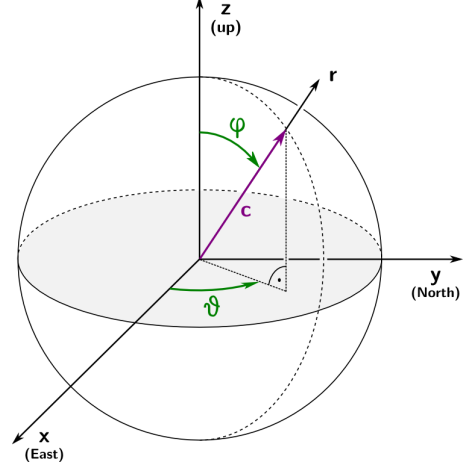
- The next neighbour **misorientation angle** γ is the angle between the c-axes of two adjacent grains:

$$\gamma_{i,j} = \arccos(\boldsymbol{c_i} \cdot \boldsymbol{c_j}) \tag{2.2}$$

- The **grain cross-section area** A from a thin section is taken as an estimate of the grain size. It is not a true representation of the grain size as the cross-section will likely cut through a grain where its radius is smaller than the maximum radius. The mean grain size $\bar{A}$ and the median grain size $\tilde{A}$ computed from the cross-section area are used to characterise the grain distribution:

$$\bar{A} = \frac{1}{N_{\mathrm{g}}} \sum_{i=1}^{N_{\mathrm{g}}} A_i \tag{2.3}$$

- The **bubble cross-section area** A_{B} $(\bar{A}_{\mathrm{B}}, \tilde{A}_{\mathrm{B}})$ is analoguously used as an estimate of the air bubble size.

- The **second-order orientation tensor** $a_{ij}^{(2)}$ provides a reference frame-invariant description of the c-axis distribution:

$$\boldsymbol{a}^{(2)} = \frac{1}{N_{\mathrm{g}}} \sum_{i=1}^{N_g} f_i^{\alpha} \boldsymbol{c}_i \otimes \boldsymbol{c}_i \qquad \text{with} \qquad f_i^{\alpha} = \frac{A_i^{\alpha}}{\sum_i^{N_{\mathrm{g}}} A_i^{\alpha}} \tag{2.4}$$

with the area-weighted volume fraction f_i^{α} as a grain-dependent weighting factor recommended by Gagliardini et al. (2004, $\alpha \neq 0$) in order to obtain an improved fabric description as compared to equal contributions of the grains to the orientation tensor. Given that the fabric influences the viscosity of the bulk material, it is sensible to include the volumetric information in the fabric description. The symmetric orientation tensor can be understood analoguously to the inertia matrix of a mass distribution with three principal axes and corresponding **eigenvalues**[2] $\lambda_{1,2,3}$ with $\lambda_1 < \lambda_2 < \lambda_3$ and $\sum_i \lambda_i = 1$.

---

[2]Depending on the publication the eigenvalue indices are assigned in reverse order.

For an isotropic distribution of c-axes the eigenvalues are equal with $\lambda_{1,2,3} = 1/3$. A perfect single maximum is defined by $\lambda_{1,2} = 0$ and $\lambda_3 = 1$. The c-axis eigenvalue λ_3 can be interpreted as a measure of the fabric strength, especially if the fabric predominantly consists of cluster fabric.

- The **uncertainty** σ_λ of the derived eigenvalues can be quantified as a function of the number N_g of c-axes from which the eigenvalues are computed (Durand et al., 2006b, eq. 26):

$$\sigma_\lambda = (-1.64 \cdot \lambda^2 + 1.86\lambda - 0.14) \cdot \frac{1}{\sqrt{N_g}} \qquad (2.5)$$

- The **woodcock parameter** κ (Woodcock, 1977) serves as classification criterion to distinguish between cluster ($\kappa > 1$) and girdle fabric ($\kappa < 1$):

$$\kappa = \frac{\ln(\lambda_3/\lambda_2)}{\ln(\lambda_2/\lambda_1)} \qquad (2.6)$$

- The **grain boundary linearity** ℓ denotes the ratio of the distance between triple junctions and the actual length of the grain boundary segment between the triple junctions. It equals 1 for a straight boundary, i.e. without undulations or curvature.

- The bubble **circularity** C_B is given by $4\pi \cdot A_B/[\text{bubble perimeter}]^2$. The bubble **aspect ratio** AR is the ratio between the major and minor axis of an ellipse that is fitted to a bubble cross-section area. Both parameters describe the deviation from a perfect circular shape.

The fabric of a sample is often illustrated in a Schmidt diagram which is the Lambert azimuthal equal-area projection of a unit hemisphere to a disk, i.e. spherical coordinates (φ, ϑ) become polar coordinates (R, ϑ). A c-axis is then represented by a dot, which is the projection of the intersection of the c-axis with the hemisphere, to the radius R. Conventionally, the c-axis distribution is projected to the equatorial plane, i.e. the centre of the projection corresponds to the vertical, core-axis parallel orientation. For vertically cut thin sections the c-axis angles have to be transformed to the horizontal reference frame.
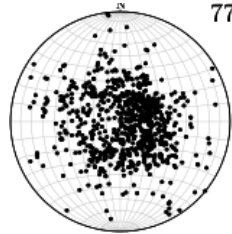
Fig. 2.3: Exemplary schmidt diagram for a thin section with 776 grains forming a weak cluster fabric (48-01 from KCC ice core).

3 Methods and materials – Data acquisition

The regions of origin of the studied glacier ice samples are introduced (sections 3.1, 3.2). All methods used for the acquirement of data which are presented and analysed in this thesis are described in this chapter. Image data (section 3.3) on the fabric and microstructure of cold Alpine glacier ice as well as laser ablation data (section 3.5.2) were collected within the frame of this study, while data from continuous flow analysis (section 3.5.1) and from a polar ice core were provided from collaborating institutes. The processing of the collected image data is detailed in section 3.4. A short glossary clarifies some recurring terms used within this thesis (appendix A., p. 135).

3.1 Alpine ice core KCC

3.1.1 Colle Gnifetti site description

Colle Gnifetti is located about 14 km southeast of Zermatt (Wallis, Switzerland) in the Monte Rosa massif of the Swiss-Italian Alps. It forms a saddle between the two high-Alpine peaks Zumsteinspitze and Signalkuppe (Fig. 3.1) with an extent of less than 700 m between the peaks and about 500 m between a steep ice cliff in the northeast and the descent to the onset of Grenzgletscher in the west. The saddle point lies at an altitude of 4450 m a.s.l. and the glacier thickness is of the order of 100 m, about a third to half of which consists of firn. It is one of few high-altitude sites in the Alps where the ice body is still cold, i.e. below 0 °C, throughout the year (Hoelzle et al., 2011), frozen to bedrock (Haeberli and Funk, 1991) and with a stable surface geometry for the last century (Lüthi and Funk, 2000), motivating numerous ice core, glaciological and geophysical studies for more than 40 years. A recent literature overview and detailed description of the glaciological setting can be found in Wagenbach et al. (2012). Some aspects relevant for this study are sketched in the following.

Refrozen melt layers occur regularly in the snow dependent on the degree of exposure to solar radiation and percolation features are observed (Alean et al., 1983). The saddle is thus classified to lie in the recrystallisation-infiltration zone (e.g. Bohleber et al., 2013). The net snow accumulation is highly variable over the saddle, partially dependent on the local occurrence of melt layers in combination with strong westerly winds that cause the loss of a significant portion of the annual snow accumulation over the ice cliff in the northeast (e.g. Haeberli and Alean, 1985). This results in an exceptionally low net accumulation on the southern slope of the saddle towards the ice cliff as low as 0.15 m w.e./year (Bohleber, 2011), mainly consisting of denser summer snow (Wagenbach and Geis, 1989), but years with exceptionally high accumulation (pers. comm. Carlo Licciulli, 2015) or complete loss of precipitation have been observed. Rapid annual layer thinning is a result from this glacio-dynamic setting as discussed by Bohleber (2011).

3.1.2 Drilling and processing of ice core KCC

In August 2013 the ice core KCC was drilled on the southern flank of CG by the Institute of Environmental Physics Heidelberg (IUP), in collaboration with the Institute of Physics, Section Climate and Environmental Physics of the University of Bern (KUP) and the Climate Change Institute of the University of Maine (CCI). The drilling site (N45° 55.736, E7° 52.576, 4484 m a.s.l., Fig. 3.2) is located approximately on the same flow line as the previously drilled ice core KCI (Fig. 3.1). The mean net accumulation was calculated from the depth of the tritium peak to 22.4 m water equivalent[1] (w.e.) per year (pers. comm. H. Hoffmann, 2014).

Fig. 3.1: Photo of Colle Gnifetti (courtesy of P. Bohleber) facing southeast with ice core positions on indicated flowlines.
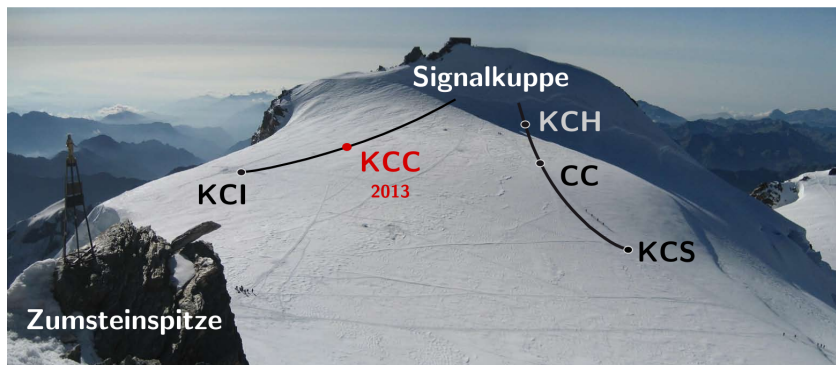
Fig. 3.2: Map of Colle Gnifetti with the position of KCC at N45° 55.736, E7° 52.576 ©swisstopo.

At a depth of about 72 m the drilling had to be stopped when presumably bedrock was reached. Small stones in the core were noticed in the last few metres. The core consists of 101 runs[2]. The core was transported at −20 °C in polystyrene boxes via train and truck from Zermatt to Bremerhaven and stored at −20 °C before processing.

The temperature in the borehole of KCC was measured in September 2014. It increases almost linearly from −13.5 °C at about 10 m depth to −12.4 °C at bedrock (pers. comm. M. Hoelzle, University of Fribourg, 2014).

---

[1] The water equivalent is the height of a water column resulting from melting the snow column.

[2] A run may have suffered breaks during the drilling and consist of several pieces, indicated by letters a,b.

Bedrock and surface slope

Eisen et al. (2003), Bohleber (2011) and Konrad et al. (2013) investigate the bedrock topography as well as the englacial structure of Colle Gnifetti by using GPR. Ice thickness was calculated from these measurements. In 2014 and 2015 new surface elevation measurements were conducted by the IUP (pers. comm. Carlo Licciulli). Fig. 3.3 illustrates the bedrock and glacier surface slope along a GPR profile measured in 2008 (Fig. 1 in Konrad et al., 2013, Profile F3). The ice core KCC was drilled in 4 m distance to the arched GPR profile. The average slope of bedrock and surface along the 180 m long profile are estimated to be about 20 % and 17 % respectively. There seems to be some roughness in the bedrock topography in the area of interest. From the radargrams the ice thickness at the KCC drilling site was not expected to exceed 63 m. However, the error in estimated thickness from GPR can be as large as 25 %. It might well be that the drilling took place over a local depression with unknown bedrock slope.
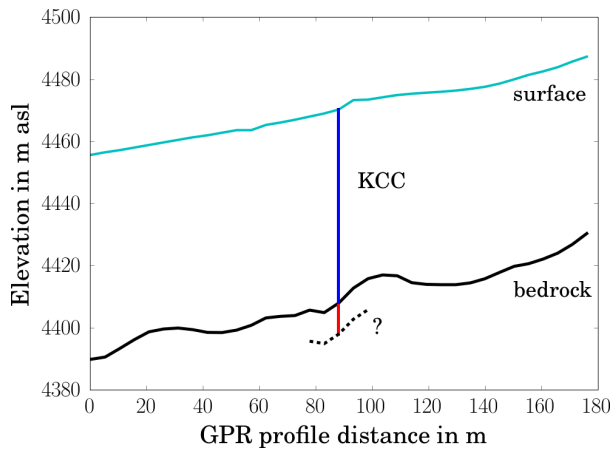
Fig. 3.3: Sketch of bedrock and surface elevation along the GPR profile F3 (Konrad et al., 2013) approx. parallel to a flowline uphill from northeast to south. Approximate position of the KCC borehole with the deeper than expected basal section of the core in red.

Aliquoting and early measurements

The processing took place at the ice laboratory of the Alfred Wegener Institute Helmholtz Centre for Polar and Marine Research (AWI). The 4-inch core was aliquoted as shown in Fig. 3.4 for subsequent measurements after logging, weighing, dielectric profiling, and microtomography (μCT, 2D scans: X2D) measurements on the full core pieces. Line scans were recorded from the middle slice before the aliquoting for physical properties (PP), continuous flow analysis (CFA) and radiocarbon dating (^{14}C). It should be noted that the surface of the PP aliquot measures only 3.4 cm in width; for many cores the upper aliquot with a width of about 7 cm is designated to be used for PP measurements. In order to avoid further material loss to the PP aliquot due to core catcher notches each core piece was rotated before the first cut if deemed necessary and the rotation was noted in hours, i.e. in multiples of 30° (Tab. 3.1, p. 23). The PP aliquots were packed in 0.1 μm thin plastic bags to avoid the bending of the ice samples during storage. The samples were stored at -20 °C until the measurements.

Depth scale

The most important information common for all measurements is the depth information to be able to align any results on a single scale. Due to the relatively short length of the core pieces

Fig. 3.4: Aliquoting scheme for KCC. The red line indicates the surface of prior interest for this study. The blue line indicates the surface exposed to line scan imaging and for laser ablation measurements (section 3.5.2, p. 32).
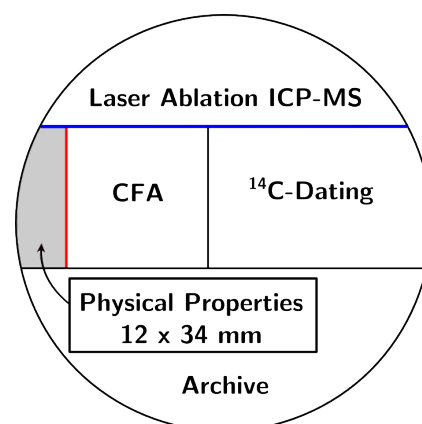
it was refrained from sawing the core into metre long sections (bags) that would make it easier to refer to depth (i.e. one metre ice core per one metre depth) but would contain almost always several pieces. Instead, during the logging of the core at AWI, each piece of the core received a mark at the last full 10 cm on the piece as measured from the top of the core and the total depth of the marker was noted. The marks were used for all further measurements to link the results to the depth scale, however, with the exception of line scan and μCT, which were less straightforward to link to the scale as is detailed in the respective sections below. The total depth of the core was measured to be 71.95 m, including the 1.60 m deep snow pit at the surface.

Fig. 3.5: Photo of KCC PP-aliquot with pencil marker for maintaining a common depth scale.
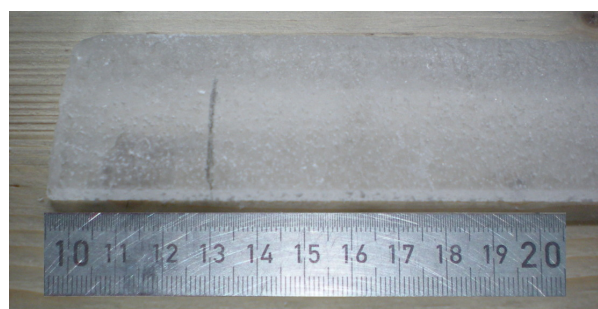
Density profile

From the weighing and volume of the single runs bulk density in coarse resolution was determined. The X2D measurements (Fig. 3.6) were used to derive the density in sub-mm resolution (pers. comm. Johannes Freitag, 2014; Freitag et al., 2004). Below 50 m depth the calculation was abandoned due to larger errors mainly induced by inclined layers. The initial depth scale used for the X2D density has a non-linear cumulative depth shift compared to the marker depth scale commonly used for the other data sets. A correction for the X2D depth scale was later derived as follows (Fig. B.6, p. 155):

- The position of each marker relative to the top of each run was measured along the ^{14}C aliquots.

- The top depth of the runs was then calculated from the absolute depth of the markers which was noted during the continuous logging.
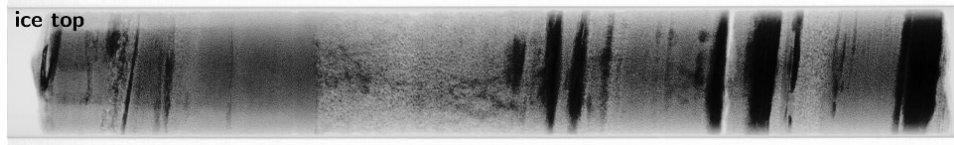
Fig. 3.6: Exemplary X2D image from μCT measurement of KCC (run 7, 87 cm long, from 6.4 m depth) used for the derivation of high resolution density. A horizontal (i.e. perpendicular to ice core axis) 1 cm wide section of about 250 px is considered for the calculation of each value. Note the influence of the layer inclination. Ice layers are visible in black.

- Due to the often sloping or even jagged ends of the runs their measured lengths might depend on the aliquot and deviate from the lengths measured during the original logging of the whole core pieces. The occasional length discrepancy between the ^{14}C aliquots and the logged lengths of the whole core was considered for the tuning of the new top depth scale.

- The X2D density data were run-wise shifted upwards in depth to meet the depths of the new top depth scale. The depth uncertainty is within a few centimetres (Fig. 3.7).
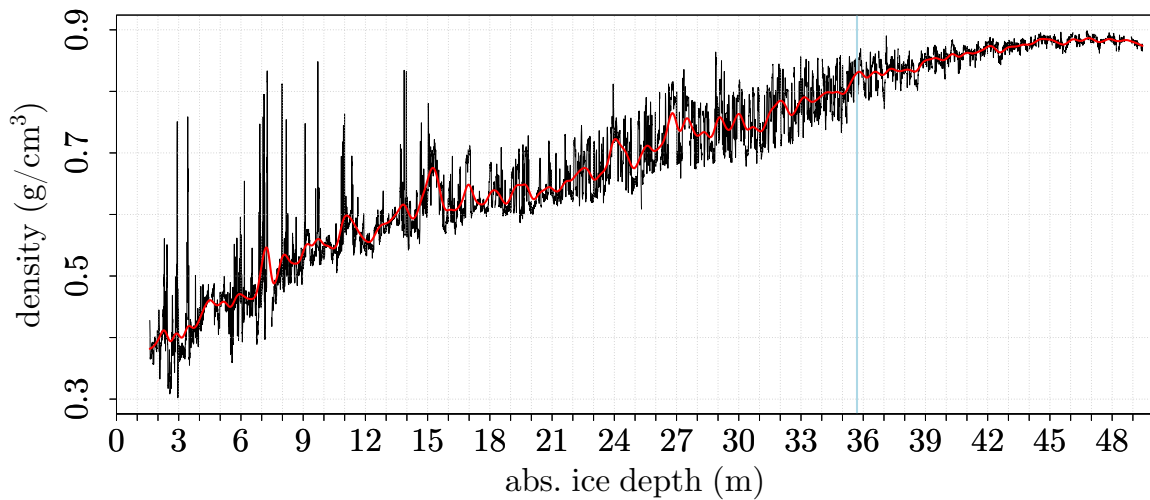
Fig. 3.7: High resolution density for the upper 50 m of the KCC ice core with corrected depth scale. The high resolution density data were smoothed with a bandwidth of 0.005 m and 0.5 m (red). The depth of the firn-ice-transition is indicated in lightblue.

From Fig. 3.7 the firn-ice-transition is estimated from the smoothed density (red curve) to be at approximately 35.7 m depth, where a density of 830 kg/m^3 is reached.

3.2 Polar ice core EDML

Within the European Project of Ice Coring in Antarctica (EPICA) an ice core was drilled in 2001-2006 at Kohnen Station[3], Dronning Maud Land, Antarctica at 75°00'S, 00°04'E. The EDML ice core was drilled to a depth of 2774.15 m.

Available fabric data

All of the fabric data from EDML were measured at AWI using the G50 instrument (section 3.3.1) and the earlier model G20 from the same manufacturer (data sets: Weikusat et al., 2013a; Weikusat et al., 2013b). About half of the thin sections are cut vertically, i.e. parallel to the ice core axis, the other half consists of horizontal thin sections, i.e. cut perpendicular to the vertical. Often a horizontal and a vertical section were prepared from the same core piece (bag). The intervals between sampled bags are of the order of 50 m but more recently some bags in the deep part of the ice core were measured with higher resolution, i.e. 10 thin sections from one bag were prepared continuously (Weikusat et al., in press). The fabric data are supplied as pairs of polar angles ϑ, φ for the c-axis of each grain in a thin section and were derived manually from each section when measured with the G20 instrument, and extracted automatically with `cAxes` as described in section 3.4 for image data from the G50 instrument. As there is no grain area data available from the G20 samples, statistical weighting with grain size during eigenvalue calculation is not feasible. No information on the azimuth of the core pieces is available, but their relative orientation has been tried to retain (Weikusat et al., in press). An overview of the EDML thin section samples used in this work can be found in appendix B.2 (p. 148).

3.3 Measurement of fabric and microstructure

The principal preparation and measurement routine for the combined Fabric Analyser (FA) and Large Area Scanning Macroscope (LASM) measurements that was applied in this study was detailed as a tutorial and can be found in appendix B.1 (p. 136), including various images of instruments and data examples. The individual parameters of each measurement procedure, most importantly the position of the marker on each aliquot, were noted and sketched in detail[4].

3.3.1 Fabric Analyser G50

For the measurements of COF from thin sections an automated fabric analyser system was used. The particular instrument at AWI's ice laboratory is a G50 model manufactured by Russell-Head Instruments (for a detailed description see, e.g., Wilson et al., 2003). The technique of polarised light microscopy applied by the instrument is based on the optical anisotropy (birefringence) of the analysed material (section 2.1, p. 5) and measures the light amplitude for each pixel of the defined measurement area under rotating crossed polarisers. From an appropriate fit to these discret values the extinction angle for each pixel can be calculated. Thus, for each pixel the c-axis azimuth and colatitude angles are determined. Two quality

---

[3]http://www.awi.de/expedition/stationen/kohnen-station.html

[4]Handwritten laboratory notes are provided as supplement to the PANGAEA® data archive.

parameters, geometric and retardation quality, are produced and provide uncertainty estimates of the c-axis determination (Peternell et al., 2009).

Sources of inaccuracy

Several factors influence the accuracy of the FA measurement, associated with both the instrument and the sample. Peternell et al. (2009) provides a more detailed discussion on these factors.

- For some of the initially prepared thin sections the FA had difficulties with the precision of its polarisers which produced a poor quality pattern associated with the measurement tiles[5]. The poor quality sections were later remeasured. A few more sections exhibit the pattern, although to a lesser extent. Notably, areas with smaller grains seem to be more affected (Fig. 3.8), the reason for this is not yet understood. The quality information is used as a threshold for the data suitability for further processing steps.

- For many samples a systematic gradient of angle values towards the tile borders can be observed (discussed in Eichler, 2013).

- Even with the G50 system c-axes which lie in the plane of the thin section cannot be measured as accurate, resulting in a systematic lower quality assignment (Weikusat et al., in press). As only vertical sections are prepared for this study, this affects especially close-to-vertical c-axes; this can be observed sometimes on pole figures (less poles on the vertical great-circle).

- Sample thickness: The thin sections are 200–350 μm thin due to repeated surface preparation and additional microtoming on some sections after the occurence of unevenly bending microtome blades. The difference in thickness affects the degree to which tilted boundaries are causing uncertainties in the automated image analysis approach. The thicker the sections the higher the influence of a tilted boundary with an apparent width on the detectability of the adjacent grains.

- Especially for the firn samples with a larger percentage of pore space surface, which is exposed during the sublimation period, the area of the pore-adjacent grains is decreasing with time as is illustrated in Fig. 3.9 and investigated by Horn (2010). Along with the change in pore space and shape GBs may also shift very quickly.

- Similarly, the width of the sublimation grooves along GBs depends on the duration of sublimation and will influence the perceived grain size as can be evaluted from surface images. Also, the sublimation of the back side, i.e. the ice surface not touching the glass slide which is exposed to the laboratory air during measurement, influences the measurement results and subsequent processing. While some samples were measured soon after the microtome polishing of the back side, others were kept overnight under a plastic cover and measured in the morning.

- The most obvious error source are linear features, i.e. scratches, from notchy microtome blades and occasional fluffs from woolen gloves that can be mistaken as GBs during image analysis.

---

[5]Resetting the polarisers before each measurement should help avoiding the pattern.

Eichler (2013) estimates the specific error contributions for the G50 at AWI (section 4.1.2 in reference) and finds the absolute error in crystal-orientation to be less than 3° (pers. comm. Mark Peternell, 2015: 2° within a grain for a different Fabric Analyser of the same type).
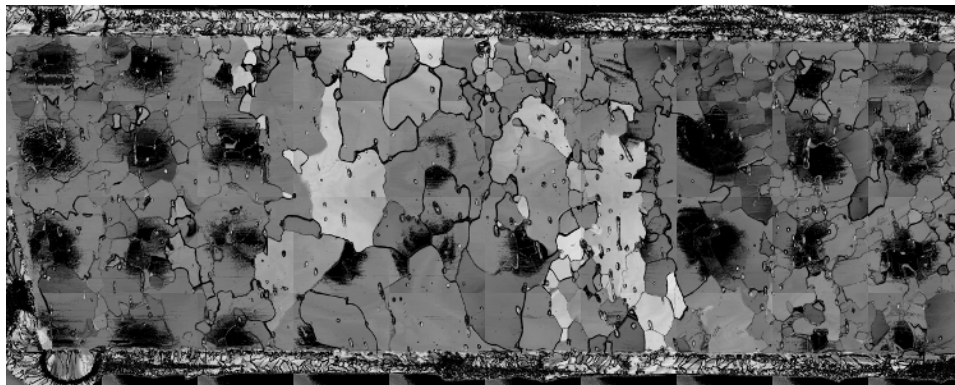
Fig. 3.8: Image as provided from FA of a thin section (sample 85-01, 10 cm wide) indicating the overall quality in grey values. Black patches aligned with measurement tiles (4×10) indicate a poor (geometric) quality.
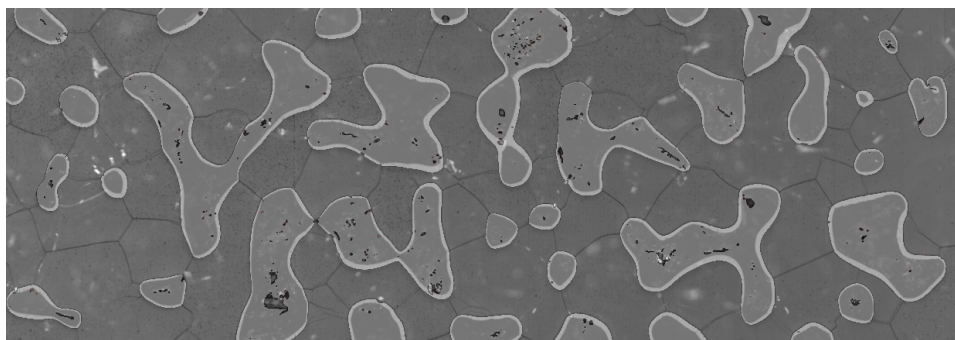
Fig. 3.9: Overlay of LASM images $(25 \times 9 \, \mathrm{mm}^2)$ for illustrating pore space increase during sublimation. Light grey margins around bubbles show material loss at the pore margins during 6 hours. For a section in run 32 (above the FIT) at densities between 0.7 and $0.8 \, \mathrm{g/cm}^3$ the pore space accounts for ca. 13.5 % of the LASM image of the fresh surface. After 4 hours of sublimation the fraction is 17.4 %, after 6 hours it is 18.7 %.

3.3.2 Large Area Scanning Macroscope

The Large Area Scanning Macroscope instrument by Schäfter+Kirchhoff at AWI's ice laboratory was designed for a quick and highly-resolved microstructure scan from a prepared ice section surface. A more detailed description can be found in Horn (2010) and Binder (2014). A microtome-polished ice surface is exposed to the dry laboratory air and sublimation leads to further smoothing and denoising of the surface. Sublimation grooves develop where microstructural features lead to enhanced sublimation due to differences in the energy binding molecules to the surface as detailed for the similar method of microstructure mapping by Kipfstuhl et al. (2006). The duration of sublimation necessary to obtain a well-prepared surface depends

mainly on the humidity and temperature of the air surrounding the sample, the density of the ice and the microtoming procedure. The surface is then illuminated and line scanned with the ice section laid out against a black background. The grooves appear darker than flat areas as they scatter the light while a smooth surface is more reflective. The measurement of a single section takes less than a minute and provides a grey value image of the surface with black bubbles, black or dark grey grain boundaries and light grey subgrain boundaries, depending on the time of sublimation. The LASM images can be used to investigate microstructural features in high resolution (Kipfstuhl et al., 2009). Binder et al. (2013) developed an open source software[6] for the purpose of processing a large amount of these images using various techniques of automated image analysis.

3.3.3 Line scan

The line scan (intermediate layer/stratigraphy scanner, LS) is a very effective means of obtaining a visual stratigraphy from an ice core. The line scan images are a supporting data set for the description of stratigraphy in this study. The instrument at AWI developed by Schäfter+Kirchhoff was used for the recording of KCC line scan images. A parallel-sided slab of ice is normally microtomed on both sides in preparation for the measurement, this was not the case for KCC, however, as half of it is firn. The ice slab is illuminated from below in oblique angles (dark-field illumination) and a camera records the scattered light above the slab while moving along its length. Layers with a high dust or bubble content produce more scatter and appear brighter in the images, clear ice layers appear dark. For a detailed description see Svensson et al. (2005).
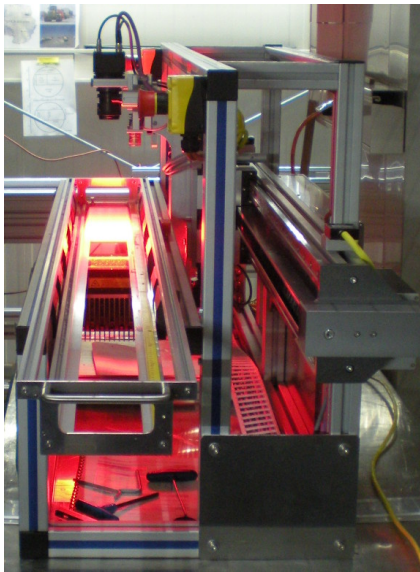
Fig. 3.10: Photo of line scan instrument at AWI. The ice slab is placed in a tray and illuminated from below while the camera records from above.

LS images of KCC were recorded during the processing after the first and second horizontal aliquoting cut, i.e. the middle slab consisting of PP-, ^{14}C- and CFA-aliquot (Fig. 3.4, p. 16) was scanned as a whole. Each ice core piece was imaged once with the focus set on the surface of the ice (33 mm above the archive cut or 1 mm below the surface) and a second time with a slightly

---

[6]Image Microstructure Analyzer (www.ice-image.org)

deeper focal plane (25 mm/9 mm below the surface). The illumination was adjusted four times to improve the contrast for deeper ice core pieces and the resolution is given by 191 px/cm. The images with deeper focus were used down to run 69 (55 m depth) as the stratigraphy appeared clearer and breaks appeared less pronounced. For the deeper runs the images with surface focus gave a better contrast for stratified features.

3.3.4 KCC fabric and microstructure image data

For six weeks between November 2013 and May 2015 thin sections were prepared and measured (both FA and LASM) from the physical properties aliquot of the KCC ice core as part of this study.

- 18 runs were chosen based on depth, aliquot quality and visual observation of stratified layers and dust layers as noted during the drilling logging. Several of these runs are adjacent, referred to in the following as range.

- The data set comprises 12 continuously prepared and measured ranges with a total number of 85 vertical thin section samples[7].

- The image data add up to almost 8 m, i.e. 11 % of the whole core length. The most shallow sample was taken in 25.6 m depth, i.e. above the FIT, with 12 samples in total above the FIT. About half of the deepest 5 m of the ice core was sampled, including the last 90 cm above bedrock, referred to as basal range/layer.

- The fabric data were measured on thin sections of 3.2 ± 0.1 cm width (Fig. 3.4, p. 16, red line), a maximum vertical length of 10 cm and a thickness of 300–350 μm, occasionally 200–300 μm for renewed sample preparation. Shorter samples occured as a result of uneven run lengths.

- The sublimation duration, i.e. the duration of exposure of the microtomed sample surface to the air in the ice laboratory before the LASM image is taken and the thin section is fixated on the glass slide, varied between 1 and 10 hours with an average sublimation duration of 4 hours. Samples from the deeper part of the core needed increasingly more time to develop clear sublimation grooves. Some samples that showed many artefacts from microtoming needed accordingly longer to develop an artefact-free surface. Artefacts include linear scratches from notches in the microtome blade or an increased number of "microtoming pits", which might result from a varying speed of the microtome sledge (images in appendix B.1, p. 136).

Table 3.1 summarises parameters of the sampled ranges, while detailed information on the individual sections can be found in appendix B.2 (p. 146).

---

[7]The samples are named for the run, the top-down order of possible samples from that run, starting with zero for the topmost sample, and the number of cut preparation, e.g. sample 66-12 would be the second prepared surface (2) from the second from top sample (1) of run 66.

Tab. 3.1: Parameters of KCC thin section image data per range.

Run numbers/ Range	Top depth (m)	Top depth (%)	Nr. of thin sections	Length (m)	Interval to next range (m)	Estimated core azimuth (°)
26	25.610	35.6	6	0.590	5.233	210
32	31.433	43.7	6	0.597	6.547	–
40	38.577	53.6	9	0.794	4.002	–
48	43.373	60.3	6	0.604	4.318	–
57a/57b/58	48.295	67.1	12	1.036	3.611	240 (57b)
66	52.942	73.6	6	0.489	3.811	–
75a/75b/76	57.242	79.6	12	1.128	4.357	330 (76)
85	62.727	87.2	5	0.505	3.768	240
92a	67.000	93.1	4	0.400	0.830	–
94/95	68.230	94.8	8	0.719	0.811	–
97b	69.760	97.0	4	0.400	1.000	–
100/101	71.160	98.9	7	0.710	–	180 (101)
		Total:	85	7.972		

The image data sets of FA and LASM images of KCC ice core measured in this study are archived on PANGAEA® Data Publisher for Earth & Environmental Science and can be downloaded and cited as `doi:10.1594/PANGAEA.864226` (Fabric Analyser data), `doi:10.1594/PANGAEA.864227` (LASM data).

All FA measurements of this study were measured with a resolution of 50 px/mm. All LASM measurements were measured with a resolution of 200 px/mm. For all image data the image top corresponds to the ice thin section and ice core top. LASM images are horizontally mirrored compared to FA images as a result of fixating the LASM scanned surface to a glass plate.

3.4 Image processing and analysis

The FA, LASM, and LS image data were processed for subsequent analysis using open source software.

3.4.1 Depth scale preprocessing for thin section data

The quality and lengths of the KCC ice core aliquots lead to some samples being shorter than 10 cm and occasionally jagged or skewed at one end. Additionally, images from FA and LASM of the same sample usually show individual and different margins. For the purpose of comparing

fabric data on a cm-scale with other data sets following steps were undertaken to derive a depth scale as accurate as possible:

- All FA and LASM images were visually checked and compared to ensure no samples are rotated in any way.

- The comparison of the provided FA images with the LASM images (with higher resolution and clearer outlines) was used to exactly measure the top margin of the FA images, i.e. the number of pixels from the top of the image to the actual start of the ice thin section. This was done as the data format in which the FA stores the pixel information (`data.cis`) cannot easily be altered to remove the margins.

- The LASM images were manually cropped, i.e. the margins were cut off.

- The position of the depth markers relative to the dimensions of the thin sections they were located on had been carefully noted during the sample preparation. From this, and the lengths of all sections as measured during sample preparation, the depth of the top of each thin section in reference to the agreed-on marker depth scale could be calculated.

- The derived thin section top depth scale is used for all parameters derived from these image data. The manually measured top margins are used for the correction shift of the coordinates for all grain features obtained from the FA image data analysis.

Despite the efforts to precisely locate the image data, the depth uncertainty lies in the likely range of $5-15\,$mm, originating from the use of markers and various breaks.

3.4.2 cAxes analysis

For the automated image analysis of a stack of FA images the open source programme `cAxes` was developed[8] (detailed description in Eichler, 2013). The programme requires a list of paths to the FA data folders containing `data.cis` and `info.txt` and the input of five parameters for the analysis, detailed below. It has to be indicated if the image data are from horizontal or vertical sections. In case of vertical sections, the c-axis angle data are automatically rotated. An optional image mask was manually prepared for every section defining the area of interest for the programme to analyse[9]. `cAxes` provides several data files with extracted grain and boundary parameters, including grain- and area-weighted[10] eigenvalues (section 2.5, p. 9) for the thin section samples, i.e. one eigenvalue triplet per section. For the illustration of the grains' c-axis orientation as identified with `cAxes` the color code shown in Fig. 3.11 is used (section 4.1.3. in Eichler, 2013). White indicates a close to vertical orientation of the c-axis while colored shades unambiguously represent the azimuth angle.

---

[8]Written in `C++` by Jan Eichler with contributions from Tobias Binder, `https://bitbucket.org/icemicrostructure`.

[9]Without the mask the programme automatically detects the image margins, but this did not always work properly in the case of KCC image data, apparently encountering a problem with the tile borders.

[10]Currently the area-weighting volume fraction exponent $\alpha = 1$ is implemented.
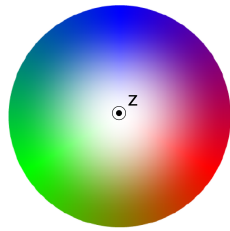
Fig. 3.11: Colorcode as used by `cAxes` for the illustration of c-axis orientation. The center corresponds to the vertical ice core axis.

Parameter choice

`cAxes` needs the input of five parameter values as detailed and illustrated in Eichler (2013):

- **geometric and retardation quality**: For each pixel of the image a geometric and a retardation quality value is calculated during the measurement. By providing a threshold value for each of the two qualities the pixels eligible for analysis are identified. While the retardation quality is always good ($\sim 80\,\%$ or higher), lower geometric quality values occur more often. Besides the poor quality pattern (Fig. 3.8) it can be observed that single whole grains have a poorer quality assigned than their neighbouring grains. While threshold values of $70\,\%$ for both qualities are advised (pers. comm. Mark Peternell, 2015), this leads to a substantial exclusion of analysis-available image area of up to $50\,\%$ (Fig. 3.12). Thus, the thresholds are set to $50\,\%$ as the error of statistical evaluation induced by reducing the sample is estimated to be much larger than the uncertainty of c-axis angle determination expressed by the quality values. From the evaluated grain and bubble area (section 3.4.5, p. 29) it was deduced that $26 \pm 6\,\%$ of KCC thin section area are rejected for the analysis.

- **tile rotation α:** The $1\,\mathrm{cm}^2$ measurement tiles composing one image are sometimes slightly rotated, resulting in possible discontinuities of GBs at the tile borders. To correct this within `cAxes`, an appropriate angle has to be specified. The KCC image data was obtained in several batches over two years. Thus, the tile rotation correction angle is determined for each batch individually (Tab. 3.2).

- **misorientation γ_{max}:** A threshold for the mean change in orientation between the c-axis unit vectors of a pixel and its neighbours is set to determine whether they belong to the same region. A suggested value of 1° is chosen (Eichler, 2013).

- **minimum grain size A_{min}:** The smallest grains that can be measured with the FA are of the order of the thickness of the section ($\sim 300\,\mu\mathrm{m} \equiv 15\,\mathrm{px}$). Any smaller regions that may be identified during the segmentation of the image are likely to be artefacts and will be rejected. A threshold of $500\,\mathrm{px}$ is used, corresponding to $0.2\,\mathrm{mm}^2$ at a resolution of $50\,\mu\mathrm{m}/\mathrm{px}$.

(a) geometric quality = 60 % and retardation quality = 70 %

(b) geometric quality = 50 % and retardation quality = 50 %
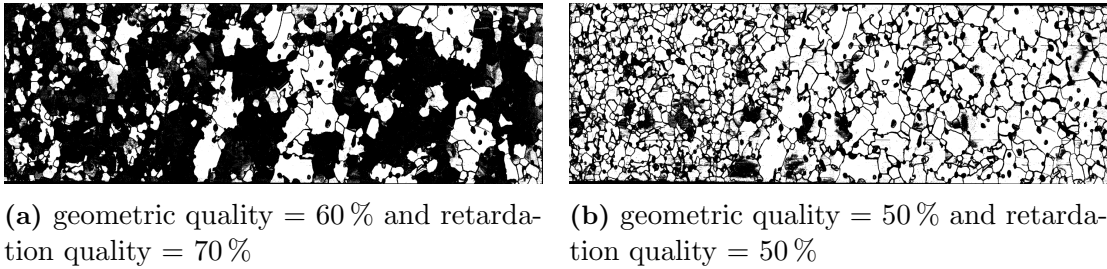
Fig. 3.12: `cAxes` output (sample 48-01, 10 cm wide) indicating in white which pixels are above the quality threshold and used for the analysis.

Tab. 3.2: Tile rotation correction angles as determined on one/two samples of each measurement series of the KCC FA image data.

Laboratory session	Tile corr. angle (°)
November 2013	0
February 2014	0
July 2014	-0.2
November 2014	-0.2
May 2015	0.4

Error estimate

The inaccuracies described in section 3.3.1 (p. 18) and their relative contribution for each sample are difficult to account for in a subsequent processing. Additionally, `cAxes` may not be able to retrieve the complete grain topology as is evident from raw images. A comparison of LASM and FA image data from the same thin section surface may offer the possibility to systematically quantify the uncertainty, when using `cAxes` with FA data to derive grain topology and grain boundary network parameters, as the LASM images provide more precise results for the microstructure. However, this requires an advanced and resource-intensive matching algorithm[11] that was not feasible as a routine procedure in this study (chapter 4 in Binder, 2014). An exemplary matching of `cAxes` result images and LASM image on one thin section (Fig. 3.13) suggests that especially very small grains are often not discerned. From this it can be assumed that the grain statistic as obtained from FA images is underestimated. On the other hand, as the thin section plane is mostly cutting through grains where they are smaller than their maximum diameter, the true average grain size will be overestimated. For the purpose of this study, focussing on the fabric information of the obtained data, the remaining error is accepted.

---

[11]Ongoing development by Tobias Binder as extension to his `Image Microstructure Analyzer` (`www.ice-image.org`).
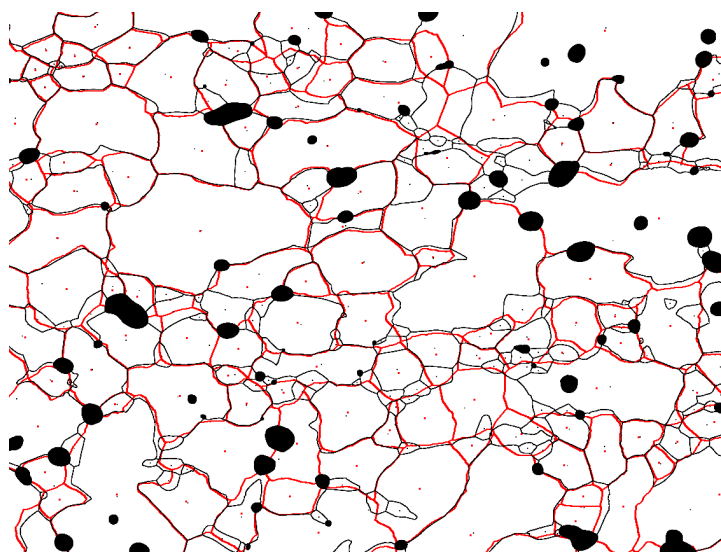
Fig. 3.13: Exemplary matching of grain boundaries (sample 48-51, $2.3 \times 1.7\,\text{cm}^2$) extracted from LASM (black) and FA (red) images (pers. comm. T. Binder, 2016). In fine-grained regions the `cAxes` algorithm shows a tendency to neglect very small grains. Part of these grains with a very similar orientation could be subgrains while others show a distinct different orientation (verified on trend image).

3.4.3 Moving average calculation

The main interest in this study are cm-scale variations in crystal-orientation fabric. Thus, to obtain sub-decimetre resolution from the thin section data a moving average is calculated for all parameters of interest[12]. The programme `rMean`[13] reads a stack of grain data files (produced by `cAxes`) and recalculates the fabric parameters for specified frame and step length. `rMean` was modified in the course of this study to read the information of top depth of every section in the stack to obtain the results within the valid depth scale instead of simply stiching the samples together. However, care must be taken as image data intervals may produce artefacts, also along the beginning and end of each depth range. Additionally, the option to choose between `center` and `radius` calculation is implemented. For `center` all grains with their center of mass within the frame are considered for the fabric parameter calculation, while for `radius` all grains whose equivalent radius lies or reaches within the frame are taken into account. The `radius` option gives larger grains added weight as they count for more frames than smaller grains, which prevents single large grains to cause spikes in the data. For the eigenvalue calculation to be based on a sufficiently large number of grains, a frame length of $2\,\text{cm}$ ($1000\,\text{px}$) is chosen which is moving in $2\,\text{mm}$ ($250\,\text{px}$) steps along the ice core (Fig. 3.14). The c-axis eigenvalues λ_3 are given as continuous lines for frame lengths 1, 2 and $4\,\text{cm}$ and the number of grains per $2\,\text{cm}$ frame are shown as points. A smaller frame length ($1\,\text{cm}$) is not appropriate as the number of grains decreases and the curve in grey exhibits many spikes which are likely to reflect the

---

[12]For direct consideration of grain data, e.g. grain size, *average* is correct, while for eigenvalues it is not an average but a windowed computation based on a smaller sample of c-axis unit vectors than in an entire thin section.

[13]Running mean calculation, by Jan Eichler.

influence of only a few grains. A larger frame length (4 cm) proved to be too large to resolve thin layers that have been observed in the image data. The error of the obtained c-axis eigenvalue data is calculated following eq. (2.5).
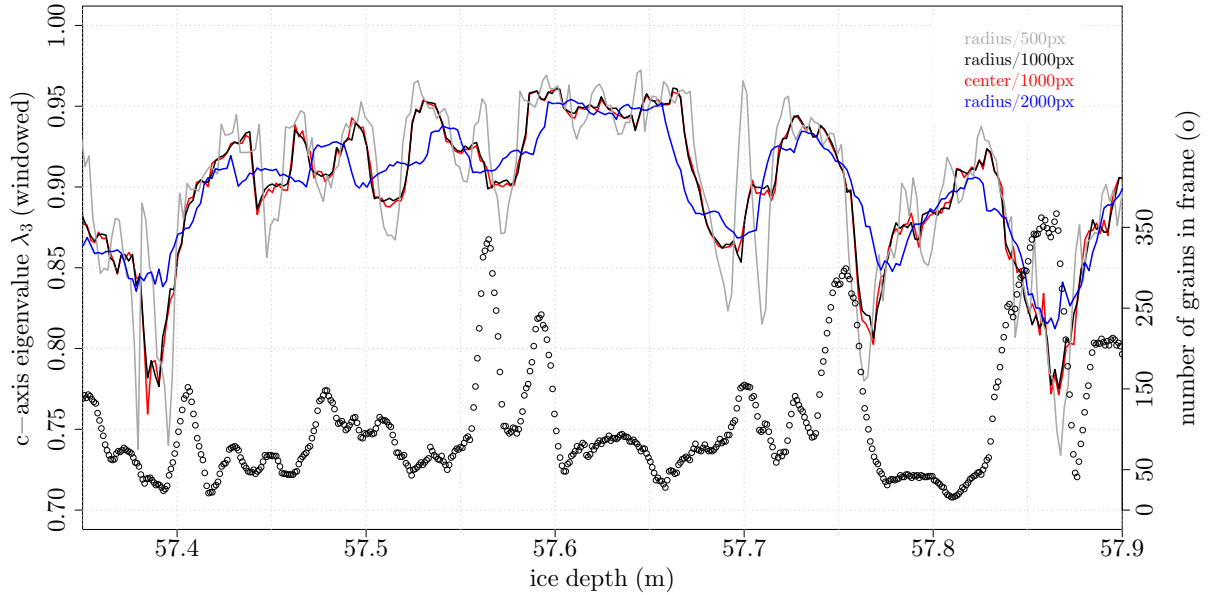
Fig. 3.14: Comparison of windowed eigenvalue computation with `rMean` for different frame length and grain-weighting (`center`/`radius`). Black circles give the number of grains in each frame.

3.4.4 Line scan grey value analysis

To quantitatively compare LS stratigraphy with fabric and impurity data, an analysis programme[14] with the ability to extract grey value information from the LS images was used[15]. The programme offers median filtering for better thresholding of melt features and options for the determination of layer inclination. However, in this study only the output of mean grey values in lines of 10 pixels width, i.e. a moving average with a bandwidth of about 0.5 mm, are considered. Deeper ice core pieces appear lighter, i.e. have increasingly higher grey values, until the illumination during the measurement was manually adjusted (Fig. 3.15, top panel). This effect, and possible conveyed information, is removed by substracting the mean grey value of each LS image, so only the information given by the residuals is considered (Fig. 3.15, bottom panel) here. By computing the mean grey value from horizontal lines, i.e. perpendicular to the core axis, a potential inclination of layers is neglected as is illustrated in Fig. 4.2 (p. 40). Instead, the transition between layers are blurred and spread out; very thin layers cannot be resolved. Artefacts in the line scan images arise from breaks where the light is scattered differently, which has to be kept in mind when regarding the obtained grey value data. While in theory the dark-field illumination produces dark ice layers, melt layers appear bright in the KCC line scans above the FIT. The new top depth scale, derived during this work from

---

[14]Written by Tobias Binder.

[15]With first output provided by Tobias Binder, 2014
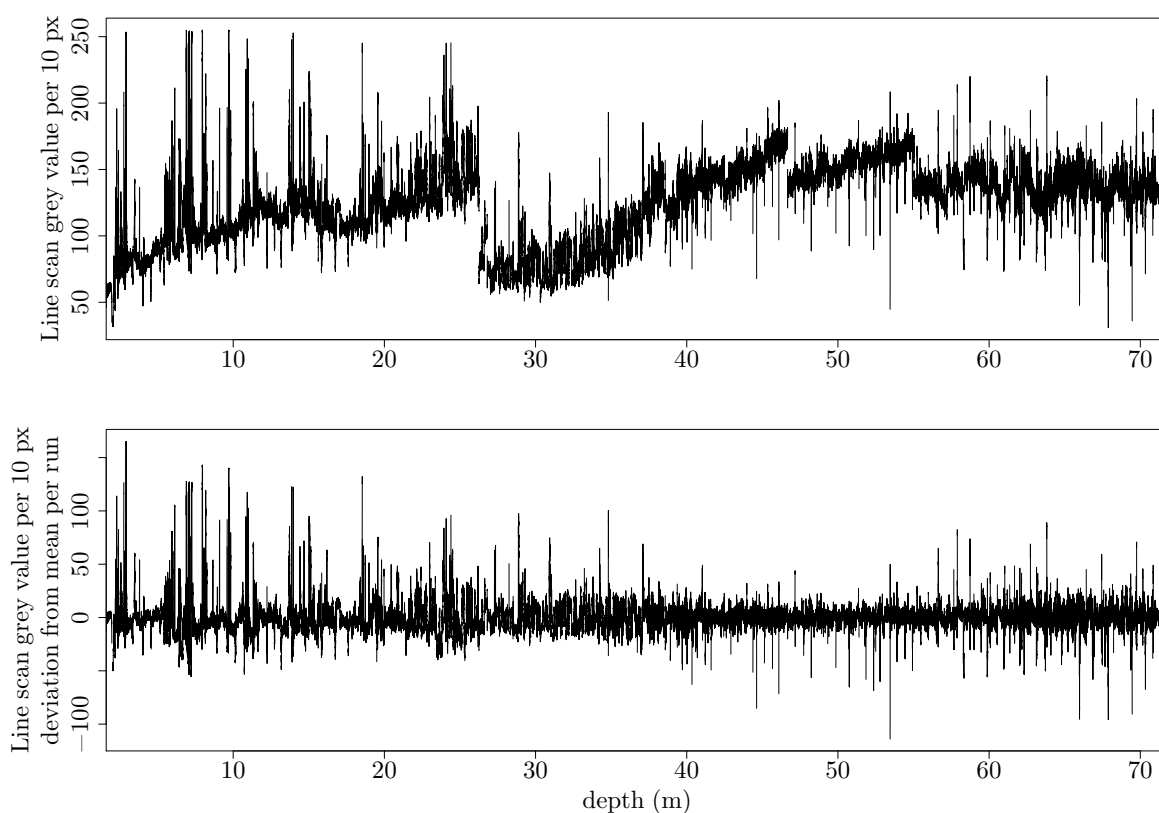
Fig. 3.15: Grey value averaged over 10 pixel lines from line scan images of KCC. Top panel: absolute grey values depending on illumination on recording of the images; jumps correspond to illumination changes. Bottom panel: Grey value difference from image mean grey value.

the marker positions on the ^{14}C aliquots (section 3.1.2, density profile), is used for the depth alignment of the LS grey value data set. However, all non-straight top and bottom ends were straightened for the analysis, resulting in a depth uncertainty for the line scan alignment of a few centimetres per run.

3.4.5 Pore analysis

The pore space visible in the LASM images is analysed using the open source software `ImageJ`[16]. For each run a grey value threshold to isolate the pores was defined and the images were processed by a macro (appendix B.6, p. 155) in batch mode. Linear features like GBs and scratches were excluded by setting a minimum circularity and a minimum size condition for the particles extracted by thresholding. The particles were analysed for area A_B, circularity $C_B = 4\pi \cdot [\text{area}]/[\text{perimeter}]^2$, and aspect ratio $AR = [\text{majoraxis}]/[\text{minoraxis}]$ of a fitted ellipse. As the parameters are given for x/y-coordinates in pixel per image, all data were fitted to the top depth scale derived from the thin section data and the common marker depth scale. Mean parameters were calculated per sample and kernel smoothing was applied to the data set to

---

[16]`imagej.net`, `https://imagej.nih.gov/ij/docs/guide/146-30.html`

obtain cm-scale resolution. The number density in frames of $2\,cm$ was calculated in steps of $2\,mm$. The images provide information from cross-sections through the ice core. The derived parameters are thus 2-dimensional and are potentially dependent on the ice core's azimuthal orientation during the aliquoting. Special care has to be taken if the core azimuth is different for different ice core pieces. Without horizontal thin sections the parameters cannot be further constrained. Thus, bubble elongation, as described by, e.g., the aspect ratio, must be considered as a minimum estimate.

3.4.6 Correlation computation

The data sets in this study are often compared by assessing their correlation to extract possible interdependencies, although it has to be kept in mind that a significant correlation coefficient alone contains no information on the causality of the bivariate data. For the computation of correlation coefficients between various data sets available in this study the argumentation in Kleitz (2015, section 5.6) is adapted:

- As the data are in general not normally distributed[17], *Spearman's rho* provides a correlation coefficient[18] by only considering the ranks of the bivariate data (e.g. Burt and Barber, 1996):

$$r_{\mathrm{s}} = 1 - \frac{6\sum_{i=1}^{n} d_i^2}{n(n^2 - 1)} \tag{3.1}$$

  with the sample size of paired values n, the rank difference d and $-1 < r_{\mathrm{s}} < 1$.
  The *Spearman* correlation coefficient r_{s} is more robust to outliers as it assesses only the monotonic relationship between the variables.

- The p-value gives the probability for the observed data under the assumption of the null hypothesis H_0, which states that the bivariate data are not correlated, and serves as criterion for significance. For a significance level of $95\,\%$ the p-value must be below 0.05 for the null hypothesis to be rejected. It is calculated asymptotically in the case of ties, i.e. for equal values of the same rank in either data set. The rate of ties is checked and does not exceed $17\,\%$ for data sets used in this study, which is small enough to be neglected (Burt and Barber, 1996, p. 396). The higher the number of paired values that are considered for a correlation computation the lower the coefficient can be while still being significant.

- Alternatively, to test the significance of the computed r_{s}, a permutation test could be applied. For this purpose one data set is permuted, e.g. 1000 times, and the correlation coefficient with the other, original data set is computed. The p-value is then given by the tail probability of the distribution of correlation coefficients from permutation relative to the actual correlation coefficient[19].

However, it has to be remarked that the described statistical tests of significance might not be appropriate for the data of this study, which can be regarded as a time series for which each data

---

[17]Open source software `R: shapiro.test`, null hypothesis H_0 : data are normally distributed.

[18]`R: cor.test(x, y, method = spearman, exact = FALSE)`, provides r_s and p-value (asymptotically instead of exact in the case of ties)

[19]I.e. by the percentage of correlation coefficients from permutation exceeding the actual correlation coefficient.

point is not necessarily independent of its neighbours (Mudelsee, 2003, "serial dependence"). By contrast, the process of random permutation changes the smoothness of the data set. This can be demonstrated, e.g., by comparing the autocorrelation of an original and a permuted data set with a small lag or by calculating the standard deviation of the differences between adjacent data points. Random data will have a very short autocorrelation length and a high standard deviation of the differences. Additionally, the effect of dispersion, in the case of CFA data, and moving average computation, in the case of fabric, ensures that many subsequences of data points exhibit monotonic behaviour, thus influencing the correlation and its p-value by introducing artificial dependence. The autocorrelation of a data series t_i of length n for a lag τ

$$r_A(\tau) = \frac{\sum_{i=1}^{n-\tau} t_i' \cdot t_{i+\tau}'}{\sqrt{\sum_{i=1+\tau}^{n} (t_i')^2 \sum_{i=1}^{n-\tau} (t_i')^2}} \tag{3.2}$$

can be used to evaluate the non-randomness of the data and provide the distance or time lag within which subsequent data points cannot be considered as independent. One might derive an effective sample size, i.e. smaller than the original sample size, from which a correlation with another data set might be calculated under the assumption of randomness of the data points. Another method for testing the significance would be the modelling of surrogate data sets by interchanging data subsequences or shifting the data sets with respect to each other and under consideration of the autocorrelation length. However, the feasibility of these approaches is limited by the already relatively short data sequences computed from continuous fabric data.

Despite the obvious reservations regarding the suitability of a standard correlation[20] and significance computation approach for the non-random, non-normally distributed data sets in this study, it is used for lack of feasible alternatives given the low statistic of the data in this study. Only eigenvalues calculated from successive, but not overlapping, frames are used to derive correlation coefficients, which limits the sample size to 50 data points per metre. By choosing a different frame set that is shifted by $2n$ mm (with $n = [1,9]$) and repeated calculation several values for the correlation coefficient are obtained, providing a robust estimate of correlation on the 2 cm scale. All bivariate data sets are downsampled to the lower resolution of the two variables. Crosscorrelation $r_C(\tau)$, i.e. the correlation between bivariate data with a lag (eq. (3.2) for two diffent data series), is applied to check for differences in the respective depth allocation of different data sets, e.g. CFA and fabric data.

3.4.7 KCC processed data sets

The data sets derived from image analysis and processed in this study are summarised in Tab. 3.3. The eigenvalue data set can be downloaded and cited as `doi:10.1594/PANGAEA.864228`.

---

[20]`http://imgs.xkcd.com/comics/linear_regression.png`

Tab. 3.3: Data sets derived from KCC image data in this study, processed using windowed computation and kernel smoothing (second resolution value for each data set) to provide information in sub-centimetre resolution on a common depth scale.

Technique	Variable	Processing steps	Resolution	Depth range (m)
Linescan	Grey values	depth scale corr., kernel smoothing (1 cm bandwidth)	0.05 mm	1.6 – 71.95 (whole core)
X2D	density ρ	depth scale corr., kernel smoothing (5 mm bandwidth)	0.2 mm, 2 mm	1.6 – 49.46
FA	eigenvalues $\lambda_{1,2,3}$ (area-weighted), mean grain size $\bar{A}$	`cAxes, rMean` (moving average, 2 cm frames)	~ 10 cm, 2 mm	25.61 – 71.87 (with intervals)
	GB linearity, misorientation γ	`cAxes`	~ 10 cm	
LASM	bubble area A_B, circularity C_B, aspect ratio AR	thresholding with ImageJ, kernel smoothing	~ 10 cm, 2mm	

3.5 Measurement of impurities

3.5.1 Continuous Flow Analysis

The impurity content of KCC was measured by continuous flow analysis (CFA) at the Institute of Physics, Climate and Environmental Physics, University of Bern, Switzerland in early 2014 (Fig. B.4, p. 154). The center aliquot (Fig. 3.4, p. 16) was processed in a standard routine detailed in Röthlisberger (2000); Kaufmann et al. (2008). The meltwater of KCC was analysed for dissolved impurities ammonium (NH_4^+), sodium (Na^+), nitrate (NO_3^-), and calcium (Ca^{2+}). Conductivity and the content of particulate dust was additionally measured. For the direct measurement of the ratio of stable oxygen isotopes $\delta^{18}O$ (Fig. B.5, p. 154) a Picarro isotopic water analyser was connected to the CFA system (Gkinis et al., 2011). The ends of the ice samples need to be flat for the procedure, resulting in small gaps in the KCC data where flattening was necessary in case of, e.g., inclined breaks. The record goes down to 70.15 m depth where the measurement had to be stopped because of a strongly increasing amount of particulates, clogging the system. The resolution of the data is of the order of 1 cm. The signal appears automatically smoothed due to the dispersion of the meltwater flow in the tubes.

3.5.2 Laser ablation-inductively coupled plasma-mass spectrometry

A novel way of operationally measuring impurities in an ice core is by laser ablation-inductively coupled plasma-mass spectrometry (LA-ICP-MS, LA). The two main advantanges over conven-

tional ice core impurity analyses (e.g. CFA) are a much higher resolution and a minimum loss of material per measurement, providing the option to repeat measurements and to revisit ice core archives. In contrast to CFA, LA measures both the dissolved and the particulate impurity content. Additionally, the new method allows for directed, localised measurements, i.e. with respect to the ice microstructure. Therein lies a large potential for the study of interaction processes of impurities and the ice microstructure. Several setups have been characterised (e.g. Müller et al., 2011; Della Lunga et al., 2014; Sneed et al., 2015) and are under continuous development.

For a pilot study in the course of this work the LA system at the Keck Laser Ice Facility at the CCI, University of Maine, described in detail in Sneed et al. (2015), could be used. Laser ablation experiments were conducted on samples from four depths of the KCC ice core to investigate the impurity content of single ice crystals in specific layers with known fabric and microstructure characteristics (section 5.2, p. 75). The samples were selected based on the available fabric and microstructure data and exhibit adjacent layers of fine and coarse grains with different fabric strength, respectively, as detailed in Tab. 3.4 and illustrated in Fig. 3.16. Impurity fractions of sodium and iron were measured with respect to the visible microstructure on the ice sample surface. While sodium is considered representative for more soluble impurities, iron should be a better indicator for more particulate impurities, i.e. the dust component (Tomadin et al., 1996; Barnes and Wolff, 2004; Fischer et al., 2007). From Fig. 3.4 (p. 16) it is evident that the surface available for LA (blue line) is not the same as for the thin section preparation (red line). It is assumed, however, that the observed microstructure is representative for the entire horizontal ice core cross-section. In the following, the measurement aspects of the pilot study are summarised.

Tab. 3.4: Overview of LA-ICP-MS measurements. Weak/strong fabric refers to less/more oriented grains.

Run	Microstructure and fabric	approx. depth (m)	Mean grain size (mm^2) $\pm$ standard dev.	c-axis eigen-value λ_3
48	larger gr., weaker fabric	below 43.40	–	0.74
	small gr., stronger fabric	above 43.40	2.48 ± 0.76	0.71
85	large gr., weak fabric	below 63.04	25.21 ± 33.71	0.69
	small gr., strong fabric	above 63.04	2.15 ± 1.81	0.95
95	large gr., weaker fabric	68.78 - 68.83	12.14 ± 10.10	0.84
	smaller gr., strong fabric	68.84 - 68.89	2.41 ± 3.63	0.96
100	small gr., strong fabric	71.40	0.98 ± 0.69	0.97

Sample preparation: The ice surface is scraped with a plate from stainless steel to remove frost from storing and irregularities. The sample is taken from the cold lab to the laser lab, placed on the tray and installed in the previously cooled cryo-cell ($-20°$ C).

Laser ablation settings: For the purpose of comparing measurements from grain boundaries with grain interiors a small spot size of $40\,\mu$m was chosen (Fig. 3.17) for a more locally concentrated signal. This is especially relevant for smaller grains with less than $0.5\,$mm^2
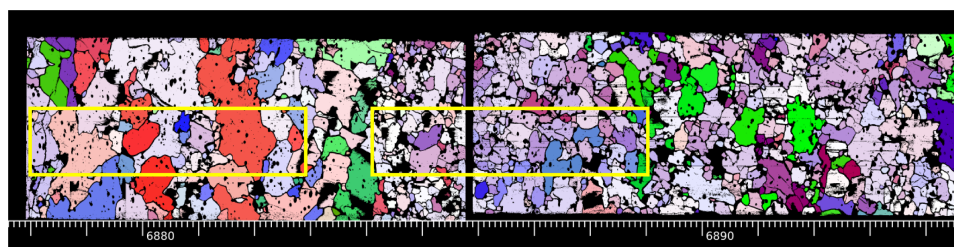
Fig. 3.16: Fabric grain images of run 95 with depth scale in cm. The yellow boxes illustrate the position of the ablation chamber seal on the ice surface which is actually perpendicular to the here displayed fabric surface.

diameter. Some measurements with a spot size of $100\,\mu$m were done when the impurity concentration was very low. The ablation speed was decreased to $40\,\mu$m/s. The focal depth was set below the ice surface, causing a deeper laser ablation trace and producing more material, while keeping it narrow. The data are recorded as counts per second.

Ablation pattern: For the purpose of comparing impurity content from within a grain and from a grain boundary a pattern was established as illustrated in Fig. 3.18. Sodium and iron were measured along different boundaries of a grain, along a path parallel to the previously measured grain boundary in 150–$250\,\mu$m distance and along a spiral raster set roughly in the center of the grain if the grain was large enough. Ablation times for the set paths were between 20 and 60 seconds. The data collection time was set to exceed the time of ablation in order to provide an estimate of the background. For each seal position on a layer of certain microstructural characteristics five grains were picked. The dimensions of each grain were estimated to later be able to calculate a grain size estimate. See Fig. 3.19 for an exemplary illustration of the measured traces. As there is currently no way of discerning the actual orientation of the picked grains, it cannot be guaranteed that all of them are representative for the statistically obtained layer characteristics.

Fig. 3.17: Photo of ice surface as viewed through the cryo-cell's microscope camera. Due to the fast sublimation in the ablation chamber the surface smoothens quickly and sublimation grooves appear as clear dark lines. Subgrain features can also be observed as sublimation continues. The laser ablation paths on and parallel to a grain boundary are $40\,\mu$m wide.
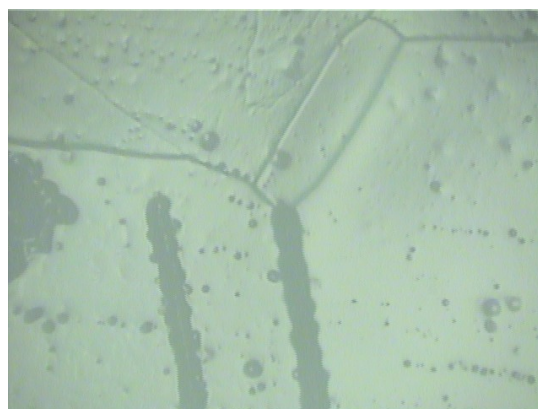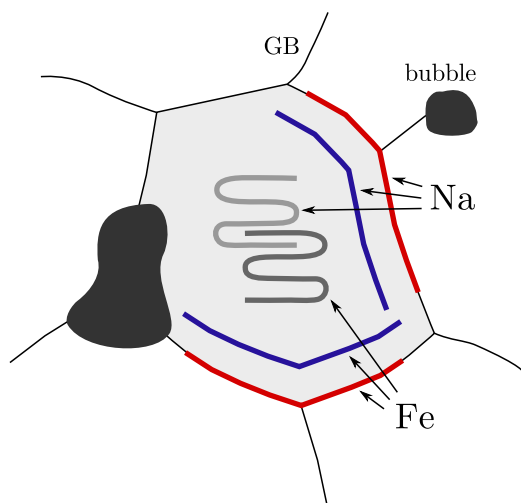
Fig. 3.18: Sketch of measurement coordination at a typical grain setting: ablation traces on and parallel to grain boundaries (red, blue) for different elements, interior raster in grey.
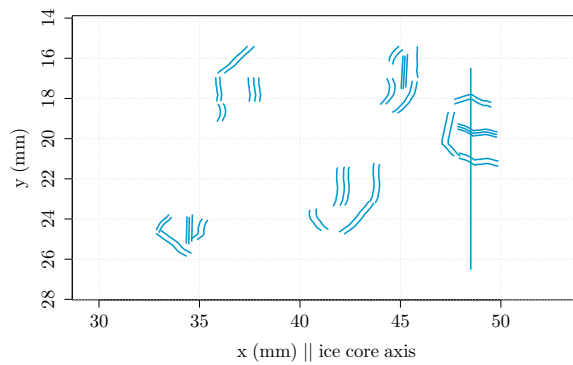
Fig. 3.19: Laser ablation traces are plotted from coordinates collected during the measurement of a large grain section. The area corresponds to the surface area of the ice accessible with the laser during a a set of measurements, i.e. within a yellow box as shown in Fig. 3.16. Features of five grains can be distinguished. The vertical line which is still visible with the naked eye on the ice surface after the measurement is used as depth anchor.

4 Fabric and microstructure of cold Alpine ice core KCC

This chapter concentrates on the fabric analysis, including a stratigraphical description and classification approach to the entire ice core (section 4.1). A classical assessment of the fabric evolution with depth in the glacier (section 4.2) is followed by the high-resolution analysis of the fabric data. The microstructure, i.e. pores and grains, is analysed (sections 4.3, 4.4) to provide supplementary information for the interpretation of the fabric results. The observations of distinct cm-scale variations in crystal-orientation fabric in the Alpine fabric data are reported in section 4.5. The synthesis and combined discussion of this chapter is presented in section 4.6.

4.1 Visual stratigraphy

The first assessment of the ice core during drilling is that of visual stratigraphy[1] and can later be repeated to some degree using line scan images (section 3.3.3, p. 21). Layers are mostly distinguished by lighter and darker shades caused from density (Fig. 3.7, p. 17), changing pore and crystal characteristics as well as dust load. Reddish shades, that only appear on visual inspection of the ice, indicate a high saharan dust load. 11 dust layers have been recognised during the drilling. The last 90 cm of the core were visibly shaded from particle load[2].

As the ice core KCC only reaches the shallow depth of 72 m, bubbles are present throughout the core and can act as scatter centres. The visual inspection of the line scans yields some qualitative information on the stratigraphy of KCC. Detailed notes for every run can be found in Tab. B.3, p. 156). The general features are summed up in the following and illustrated in Fig. 4.1:

Melt features:

- In 12 runs above 28 m depth thin melt layers of a few millimetres can be observed. They do not appear to persist in greater depths.
- Thicker melt layers (1–4 cm, as in Fig. 4.2) are found about 20 times down to 43 m depth.
- Ice lenses, i.e. smaller melt features, occur in 19 runs above 35 m depth.
- Larger melt features that probably originate from percolating melt (Fig. 4.1b) appear in $\sim$ 24 and 29 m respectively (runs 24 and 29b).

---

[1]See the stratigraphy logging from the drilling.

[2]As was later encountered during thin section sample preparation, causing fast blunting of the microtome blades.

- In the lower part of the core below 48 m at least 15 clear layers appear as darker layers and mostly coincide with a break of the core piece.

Coarse grain regions: Close to melt features the occurrence of very coarse grains can often be observed (Fig. 4.1a).

Transitions > bands > layers: Based on the quality and extent of alternating lighter and darker segments, several depth regions are distinguished that may change gradually into each other. Transitions describe the change between contrasting regions (e.g. Fig. 4.21), bands are broad layers of the order of 5–20 cm (Fig. B.18, p. 172), that might alternate and have irregular thickness, and layers refer to a few centimetre wide, alternating sections:

   I. Snow/firn, down to ca. 14 m: Bands of varying extent and weak contrast are discernible at close examination in most images. The variable thickness per image ranges between 2–10 cm and 20–25 cm. While it appears mostly to be a difference in porosity that causes the perceived change, sometimes bands of rather coarse grains or transitions between coarser and finer grains can be identified (Fig. 4.1a).

   II. Firn between 14 and 38 m: The transitions between lighter and darker bands become more clear with irregular thickness of 2–20 cm, with the mean thickness decreasing with depth. In 30 and 32 m depth 16 resp. 19 bands per run (30b and 32) could be counted. The transitions are never sharp but mostly well defined. In the last few metres above the FIT the transitions become blurred and the bands thinner than 10 cm disappear (Fig. 4.1b).

   III. Ice between FIT and 55 m: The images appear more uniform or noisy but transitions between lighter and darker bands can be found again, however, in larger intervals than the banding above the FIT (~ 36 m depth). This seems to be sometimes overlaid by barely identifiable layers of only a few centimetres thickness (Fig. 4.1c).

   IV. Ice between 55 and 64 m: The banding is again clearer to recognize, although somewhat blurred. The thickness is difficult to constrain but appears often of the order of a few centimetres.

   V. Ice between 64 and 71 m: Light layers of 1–2 cm thickness begin to stand out with better contrast. The transitions appear sometimes rough or even disturbed. Soon, steep features almost perpendicular to the layer inclination can sometimes be observed. Below 69 m the banding becomes very irregularly overlaid with lighter and darker patches. Little stones were observed during the drilling at 69 and 70 m i.e. within 3 m above bedrock (Fig. 4.1d).

   VI. Basal ice, last 90 cm: A few darker layers can be distinguised against a rather uniform background. Else, no banding can be observed (Fig. 4.1e).

Inclination: The inclination has to be considered with caution as it is largely dependent on the azimuthal orientation of the core piece and a possible depth-dependent borehole inclination. All roughly estimated angles, in reference to the horizontal and relying on melt layers and well defined layer transitions, have to be considered as minimum values. Again, several depth regions can be differentiated based on this property:

   i. Firn: From the very shallow firn down to 43 m in 36 from 61 images (59 %) a layer inclination could be observed and estimated to $\pm\ 5-15°$, sometimes varying strongly

(a) Thin melt layers, ice lenses and coarse grains in run 6b (6 m depth).

(b) Banding and large ice lense, presumably from percolating melt in run 24 (24 m depth).

(c) Barely visible transitions and no inclination in run 55 (47 m depth).

(d) Inclined layers in run 88 (65 m depth).

(e) Disturbed layers appear to run crosswise in run 98 (70 m depth).
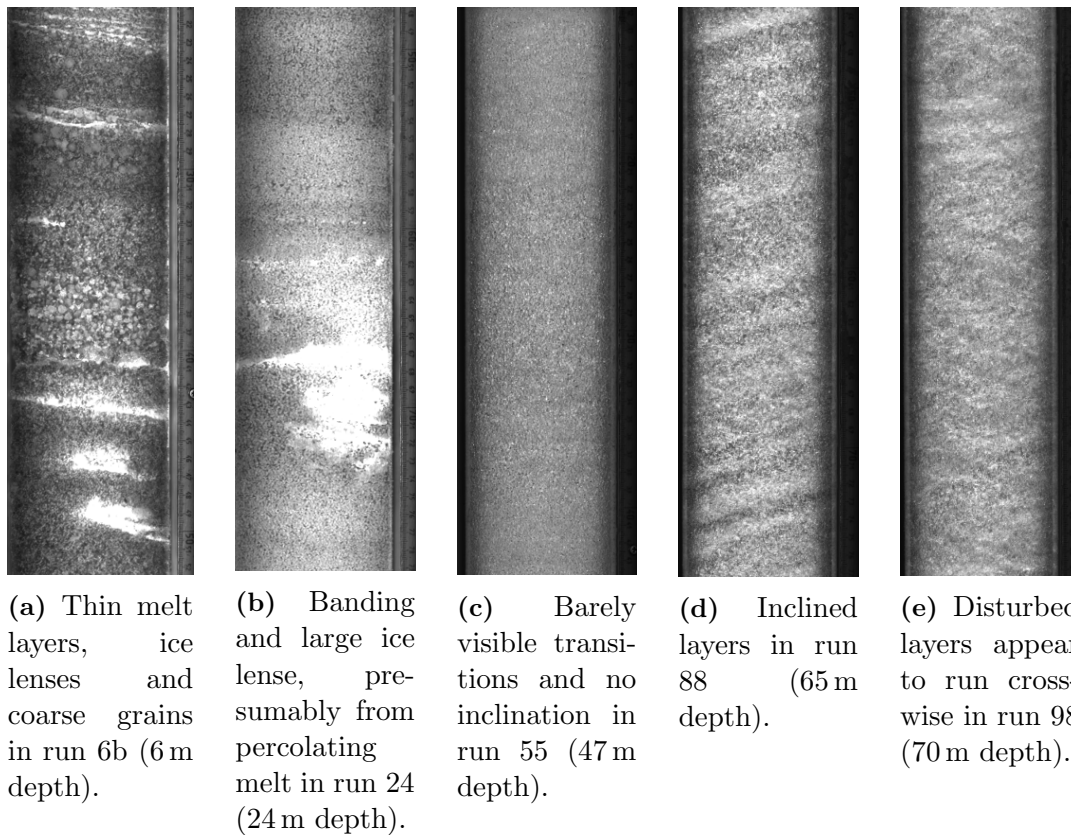
Fig. 4.1: Line scan image details (31 cm length, image top equals ice core top) illustrating different stratigraphic features observed in the KCC ice core.

within one run. Considering the approximate core azimuth measurement, it appears that the slope was mostly similarly oriented with some exceptions.

ii. Ice between 43 and 51 m: No inclination can be observed regardless of the core azimuth.

iii. Ice between 51 and 63 m: Layer inclination is of the order of 10–15°.

iv. Ice between 63 m and bedrock: Layer inclination is of the order of 15–20° with maximum values of 30°. In the last 3 m some runs show no distinct inclination.

Following earlier studies (e.g. Rau, 2008) the grey value from LS is compared with the density profile. Fig. 4.3 shows the detrended LS grey value (Fig. 3.15, bottom panel, p. 29), which is kernel smoothed (20 cm bandwidth), in comparison with the equally smoothed density. The general trend of the density, computed with a strong kernel smoothing (3 m bandwidth), was substracted to only show the remaining density variations (residuals). The extrema of both curves match well for the upper 40 m. Significant rank correlation coefficients were computed 50 times from the 50 different subsamples consisting each of every 50th pair of data points (610 pairs per subsample with intervals of 7.9 cm). The interquartile range (25 %–75 %) of the resulting distribution of correlation coefficients is 0.564–0.566.

The grey value residuals show strong variations in the firn part in accordance with stronger

density variations due to the larger and varying portion of pore space. Below 40 m the variation decreases for 10 to 15 m but increases again for the last 15 m.
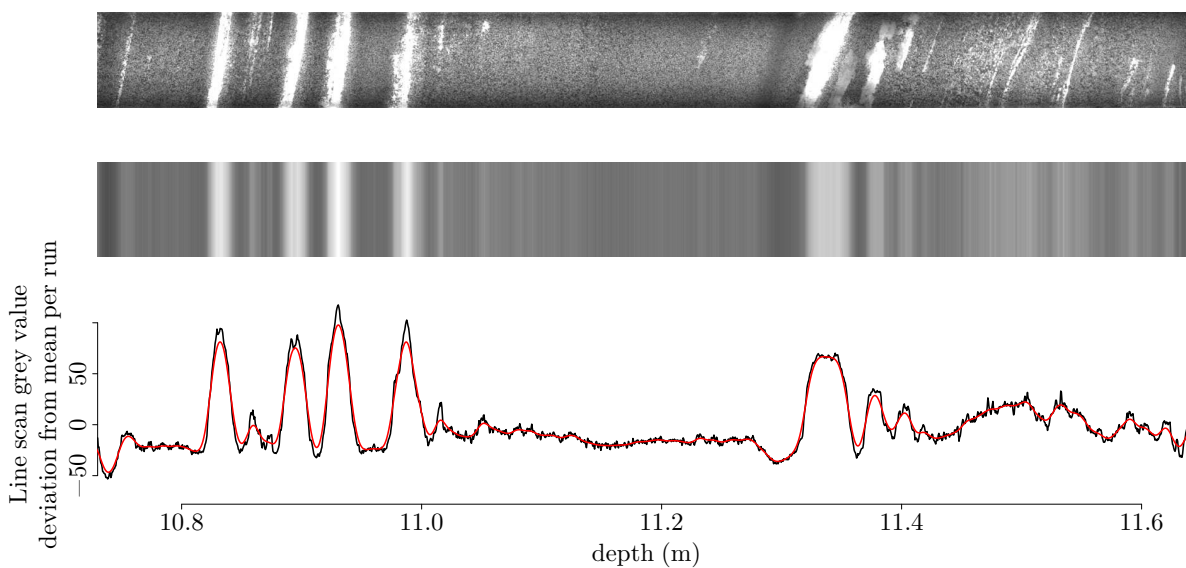
Fig. 4.2: Illustration of grey value stratigraphy from line scan images (run 11b, 93 cm long, from 10.7 m depth). Top panel: Line scan raw image. Middle: Grey value image. Bottom panel: Grey value line graph in 0.05 mm resolution (black) and smoothed with 1 cm bandwidth (red).
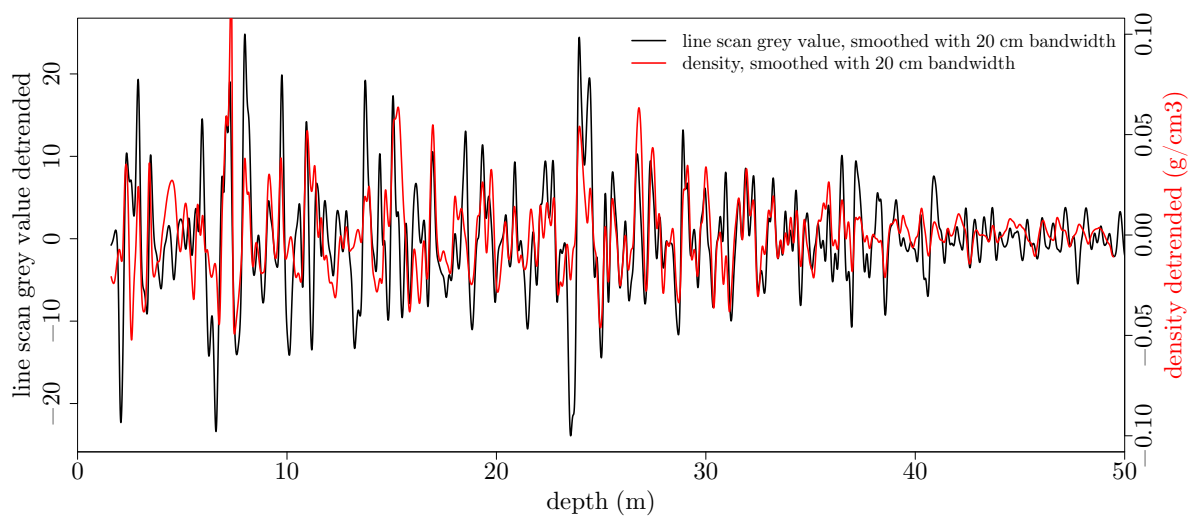
Fig. 4.3: Comparison of line scan grey value (black) and density profile (red). Both curves show the remaining variations after substracting the mean grey value respectively the general density trend and subsequent smoothing with a 20 cm kernel.

4.2 Fabric evolution

The comprehensive data set obtained from fabric analysis is presented. Each data point represents the information from an entire thin section. Fig. 4.4 illustrates the difference between area- and grain-weighted c-axis eigenvalue λ_3 (section 2.5, p. 9) for the KCC data. The difference is mostly small with maximum values of up to -0.08 in 57–70 m depth where area-weighted eigenvalues are generally lower. All eigenvalues shown in the following are area-weighted unless stated otherwise.
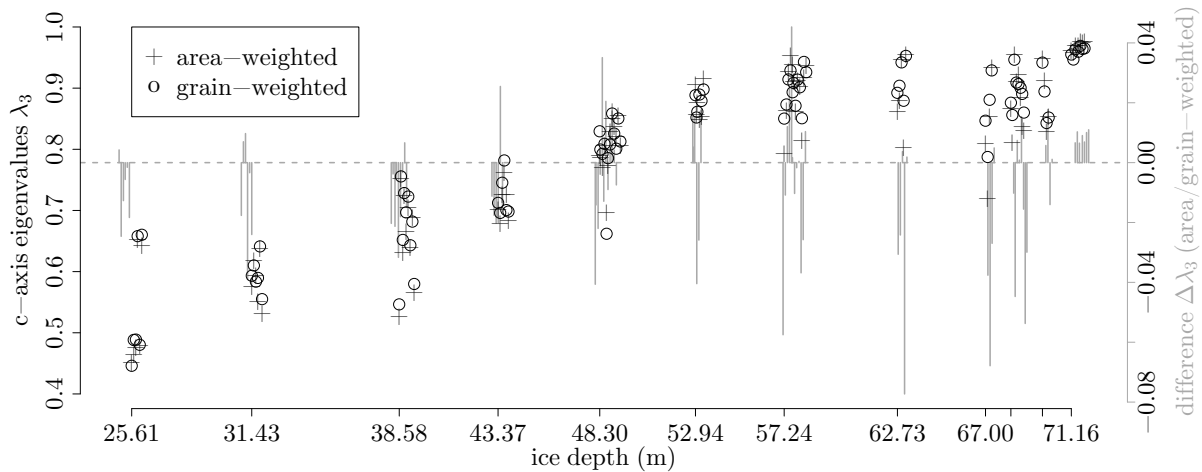
Fig. 4.4: Comparison of KCC c-axis eigenvalues for area- and grain-weighted computation. The difference $\Delta\lambda_3$ is illustrated in grey bars and is mostly restricted to ± 0.04 with some larger differences in the lower part of the core.

Fig. 4.9 displays the evolution of eigenvalues with depth[3]. The eigenvalue uncertainty is calculated with eq. (2.5). The mean grain size (section 4.3), number of grains per section, density, temperature and line scan grey value residuals (section 3.4.4) are additionally given. The schmidt diagrams represent each the c-axis distribution for all sections in one of the 12 ranges (Tab. 3.1, p. 23). All schmidt diagrams for single thin sections can be found in appendix B.3 (p. 151). The c-axis eigenvalues from the KCI (Fig. 3.1, p. 14) ice core (pers. comm. Ilka Weikusat and Jan Eichler, 2013) are displayed for comparison, including one continuously measured run, providing 8 thin sections. The firn-ice-transition at KCI was found to lie at only 27 m (Bohleber et al., 2013, Table 1), due to the very low accumulation, so that the ice column of KCI and KCC are almost of the same thickness, which is why the KCI eigenvalues are displayed here on the KCC depth scale, i.e. with an offset of 10 m.

As observed in many polar ice cores (Faria et al., 2014) and to be expected for deforming ice, an anisotropy of c-axes evolves. This has never been described for an Alpine glacier before. Thus, in the following the evolution of crystal-orientation fabric in the KCC ice core is described in detail. Starting from an already weakly anisotropic fabric at 25 m depth above the FIT with eigenvalues $\lambda_{1,2}$ around 0.2 and c-axis eigenvalues around 0.5 the fabric strength increases with depth and develops a broad single maximum with a minimum cone angle of 9° (Fig. 4.7). Remarkable here is the already high variability within the first run (0.4 and 0.6),

---

[3]doi:10.1594/PANGAEA.864228
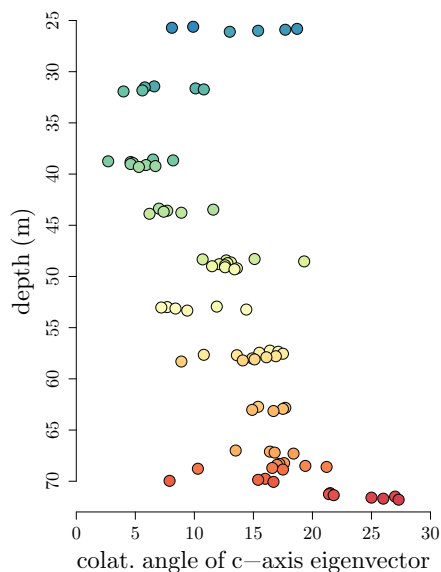
Fig. 4.5: Colatitude angle of c-axis eigenvector with respect to the ice core axis for each sample. Color as in Fig. 4.6.
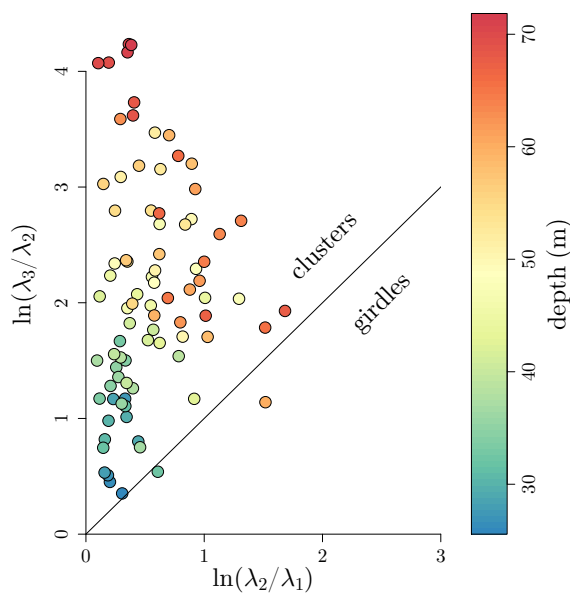
Fig. 4.6: Woodcock diagram illustrating the predominant cluster classification of KCC fabric.
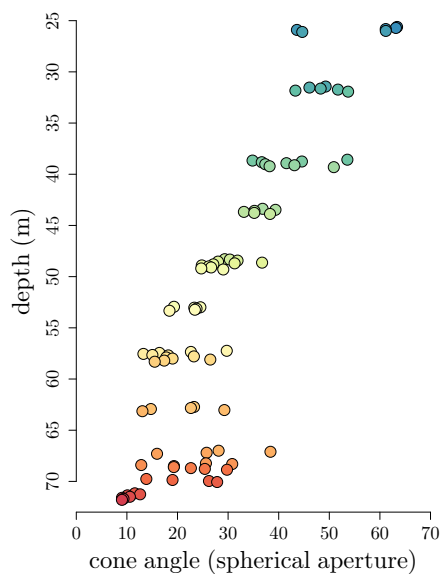
Fig. 4.7: Cone angle (spherical aperture) as calculated for KCC thin section fabric. Color as in Fig. 4.6.
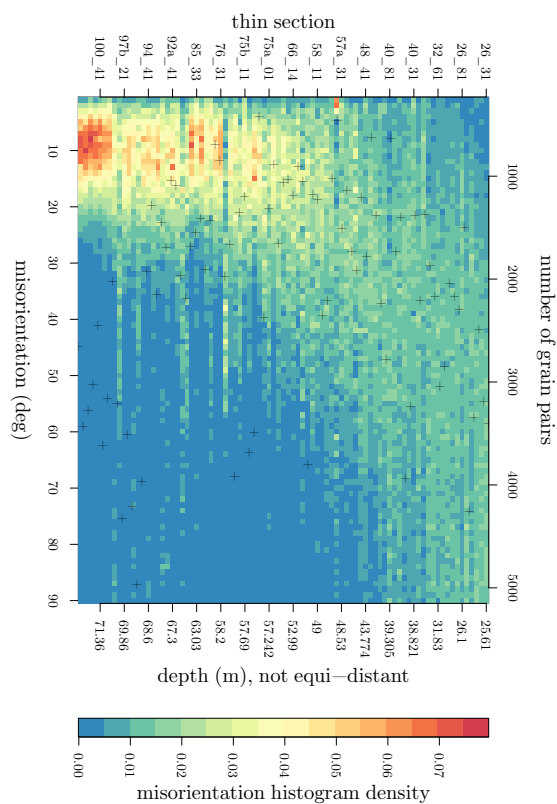
Fig. 4.8: C-axis misorientation angle γ distribution for adjacent grains in each thin section. Crosses indicate number of grain pairs.
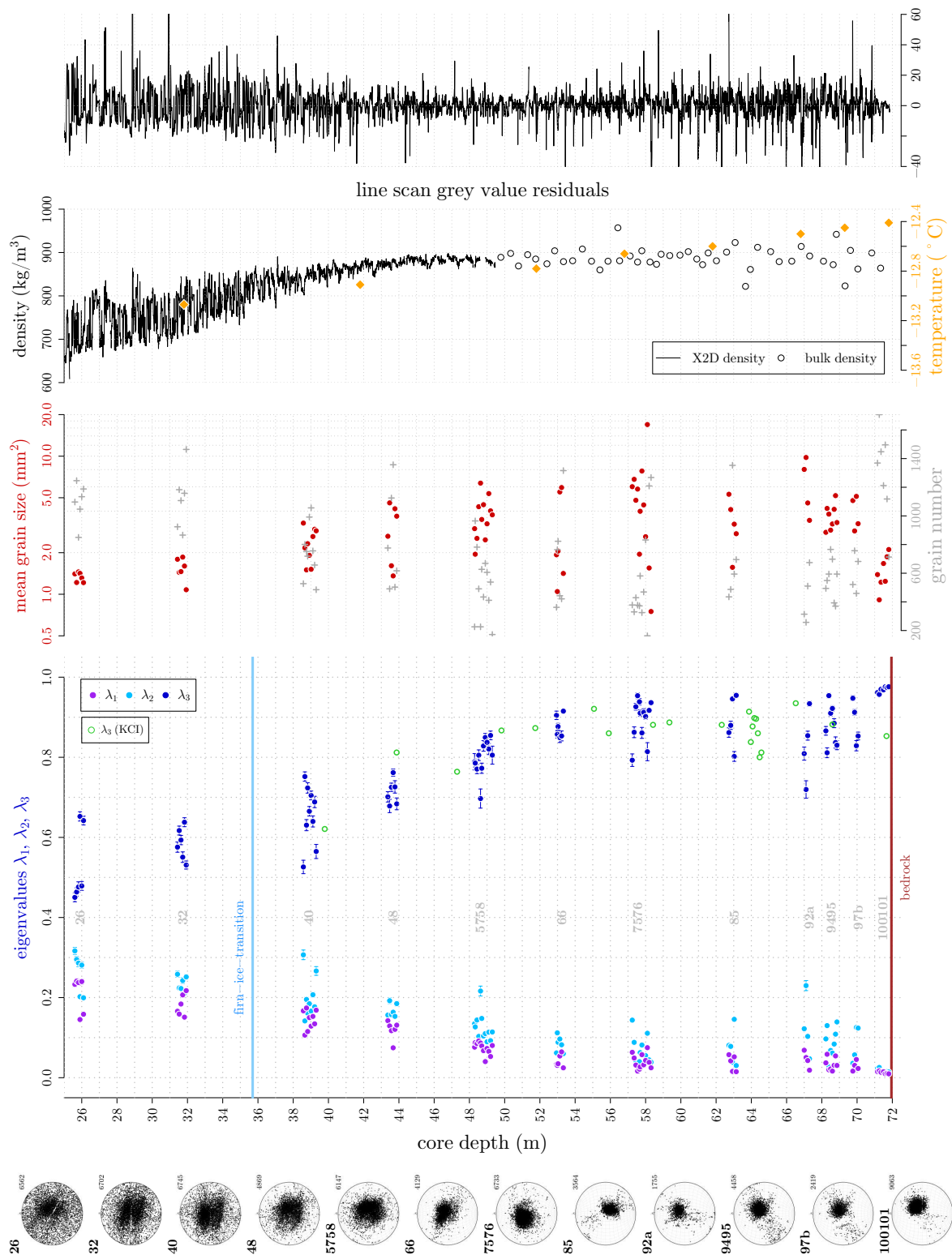
Fig. 4.9: Illustration of KCC fabric evolution with depth. Schmidtplots in classical glaciology projection (center of diagramm refers to vertical core axis) show the c-axis distribution with the total number of grains indicated on the top right. Eigenvalues of the orientation tensor are shown with uncertainty. Mean grain size, density, temperature and line scan grey value residuals are shown for comparison.

43

Tab. 4.1: Mean c-axis eigenvalues λ_3 with standard deviation from thin sections and variability span within each measurement range.

Run numbers	Top depth (m)	Length (m)	Mean c-axis eigenvalue $\bar{\lambda}_3$	Variability span $\lambda_{3,\max} - \lambda_{3,\min}$
26	25.610	0.590	0.53 ± 0.09	0.20
32	31.433	0.597	0.58 ± 0.04	0.11
40	38.577	0.794	0.66 ± 0.07	0.23
48	43.373	0.604	0.71 ± 0.03	0.08
57a/57b/58	48.295	1.036	0.80 ± 0.04	0.16
66	52.942	0.489	0.88 ± 0.03	0.07
75a/75b/76	57.242	1.128	0.89 ± 0.05	0.16
85	62.727	0.505	0.89 ± 0.06	0.15
92a	67.000	0.400	0.83 ± 0.09	0.21
94/95	68.230	0.719	0.88 ± 0.05	0.14
97b	69.760	0.400	0.89 ± 0.05	0.12
100/101	71.160	0.710	0.97 ± 0.01	0.02
			Average:	**0.14 ± 0.02**

which cannot be explained by statistical effects of cutting through a population given by error bars (eq. (2.5)). The fabric anisotropy increases with depth down to ca. 53 m depth, while the density is still increasing, i.e. where vertical compression is dominating. This observation is supported by Fig. 4.8 which illustrates the distribution of the misorientation angle between adjacent grains. The distribution is, at first, very broad, including all possible misorientation angles, although less than 0.5 % of all grain pairs have misorientations $<$ 10°, the reason for this is unclear. The distribution then becomes narrow in the upper 50 m and settles around 10°. At the same depth, the decreasing variability trend in the LS grey value record reaches a turning point and increases to greater depths, corresponding to the transition from region III to IV (section 4.1). The fabric can be classified almost everywhere as cluster fabric (Fig. 4.6). In run 66 at 53 m the single maximum appears elongated, followed by a faint girdle structure, overlaid by a strong single maximum, apparent in the schmidt diagrams of the deeper ranges in the 10 m above the bed. However, the girdle does not appear as clearly when the schmidt plots of the single sections are examined (Fig. B.1, p. 151). Especially in ranges 94/95 and 97b a second maximum could be distinguished in some sections. The single maximum is never exactly vertical and the angle of the c-axis eigenvector increases with depth up to 27° (Fig. 4.5). The horizontal azimuth of the single maximum as well as the faint girdle appear to be rotating. Despite the effort to account for the rotation of the core pieces with respect to each other it cannot be excluded that the correction was insufficient, e.g. for run 85, where the corrected azimuth contrasts with neighbouring ranges.

An important result of this study is the distinctive change in fabric strength on the scale of thin sections. In almost every depth the c-axis eigenvalues that were calculated from adjacent samples in a range can differ substantially. Tab. 4.1 lists the mean c-axis eigenvalue $\bar{\lambda}_3$ calculated as average for each depth range and the variability span calculated from minimum and maximum eigenvalue. No trend in the variability is discernible from this data set. The basal depth range with runs 100/101 is special in that there is almost no variability and the eigenvalue is close to 1. On the other hand, the variability in mean grain size is increasing from shallower depths to a depth of around 58 m but decreases slowly towards the bed and diminishes abruptly in the basal range (section 4.3). The KCI c-axis eigenvalue shows a depth evolution comparable to the KCC data.

4.3 Grain topology and boundary hierarchy

Grain size

The 2D cross-section grain area is derived from fabric images. Fig. 4.10 shows the median grain size and the interquartile range, within which 50 % of the entire population lie, the mean grain size as already shown in Fig. 4.9 and the maximum grain size, i.e. of the largest grain in a thin section. The minimum grain size, that can be detected, is defined by the image analysis parameter ($0.2\,\mathrm{mm}^2$, section 3.4.2, p. 24). The median grain size ranges from 0.5 to $2\,\mathrm{mm}^2$ for the KCC ice core with 75 % of the entire grain population below $8\,\mathrm{mm}^2$. However, the largest 25 % of the grain population reach maximum values of more than $4\,\mathrm{cm}^2$. Thus, the mean grain size is preferably used to describe the grain size characteristic of a sample as it better reflects the occurrence of large grains. Fig. 4.11 shows the grain size distribution for entire measurement ranges. In the firn the distribution is slightly bimodal, as observed in polar firn by Horn (2010) and Alley and Bentley (1988), and narrow with close mean and median values and grains up to $10\,\mathrm{mm}^2$. With increasing depth the tail of the distribution grows to larger grain sizes as the size of the largest grains grows approximately exponentially to a depth of about 50 m. At the same time the number of very small grains increases, shifting the maximum of the distribution to smaller sizes. Below 50 m large grains occur regularly in most sections without further increasing the maximum grain size. Below 60 m the largest grains are mostly below $2\,\mathrm{cm}^2$. In the basal range 100/101 the grain size drops abruptly, with 50 % of the population below $1\,\mathrm{mm}^2$ and maximum grain sizes of $0.5\,\mathrm{cm}^2$. Both during the CFA measurement and the thin section preparation, a high dust load was encountered in the basal runs. This dust load and the high shear that is expected in the layers close to the bedrock due to low temperatures well below pressure melting point ($-12.4\,°\mathrm{C}$, Fig. 4.9) can explain this sudden drop. The variability in mean grain size between the adjacent samples of a range is considerable. In contrast to the c-axis eigenvalues (Fig. 4.9, Tab. 4.1) this variability increases with depth along with the increase in maximum grain sizes (Tab. 4.2).

Grain shape

The LASM images were qualitatively analysed to provide an overview of the evolution of grain shape and distribution, air bubble distribution, and occurrence of recrystallisation features in the KCC ice core. The analysis is not exhaustive but serves to give an impression of the various microstructural features observable in the KCC ice core. Especially for the medium ranges, the variety of observable patterns in adjacent thin section is vast. The microstructure is most
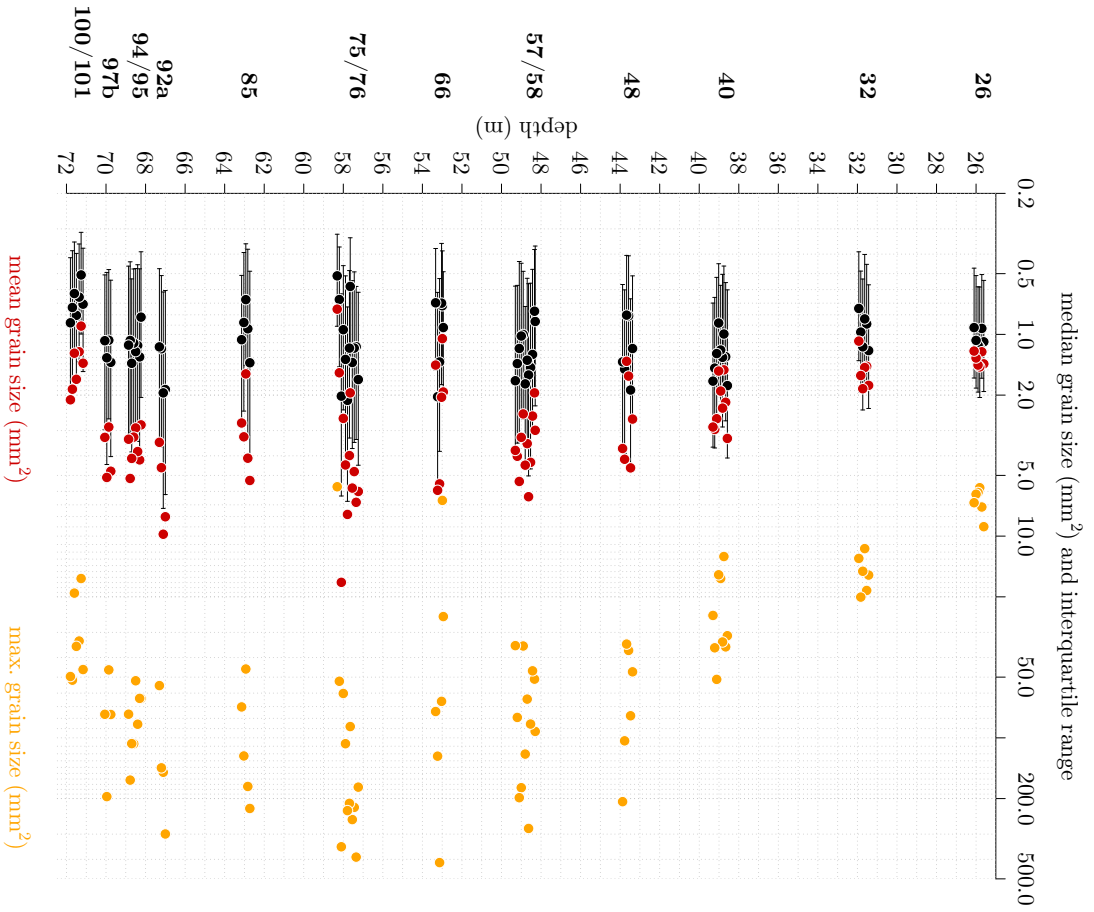
Fig. 4.10: The median grain size and interquartile range for the thin section data is presented (black), on a log-scale. Mean grain sizes and maximum grain size are additionally shown (red and orange respectively).
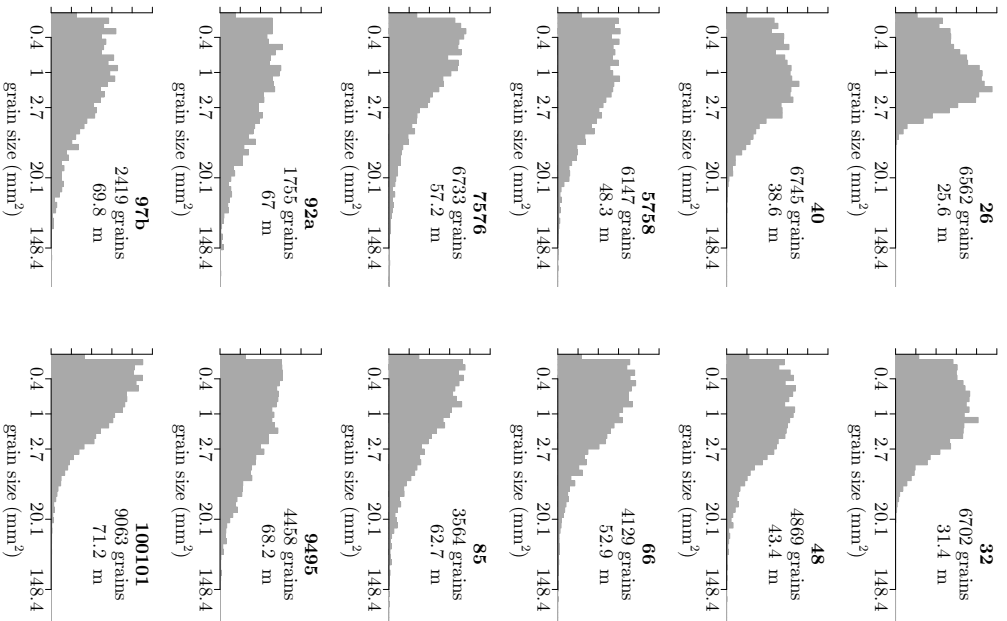
Fig. 4.11: The grain size distributions are shown, summarising the thin section data for each range, on a log-scale, with normalised frequencies. Total grain numbers and depth are indicated.

46

Tab. 4.2: Mean grain size with standard deviation from thin sections and variability span within each measurement range.

Run numbers	Top depth (m)	Length (m)	Mean grain size $\bar{A}$	Variability span $\bar{A}_{\max} - \bar{A}_{\min}$
26	25.610	0.590	1.34 ± 0.10	0.24
32	31.433	0.597	1.54 ± 0.28	0.78
40	38.577	0.794	2.35 ± 0.64	1.78
48	43.373	0.604	3.01 ± 1.35	3.23
57a/57b/58	48.295	1.036	3.75 ± 1.27	4.43
66	52.942	0.489	2.98 ± 2.16	4.88
75a/75b/76	57.242	1.128	5.29 ± 4.27	16.20
85	62.727	0.505	3.39 ± 1.41	3.73
92a	67.000	0.400	6.46 ± 2.96	6.36
94/95	68.230	0.719	3.70 ± 0.79	2.37
97b	69.760	0.400	4.00 ± 1.11	2.24
100/101	71.160	0.710	1.49 ± 0.42	1.20

revealing for the identification of recrystallisation processes (Kipfstuhl et al., 2009; Azuma et al., 2012; Llorens et al., 2016a). Fig. 4.12 shows exemplary image details from the measurement ranges. The description is presented in Tab. 4.3.

Tab. 4.3: Description of KCC μS based on LASM images from the measurement ranges of this study. SubGBs: subgrain boundaries.

Range	Description
26	Four out of nine thin sections show 2–3 layers with smaller and larger bubbles (Fig. 4.12a), associated with a slight grain size difference. Grains appear regular, often as hexagons, and many triple junctions are regular with almost equal angles. GBs are mostly straight but are more curved and sometimes bulging within the small bubble layers. SubGBs can be found, more frequently in the small grain/bubble layers, and appear as mostly straight features, dividing grains. Large pores are tubular with complex shapes but seem to be closed off. Pores are always located on GBs, often at triple junctions.
32	Small grain layers and clusters of very small grains occur, sometimes accompanied with very small bubbles (Fig. 4.12b). Accordingly, the variation in bubble sizes is larger than in 26. Grains are still regular in the larger grain section but GBs become more bulging. SubGBs are generally observed but more frequently in small grain/bubble layers. More complex subGBs and island grains can be found.

Range	Description
40	Grains have more distorted shapes. Bubbles are mostly rounded and seem to be distributed not equally but loosely clustered (Fig. 4.12c), sometimes aligned, with bubble-free grain clusters inbetween. Only few bubbles lie within grains. SubGBs are abundantly observed. Grain/bubble size layering is only observed in the lower sections of the run.
48	Distorted, bulging grain shapes are observed, small grains are more angular. Single small grains are found between large grains (Fig. 4.12d). Bubble size variation in layers has diminished. First very large grains are found, often with bubbles inside the grain cross-section. Zigzagging subGBs occur often but the large and very large grains exhibit far less subGBs.
57/58	Grains are irregular shaped and angular with many kinks and protruding sub-grains (Fig. 4.12e), a large variety of grain sizes per thin section is observed. Many small island grains within large grains and many ragged subGBs are apparent. Again, bubbles are often located like beads on a string. There are no bubbles inside of small grain cross-sections.
66	The grain shapes might be a bit less angular than in 57/58. Many subGBs are still visible. Within a small grain layer strings of very small grains can be found (Fig. 4.12f).
75/76	Enormously large subGB-free grains lie next to small grains (Fig. 4.12g). Distinct subgrain features are persistent with many island grains. Medium sized grains are often interlocking shaped. The small grains can appear angular, depending on the core azimuth. Bubbles are irregularly distributed in the small grain sections.
85	The grain shapes of large grains are distorted, bulging and interlocking, small grains appear often angular (Fig. 4.12h). Many horizontally elongated bubbles with a slight tilt are apparent (section 4.4). Many zigzagging subGBs and other subgrain features are visible, including protruding subgrains and island grains. The bubble distribution is very heterogeneous.
92a	The grain shapes are very irregular and grains of different size are heterogeneously distributed. Many island grains are found. Several straight (sub)GBs run parallel in a steeply inclined angle (Fig. 4.12i). Bubbles are found both on GBs and within grains. Often bubbles in the same large grain are slightly flattened along the same inclination, which is related to the crystal orientation.
94/95	Similar to 92a.
97b	Similar to 92a and 94/95.
100/101	Grains are all small but inclined layers or clusters of smaller grains are sometimes found (Fig. 4.13). Grain shapes are angular, similar to 85. SubGBs are also apparent.
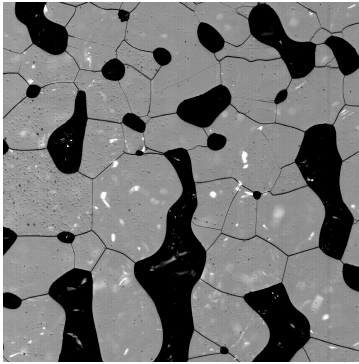
(a) Typical firn μS in 25.9 m depth, sample 26-61.
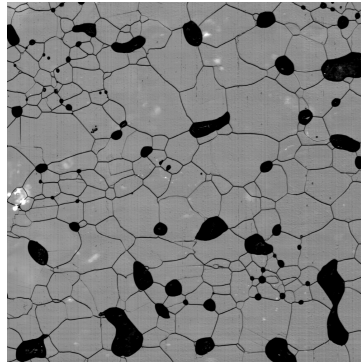
(b) Small grain/bubble clusters in 31.63 m depth, sample 32-41.
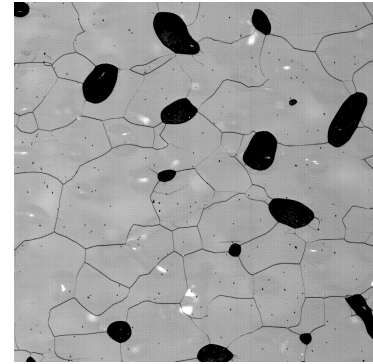
(c) Loose bubble cluster in 38.66 m depth, sample 40-11.
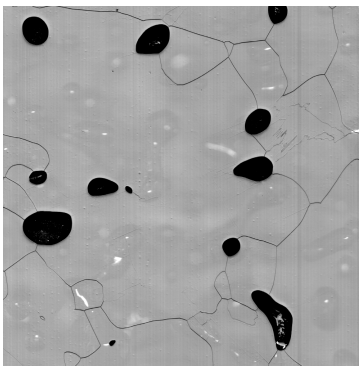
(d) Small single grains and zigzagging subGB in 43.87 m depth, sample 48-51.
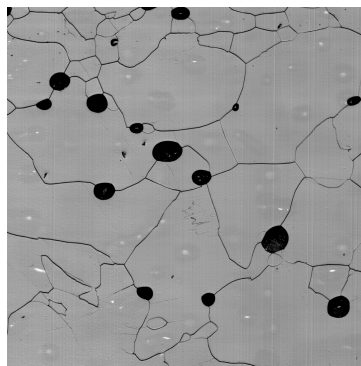
(e) Protruding and island grains and bubble alignment in 49 m depth, sample 58-11.
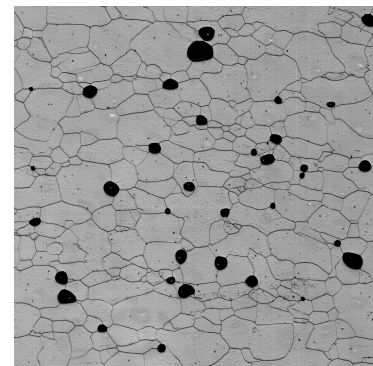
(f) Heterogeneous small grain section in 53.03 m depth, sample 66-21.
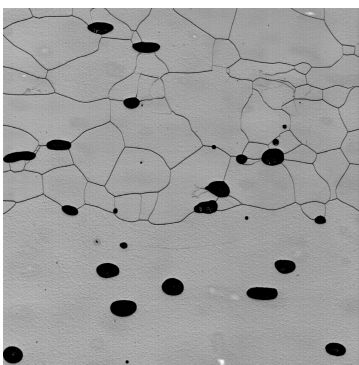
(g) Transition from small grain section to enormously large grain in 57.35 m depth, sample 75a-12.
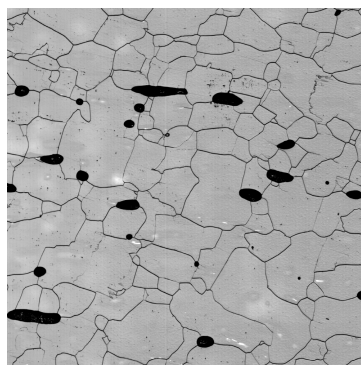
(h) Angular grains in inclined small grain section in 62.93 m depth, sample 85-22.
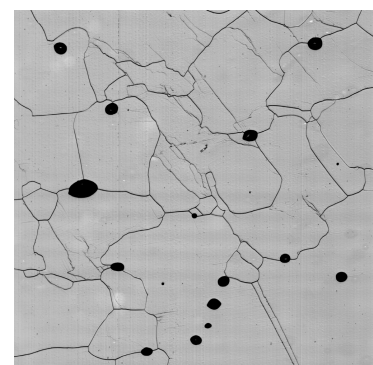
(i) Parallel GBs at high inclination in 67.1 m depth, sample 92a-21.

Fig. 4.12: LASM image details (1 cm^2), highlighting features from each range of KCC.

Fig. 4.13: LASM image detail ($2\,\mathrm{cm}^2$) from $71.26\,\mathrm{m}$ depth, sample 100-31, illustrating small grain distribution in basal section.
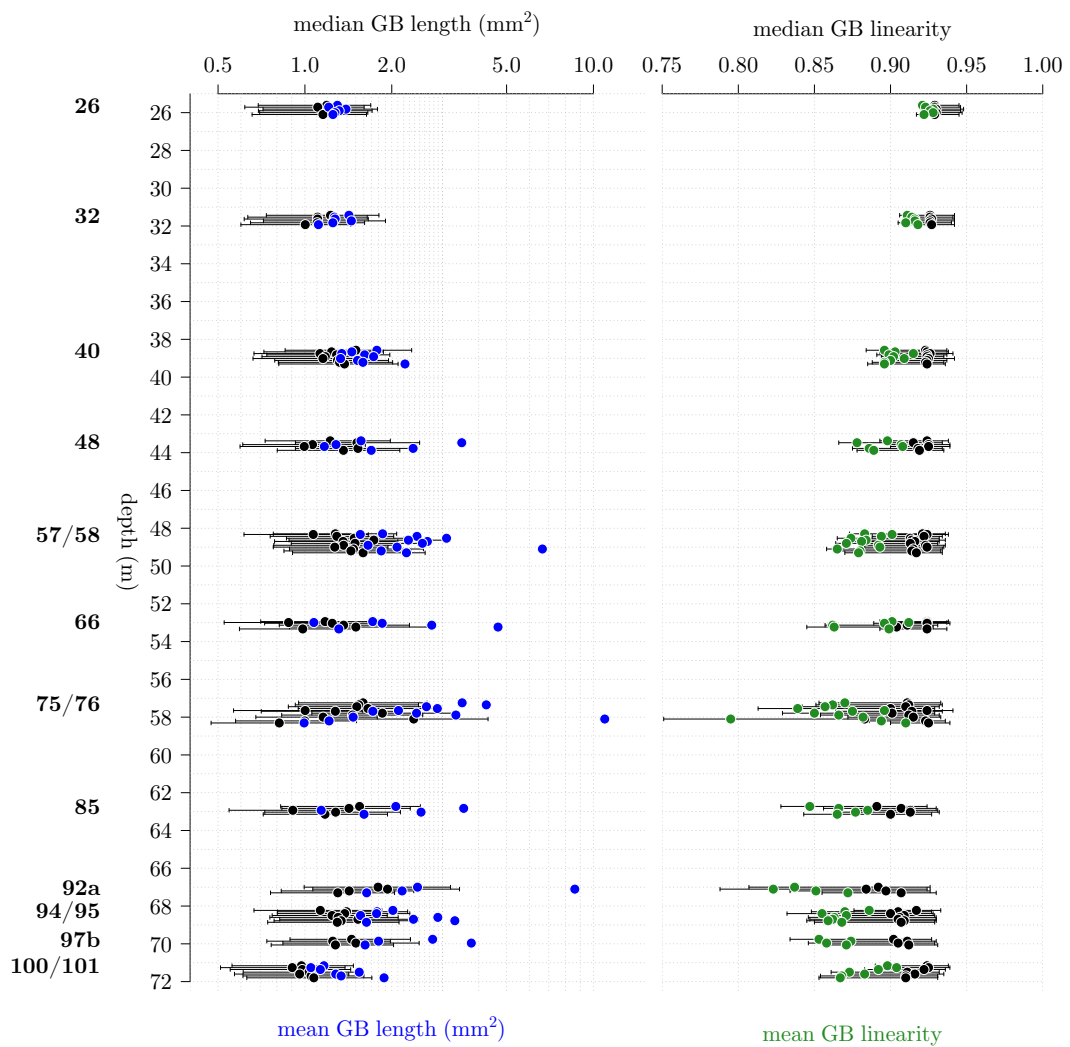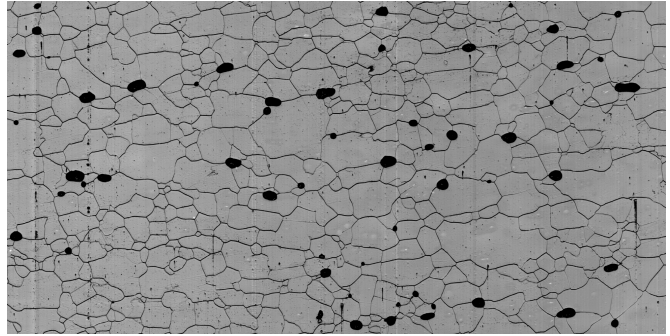
Fig. 4.14: The evolution of grain boundary length and linearity with depth. Median values and interquartile range per thin section sample are shown in black, mean values are shown in blue (GB, on a log-scale) and green (linearity).

Grain boundaries

A quantitative analysis of the grain boundaries is provided by `cAxes`. Grain boundary length and linearity, i.e. the distance between two junctions divided by the length of the boundary, as well as slope and misorientation (Fig. 4.8) are calculated for each thin section. GB length and linearity are shown in Fig. 4.14. As is to be expected from the grain size distribution (Fig. 4.10), the mean GB length increases with depth and decreases in the basal region. The variability is large with maximum values for the large grain sections in ranges 75/76 and 92a. The mean GB linearity decreases in accordance, indicating that longer grain boundaries are more likely to be tortuous. The exceptional results for run 85 (Fig. 4.16a,b) are a consequence of the aliquoting with rotated core azimuth (Tab. 3.1, p. 23). The cross-section reflects a different plane in the glacier. For this depth, GBs are in average shorter and straighter.

4.4 Pore space analysis

Above the firn-ice-transition pores are observed rather than bubbles, which refes to the isolated gas inclusions below. Nonetheless, the term bubbles is used in the following. The thin section LASM image data were analysed to extract bubble parameters as described in section 3.4.5 (p. 29). Fig. 4.15 shows the evolution of bubble cross-section area for entire measurement ranges on a logarithmic scale. The frequencies are normalised as the different range lengths are not comparable with the total bubble number. The bubbles are approximately log-normally distributed in the firn ranges with most bubbles of the order of $1\,\mathrm{mm}^2$. The maximum of the distribution quickly shifts towards $0.1\,\mathrm{mm}^2$ and remains there for the entire core. The distribution evolves into a clearly bimodal distribution, as first described by Lipenkov (2000), which becomes especially pronounced below $53\,\mathrm{m}$ depth, with a second, smaller frequency maximum at very small bubbles[4].

Fig. 4.17 shows bubble parameters for single thin section samples. Instead of mean area the median area is shown with the interquartile range to account for the non-normal distribution of bubble area. The bubble number density in counts/cm² decreases to a depth of $50\,\mathrm{m}$ with an inter-section variability of approximately $25\,\%$. Below $50\,\mathrm{m}$ the variability increases, as well as the average number density per range. Run 85 must be regarded as an exception as discussed later. For the deep and basal ranges (92a–100/101) the bubble number density increases strongly, which appears to coincide with a drop in the stable oxygen isotope ratio $\delta^{18}O$. The total area fraction, i.e. the fraction of a thin section filled by bubbles or the porosity, is decreasing with depth in proportion to the increase in density, as is to be expected from the relation $\rho = (1 - \mathrm{porosity}) \cdot 917\,\mathrm{kg/m}^3$ (density and total area fraction axes are scaled accordingly). The median bubble area $\tilde{A}_B$ decreases exponential to a depth of approximately $53\,\mathrm{m}$ and remains stable before it drops in the basal region in accordance with the increase in number density while the total area fraction is unchanged at about $2\,\%$. The circularity is low in the firn, where the bubbles have bulging shapes. Below the firn-ice-transition it rapidly approaches a value of 0.9. It decreases for run 85 with the lower quartiles indicating a large portion of bubbles with lower circularity down to 0.7. One outlier in run 85 with exceptionally low circularity values is biased from image analysis and must be disregarded.

---

[4]The minimum size threshold for identifying particles in `ImageJ` was lowered stepwise at ranges 57/58, 75/76 and 92a, respectively, and applied to the following ranges.
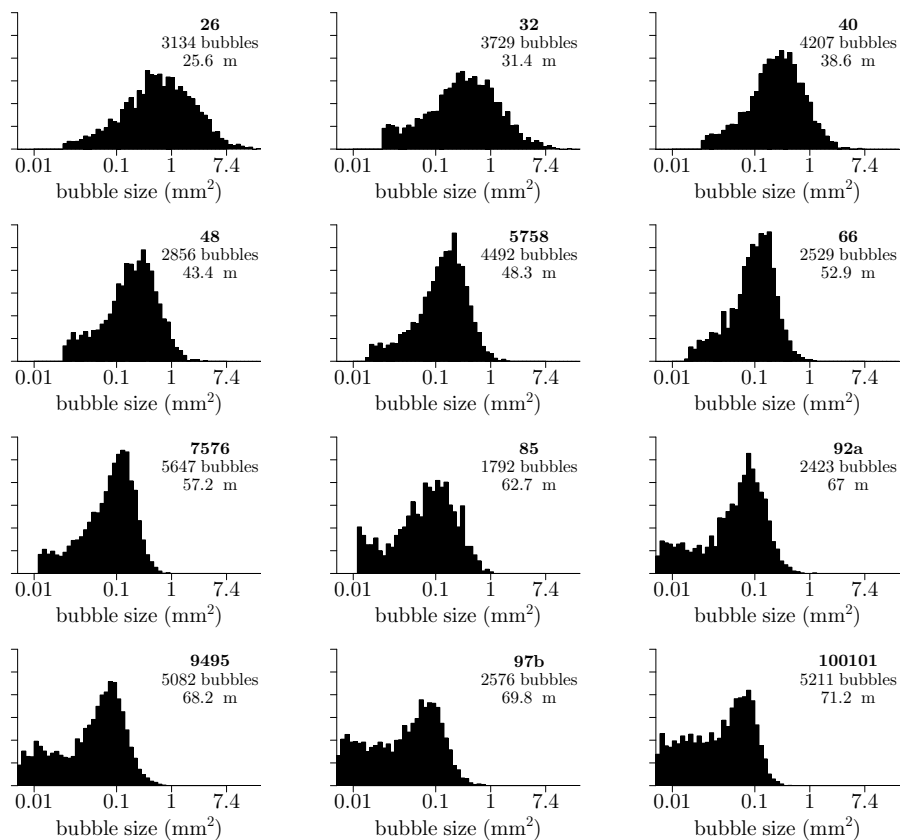
Fig. 4.15: Bubble size distributions for all KCC ranges. The bins are logarithmically spaced. The frequencies are normalised but total bubble number per range is indicated.
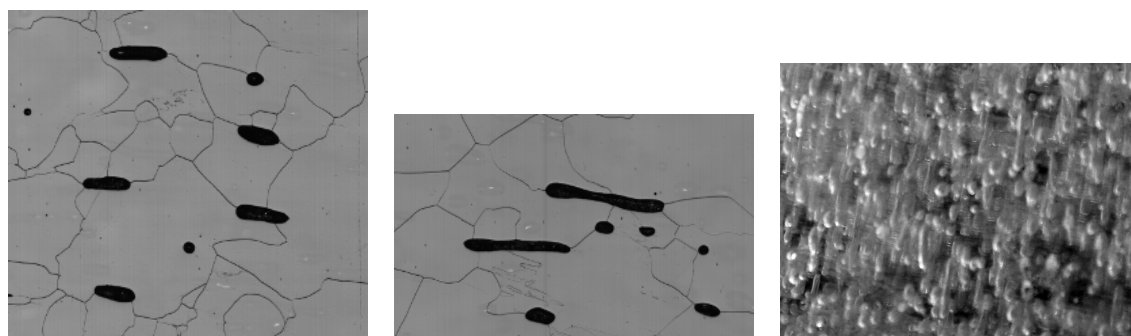
(a) LASM image detail from sample 85-01, $9 \times 8 \, \text{mm}^2$.

(b) LASM image detail from sample 85-11, $9 \times 6 \, \text{mm}^2$.

(c) Photo detail from ^{14}C aliquot of run 77a, approx. $1 \times 1.5 \, \text{cm}^2$.

Fig. 4.16: Clearly elongated bubbles were observed only in thin section image data from run 85. Visual inspection of an ice aliquot from run 77a in metre 59 of the ice core, 4 metres from run 85, exhibits abundant elongated bubbles.
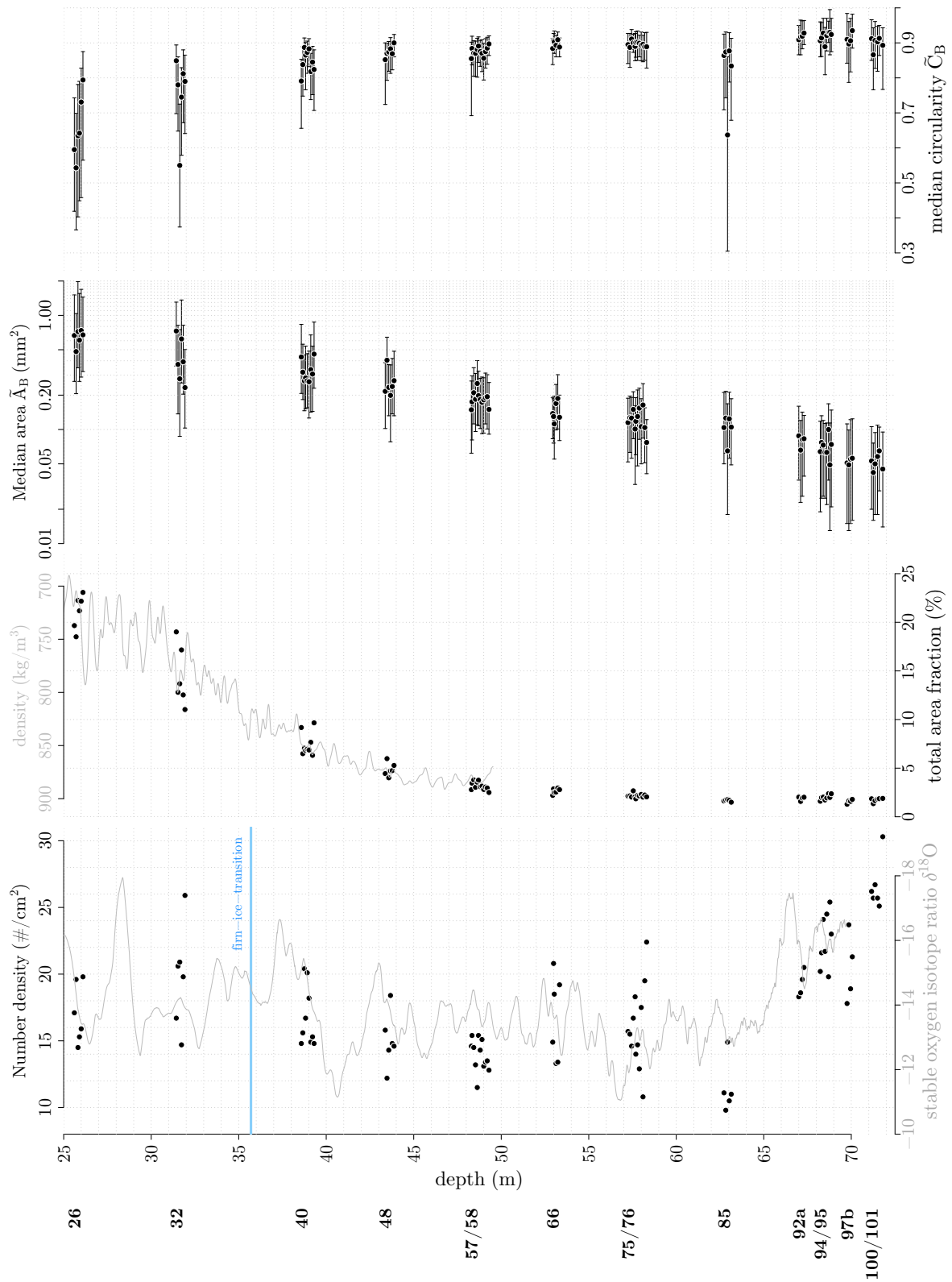
Fig. 4.17: Illustration of KCC bubble parameter evolution with depth. Median bubble area is on a logarithmic scale. In grey, XCT density and stable oxygen isotope ratio $\delta^{18}O$ (on an inverted scale) are shown for comparison.

Bubbles are mostly observed on grain boundaries, especially in fine-grained layers. With increasing depth and frequent occurrence of larger grains bubbles can be found within the large grain cross-section area (Tab. 4.3). Loose clusters of bubbles can be observed, sometimes congruent with small-grain clusters, but also independently. The bubbles are not evenly spaced but often appear closer to their neighbours along network-like paths across the thin section which do not coincide with the GB network. The quantification of this perceived bubble heterogeneity is not straightforward, as many bubbles are also distributed along the GB network, especially when there are large grains. This hypothesised bubble network appears, however, on a scale larger than the average grain size.

4.5 Fabric variations on the cm-scale

The assessment of fabric variations on a sub-decimetre scale is the main aim of this study. The stratigraphy based on LS images (section 4.1) can be extended to the short-scale by examining the microstructure images obtained from FA or LASM (Fig. 4.20). In all depths a layering of only a few centimetres thickness can be observed, on top of intra-thin-section differences. These layers are primarily marked by a sudden or gradual change in grain size. In the entire data set of 85 thin sections, transitions between smaller and larger grain layers as well as the occurrence of fine- or coarse-grained layers were counted:

- 29/85 sections exhibit up to three layer transitions (e.g. Fig. 4.20e), mostly between 39 and 69 m depth.

- 13 sections between 48 and 69 m depth show thick layers (up to section length) with extremely large grains.

- 19 sections have fine-grained layers, sometimes several in one section (e.g. Fig. 4.20b). While they can be observed in the entire core they occur most frequently in the depth between FIT and ~ 60 m.

- 26/85 sections show a heterogeneous distribution of grain sizes with no clear vertical transition between different populations. Especially between 62 and 70 m depth grains of similar size are often clustered.

In the basal sections (range 100/101) steeply inclined structures marked by a slightly different c-axis orientation can be faintly distinguished (Fig. 4.18).

From these observations it follows that fabric and microstructure data need to be studied on a shorter scale than is possible by using entire thin section data to investigate the origin of these layers. Additionally, the sequence of layers, even if they are of the order of 10 cm, cannot be extracted by looking at separate thin sections. The windowed computation and kernel smoothing of available fabric and microstructure data is described in sections 3.4.3–3.4.5 (p. 27). Figures 4.21 and 4.22 show the high resolution data of two exemplary ranges (see appendix B.10, p. 162, for all other ranges including their specific description). For the fabric representation only c-axis eigenvalues are shown as it was demonstrated that cluster fabric is the dominant fabric type. Absolute values as well as the deviation from mean c-axis eigenvalue of the entire run are provided. Eigenvalue λ_3, mean grain size $\bar{A}$, grain number N_g and bubble number N_b were calculated for 2 cm frames moving in 2 mm steps. The bubble area A_B, line
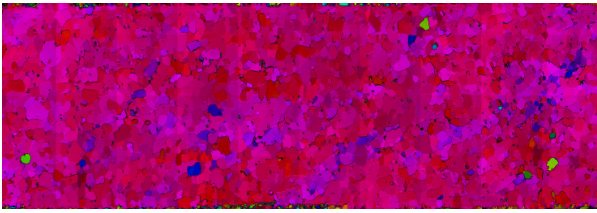
Fig. 4.18: Trend image of section 101-11 $(3.2 \times 10\,\mathrm{cm}^2)$, ice top on the left. Steeply inclined chains of similarly oriented grains can be observed. Red and pink shades correspond to (near-) vertical c-axis orientation.
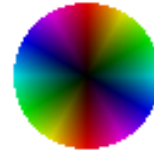
Fig. 4.19: Trend color code: center corresponds to thin section normal, red indicates vertical c-axis orientation.

scan grey value and density ρ are smoothed with a gaussian kernel of 5 mm bandwidth. The grain images resulting from image analysis with `cAxes` and line scan images are provided for visual comparison. In case of larger gaps between thin sections the data might show artificial spikes which cannot be interpreted. The fabric record exhibits a high variability on a scale shorter than 10 cm with steep gradients of up to 0.2 change in eigenvalue over a few centimetres. This is dependent on the chosen frame and step length for the computation, however. For the 2 cm frames the number of grains is mostly sufficient to keep the uncertainty range small compared to the variations. Analoguously to section 4.2 the variability span of the eigenvalues from windowed computation within a range were estimated (Tab. 4.4). The variability of the window-computed eigenvalues is with 0.28 ± 0.12 twice as high as from considering section-computed eigenvalues. Thus, the short-scale change in fabric strength cannot be captured entirely by considering only entire thin sections. It is, however, not straightforward to infer a fabric stratigraphy from the eigenvalue record without consultation of the thin section images. Often, the eigenvalue changes gradually and it cannot objectively be concluded where a layer begins or ends. The results of frames with lower grain numbers are more susceptible to outliers, which also explains the smoother curve in regions with more grains. These effects are, however, closely linked to the processing method and there is potential for development. For the deep ranges 94/95 (Fig. 4.22) and 97b (Fig. B.16, p. 170), instead of layers of changing fabric strength, several grains with high colatitude, i.e. with their c-axis close to the horizontal plane, appear scattered in the polycrystal (Fig. 4.24), lowering the overall fabric strength of this region. While for the upper ranges down to 50 m depth (26–57/58) the eigenvalue varies around the mean value, it appears for the lower ranges, that less oriented large-grained layers are embedded in a better oriented environment (e.g. Fig. B.13, p. 167). In contrast to these thicker layers fine-grained layers (Fig. 4.20), that appear to be better oriented from the visual inspection of the images, cannot be well resolved, as they are often thinner or of the order of the computation window. From these data it can be concluded that a short-scale fabric stratigraphy is not exceptional but the rule, at least for this Alpine ice core.

The comparison of eigenvalue with the microstructural parameters yields partially consistent but also diverging qualitative results over the whole depth of the ice core:

- The mean grain size often changes in accordance with the eigenvalue. Layers with larger grains $(\bar{A} \geq 4\,\mathrm{mm}^2)$ that are only and increasingly found below 40 m depth have mostly lower eigenvalues. However, lower eigenvalues are not always associated with larger grains,

(a) From run 32, top at 31.63 m depth.

(b) From run 48, top at 43.57 m depth.

(c) From run 66, 75a, top at 53.03 m 57.24 m depth.

(d) From run 76, top at 58 m depth.

(e) From run 76, top at 58 m depth.

(f) From run 85, top at 62.73 m depth.

(g) From run 100, top at 71.26 m depth.
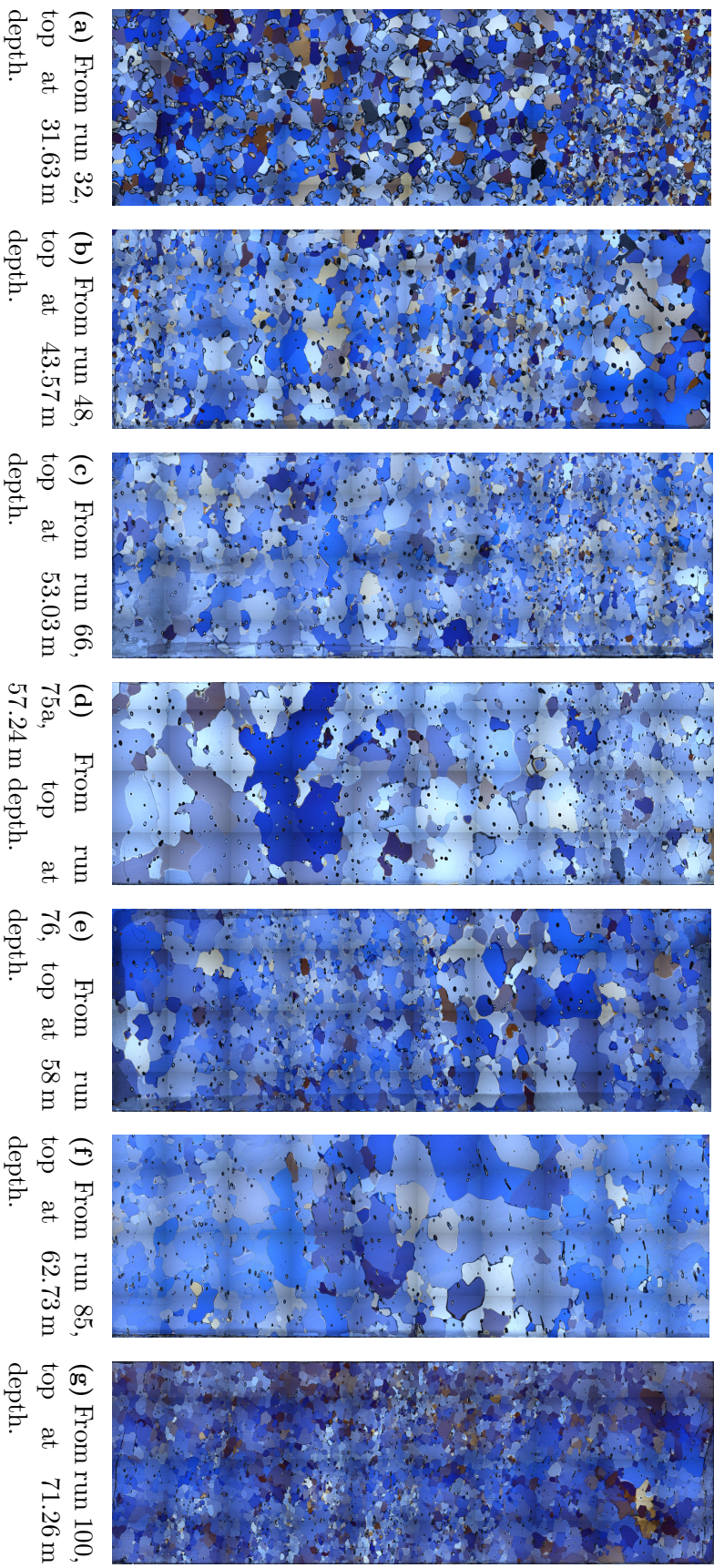
Fig. 4.20: Examples for thin section raw images from fabric analyser measurements ($10 \times 3.2\,\mathrm{cm}^2$) from seven depths between the firn-ice transition and bedrock, illustrating the frequent occurrence of grain size layer transitions. Based on the working chronology from annual-layer counting from CFA and LA-ICP-MS data (pers. comm. P. Bohleber) the thin sections would comprise (from b) to f)) 3, 10, 12, 22 and 35 years, respectively.
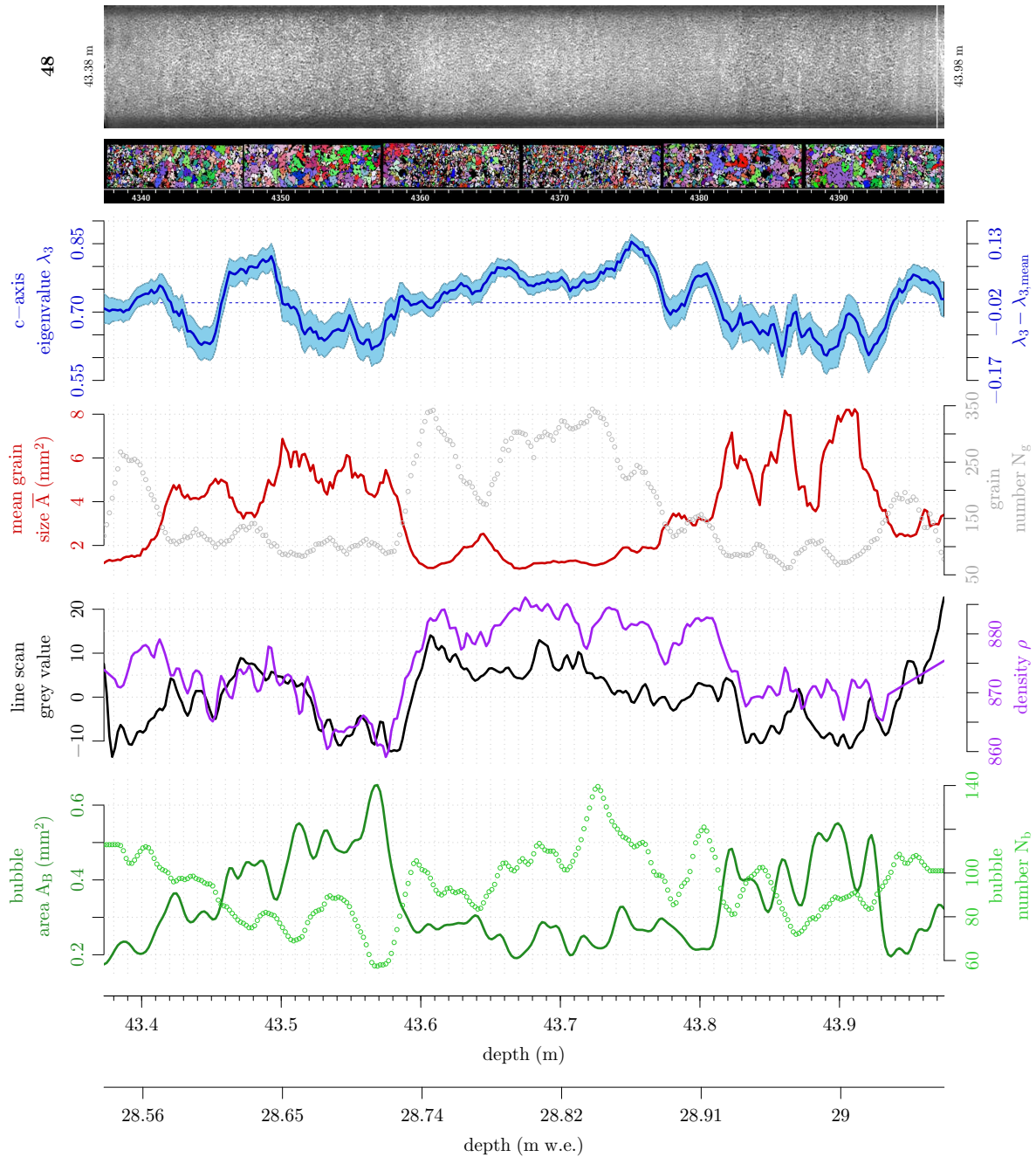
Fig. 4.21: Fabric and microstructure parameters in cm-resolution for KCC run 48. At the top the line scan image is shown (ice top to the left, white lines indicate the beginning and/or end of the section which corresponds to the parameter records), followed by the grain images produced with `cAxes` showing the identified grains and their orientation (colorcode described in Fig. 3.11). The panels show the parameters as calculated for moving frames of 2 cm width in 2 mm steps (c-axis eigenvalue λ_3 with uncertainty range (eq. (2.5)), mean grain size $\bar{A}$, bubble and grain number) or kernel smoothed with a bandwidth of 5 mm (line scan grey value, high-resolution density ρ, bubble area A_B). The mean c-axis eigenvalue is indicated with the dashed blue line. Depth is additionally provided in metre of water equivalent (m w.e.).

and vice versa. A grain size-based short-scale stratigraphy as described above (Fig. 4.20) would not entirely match a fabric-based stratigraphy. Although mean grain size is a good indication for fabric strength, especially for strong grain size differences, it cannot serve as a stand-alone substitute. Fig. B.16 (p. 170) is an example where eigenvalue and mean grain size appear both positively and negatively correlated in certain sections of this range.

- The high resolution density (only available down to run 48) is in good accordance with the line scan grey value and appears inversely proportional to the mean grain size. Only for
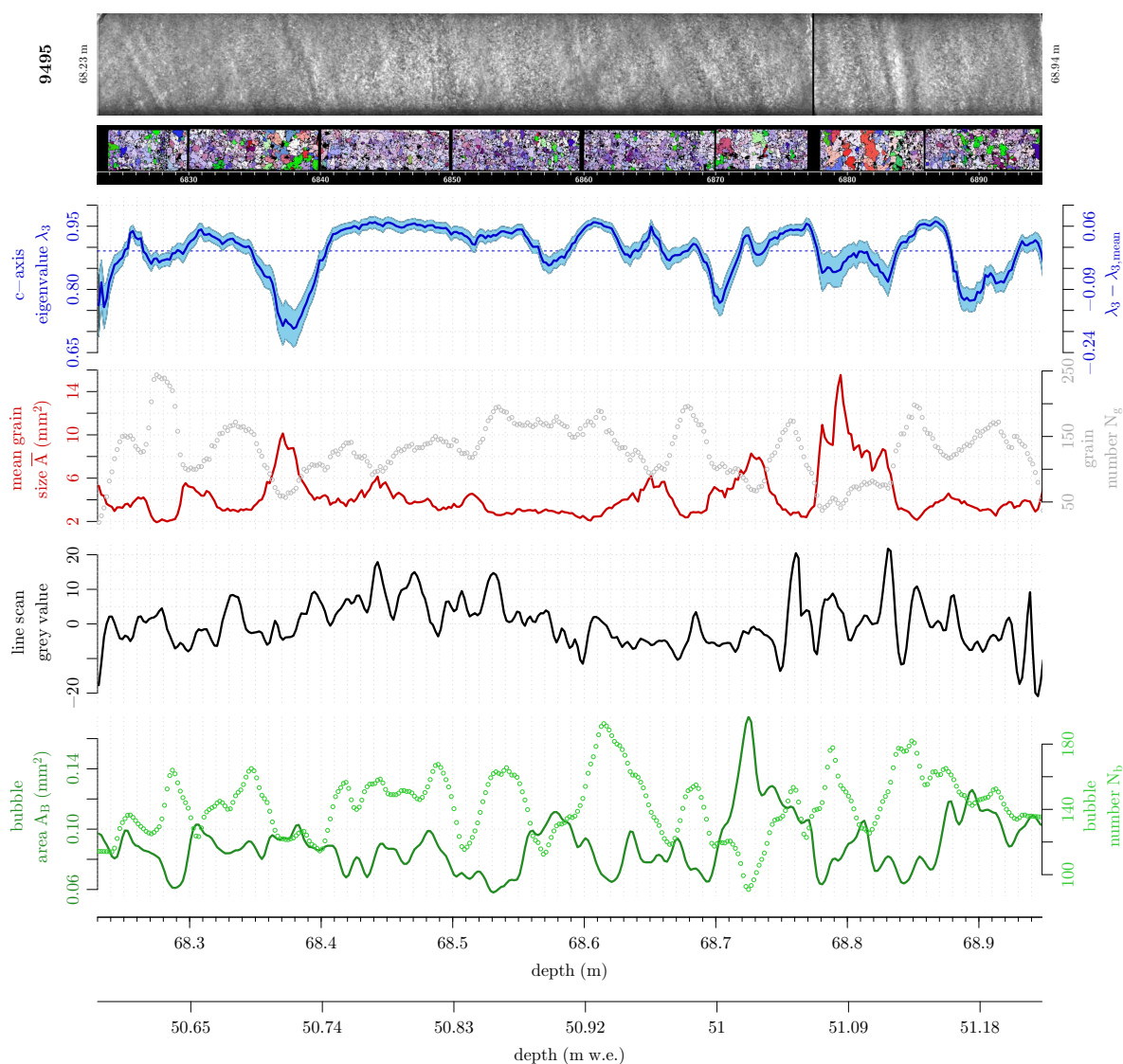
Fig. 4.22: Fabric and microstructure parameters in cm-resolution for KCC range 94/95. Some less oriented large-grain layers or single grains can be observed. The microstructural parameters appear more independent, other than the occasional inverse eigenvalue/mean grain size relationship. The line scan shows inclined layers down to the order of 1 cm thickness which have no representation in the eigenvalue.

Tab. 4.4: Minimum and maximum c-axis eigenvalues λ_3 from windowed computation and variability span within each measurement range.

Run numbers/ ranges	Top depth (m)	Length (m)	Min. c-axis eigenvalue $\lambda_{3,\text{min}}$	Max. c-axis eigenvalue $\lambda_{3,\text{max}}$	Variability span $\lambda_{3,\text{max}} - \lambda_{3,\text{min}}$
26	25.610	0.590	0.37	0.85	0.48
32	31.433	0.597	0.42	0.73	0.31
40	38.577	0.794	0.44	0.84	0.4
48	43.373	0.604	0.6	0.85	0.25
57a/57b/58	48.295	1.036	0.62	0.96	0.34
66	52.942	0.489	0.76	0.95	0.19
75a/75b/76	57.242	1.128	0.76	0.97	0.21
85	62.727	0.505	0.67	0.97	0.3
92a	67.000	0.400	00.51	0.96	0.45
94/95	68.230	0.719	0.71	0.96	0.25
97b	69.760	0.400	0.79	0.96	0.17
100/101	71.160	0.710	0.93	0.98	0.05
				Average:	**0.28 ± 0.12**

run 48 the eigenvalue develops similar to the density and the line scan grey value. Lighter, denser sections coincide here with higher eigenvalues, although not on a cm-scale. The comparison of line scan and grain image supports this observation. Unfortunately, while density and line scan grey value match well enough in the upper half of the core, this cannot be automatically extended to the lower half of the core, where line scans appear more disturbed. No further agreement between grey value and eigenvalue can be found in the lower half of the core.

- The bubble area and number are mostly inversely related: the more bubbles there are, the smaller the smoothing-averaged bubble area. The grain number and bubble number have a similar course; the similarity grows less with depth, however. Analogously, the bubble area develops similarly to the mean grain size and inversely to the density, but again only down to 50 m depth. Below, the bubble area signal appears largely different and more modulated than both mean grain size and eigenvalue record.

Correlation analysis of fabric and microstructure parameters

For a quantitative assessment correlation coefficients were calculated. As described in section 3.4.6 (p. 30) several subsets of all available data points are used for the correlation computation. For the c-axis eigenvalue each subset consists of values calculated from independent, i.e.

non-overlapping, 2 cm frames. The autocorrelation computation for the fabric, microstructure and physical properties data sets shown in cm-resolution (e.g. Fig. 4.21: λ_3, $\bar{A}$, $\bar{A}_B$, N_b, ρ and line scan grey value) yields an estimated average lag of 4 cm for which they autocorrelate, i.e. for which it can be assumed that the data points are not independent of each other (example in appendix B.9, p. 161). However, with a data point interval of 2 cm the sample size of pairs of data available for the correlation computation is already reduced to 19–55 (Tab. B.4, p. 160).

Fig. 4.23 summarises the obtained correlation coefficients for all combinations of the data sets and all measurement ranges. The values represent the median from the coefficient distribution for each pair of data sets. Only significant coefficients were considered for the median calculation. The high number of non-significant values can partly be ascribed to the low number of data pairs and should not directly be interpreted as evidence for the absence of correlation. However, significance is also dependent on the strength of correlation.

Stronger correlations are given in the upper half of the core, which has also qualitatively been observed. More continuous measurements are needed to provide a larger data basis. The results largely confirm the observations described above:

- Eigenvalue and mean grain size anticorrelate well, stronger in greater depths, where the grain size distribution is broader, with exception of the basal range. There, both grain size and eigenvalue do not vary much.

- The mean grain size correlates/anticorrelates strongly with bubble area and number density.

- Consequently, the eigenvalue anticorrelates/correlates, a little weaker, with the bubble area and number density.

- Eigenvalue and grey value, cautiously taken as a density proxy based on a correlation coefficient ~ 0.56 (section 4.1), show a positive correlation for most depths.

- The good anticorrelation between grey value and bubble area close to the firn-ice-transition is not confirmed for greater depths.

The correlations with eigenvalue are generally weaker than those between the microstructure (-based) parameters. The grain number is not included as it must obviously change in dependence of the mean grain size.

Measurement range

Spearman correlation coefficient estimate r_s

Bivariate data	100101	97b	9495	92a	85	7576	66	5758	48	40	32	26
Eigenvalue / Mean grain size	0.365	n.s.	n.s.	−0.793	−0.703	−0.531	n.s.	−0.393	−0.646	−0.332	n.s.	−0.418
Eigenvalue / Grey value	0.429	0.486	0.407	0.492	−0.438	n.s.	0.438	0.328	0.667	0.431	n.s.	n.s.
Eigenvalue / Bubble area	n.s.	−0.523	n.s.	n.s.	−0.518	−0.362	n.s.	−0.451	−0.606	−0.359	n.s.	n.s.
Eigenvalue / Bubble nr	n.s.	n.s.	0.415	0.482	0.41	0.537	n.s.	0.487	0.506	0.32	n.s.	n.s.
Eigenvalue / Density	—	—	—	—	—	—	—	—	0.713	n.s.	n.s.	n.s.
Mean grain size / Grey value	n.s.	n.s.	n.s.	n.s.	n.s.	n.s.	0.484	n.s.	−0.6	−0.543	−0.689	−0.538
Mean grain size / Bubble area	n.s.	n.s.	n.s.	n.s.	0.615	0.656	0.857	0.409	0.781	0.766	0.802	0.498
Mean grain size / Bubble nr	n.s.	−0.555	−0.377	−0.502	−0.442	−0.733	−0.909	−0.641	−0.675	−0.648	−0.877	−0.544
Mean grain size / Density	—	—	—	—	—	—	—	—	−0.757	−0.619	−0.792	−0.605
Grey value / Bubble area	0.417	n.s.	−0.398	n.s.	n.s.	0.271	0.56	n.s.	−0.446	−0.688	−0.791	−0.57
Grey value / Bubble nr	n.s.	0.49	0.375	n.s.	n.s.	n.s.	−0.471	n.s.	n.s.	0.494	0.73	0.673
Grey value / Density	—	—	—	—	—	—	—	—	0.679	0.575	0.907	0.855
Bubble area / Bubble nr	n.s.	n.s.	−0.489	−0.46	−0.532	−0.726	−0.825	−0.636	−0.789	−0.665	−0.922	−0.644
Bubble area / Density	—	—	—	—	—	—	—	—	−0.697	−0.634	−0.869	−0.499
Bubble nr / Density	—	—	—	—	—	—	—	—	0.642	0.559	0.872	0.664

Fig. 4.23: Spearman's rank correlation coefficient r_s for fabric and microstructure parameters for all 12 measurement ranges. Values represent the median of the correlation coefficients from all possible subsets of the bivariate data with a sample interval of 2 cm. The sample size lies between 19 and 55 pairs per calculation, depending on the length of the range. Non-significant (n.s.) values are excluded. Density data is only available for the upper four ranges. Blue shades indicate negative, red shades positive correlation.

4.6 Discussion of fabric and microstructure results

The crystal-orientation fabric results presented here prove that the fabric evolution on this non-temperate, mid-latitude, high-altitude glacier is comparable to the fabric evolution on a much larger scale in polar ice sheets, as shown by numerous fabric studies (reviewed in Faria et al., 2014). Changing fabric patterns can be observed and evidence for dynamic recrystallisation is found.

Short-scale fabric variations appear to be the rule rather than the exception at CG, as they were found in all studied ranges, which comprise more than 10 % of the entire ice core. First indications exist that this may also be the case for polar ice cores (Kleitz, 2013; Kleitz, 2015, and pers. comm. Sepp Kipfstuhl and Ilka Weikusat, 2016). This study is, however, the first to demonstrate this for many depths in an ice core and a high fraction of the total length. An immediate recommendation for similar continuous fabric measurements in polar ice cores arises from this study.

Fabric evolution

The fabric anisotropy is already apparent in the deeper firn, as hypothesised by Diez et al. (2014) from seismic velocity analysis on CG. This is likely due to a horizontal shear component in the firn, resulting from the relative high slope at the southern slope of CG, that enhances the development of preferred crystal orientations. The dominant fabric is cone fabric, indicative of vertical compression in the upper part of the glacier and simple shear dominating in the lower part (Azuma, 1994). The described faint girdle in the last 10 m above the bed suggests a component of diverging flow (Gow and Meese, 2007) as part of a complex flow pattern close to the bed. The flow line on which the KCC ice core is drilled runs towards the ice cliff (Fig. 3.1, p. 14) but at the same time the saddle is broadening, potentially resulting in some extension towards the saddle point (Fig. 4.25). Although, some individual sections in these depths could also be described as exhibiting multiple maxima (e.g. sample 97b-41 in Fig. 4.24), implying strain-induced grain boundary migration and nucleation (discussed in Faria et al., 2014). A check of the associated LASM image did not reveal any salient differences in subGB characteristics between grains of different maxima, indicative of a different recrystallisation history, but this has to be investigated in more detail. As these multiple maxima, observable in adjacent thin sections, add up to a faint girdle over the entire range, the question arises whether these processes act in conjunction.

Several principal zones can be identified in the ice core, based on line scan, fabric and microstructure results, partially corresponding. The most pronounced transition is found to be at approximately 53–55 m depth, i.e. at or below the described elongated single maximum, indicative of pure shear (Azuma, 1994). Here, the respective trends in fabric eigenvalues and mean grain size appear to stabilise, while the variability in grey value and bubble number density reaches a turning point and increases towards the bed. This could mark the changing dominance from compression (pure shear) to simple shear, which appears to be stable from this depth downwards. A current study applying a 3D full Stokes ice flow model of CG, fully thermo-mechanically coupled and with consideration of firn rheology (Gagliardini and Meyssonnier, 1996) or anisotropy (Gillet-Chaulet et al., 2005), which is still in a preliminary state (pers. comm. Carlo Licciulli, 2016), could offer further insights concerning this hypothesis.

(a) Schmidt diagram for section 97b-41 in 70 m depth.

(b) Grain image for section 97b-41 $(7 \times 3.2\,\mathrm{cm}^2)$, color code as shown in Fig. 3.11 (p. 25), ice top to the left.
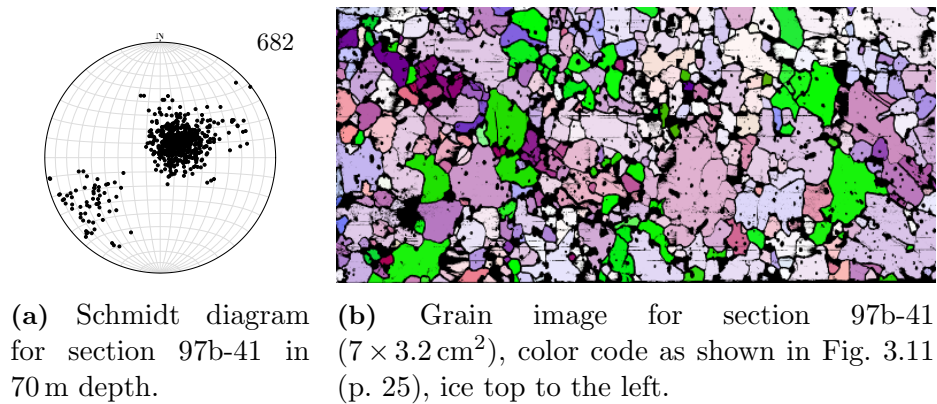
Fig. 4.24: Next to a slightly inclined strong single maximum a second maximum appears in the schmidt diagram, corresponding to the green grains, oriented approximately 90° away from the first. They consist of both large and small grains, sometimes clustered but otherwise distributed in the single maximum grain matrix.
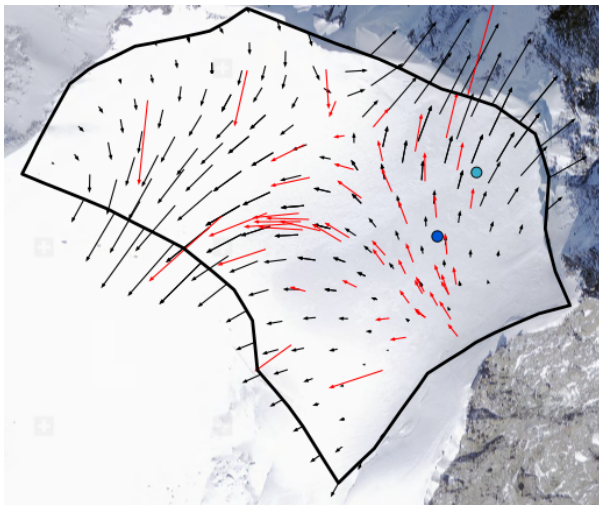
Fig. 4.25: Surface velocity on CG, measured (red) and modelled (black, preliminary results, pers. comm. Carlo Licciulli, 2016). The KCC site is indicated with a blue spot, KCI with a light blue spot further down the flow line. From the surface velocites indicating direction and strength of flow it can be hypothesised that a diverging flow component at the KCC site could be reflected in the fabric.

In contrast to the fabric variability, the grain size variability increases with depth. This can be interpreted as an indication for the dominant effect of deformation on fabric, while grain size (and shape) is possibly controlled by recrystallization processes mainly. By including anisotropic deformation and most relevant recrystallisation mechanisms this has been predicted by microstructural modelling (Llorens et al., 2016a) for small strain rates. Resulting from the deformation scenario inferred from the fabric evolution, the occurence of dynamic recrystallisation is to be expected and, despite the small thickness of the glacier, evidence can be found. The change in grain size distributions with a shift to smaller grains at simultaneous broadening (Fig. 4.11) as well as the massive increase of the maximum grain size (Fig. 4.10) are indicative of active recrystallisation processes. The visual inspection of microstructure LASM images provides evidence of various grain and subgrain topological features, which have been described and associated with specific recrystallisation processes also in firn (Kipfstuhl et al., 2009; Weikusat et al., 2009). The detailed analysis of these features is beyond the scope of this

thesis. It appears clear, however, that despite the relatively small thickness of Colle Gnifetti, all mechanisms of dynamic recrystallisation are present and can be observed in this Alpine firn and ice core. A detailed study of the available material should be done to test the conclusion from the fabric analysis.

Inclined single maximum

Although no borehole inclination could be measured directly after the drilling of the ice core, it is not to be expected, given the short length of the ice core, that a possible borehole inclination could account for the high inclination of the single maximum of 15° in average below 55 m depth. However, the layer inclination visible in the line scans below 51 m depth (section 4.1) lies within the same range. It could be assumed that the fabric cone inclination is a result of vertical drilling into inclined layers, as mapped by GPR (Eisen et al., 2003; Bohleber, 2011; Konrad et al., 2013). On the other hand, from the flank flow regime at the drilling site, an oblique single maximum as a result of dominating simple shear in the lower region of the glacier, as hypothesised above, could be expected (Llorens et al., 2016b). Without inclination data this cannot be further constrained[5]. Another indication for this deformation regime change could be, that a borehole camera lowered into the neighbouring ice core KCI borehole in 2013 got stuck at a depth of 52 m where the borehole gave the impression of tilting away. Accounting for the shorter length of KCI, due to the shallower firn-ice-transition, and the 8 years since the drilling in 2005, this qualitative observation would support the hypothesis. The schmidt diagrams for KCI fabric (pers. comm. Jan Eichler, 2013, Fig. B.2, p. 152) show an elongated single maximum at 48 m depth and a near-vertical single maximum below that depth, in contrast to the inclined single maximum in KCC. The comparison of fabric data from the two neighbouring (ca. 100 m apart) cores KCI and KCC (Fig. 4.9), on a common depth scale, suggests that the fabric evolution on a metre-scale is continuous over the lateral extension of a few hundred metres on the glacier. However, the short-scale variability, as apparent in one continuously sampled run of KCI, might be different. This hypothesis can only be tested by fabric measurements on twin cores drilled in short distance to each other.

Short-scale fabric variations

The strong differences in fabric strength in the firn correspond, to a certain extent, to the clearly distinguishable layers in the line scan and could be attributed to the associated density fluctuations. This is most prominently apparent in run 48, for which the stratigraphic layering exhibits two levels: Strong transitions in density, and associated grey value, correspond to changes in mean grain size and eigenvalue, but annual layers (Fig. 5.2, p. 72), which are faintly discernible in the line scan, are embedded in the more obvious stratigraphy, corresponding to a multi-year cycle. This is evidence that fabric variations, which appear as a single layer, can, in fact, correspond to the coalescence of several initial layers, similar to the multi-year cycles observed in impurity records at CG (Wagenbach et al., 2012). It remains unclear if this process might be happening in several stages, repeatedly merging adjacent layers to new layers. It is inferred that, from the data examined here, the short-scale variations do not reflect, but might be indirectly dependent on annual-layer thinning. This hypothesis could be tested on a polar

---

[5]Only very recently (October 2016) borehole inclination data from the KCC borehole became available. Preliminary analysis indicates less than 5° inclination in the upper 55 m and an abrupt increase to 7–10° below 60 m.

core, exhibiting short-scale fabric variations, that is dated by annual-layer counting with a high certainty.

While the fabric variations appear more regular in the shallower part of the core, the strongest short-scale variations occur in the deep part of the core with thick layers of large grains. This observation leads to the speculation that some layers are singled out, for causes not yet understood, and devoloped further by deformation and recrystallisation, while other layers are assimilated as the anisotropy increases. Although melt layers are a frequent feature in the firn of Colle Gnifetti, it is unclear how they evolve with depth and whether a melt layer has implications for the fabric evolution, e.g. for such large-grain layers observable in depth. Fig. 4.26 shows the lowermost section (approximately less than a metre) of the unconstrained KCC borehole, two years after drilling. The qualitative impression of the borehole wall is that of a pancake stack, i.e. the deformation of the borehole occurs in alternating rings of approx. a few centimetres thickness. No borehole deformation measurement could be realised so far. The comparison of short-scale fabric variability and borehole deformation could, however, provide direct evidence of a causal relationship between these layers and the localisation of deformation on the same scale.

Fig. 4.26: Photo from bedrock section taken with borehole camera in KCC borehole in 2015. Two years after the drilling the unconstrained borehole has started to deform irregularly.

Similar grain size and associated fabric layering as observed in the KCC ice core is reported from Siple Dome, Antarctica (DiPrinzio et al., 2005), in Holocene ice and glacial ice. They find that fine-grained layers lack evidence of recrystallisation. A significant lower occurrence of subgrain boundaries in fine-grained ice is also described by Weikusat et al. (2009). Subgrain features like dislocation walls, subGBs of various forms, island grains, the pinning of GBs by bubbles (Azuma et al., 2012), and the bending of GBs to a higher subGB density (Weikusat et al., 2009) can be identified for the greater part of the KCC core starting from above the firn-ice-transition down to bedrock. The observation by DiPrinzio et al. (2005) and Weikusat et al. (2009) cannot currently be confirmed nor contradicted based on the KCC microstructure data due to lack of a statistical evaluation, but it could not be observed that large grains exhibit a higher density of recrystallisation related features. On the contrary, in the firn samples fine-grained layers were observed to contain more subGBs. Further investigations are needed to clarify this. From the qualitative assessment illustrated in Fig. 4.12 and described in Tab. 4.3 the available data set is considered to be ideally suited for a comprehensive study on subgrain structures evolving under dynamic recrystallisation and in interaction with bubbles, while the fabric information is also supplied.

Basal layer

The basal layer comprises the deepest 75 cm below 71.16 m depth as inferred from fabric analysis (runs 100/101). Considering the onset of a high dust load, described in section 3.5.1 (p. 32), it might already begin at ca. 70.15 m, i.e. including runs 98 and 99, but the line scans of these runs exhibit a different quality than those of runs 100/101. A similar silt layer of approximately 1 m depth above bedrock has been found in two other cores from CG (Wagenbach et al., 2012). In the last 90 cm the sudden change in grain size and eigenvalue are evidence of a strong shear strain at the frozen base of the glacier, as described by Samyn et al. (2005) for cold based Antarctic glaciers. Again, the runs 98/99 might reveal a more gradual change. Remarkably, the first small stones were observed during the drilling in a depth of ca. 69.40 m (run 96), well above this basal layer. It is speculated here, that ice flow perturbations above the basal layer, which could also account for the disturbed line scans (section 3.3.3, region V, p. 21), could incorporate bedrock particles from further uphill along the flow line. Furthermore, the inclined structures in some basal thin sections (Fig. 4.18) bear resemblance to the tilted-lattice bands recently described for the NEEM ice core by Jansen et al. (2016), where they are identified in ice with strong anisotropy under layer-parallel shear as a result of small random disturbances.

Bubble analysis

Bendel et al. (2013) describe the bimodal size distribution of micro- and normal bubbles in the EDML ice core. They observe that microbubbles, which become trapped in the ice matrix already above the close-off depth (Lipenkov, 2000), disappear with depth, as a consequence of normal bubbles growing. However, the KCC bubble size distribution develops the bimodal distribution with increasing depth.

From the higher bubble elongation in run 85 it can be concluded that the thin section plane of run 85 is probably closer to the plane also containing the direction of ice flow than the other runs. The number density in this plane is lower than in the neighbouring ranges. It is suggested that the average next-neighbour distance is increased by plastic displacement in the deforming ice. The density can be deduced from the total area fraction in 2D cross-sections in good approximation. The visual inspection of the ^{14}C aliquot of run 77a (Fig. 4.16c) revealed that the occurrence of tubularly elongated bubbles is not restricted to run 85. It can be assumed that it would be commonly found in this depth region (58–63 m) and possibly above and below. However, in run 57b in ca. 49 m depth, that was allegedly aliquoted under the same core azimuth orientation as run 85, the majority of bubbles is not strongly elongated. Additionally, it was realised that the direction of elongation is close to perpendicular to the surface of the PP aliquot for the majority of runs, likely concealing a possible evolution of bubble elongation almost entirely. To obtain the full information on bubble elongation a visual inspection of the KCC archive pieces is necessary. For a quantitative assessment 3D imaging by CT would be desirable. The bubble elongation is indicative of a high strain rate in this depth region (Alley and Fitzpatrick, 1999).

The stable oxygen isotope ratio $\delta^{18}O$ is shown in Fig. 4.17 (p. 53) together with the bubble number density. This speculative comparison is inspired by the findings by Bendel et al. (2013) concerning the correlation of the two parameters on the large scale, accompanied by an anticorrelation with dust content, which they conclude to be the actual driver for high number densities. The basal isotope anomaly ("basal layer enigma", Wagenbach et al., 2012), which

is apparent in earlier cores from CG as well as in the KCC ice core, might coincide with the sudden increase of the number density, which seems to arise before the increase in dust in the basal layer and the associated decrease of the mean grain size. This could be merely a coincidence, arising from unrelated processes. Further analyses should follow this observation to clarify the dependencies.

5 Fabric and climate proxies at Colle Gnifetti

Impurity data from the Alpine ice core were analysed together with the fabric data, addressing the hypothesis of short-scale fabric variability conveying information on local climatic conditions (section 5.1). Similarly, stable oxygen isotope ratio $\delta^{18}O$ data from the KCC ice core were examined to evaluate if fabric could likely bear any memory of the local temperature during deposition. A pilot study demonstrating the potential of laser ablation-inductively coupled plasma-mass spectrometry for the investigation of the spatial distribution of impurities in relation to the ice microstructure is included (section 5.2). The main findings of this chapter are discussed in section 5.3.

5.1 Fabric and continuous flow analysis data

To further investigate the origin of the fabric variations described in section 4.5 (p. 54) the impurity records obtained from CFA (section 3.5.1, p. 32) and the stable oxygen isotope ratio $\delta^{18}O$ are considered along the c-axis eigenvalue λ_3, which serves as a representative parameter of fabric strength. This is done to assess if a direct influence of the impurities on fabric strength is apparent on the short scale. It is established that the stark change in dust load during climatic transitions, i.e. glacial/interglacial or Dansgaard-Oeschger-events (factor 8–80 in mineral dust during the last glacial maximum as compared to Holocene polar ice, Fischer et al., 2007), significantly changes the grain size and fabric in polar cores (e.g. Durand et al., 2007). The seasonal variations in dissolved impurity content of the KCC ice core (Fig. B.4, p. 154) do not exceed $2000\,\mathrm{ng/g}$ (ppb) for calcium, sodium, ammonium and nitrate. The dust load reaches maximum values of the order of $4 \cdot 10^5$ particles per ml with a minimum particle size of $1.2\,\mu\mathrm{m}$. The question arises if these seasonal variations are large enough to exert influence on the development of the fabric strength on the short scale. The $\delta^{18}O$ record cannot be considered a direct proxy for air temperature during accumulation. Bohleber et al. (2013) showed the large influence of local conditions during deposition ("glacio-meteorological noise") which obstruct the derivation of a regional temperature proxy record from the CG multi-core array. However, the observed and described variations in fabric could also be the reflection of an evolution that is specific for the drilling location. Under the assumption that the isotope record can be regarded as a proxy of local temperature, the hypothesis that the temperature conditions during deposition determine the ensuing fabric evolution is tested.

Analoguously to section 4.5 three exemplary ranges are presented (Fig. 5.1, 5.2 and Fig. 5.3, see appendix B.11, p. 172, for all other ranges) with one from above the firn-ice-transition and two from below. Again, line scan and grain image are shown along with c-axis eigenvalue λ_3, mean grain size $\bar{A}$ and grain number per frame for the windowed computation. The lower panels show the dissolved impurities calcium (Ca^{2+}), sodium (Na^+), ammonium (NH_4^+) and nitrate (NO_3^-), the conductivity of the melt water, the particulate dust content and the stable oxygen isotope ratio $\delta^{18}O$. For the two upper ranges shown here, vertical grey solid lines indicate annual-layers as picked from CFA data (working chronology of KCC ice core, March 2015, pers. comm. P.

Bohleber). The layer thickness decreases rapidly with depth (section 3.1) from an average of $\sim 16\,\mathrm{cm}$ in run 32 to an average of $\sim 4.3\,\mathrm{cm}$ in run 48 and an estimated thickness of $\sim 0.5\,\mathrm{cm}$ in range 75/76 at approx. 80 % depth.

The impurity data show the same trends with shared major peaks. On a finer scale, considering the signals' relative amplitude and more of the CFA data than is shown here together with fabric data, the ammonium and nitrate signal run often very similar, while calcium and sodium signal match closely with the dust record. The sodium signal appears smoother than calcium and dust record. The conductivity signal reflects the contribution of both groups. The $\delta^{18}O$ shows a high-frequency modulation on top of an oszillation with a changing wavelength that mostly matches the CFA baseline down to run 85. The wavelength decreases with depth and is larger than the fabric layers typically observed in the KCC data for the upper fabric ranges and smaller for the deeper fabric ranges, where the thick large-grain layers were observed.

A strong connection on the scale of a few centimetres between the impurities and the grain size and number is apparent in all depths. The general trend of the impurity amplitude on the scale of decimetres, i.e. the trend obtained by strong smoothing, or the baseline, appear weakly related to the respective trend in the eigenvalue: For the firn runs they are opposed (Fig. B.18, p. 172), while below the firn-ice-transition, for the medium ranges, the connection is positive (Fig. 5.2, B.20, B.21, p. 174), also with the isotope record. Sometimes, similar features on a sub-decimetre scale can be observed in both impurities and fabric as for example in range 75/76 (Fig. 5.3). On the other hand, most sub-decimetre fabric layers do not find a direct counterpart in the impurity signal. Considering the four large-grain sections in this range at 57.32 m, 57.39 m, 57.87 m and 58.20 m depth, where the high resolution eigenvalue drops below 0.8 (average of 0.9 in this range), it appears that for the upper two layers the impurity concentrations are elevated, while for the lower two layers it is rather low. A connection between impurities and short-scale fabric becomes even less clear in the deep ranges. However, most of the very large-grained sections in the deeper ranges have a lower impurity content than the finer grains in the same range. It has to be kept in mind that this comparison is likely to be sensitive to the chosen parameters for windowed computation and the different resolution and dispersion of the CFA data. The impurity records can be linked to various degrees to the line scan images. In the firn, every major impurity peak is found as a light layer in the line scan and represents a seasonal or annual layer. In the medium ranges, e.g. run 48, a 25 cm thick lighter section corresponds to several peaks identified as annual layers, forming a multi-year cycle (Bohleber et al., 2013), weakly discernible in the line scan. Only in the case of run 48, it can be confidently concluded that the sequence in grain size layers and the associated variation in fabric strength corresponds to the multi-year cycle sequence found in the impurities.

Correlation analysis of fabric and microstructure parameters with impurity and isotope data

The correlation coefficients overwhelmingly confirm the observations concerning the mean grain size and the grain number: The impurities are clearly anticorrelated/correlated with the mean grain size and grain number, which naturally anticorrelate. For the ranges 92a and 94/95 no significant coefficients could be obtained, probably due to a small sample size. For the fabric and impurity coefficients two main results can be reported:

- Negative correlations between eigenvalue and impurities are calculated in the firn ranges,
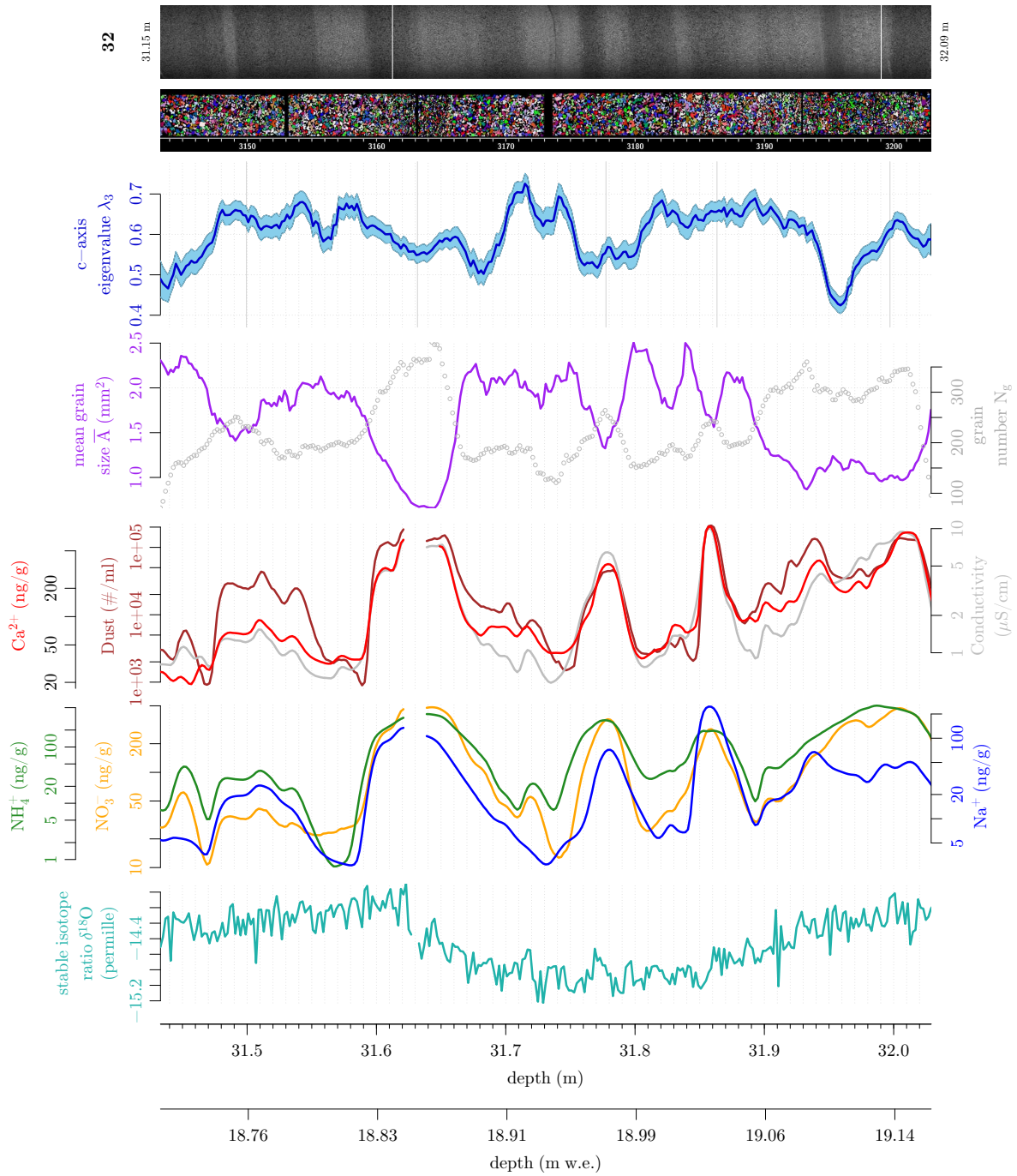
Fig. 5.1: Fabric and microstructure parameters in cm-resolution in comparison with CFA data for KCC range 32. Calcium (Ca^{2+}, red), sodium (Na^+, blue), ammonium (NH_4^+, green) and nitrate (NO_3^-, orange), the conductivity of the melt water (gray), the particulate dust content (brown) and the stable oxygen isotope ratio $\delta^{18}O$ (in ‰, turquoise) are shown. Vertical grey solid lines indicate annual-layers as picked from CFA data.
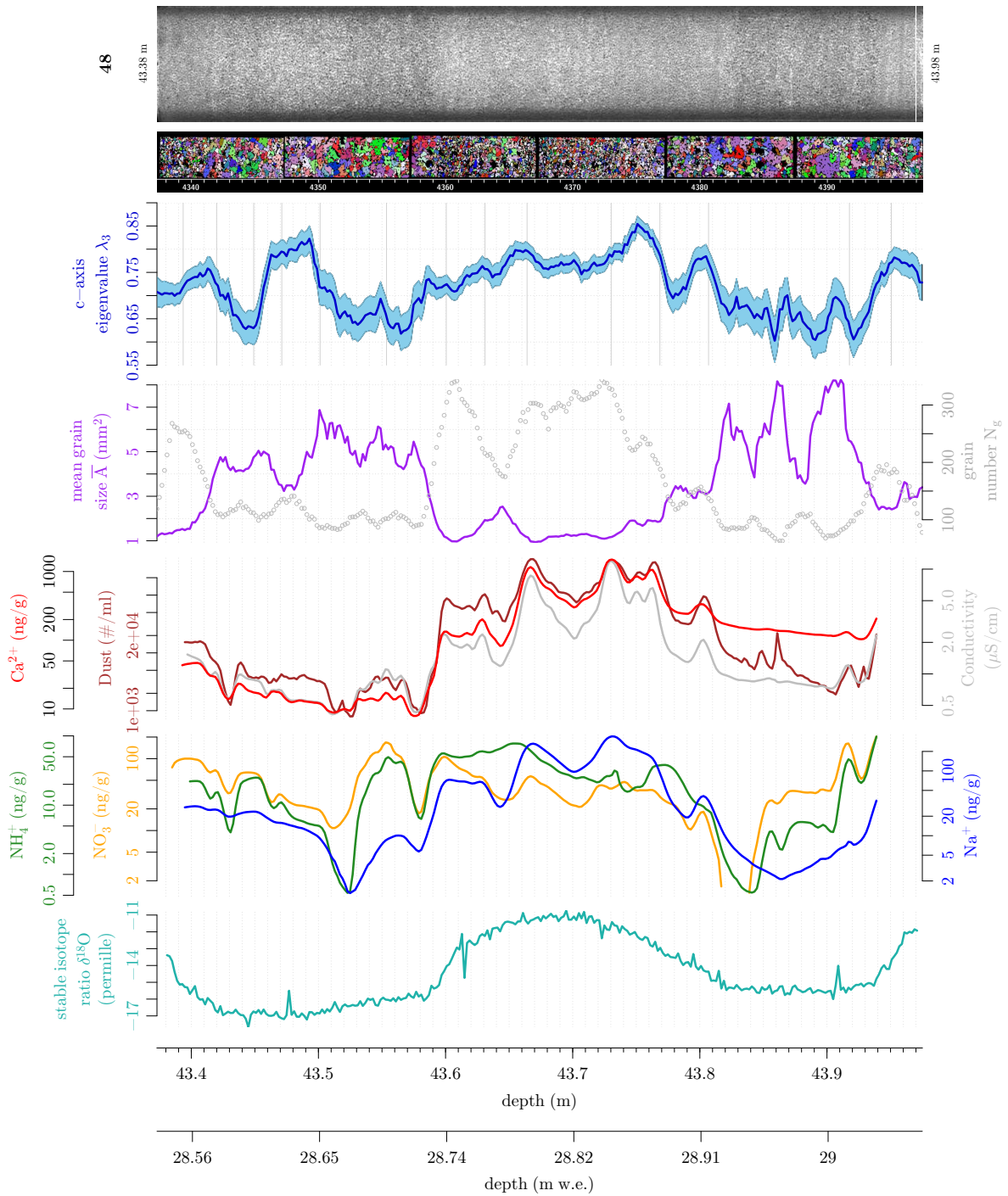
Fig. 5.2: Fabric and microstructure parameters in cm-resolution in comparison with CFA data for KCC range 48. Vertical grey solid lines indicate annual-layers as picked from CFA data. In this run correlations between all parameters can be found.
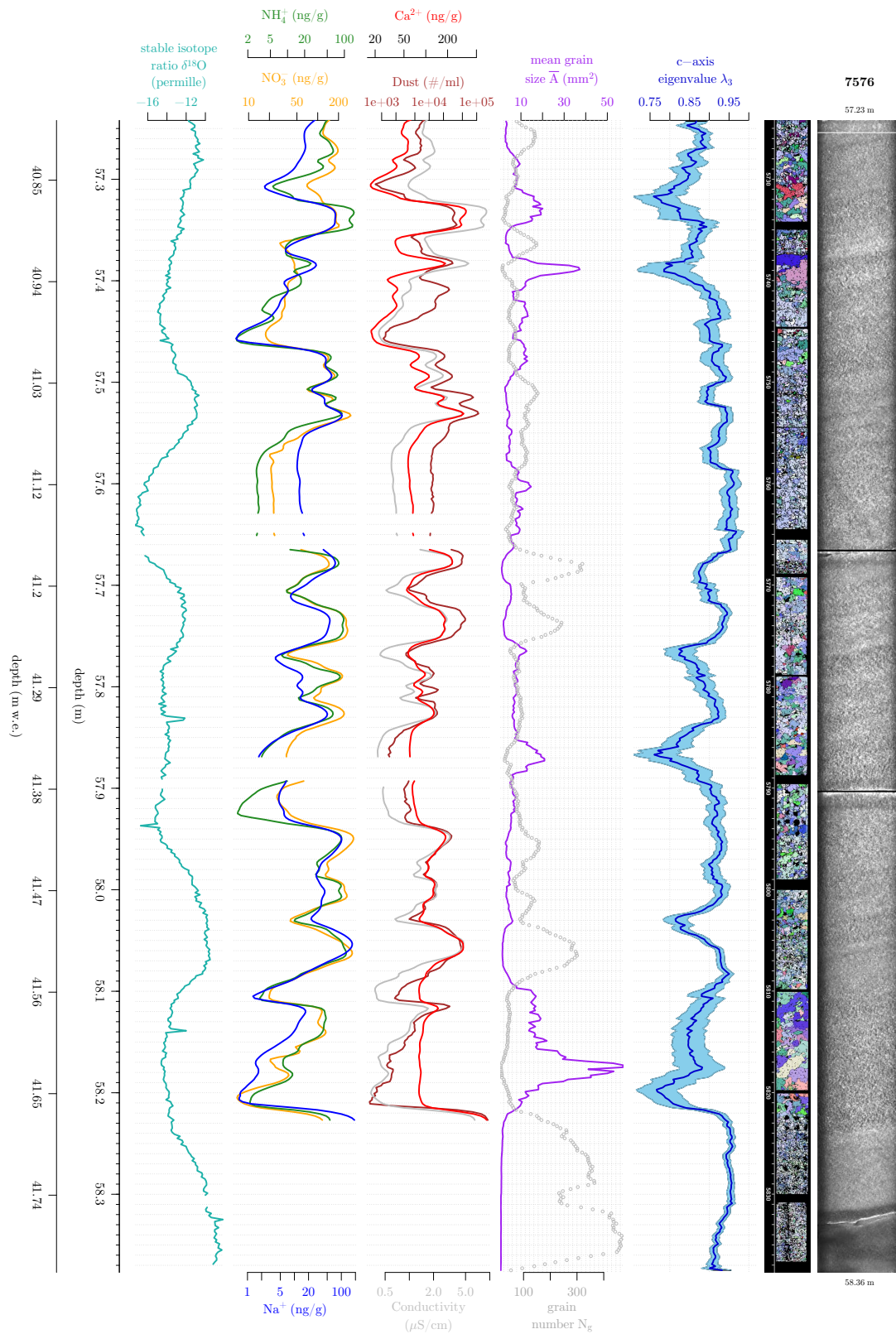
Fig. 5.3: Fabric and microstructure parameters in cm-resolution in comparison with CFA data for KCC range 75/76.
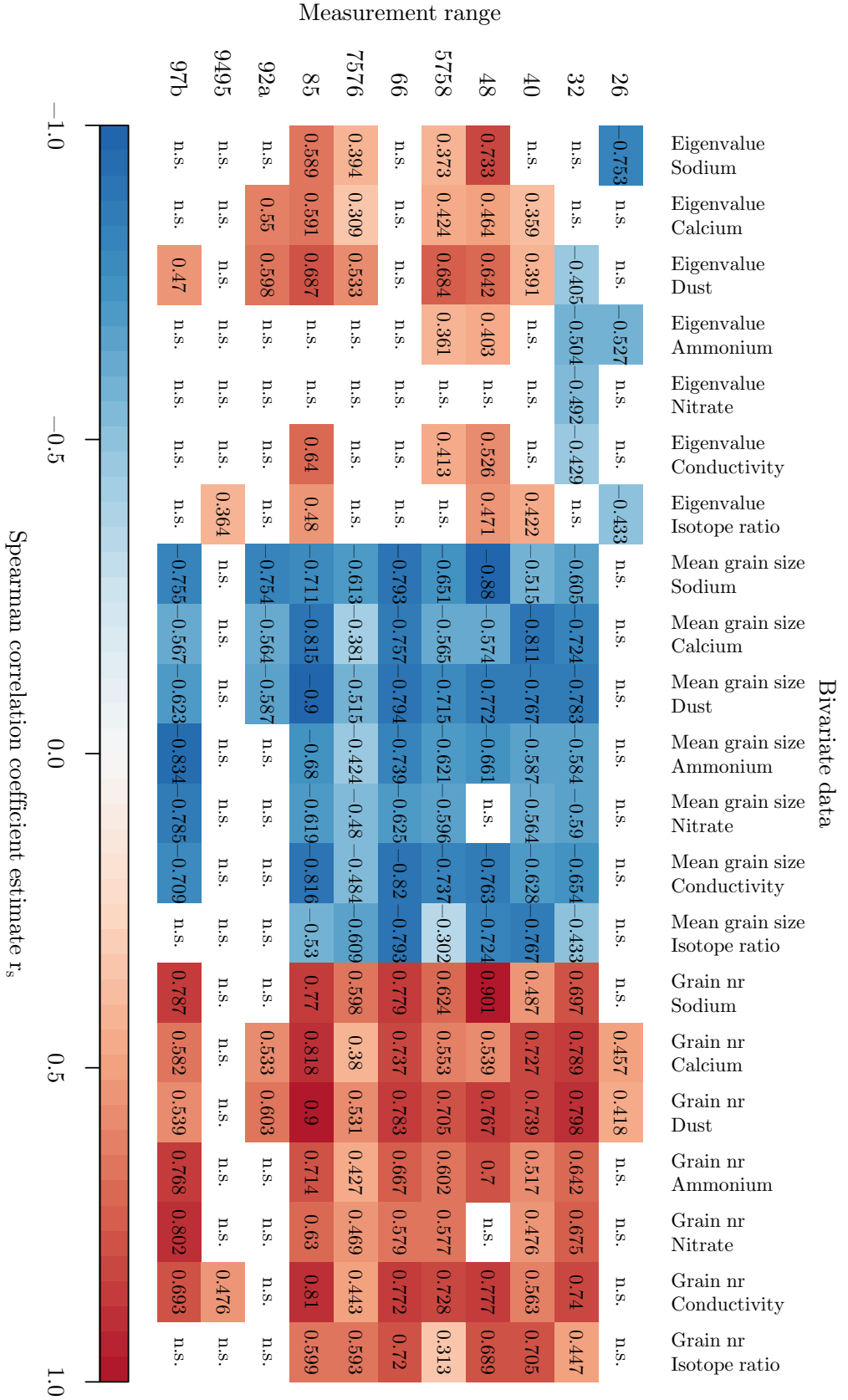
Fig. 5.4: Spearman's rank correlation coefficient r_s for c-axis eigenvalue, mean grain size and grain number with impurities from CFA and stable oxygen isotope ratio for 11 measurement ranges (no CFA data available for bottom range). Values represent the median of the correlation coefficients from all possible subsets of the bivariate data with a sample interval of 2 cm. The sample size lies between 13 and 53 pairs per calculation, depending on the length of the range and the occurrence of missing intervals in the CFA data. Non-significant (n.s.) values are excluded, i.e. if the p-value > 0.05 (section 3.4.6, p. 30). Blue shades indicate negative, red shades positive correlation.

Axes: Measurement range (26, 32, 40, 48, 5758, 66, 7576, 85, 92a, 9495, 97b) · Bivariate data · Spearman correlation coefficient estimate r_s (colour scale from −1.0 to 1.0).

Bivariate data	26	32	40	48	5758	66	7576	85	92a	9495	97b
Eigenvalue Sodium	−0.753	n.s.	n.s.	0.733	0.373	n.s.	0.394	0.589	n.s.	n.s.	n.s.
Eigenvalue Calcium	n.s.	n.s.	0.359	0.464	0.424	n.s.	0.309	0.591	0.55	n.s.	n.s.
Eigenvalue Dust	n.s.	−0.405	0.391	0.642	0.684	n.s.	0.533	0.687	0.598	n.s.	0.47
Eigenvalue Ammonium	−0.527	−0.504	n.s.	0.403	0.361	n.s.	n.s.	n.s.	n.s.	n.s.	n.s.
Eigenvalue Nitrate	n.s.	−0.492	n.s.	n.s.	n.s.	n.s.	n.s.	n.s.	n.s.	n.s.	n.s.
Eigenvalue Conductivity	n.s.	−0.429	n.s.	0.526	0.413	n.s.	n.s.	0.64	n.s.	n.s.	n.s.
Eigenvalue Isotope ratio	−0.433	n.s.	0.422	0.471	n.s.	n.s.	n.s.	0.48	n.s.	0.364	n.s.
Mean grain size Sodium	n.s.	n.s.	−0.605	−0.88	−0.651	−0.793	−0.613	−0.711	−0.754	n.s.	−0.755
Mean grain size Calcium	n.s.	n.s.	−0.724	−0.574	−0.565	−0.757	−0.381	−0.815	−0.564	n.s.	−0.567
Mean grain size Dust	n.s.	n.s.	−0.811	−0.772	−0.715	−0.794	−0.515	−0.9	−0.587	n.s.	−0.623
Mean grain size Ammonium	n.s.	n.s.	−0.767	−0.661	−0.621	−0.739	−0.424	−0.68	n.s.	n.s.	−0.834
Mean grain size Nitrate	n.s.	n.s.	−0.584	n.s.	−0.596	−0.625	−0.48	−0.619	n.s.	n.s.	−0.785
Mean grain size Conductivity	n.s.	n.s.	−0.654	−0.763	−0.737	−0.82	−0.609	−0.816	n.s.	n.s.	−0.709
Mean grain size Isotope ratio	n.s.	n.s.	−0.433	−0.724	−0.302	−0.793	n.s.	−0.53	n.s.	n.s.	n.s.
Grain nr Sodium	n.s.	n.s.	0.697	0.901	0.624	0.779	0.598	0.77	n.s.	n.s.	0.787
Grain nr Calcium	0.457	n.s.	0.789	0.727	0.553	0.737	0.38	0.818	0.533	n.s.	0.582
Grain nr Dust	0.418	n.s.	0.798	0.739	0.705	0.783	0.531	0.9	0.603	n.s.	0.539
Grain nr Ammonium	n.s.	n.s.	0.642	0.7	0.602	0.667	0.427	0.714	n.s.	n.s.	0.768
Grain nr Nitrate	0.689	n.s.	0.675	n.s.	0.577	0.579	0.469	0.63	n.s.	n.s.	0.802
Grain nr Conductivity	0.74	n.s.	0.563	0.777	0.728	0.772	0.443	0.81	n.s.	0.476	0.693
Grain nr Isotope ratio	0.447	n.s.	n.s.	0.689	0.313	0.72	0.593	0.599	n.s.	n.s.	n.s.

74

while positive correlations occur for the ice part.

- The strongest correlations are found for sodium, calcium and dust. Especially for ammonium and nitrate only few significant correlations with the eigenvalue were calculated.

5.2 Pilot study: spatial distribution of impurities with LA-ICP-MS

Motivation for microstructure-guided impurity measurements by laser ablation

The collaboration of CCI in Maine and IUP in Heidelberg concerning the KCC ice core gave rise to the opportunity of a pilot study addressing the question of the spatial distribution of impurities with respect to the ice microstructure. Impurity data measured by CFA represents a bulk signal of the melted ice without consideration for the original microstructure of the ice matrix (section 3.5.1). However, with LA-ICP-MS it is possible to sample the ice surface with a spatial resolution high enough to investigate if the signal variability is dependent on microstructural features. This allows to test the hypothesis that inhomogeneous impurity distributions develop with depth due to ongoing recrystallisation processes and associated dragging or pinning effects (Alley et al., 1986; Weikusat et al., in press). It is then to be expected to find a radial gradient between grain interior and grain boundary towards the latter, which becomes stronger with depth. This might be different for different impurity species due to mobility and electronegativity differences. This has several implications:

- A changing impurity distribution with respect to the ice microstructure might then provide a different feedback to ongoing recrystallisation and deformation processes, thus exerting an indirect influence on fabric evolution.

- The integrity of the climate-governed impurity signal could be affected by a microstructure-modulated impurity signal in a significant way (Iliescu and Baker, 2008; Faria et al., 2010), which would be especially relevant for depths in which ice crystals are frequently larger than the expected annual-layer thickness (Fig. 5.5).

The feasibility of this kind of study with this LA-ICP-MS setup had not been tested before.

Results for sodium and iron impurity content

For the estimation of the local impurity content, i.e. along a GB or within a grain, the integrated signal for each separate measurement (section 3.5.2, p. 32), normalised to the duration of ablation, is assessed. The raw data is corrected by substracting the background that is estimated based on the mean of the last 50 data points, i.e. the last 10 seconds of ablation. The integral of the corrected data is calculated as impurity content in counts per millimetre in order to compare the data quantitatively (Fig. 5.6). For each grain that was measured in the sections detailed in Tab. 3.4 (p. 33) the impurity content from different locations (Fig. 3.18, p. 35), i.e. either ablating along or parallel to a GB or in the grain interior, are compared (Fig. 5.7 and appendix C., p. 180). The results of all measurements are summarised in Fig. 5.8 and 5.9. In Fig. 5.10 and 5.11 the ratio of impurity content in grain boundaries and parallel lines is shown.

Fig. 5.5: Illustration of maximum grain sizes obtained from KCC thin sections in comparison with annual-layer thickness from stratigraphic counting (working chronology, March 2015, pers. comm. P. Bohleber). Below 35 m w.e. grain diameters can exceed the layer thickness.
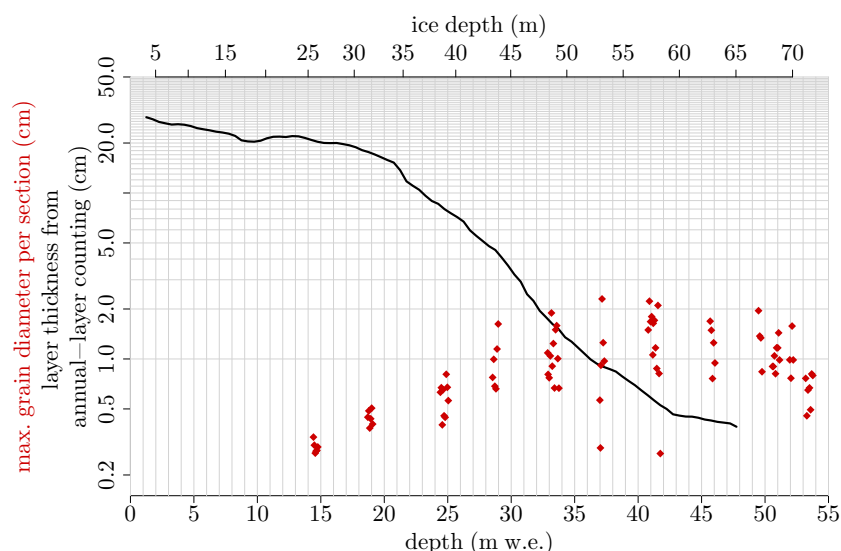
Fig. 5.6: Illustration of laser ablation data processing. The integral (shaded in grey) is calculated with respect to an individual measurement background. For further data illustration the high-frequency component of the data is smoothed with a gaussian kernel with bandwidth of 2 seconds.
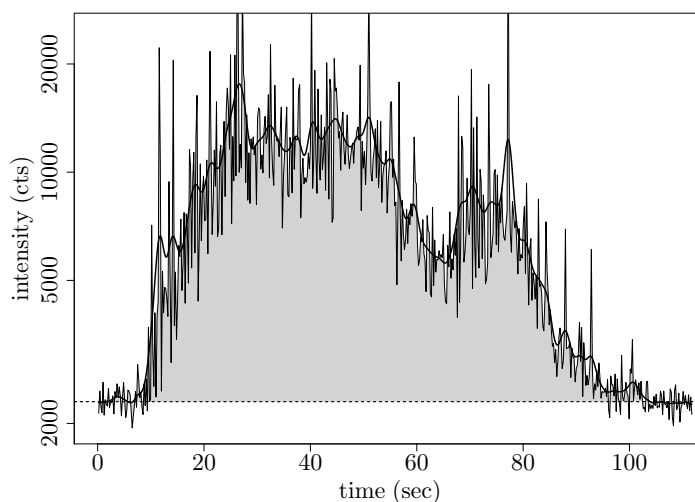
The findings and conclusions of the pilot study can be summarised as follows:

- The sodium content is in average always higher in grain boundaries than parallel to grain boundaries, i.e. 150–250 μm towards the grain interior. However, it has to be kept in mind that outliers can significantly alter the mean value due to the small sample size. The densities for 100 μm spot size are much higher, as would be expected from the larger ablation volume, and can not be compared quantitatively with the other sections but they exhibit the same gradient from grain boundaries towards the interior.

- The sodium content gradient can be observed regardless of the measurement section being a small or a large grain section (Fig. 5.8).

- The relative level of sodium content is comparable to the CFA mean values for the laser ablation measurement sections.

- The range of calculated values for each location and section is often rather large (covering several orders of magnitude), implying a spatially heterogeneous distribution of the overall
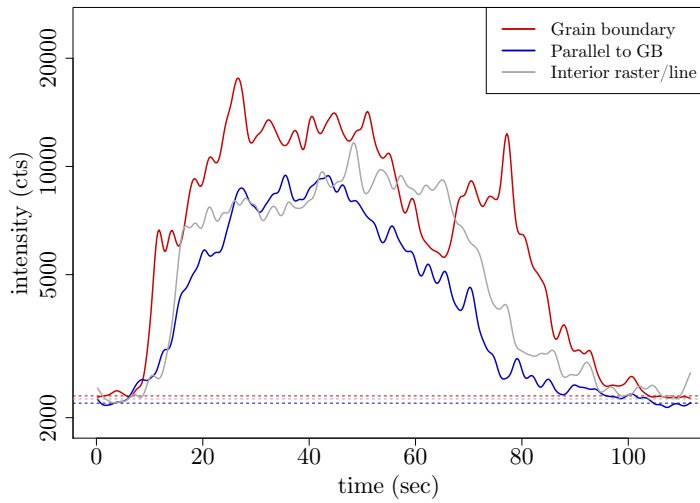
Fig. 5.7: Exemplary laser ablation data of three locations in one grain for sodium (run 48, small-grain layer, grain 5). The calculated background level for each measurement is indicated (dashed lines); the values vary slightly in this example. The GB is clearly enriched in sodium, while the grain interior is depleted; this pattern holds true for the majority of the collected sodium data.

impurity content within the section, i.e. from grain to grain. The sections are between 1.9 and 3.6 cm thick, which is enough to hold several annual layers as estimated from layer counting, thus possibly explaining the differences. On the other hand these results could indicate that the lateral variation in impurity content is not negligible compared to annual variation, which would have to be considered when interpreting down-core laser ablation signals.

• The bedrock section has lowest sodium values, while it is enriched in iron. It can be assumed that particles from bedrock contribute to the iron signal here. The corresponding
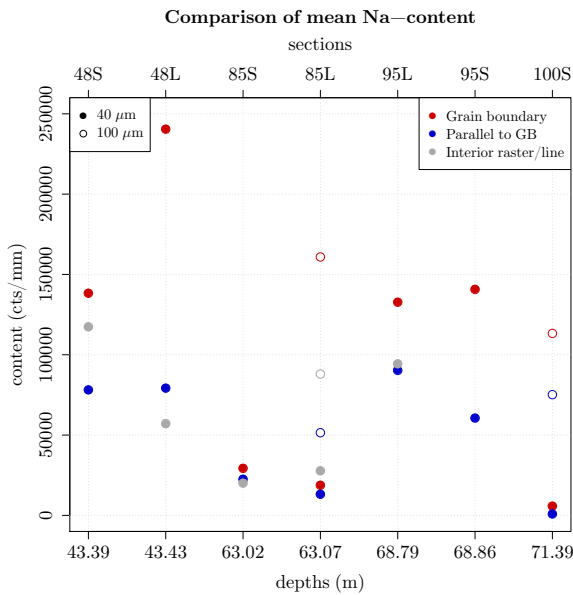
Fig. 5.8: Summary of the mean sodium content from all grains of each section for different locations. S and L denote small- or large-grained.
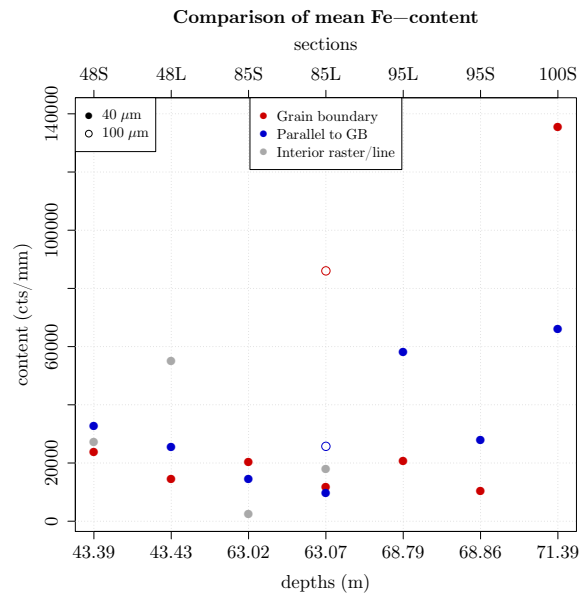
Fig. 5.9: Summary of the mean iron content from all grains of each section for different locations.

Fig. 5.10: The sodium content in grain boundaries is scattered against the content in the associated parallel lines, illustrating their ratio. Each symbol represents a pair. Filled symbols represent small and open symbols large grains, different symbols indicate the four depths with colors for for visual support, the larger spot size is indicated by black crosses, both axes are logarithmic, the dashed line indicates the 1:1 ratio.
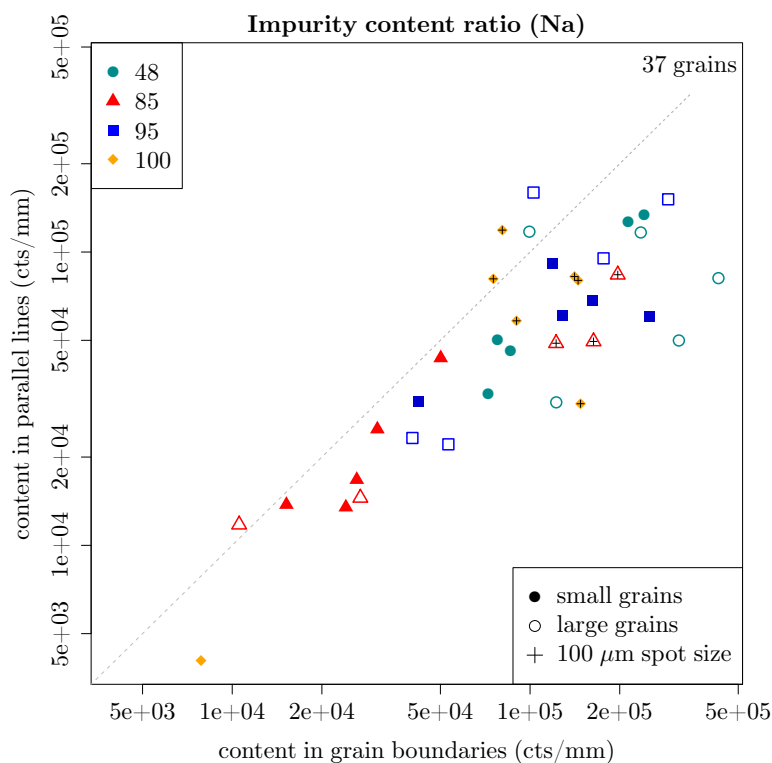
Fig. 5.11: The ratio of iron content is illustrated. For about a third of all grains the ratio is above 1, indicating higher iron content in the grain interior. Some grains of the basal section appear as outliers.
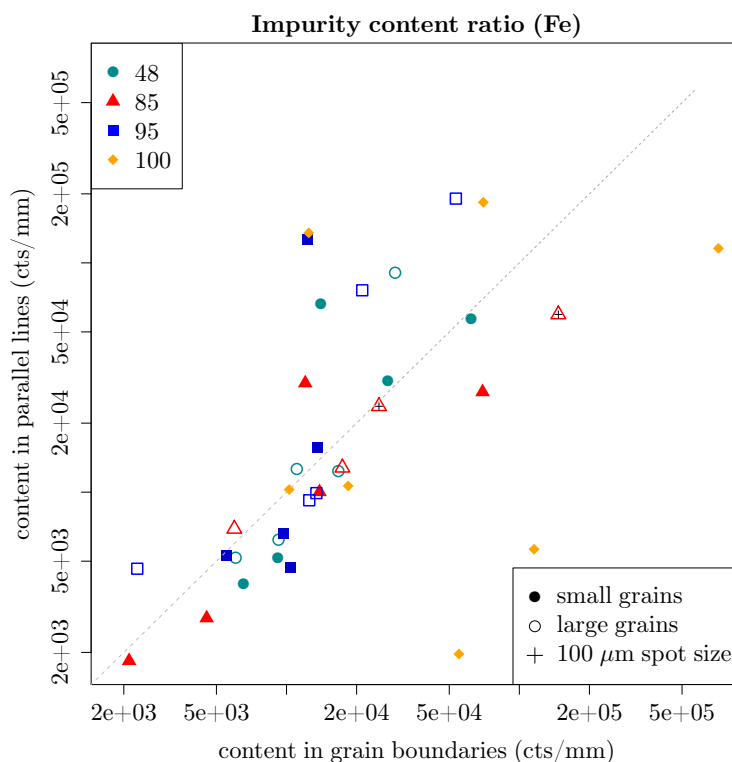
values should be considered as outliers.

- The ratio of logarithmic sodium content in parallel lines to the logarithmic sodium content in grain boundaries is below 1 for $86\,\%$ of the sampled grains (Fig. 5.10), regardless of grain size. It appears that for a given total sodium content in a grain the fractionation in GB and grain interior follows some yet undefined law. Following the assumption that sodium is mainly present as soluble impurity, this law could be chemically driven.

- Iron content does not differ in a consistent way between grain boundaries and parallel lines. The data per grain show many different patterns compared to the sodium data and are more difficult to classify. In some cases the grain interior is enriched compared to the parallel lines and grain boundaries. Some extreme grain results could have a strong effect on the mean values which need to be treated with caution. As apparent from the smoothed data for each grain, the signal is often dominated by narrow peaks.

- Based on the very limited statistic, no causal relationship between grain size or anisotropy (Tab. 3.4) and the spatial impurity distribution could be deduced.

5.3 Discussion of fabric and climate proxy interaction

Fine-grained layers

It is evident from the good correlation, from visual inspection and computation, between the impurity records and the grain number that a higher impurity content can be found in fine-grained layers, which often have a stronger fabric. At least 20 of these were observed in this study. While there are small-grain regions throughout the core, a fine-grained layer refers to a layer of max. a few centimetres sandwiched between larger grains with a clear grain size contrast (Fig. 5.12). While fine-grained and well-oriented layers are not commonly observed (in polar cores) they have been reported (e.g. Gow and Williamson (1976); DiPrinzio et al. (2005); Durand et al. (2006a); Fitzpatrick et al. (2014)) but under different conditions. Fitzpatrick et al. (2014) describe them, however, only in the depths $> 2000\,\mathrm{m}$. Volcanic ash has been suggested as a cause for the well-oriented fine-grained layers (Durand et al., 2006a; Gow and Meese, 2007). It has not been investigated in this study if the occurrence of tephra might play a role in the genesis of these layers. A more complex analysis of the combined effect of the impurities under consideration of their absolute concentrations on the grain size might also provide new insights.

Fig. 5.12: Example $(3 \times 2.3\,\mathrm{cm}^2)$ of a fine-grain layer ($\sim 7.5\,\mathrm{mm}$ thickness) at $68.3\,\mathrm{m}$ depth (sample 94-01).
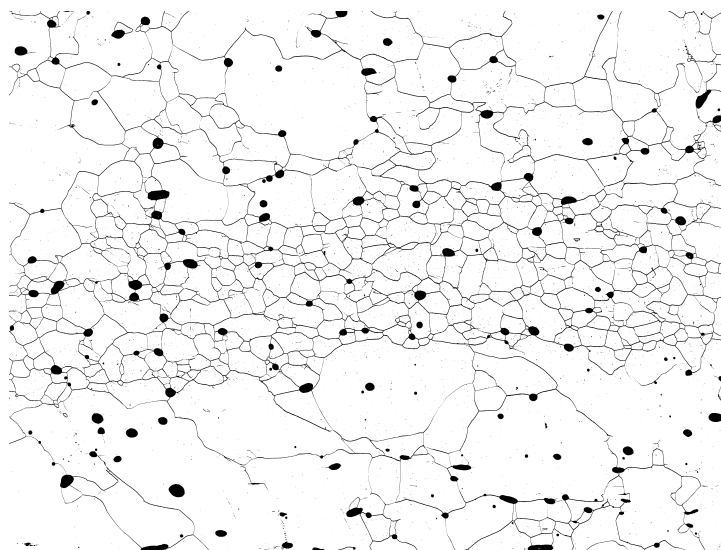
Fabric as climate proxy

The correlation evaluation leads to the conclusion that the widely-accepted view of impurity-controlled grain size (e.g. Thorsteinsson, 1996; Durand et al., 2006a; Fitzpatrick et al., 2014) can largely be confirmed for the sub-decimetre scale in the KCC ice core. Sodium, calcium and dust are closely connected with the grain size and number. Kleitz (2013) finds only weak correlations for the comparison between the mean grain size and sodium in a short-scale analysis of continuously measured bags from the polar NEEM ice core (Greenland). Thorsteinsson (1996) found threshold values of impurities, for which anticorrelation of crystal size and impurities in the GRIP ice core could be observed, e.g. 12 ppb for calcium. The calcium content in KCC is well above this value. Although the correlation between mean grain size and eigenvalue is also strong in the KCC ice core, the detailed comparison of the records reveals that this behaviour

is not always the case as discussed in section 4.5. The conditions for these seemingly random changes between positive and negative or no correlation could not be identified yet.

Based on the findings of this study, the hypothesis of short-scale fabric variations reflecting an immediate dependence on the impurity content is thus rejected. A partial influence, conveyed and filtered through an impurity-governed grain size, subjected to the local deformation regime, is considered more likely (section 4.6). It is a common challenge in such multi-proxy and multi-approach studies between physical and climate properties in an ice core that certain strong signals can be attributed to a few parameters and processes, while most of the signals seem to be caused by their combined impact. The collective influence of several impurity species on grain size has recently been investigated by Fitzpatrick et al. (2014).

An interesting observation is the change from negative to positive correlation between the c-axis eigenvalue and the impurity content at the firn-ice-transition, markedly sodium, dust and ammonium. However, more data is needed to confirm this finding.

Challenges for these comparative short-scale studies are:

- The relative uncertainties in the depth scales of data sets measured on different aliquots, in different states (solid or melted) and with different methods.

- The sensitivity to various processing parameters from image analysis to correlation computation.

- The lack of abundant data, allowing for different analysis options, e.g. time series analysis, and reliable statistic.

The findings of this study are, however, unprecedented and promising. A continued investigation of the KCC ice core fabric stands to reason.

Potential of LA-ICP-MS measurements on ice microstructure

The outcomes of the pilot study are:

- It could be demonstrated successfully that LA is an effective tool for the analysis of the spatial distribution of impurities with respect to the ice microstructure.

- Evidence for a spatial gradient of sodium in ice crystals in KCC samples was found. This is in line with the observations from, e.g., Barnes and Wolff (2004) who report the observation of sodium in grain boundaries. It partially contradicts the findings of Ohno et al. (2005) who found sodium as part of salt inclusions mainly in the grain interior. However, the presented results specifically indicate a systematic difference between grain boundary and grain interior for most grains.

- The variation of the signal along a GB suggests that measurements running perpendicular to the GB (Della Lunga et al., 2014) should be considered with caution. Single data points in a GB cannot be considered as representative for the impurity content.

- The observed peaks in the iron signal could be interpreted as an indication for a more particulate contribution, hence confirming the initial assumption. The lack of a pattern

linked to the microstructure could be an argument for the particulate impurity distribution being less subjected to microstructural processes, i.e. dragging or pinning, in the KCC ice core, as described for micro-inclusions in the EDML core by Faria et al. (2010). Only for the basal section several grains have clearly iron-enriched grain boundaries, indicating a specific dependence on basal deformation or a threshold concentration.

- The data provide no evidence of a dependency between impurity content or spatial distribution with the orientation or size of grains.

- Comparing the data from individual grains, a similarity between the signals on different locations along the parallel ablation paths can often be found. No explanation could be offered so far.

- It cannot be excluded that the observed spatial sodium gradient may be influenced by the premelting of the exposed surface and diffusion (Dash et al., 1995; Rempel et al., 2001) during ice storage. However, the fact that outliers to the pattern in the spatial sodium distribution are observed in most sections would argue against that, as well as the successful reproduction of a down-core signal from CFA (Sneed et al., 2015). The comparison of the concentration levels associated with a climate signal and the concentrations measured for the grain gradients is envisaged.

- Based on this pilot study, further studies of this kind are highly recommended.

6 Fabric and seismic velocitites

The application of seismic techniques to the glacier surface yields two-dimensional information about the internal structure of the ice body. One-dimensional fabric information from the analysis of ice core thin sections in a high-resolution complements the two-dimensional results and allows for an improved interpretation of the fabric structure of the study area. An overview on seismic wave propagation in an anisotropic medium is provided in section 6.1. An existing approach of calculating theoretical seismic interval phase velocities from fabric data, making use of fabric symmetries, is challenged with a new calculation approach (section 6.2). The comparison of the two methods is demonstrated with two case studies using fabric data from a polar and an Alpine ice core respectively (section 6.3). Implications for the future combination of seismic measurements and fabric data are discussed (section 6.4).

6.1 Seismic wave propagation in anisotropic media

A medium for which the measurement of seismic velocities yields different results depending on the direction of wave propagation is called anisotropic with respect to the propagation of seismic waves. If the velocity changes also along a specific direction, the medium is heterogeneous, e.g. a layered medium, and it may be useful to consider the velocities within homogeneous sections.

In a glacier, this seismic anisotropy is influenced by the fabric anisotropy, investigated in the previous chapters. To study this influence of fabric anisotropy on seismic velocites, theoretical velocities can be calculated if the fabric anisotropy is known and quantitatively described. If the ice is only weakly anisotropic, it might be that the anisotropy cannot be resolved with current measurement techniques. Therefore, it is important to investigate the strength of seismic anisotropy that can be expected due to crystal-orientation fabric to recognise the accuracy that is needed to resolve it.

In the following a short summary of the mathematical concepts for the calculation of seismic phase velocities in anisotropic ice is given, mainly based on Tsvankin (2001, ch. 1), where it is discussed in more detail. Group velocities are not subject of this study and hence disregarded.

The elasticity tensor

The propagation of seismic waves in any medium is dependent on the strain τ resulting from an applied stress σ. Stress and strain are each given for the three directions in Euclidean space by a symmetric second-order tensor. For an anisotropic elastic medium – ice behaves elastically for the propagation of seismic waves, i.e. small strain – stress and strain are linearly connected following the generalised Hooke's law:

$$\sigma_{mn} = c_{mnop}\tau_{op} \qquad \text{with} \quad m,n,o,p = 1,2,3 \tag{6.1}$$

where c_{mnop} is the elasticity tensor, a fourth-order tensor, describing the medium's elastic properties. The inverse relation uses the compliance tensor s_{mnop}, which is needed for the concept of Reuss and Voigt bounds, discussed later:

$$\tau_{mn} = s_{mnop}\sigma_{op} \qquad \text{with} \quad m, n, o, p = 1, 2, 3 \tag{6.2}$$

Due to the symmetry of strain and stress tensor, the respective indices can be interchanged:

$$c_{mnop} = c_{nmop} = c_{mnpo} \tag{6.3}$$

Further, thermodynamic considerations (Aki and Richards, 2002) lead to:

$$c_{mnop} = c_{opmn} \tag{6.4}$$

Thus, the 81 (3^4) unknowns of the elasticity tensor reduce to 21 independent components for general anisotropy. The elasticity tensor can then be expressed in a simplified manner, known as Voigt notation (Voigt, 1910), where pairs of indices from the fourth-order tensor are replaced by single indices as follows:

$$11 \rightarrow 1; \quad 22 \rightarrow 2; \quad 33 \rightarrow 3; \quad 23, 32 \rightarrow 4; \quad 13, 31 \rightarrow 5; \quad 12, 21 \rightarrow 6.$$

The resulting elasticity tensor in Voigt notation C_{ij} ($i, j = 1, 2, 3, 4, 5, 6$) is a symmetric second-order tensor, that can be written as 6×6 matrix. The most general anisotropic case with $C_{ij} \neq 0$ and 21 independent components is referred to as triclinic. In case of monocrystalline ice I_h, laboratory measurements have provided the elastic constants that are the components of the elasticity tensor. For its hexagonal crystal symmetry five independent elastic constants were found (e.g. Jona and Scherrer, 1952; Bennett, 1968; Gammon et al., 1983, etc.). An ice monocrystal constitutes a vertical transversely isotropic (VTI) medium, i.e. the elastic anisotropy is invariant under rotation of the crystal around the symmetry axis, analoguous to the optical anisotropy. Several sets of values for the elastic moduli have been found by different authors as is summarised in Diez et al. (2015). Here, the monocrystal elasticity tensor $\mathbf{C}_m$ by Gammon et al., 1983, as measured on samples of artificial ice at $-16\,°\text{C}$ by means of Brillouin spectroscopy, is reported and used for the calculations below:

$$\mathbf{C}_{\text{m}} = \begin{bmatrix} 13.929 & 7.082 & 5.765 & 0 & 0 & 0 \\ 7.082 & 13.929 & 5.765 & 0 & 0 & 0 \\ 5.765 & 5.765 & 15.010 & 0 & 0 & 0 \\ 0 & 0 & 0 & 3.014 & 0 & 0 \\ 0 & 0 & 0 & 0 & 3.014 & 0 \\ 0 & 0 & 0 & 0 & 0 & 3.424 \end{bmatrix} \cdot 10^9\,\text{N/m}^2 \tag{6.5}$$

with $C_{22} = C_{11}$, $C_{23} = C_{13}$, $C_{44} = C_{55}$, $C_{66} = (C_{11} - C_{12})/2$; errors are negligible for the purpose of this study. Vertical transversely isotropy is a special case of orthorhombic symmetry, which exhibits three mutually orthogonal planes of mirror symmetry and nine different components C_{ii}, C_{12}, C_{13} and C_{23}. The orthorhombic model is used by Diez and Eisen (2015) to describe their three fabric classes (section 6.2).

From monocrystal to polycrystal

In the study of large ice sheets and glaciers, the elastic properties of the polycrystal are of interest. The polycrystal is described by crystal-orientation fabric. The understanding of the elastic behaviour of a monocrystal can be used together with the fabric description to estimate the elastic properties of the polycrystal (e.g. Mainprice et al., 2011). This is not trivial, especially in the case of anisotropic fabric. Different theoretical models have been developed for the estimation of the elasticity tensor of an anisotropic polycrystal, usually making use of fabric symmetries (e.g. Nanthikesan and Sunder, 1994; Maurel et al., 2015).

Concept of Voigt and Reuss bounds

Nanthikesan and Sunder (1994, among many others) review the often referred to assumptions of Voigt (1910) and Reuss (1929) for the calculation of an isotropic polycrystal from anisotropic monocrystal properties. They provide the upper and lower limits for the elastic moduli of the polycrystal, as was shown by Hill (1952), with the Reuss bound exceeding the Voigt bound. Voigt proposes that the strain is uniformly distributed on all crystals (homogeneous strain), resulting in a violation of equilibrium of forces between the grains. Reuss, on the other hand, assumed a constant stress on all crystals (homogeneous stress), implying an unequal distortion of the grains, violating the compatibility between them. Both approaches must be considered as approximative but are used often for estimates of polycrystal elastic properties. Nanthikesan and Sunder (1994) generalise the concept for anisotropic, notably transversely isotropic and orthotrophic, polycrystals and find that the difference of the Voigt-Reuss bounds for the elastic moduli of polycrystalline ice does not exceed 4.2 % and conclude that either of the bounds or an average is a good approximation. This conclusion is confirmed and followed by the study of Diez and Eisen (2015).

Microstructural considerations for the elastic properties of a polycrystal

Certain processes on the grain scale might have to be considered in order to derive a reliable estimate of the elastic moduli of a polycrystal aggregate (Mainprice et al., 2011). Elvin (1996) estimates the minimal number of grains needed to "homogenise the elastic properties of polycrystalline ice" to be about 230. This is understood to be the minimum number of grains in a polycrystalline aggregate that are needed to render the elastic properties of the bulk material independent of the elastic properties of the specific single grains. This finding is based on numerical finite element simulations of uniaxial loading on generated samples with girdle fabric while varying grain number via sample size, the grain geometry and orientation. In reference to this work Diez and Eisen (2015) estimate that with typical seismic wavelengths of the order of 10 m this homogenisation threshold is always exceeded. Elvin (1996) also investigates the influence of grain boundary sliding and grain shape on the elastic properties of a polycrystal and states that, if no grain boundary sliding is permitted, the polycrystal's elastic properties will be dominated by the single crystals' anisotropy. In this case, the numerical results are within the Voigt and Reuss bounds for the tested aggregates. In other words, Voigt and Reuss bounds do not consider hypothetical grain boundary slip. If grain boundary sliding is allowed in the simulations, the bulk properties will be based not only on anisotropy but also on the shape of the polycrystal's constituents. Gold (1958) concludes from laboratory experiments that GBS is involved in the elastic response of polycrystalline ice. Helgerud et al. (2009) finds evidence of rapid intergranular bonding in polycrystalline ice in dependence of wave speed. Despite these

indications of grain sensitive processes affecting the wave propagation, it is currently unknown whether GBS is significant or even occurs at all. It is therefore not considered further in the analyses below.

The Christoffel equation

For a linearly elastic, arbitrarily anisotropic homogeneous medium the wave equation is expressed as a partial differential equation of the form

$$\rho \frac{\partial^2 u_m}{\partial t^2} - c_{mnop} \frac{\partial^2 u_o}{\partial x_n \partial x_p} = 0 \tag{6.6}$$

with the density ρ, the displacement vector $\boldsymbol{u}$ and the location vector $\boldsymbol{x}$. No source of elastic energy is considered here. A harmonic steady-state plane wave

$$u_o = U_o \exp(\mathrm{i}\omega(n_n x_n / v_{\mathrm{ph}} - t)) \tag{6.7}$$

with the polarisation vector $\boldsymbol{U}$, angular frequency ω, phase velocity v_{ph}, time t and the unit vector normal to the plane wavefront $\boldsymbol{n}$ (i.e. the direction of wave propagation) can be used to solve eq. (6.6). Inserting eq. (6.7) into the wave equation (6.6) leads to the Christoffel equation

$$\begin{bmatrix} G_{11} - \rho v_{\mathrm{ph}}^2 & G_{12} & G_{13} \\ G_{21} & G_{22} - \rho v_{\mathrm{ph}}^2 & G_{23} \\ G_{31} & G_{32} & G_{33} - \rho v_{\mathrm{ph}}^2 \end{bmatrix} \begin{bmatrix} U_1 \\ U_2 \\ U_3 \end{bmatrix} = 0 \tag{6.8}$$

$$\text{with} \quad G_{mo} = c_{mnop} n_n n_p \tag{6.9}$$

$$\text{or} \quad [c_{mnop} n_n n_p - \rho v_{\mathrm{ph}}^2 \delta_{mo}] U_o = 0 \tag{6.10}$$

where δ_{mo} is the Kronecker delta and G_{mo} is the positive definite, thus symmetric Christoffel matrix. Eq. (6.10) constitutes an eigenvalue problem for G_{mo}. The real and positive eigenvalues are identified with the phase velocities $v_{\mathrm{p}}, v_{\mathrm{sh}}, v_{\mathrm{sv}}$ for P-wave, SH-wave and SV-wave respectively. Different solutions are proposed, depending on the form of the elasticity tensor as introduced above and often making use of approximations for specific symmetries. The solution used in this study for an arbitrarily anisotropic medium is outlined in section 6.2.

Temperature and density dependency

Temperature and density are two factors that need to be considered when comparing seismic velocities. While the temperature might change over the whole depth of a glacier, the density gradient is very strong only in the firn column. Kohnen (1974) found the seismic P-wave velocity to depend linearly on the ice temperature with a gradient of $-(2.30 \pm 0.17)\,\mathrm{m\,s^{-1}\,K^{-1}}$. As this study is concerned with the comparison of calculation frameworks that use the same elastic moduli from Gammon et al. (1983) measured at $-16\,°\mathrm{C}$, a temperature correction will generally not be applied if not stated elsewise. In the firn column, the increasing density leads to strongly increasing seismic velocities. Kohnen (1972) provides an empirical relationship that

compares the change in density with the change in seismic P-wave velocity $\Delta v_{\mathrm{p}} = v_{\mathrm{p,ice}} - v_{\mathrm{p,firn}}$:

$$\frac{\rho_{\mathrm{ice}}}{\rho(z)} = 1 + (\Delta v_{\mathrm{p}}/2250)^{1.22} \tag{6.11}$$

where $v_{\mathrm{p,ice}}$ gives a reference value of isotropic ice, as can be calculated, e.g., from random cone fabric with cone angle $\varphi = 90°$ ($v_{\mathrm{p,iso}} \approx 3875$ m/s), and $v_{\mathrm{p,firn}}$ is the velocity corrected for the firn density. For firn with an already preferred orientation the reference velocity is the velocity in ice for the specific fabric. For S-wave velocity Diez et al. (2014) derive a similar relationship between density and velocity ($v_{\mathrm{s,iso}} \approx 2035$ m/s).

Fabric dependency

Below the firn-ice transition, where density fluctuations and temperature amplitude (in case of a cold glacier and dependent on height above bedrock) have diminished, the remaining influence on the seismic velocity is the anisotropy of the ice crystals. The maximum anisotropy is given for a theoretical glacier body where all ice crystals are oriented parallel, e.g., towards the main compression axis, i.e. the vertical (vertical single maximum, VSM). The associated elasticity tensor given by eq. (6.5) would lead to anisotropic seismic phase velocities as shown in Fig. 6.1. For the P-wave a maximum anisotropy of 7 % can be found, for SV-wave it amounts to about 18 %, while for SH-wave the anisotropy is given by about 7 %.
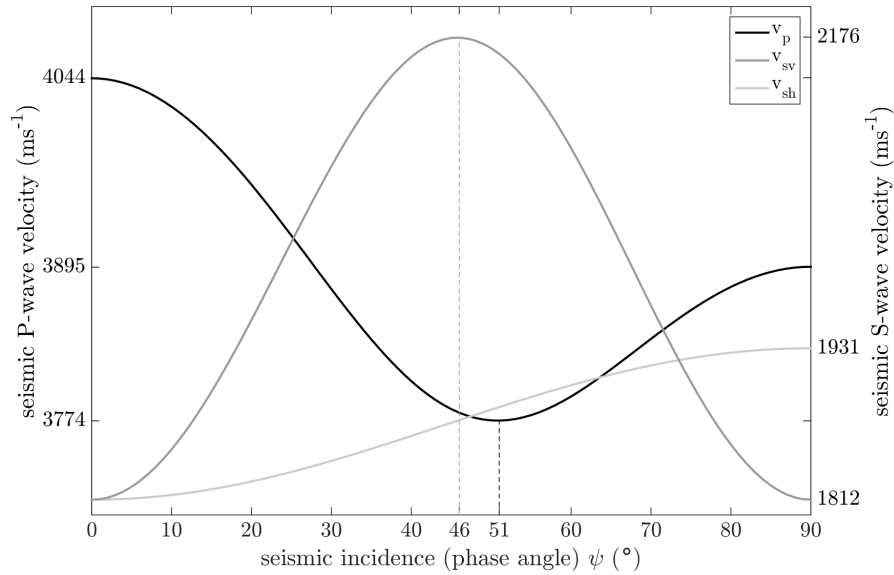
Fig. 6.1: Seismic phase velocities in a VSM medium, equivalent to a monocrystal in its local coordinate system. Left axis: P-wave velocity (black) with a minimum at 51°. Right axis: S-wave velocity (grey) with SV-wave velocity reaching a maximum at 46° and exceeding SH-wave velocity for phase angles below 73.5°. Curves are calculated with eq. (1.36) and (1.43) for VTI media from Tsvankin (2001).

6.2 Calculation of effective seismic velocities from fabric data

In Diez and Eisen (2015) a framework for calculating seismic velocities from COF data is presented (for detailed description see section 4.2 in Diez, 2013):

1. The fabric data in the standard parameterisation of second-order orientation tensor eigenvalues are sorted into three fabric classes (cone, thick girdle, partial girdle) where each is defined by one or two opening angles χ, φ, symmetrical with respect to the vertical, and enveloping the c-axis distribution of a sample.

2. The opening angles characterising the fabric of each sample are used to integrate the elasticity tensor of a monocrystal (as defined in section 6.1) to obtain the elasticity tensor of the polycrystal, that is to say the elasticity tensor of the effective medium, which exhibits an orthorhombic symmetry with respect to the vertical.

3. From the effective elasticity tensor the approximative solutions to the Christoffel equation (eq. 6.10) for the orthorhombic case provided by Daley and Krebes (2004) are applied to obtain seismic interval phase velocities

$$v_{\mathrm{p}}^{\mathrm{ev}}, v_{\mathrm{sh}}^{\mathrm{ev}}, v_{\mathrm{sv}}^{\mathrm{ev}} \qquad (6.12)$$

that can be used for comparison with measured seismic data. Voigt calculation is used following the argument that Reuss and Voigt bounds are close enough.

In the following, this framework is referred to as *eigenvalue framework* and associated variables are indicated with "ev".

The advantages (+) and disadvantages (−) of this approach are (Diez and Eisen, 2015):

+ Eigenvalues are a standard parameter for expressing the strength of fabric and can be directly used for the eigenvalue framework without additional information about the particular measurement of thin sections from an ice core.

+ By restraining to an orthorhombic symmetry, i.e. for all three fabric classes the three mutually orthogonal planes associated with the Cartesian coordinate system are planes of mirror symmetry (Tsvankin, 2001, p. 10), the solution to the Christoffel equation can be readily found. No information on the azimuthal orientation of the ice core (relative to any seismic measurements on a glacier) is needed, although this would could be considered to improve the results in case of girdle fabric.

− By restraining to an orthorhombic symmetry while using opening angles to describe the c-axis distribution any information on asymmetric fabric (with respect to the vertical) is dismissed and approximation errors are introduced for more asymmetric c-axes distributions.

− The classification into fabric groups based on threshold values for the eigenvalues can introduce artificial discontinuities in the calculated velocity profile.

This part of the thesis aims to estimating the error introduced by the approximation of the eigenvalue framework and to assess the potential of the hitherto neglected information for future analyses. For that purpose the exact angle information of each c-axis is used in the following to

derive the effective elasticity tensor $\mathbf{C}_\mathrm{p}$ of the polycrystal of a sample and the phase velocities in an arbitrarily anisotropic medium are calculated.

6.2.1 Deriving the effective elasticity tensor of the polycrystal from c-axis data

This study considers the elastic properties of the effective (Maurel et al., 2015), i.e. polycrystalline, medium. If not indicated differently, elasticity/compliance tensors and velocities are calculated for the effective medium, which, in this study, is typically represented by a thin section comprising a number N_g of grains of the order of a hundred to a thousand.

A data set of COF from an ice core is considered that gives pairs of angles determining the c-axis of each grain $\boldsymbol{c}(\vartheta, \varphi)$ in a grain ensemble per thin section with the azimuth angle ϑ in the interval $(0, 2\pi)$ counted anticlockwise and the colatitude φ in the interval $(0, \pi/2)$ counted from the vertical (Fig. 2.2, p. 10). Following steps are undergone to obtain the effective elasticity tensor for a thin section sample, referred to as *c-axes framework* with associated variables indicated with "cx":

1. Transformation of the monocrystal elasticity tensor: Considering the monocrystal elasticity tensor $\mathbf{C}_{\mathrm{m},n}$, given by eq. (6.5), in the n-th grain's local coordinate frame $\{p, q, r\}$ with $\boldsymbol{c} = (0, 0, 1)$, a transformation (indicated by t) to the global coordinate frame $\{x, y, z\}$ is necessary:

$$\mathbf{C}_{\mathrm{m},n}^\mathrm{t} = \mathbf{R}_{\mathrm{C},z}^\top \, \mathbf{R}_{\mathrm{C},y}^\top \, \mathbf{C}_{\mathrm{m},n} \, \mathbf{R}_{\mathrm{C},y} \, \mathbf{R}_{\mathrm{C},z} \tag{6.13}$$

with rotation matrix $\mathbf{R}_\mathrm{C}$ as given by eq. (D.4) (p. 184) and $\mathbf{R}_\mathrm{C}^\top$ its transpose matrix. $\mathbf{C}_{\mathrm{m},n}^\mathrm{t}$ is likely not to have VTI symmetry anymore as most c-axes in a real fabric do not coincide with the z-axis but will lie obliquely in the $\{x, y, z\}$ coordinate frame.

2. Grain area weighting: If grain size information is available each transformed monocrystal elasticity tensor $\mathbf{C}_{\mathrm{m},n}^\mathrm{t}$ is multiplied by the grain cross-section area fraction $f_n = A_n / \sum_n A_n$. Otherwise, it is multiplied by $1/n$ for an equal contribution of all grains to the effective medium elasticity tensor.

3. Discrete summation over the transformed monocrystal elasticity tensor for all grains to obtain the polycrystal elasticity tensor $\mathbf{C}_\mathrm{p}$:

$$\mathbf{C}_\mathrm{p} = \sum_n \mathbf{C}_{\mathrm{m},n}^\mathrm{t} \tag{6.14}$$

Derivation via the compliance tensor: For the aim of considering Reuss and Voigt bounds as introduced above, the polycrystal elasticity tensor is also calculated via the compliance tensor $\mathbf{S}_\mathrm{m}$, i.e. the monocrystal elasticity tensor is inverted: $\mathbf{S}_\mathrm{m} = \mathbf{C}_\mathrm{m}^{-1}$. Steps 1 to 3 are then applied accordingly using eq. (D.5) (p. 184) to derive the compliance tensor of the polycrystal $\mathbf{S}_\mathrm{p}$, which is then again inverted to $\mathbf{C}_\mathrm{p}^\mathrm{R}$ and indicated with "R" (for Reuss). If $\mathbf{C}_\mathrm{p}$ is not indicated, it is expressing the Voigt bound.

6.2.2 Solution for the phase velocities in arbitrarily anisotropic media

Following Tsvankin (2001, p. 56, Appendix 1A) the phase velocities are obtained from the polycrystal elasticity tensor $\mathbf{C}_p$ by finding the eigenvalues v_{ph} of the Christoffel matrix. From the characteristic polynomial of eq. (6.10) a cubic equation can be derived with the substitution $\rho v_{ph}^2 \to y - a/3$:

$$\det[G_{mo} - \rho v_{ph}^2 \delta_{mo}] = 0 \qquad (6.15)$$

$$\Rightarrow \quad y^3 + dy + q = 0 \qquad (6.16)$$

where the coefficients d and q follow from combinations a, b, c given by the components of the Christoffel matrix G_{mo}:

$$a = -(G_{11} + G_{22} + G_{33}) \qquad (6.17)$$

$$b = G_{11}G_{22} + G_{11}G_{33} + G_{22}G_{33} - G_{12}^2 - G_{13}^2 - G_{23}^2 \qquad (6.18)$$

$$c = G_{11}G_{23}^2 + G_{22}G_{13}^2 + G_{33}G_{12}^2 - G_{11}G_{22}G_{33} - 2G_{12}G_{13}G_{23} \qquad (6.19)$$

$$d = b - a^2/3 \qquad (6.20)$$

$$q = 2a^3/27 - ab/3 + c \qquad (6.21)$$

For $k = 0, 1, 2$ the velocities v_p^{cx}, v_{sh}^{cx}, v_{sv}^{cx} are found from:

$$v_{ph}(k) = \sqrt{\left(\left(\left(\frac{2}{\sqrt{3}}\sqrt{-d}\cos\left(\frac{1}{3}\left(\arccos\left(-\frac{q}{2\sqrt{(-d/3)^3}}\right) + 2\pi k\right)\right)\right) - \frac{a}{3}\right)\rho^{-1}} \qquad (6.22)$$

and are real under the conditions:

$$\frac{q^2}{4} + \frac{d^3}{27} \leq 0 \qquad \text{and} \qquad 0 \leq \arccos\left(-\frac{q}{2\sqrt{(-d/3)^3}}\right) \leq \pi \qquad (6.23)$$

The algorithm is implemented in MATLAB® for this study.

Root mean square velocity

If the two-way traveltime (TWT) to a certain depth is of interest, the root mean square velocity v_{rms} gives the velocity of the homogeneous half-space equivalent to the stack of N horizontal layers to this depth:

$$v_{rms}(N) = \sqrt{\frac{\sum_{i=1}^{N}[v^{(i)}]^2 t_0^{(i)}}{\sum_{i=1}^{N} t_0^{(i)}}} \qquad (6.24)$$

with the TWT of a single layer for zero-offset t_0, i.e. twice the time a seismic wave would need to travel vertically with the corresponding interval velocity $v^{(i)}$ through the layer.
For a layered anisotropic medium a reliable depth-conversion from traveltimes is only feasible if the rms-velocity for zero-offset can be deduced (detailed in Diez et al., 2014).

6.2.3 Comparison of velocity calculations

The two frameworks were compared by looking at cone fabric for all opening angles. For this symmetric fabric the two methods should yield the same results. The P-wave velocity was directly calculated from the opening angles with the equations used in the eigenvalue framework. For the calculation with the c-axes framework 1000 c-axes, equally distributed in a solid angle, were randomly generated per opening angle. Fig. 6.2 and Fig. 6.3 show the theoretical P-wave velocity distribution for all cone angles and incidence angles. Fig. 6.4 gives the difference between the calculations that is mainly reflecting the different set of equations used in the two frameworks. This comparison does not consider the derivation of opening angles by the eigenvalue framework from the eigenvalues of the random generated c-axis ensembles. The velocities differ the most for cone fabric with opening angles of approximately 50–60° at vertical incidence.
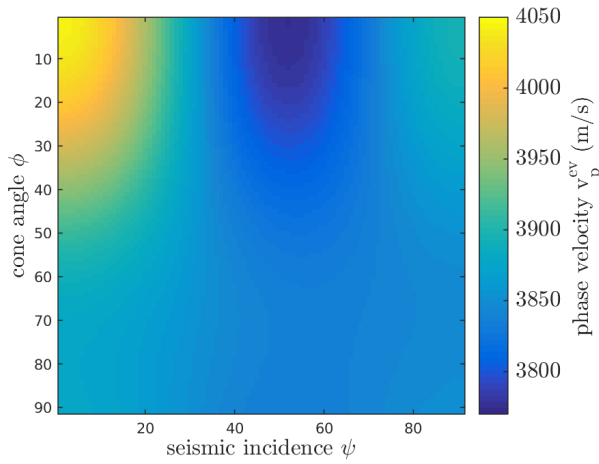
Fig. 6.2: P-wave velocity v_p^{ev} for cone fabric using equations from eigenvalue framework.
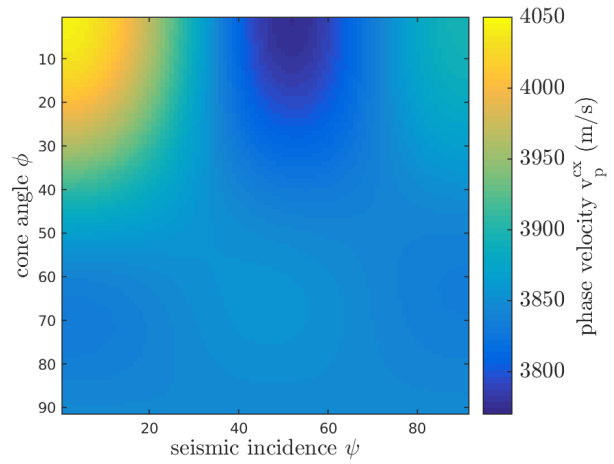
Fig. 6.3: P-wave velocity v_p^{cx} for cone fabric from random c-axes using the c-axes framework.
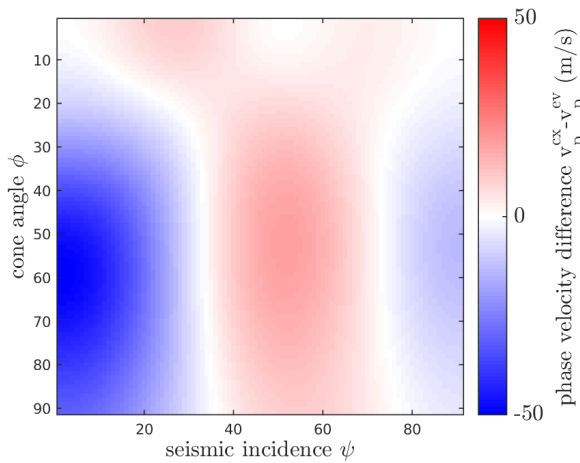
Fig. 6.4: Difference in P-wave velocity between the two frameworks for cone fabric. Blue color shows where the eigenvalue framework obtains higher velocities than the c-axes framework. Red shades indicate the opposite. They differ by -50 to $20\,\mathrm{m/s}$.

6.3 Seismic velocities from fabric data - case studies

The methodology proposed in section 6.2, termed c-axes framework, is applied to two fabric data sets from ice cores in Antarctica and in the European Alps, respectively, to investigate the potential of the framework with respect to the earlier established eigenvalue framework developed by Diez (2013). Additional figures referred to in the text can be found in appendix D.3 (p. 191). The c-axes framework uses exact analytical solutions for the calculation of seismic velocities and the full fabric information, while the eigenvalue framework relies on several approximations. Therefore, the results obtained with the c-axes framework are considered to be more accurate for the purpose of comparing the frameworks in the following case studies. It not stated else, all velocities are interval velocites, i.e. the velocity in a layer, for which an elasticity tensor is calculated based on fabric.

6.3.1 Polar ice core EDML

The polar ice core EDML is introduced in section 3.2 (p. 18). The fabric data obtained from FA measurements are used here to calculate seismic velocities following section 6.2. An overview of all EDML thin section samples used in this thesis can be found in appendix B.2 (p. 148). Diez et al. (2015) calculate seismic zero-offset P-wave velocities from eigenvalue data from the polar ice core EDML with the eigenvalue method outlined in section 6.1. They evaluate the results by comparing them to data from a vertical seismic profiling measurement within the borehole. The grain-weighted eigenvalue data consist of 145 samples between 104 and 2563 m depth (subset of data sets: Weikusat et al., 2013c; Weikusat et al., 2013d). The calculation of the elasticity tensor uses Gammon's monocrystal elasticity tensor for reasons discussed in detail in Diez et al., 2015. The threshold values for classifying the fabric are as follows: girdle fabric is given if $\lambda_2 \geq 0.2$ and $\lambda_1 \leq 0.1$, with thick girdle fabric for $0.05 < \lambda_1 \leq 0.1$ and partial girdle for $\lambda_1 \leq 0.05$; cone fabric is identified otherwise.

For the purpose of evaluating the study of Diez et al. (2015) by comparison with the newly calculated seismic velocities following the c-axes framework almost the same data set (c-axis angles and eigenvalues) is used, with additional thin sections that were measured only recently. The total data set comprises 154 samples between 104 and 2563 m depth with a coarse sampling interval and 40 additional samples from four bags between 2359 and 2380 m that were measured continuously, i.e. without intervals between the samples. These samples were not used for the calculation of seismic velocities before. The seismic velocities were calculated for both frameworks, following the instructions of Diez and Eisen (2015) and section 6.2, respectively. The velocities are not corrected for temperature in the borehole or density as the resulting shift is of no relevance here.

Seismic P-wave velocity for vertical incidence

Figure 6.5 illustrates the difference between the eigenvalue and the c-axes framework for the P-wave velocity v_{p0} at vertical incidence of a seismic wave, i.e. $\psi = 0$, with focus on the effect of fabric classification. The azimuthal information gained by applying the c-axes framework that has to be considered with caution is of no consequence in this case, as the P-wave velocity for vertical incidence is invariant under azimuthal rotation of the seismic plane or the core. It is therefore possible to assess the uncertainty introduced by using the eigenvalues.
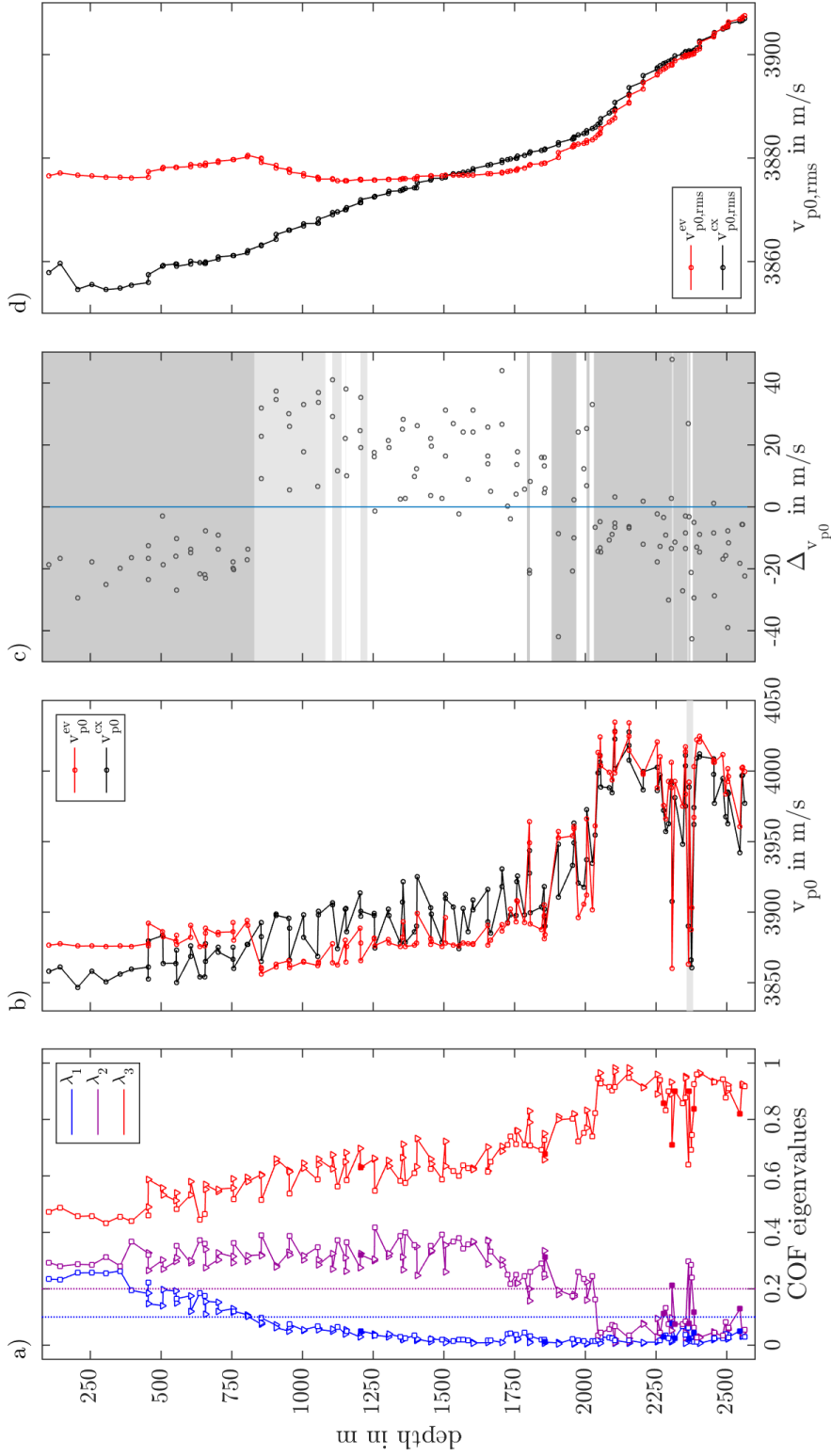
Fig. 6.5: Comparison of zero-offset P-wave velocities calculated from EDML fabric data (without high resolution samples) via eigenvalue and c-axis framework. The Voigt bounds are considered here. Panel **a)** shows eigenvalues (symbols are explained in Fig. 6.6) and threshold values for fabric classification as chosen by Diez and Eisen (2015) are indicated with dotted lines. Panel **b)** presents the calculated P-wave velocities for the two frameworks. A shaded interval indicates, where high resolution measurements where taken (Fig. 6.6). Panel **c)** relates the difference $v_{p0}^{cx} - v_{p0}^{ev}$ to the fabric classes that are indicated by shading (dark gray: cone fabric, light gray: thick girdle, white: partial girdle). The shading extends for each data point to half the distance to the neighbouring data points. Panel **d)** shows the RMS-velocities resulting from the interval velocities without taking into account density, temperature and confining firn layer.

The evolution of the fabric becomes apparent from assessing the eigenvalues (Fig. 6.5a): In the upper 450 m the c-axes are nearly isotropically distributed and change towards a broad great-circle girdle, which then narrows. Below 1650 m the girdle develops slowly towards a single maximum, but at 2050 m the drop of the second eigenvalue λ_2 indicates a sudden change to a sharp single maximum, which is then disrupted in a narrow layer around 2350 m by the occurance of girdle fabric (Weikusat et al., in press).

Following observations are made:

- The general trend of the velocities of the two frameworks is in good agreement, with a mean deviation of ± 17 m/s and maximum deviation of 48 m/s. However, a systematic difference can be observed (Fig. 6.5c): for cone fabric the P-wave velocity is overestimated by the eigenvalue framework, for girdle fabric the opposite is the case.

- In the upper 1785 m, before individual peaks can be observed, the c-axes velocity clearly exhibits a higher variability, as quantified by the standard deviation (Tab. 6.1). Below that depth, the eigenvalue velocity appears to vary stronger, but this is due to several transitions between fabric classes in the depth range of 1800 to 2035 m; notably the prominent peak at 1802 m is clearly enhanced by this.

- In the lower part of the core at 2306 m a sudden weakening of the fabric is reflected in the results of both frameworks. The velocity is, however, underestimated by the eigenvalue framework by 48 m/s by switching from cone to girdle fabric classification. Two more close peaks are visible in both velocity calculations and will be discussed in reference to Fig. 6.6, which shows a close-up of this depth range and additional data points sampled at 10 cm intervals.

- RMS velocities were calculated from the interval velocities (Fig. 6.5d) using eq. (6.24) in order to assess the cumulated effect of the velocity deviation. In the anisotropic case zero-offset velocities are needed for the depth conversion, i.e. the zero-offset RMS velocity (Diez et al., 2014). However, temperature and density in the firn column are ignored here. For the purpose of assessing the effect of different velocity models in the first approximation, this is negligible. The RMS velocities for EDML for the two methods converge towards the bedrock as a result of the compensation of the systematic under- and overestimation described before.

Figure 6.6 is a close-up of the shaded depth in Fig. 6.5b and includes recent high resolution measurements (pers. comm. Ilka Weikusat, 2016), i.e. four bags were sampled continuously, providing ten data points per metre. The two close peaks in figure 6.5 at 2365 and 2375 m from vertical sections measured with the G20 instrument are confirmed by the new data (Fig. 6.6a), which exhibit a strong submetre-scale variability in fabric strength. This causes the fabric classification of the eigenvalue framework to switch several times within two metres. The velocities differ stronger from each other than is observed in Fig. 6.5c, with differences for single thin sections, notably in 2359 and 2380 m depth, of up to 90 m/s, where the eigenvalue framework produces more pronounced peaks than the c-axes framework. This is reflected in the standard deviations for the continuously sampled depth ranges as stated in Tab. 6.1. In synthetic seismograms derived from the modelled velocities, such artefacts would result in artificial reflectors.

Tab. 6.1: Standard deviation of interval P-wave velocities at vertical incidence for several depth ranges. Continuously sampled depths are shaded.

depth in m	std. dev. $s(v_{p0}^{ev})$ in m/s	std. dev. $s(v_{p0}^{cx})$ in m/s
$0 - 1785$	10.9	20.3
$1802 - 2035$	32.8	24.1
$2045 - 2563$	38.5	36.4
$2359 - 2360$	48.3	27.9
$2372 - 2374$	32.3	23.0
$2379 - 2380$	40.3	21.3

Figure 6.7 offers additional information on the c-axis distributions. No information on the core pieces' azimuth angle relative to the ice sheet or to each other is provided. It is however assumed that no sudden short-scale change in the flow regime can occur. Thus, abrupt offsets in girdle orientation must be caused by the unnoticed rotation of core pieces or of thin sections during sample preparation. This needs to be corrected, or at least highlighted, to avoid misinterpretation of the results from applying the c-axes framework for seismic velocity calculation considering phase angles > 0. For the EDML data set several single thin sections that were clearly mirrored or rotated during fabric measurement were corrected according to the girdle orientation of the neighbouring thin sections (Tab. B.2, p. 148). Some jumps in the depth range 755–855 m, which are more evident when assessing the stereographic projections of the EDML samples, where a very broad girdle becomes apparent, were not corrected. Otherwise, the core azimuth in the cone fabric zones is rather randomly distributed, as is to be expected. It changes smoothly in the partial girdle fabric zone, with the exception of a sharp change of girdle direction of about 45° in 1705 m (Weikusat et al., in press), which could not be corrected either and has to be kept in mind when looking at the velocity calculation results for non-vertical incidences.

Reuss-Voigt-Bounds

To be able to evaluate the significance of the observed high variability in seismic P-wave interval velocity as quantified in Tab. 6.1 it is necessary to consider also the Reuss bound, i.e. the results from velocity calculation using the compliance tensor (section 6.2). The mean deviation Δv_{p0}^{cx} of the Reuss bound velocity $v_{p0}^{cx,R}$ from the Voigt bound velocity v_{p0}^{cx} (Fig. 6.5b) for the complete EDML data set was calculated:

$$\Delta v_{p0}^{cx} = -22.3 \pm 4.5\,\text{m/s} \tag{6.25}$$

The bounding velocities lie within 1 % of each other for the seismic P-wave zero-offset velocity of the considered EDML data set.
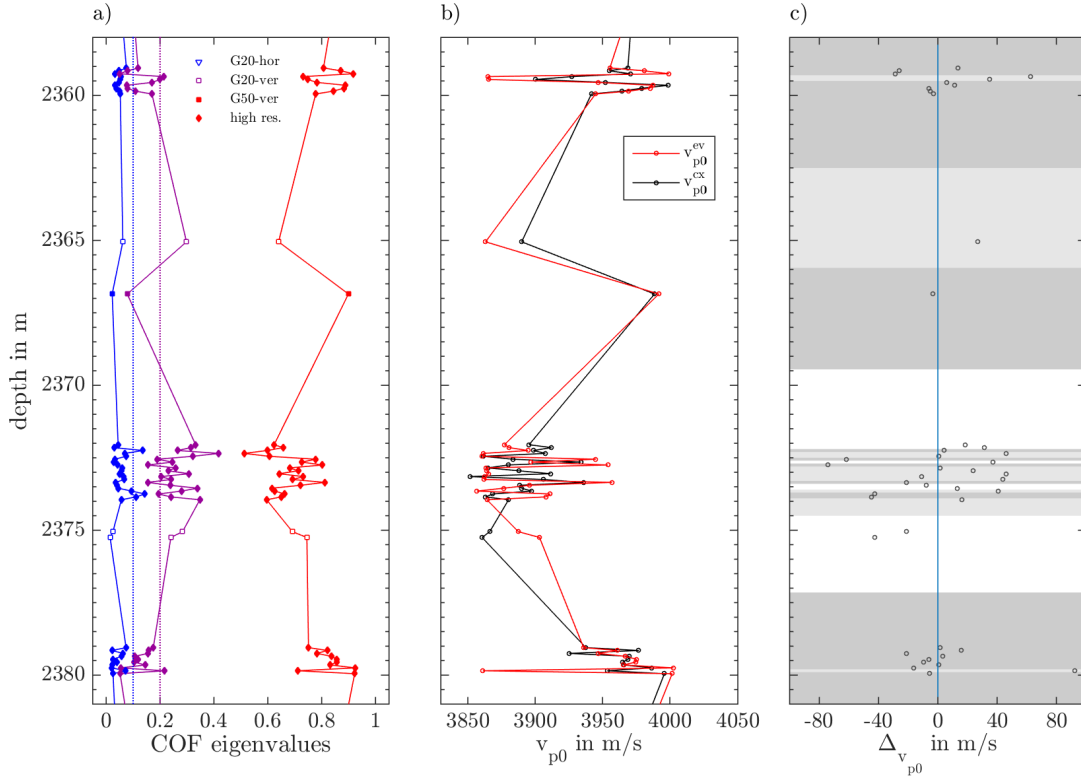
Fig. 6.6: Comparison of P-wave velocities at vertical incidence, calculated from EDML fabric data that was measured in high resolution between 2358 and 2380 m depth . The panels show the same variables as in Fig. 6.5, lines are for visual assistance. The different symbols used for eigenvalue data indicate horizontal (hor) and vertical (ver) thin sections, and fabric analyser model. The recent measurements in high resolution (diamonds) were done with the G50 instrument.

Seismic P-wave velocity for inclined incidence

As the anisotropy of the effective medium is no longer restricted to symmetry with respect to the vertical, using the c-axes framework, the variation of seismic P-wave velocities under a rotating seismic plane can be studied. The seismic plane is the vertical x–z–plane that contains the seismic profile, which runs along the surface of the glacier, and the ice core axis in z–direction, along which fabric information is collected. The relative azimuthal angle of the seismic plane and the oriented ice core is denoted with ϑ_{s}. The zero orientation of the core is not associated with any specific geographical direction.

The difference between the framework velocities $v_{\mathrm{p}}^{cx}(\psi) - v_{\mathrm{p}}^{ev}(\psi)$ is shown in Fig. 6.8, top left panel, for $\vartheta_{\mathrm{s}} = 0$, i.e. the core's orientation is defined to lie in the seismic plane (Fig. D.2, p. 191, for $\vartheta_{\mathrm{s}} > 0$). The seismic plane is then rotated around the ice core axis in steps of $\Delta\vartheta_{\mathrm{s}} = 45°$. $v_{\mathrm{p}}^{ev}(\psi)$ is invariant under the rotation of the seismic plane in case of cone fabric. If the orientation of girdle fabric is known, this could, in principle, be accounted for when using the eigenvalue framework, which would make $v_{\mathrm{p}}^{ev}(\psi)$ sensitive to the seismic plane azimuth. As this is not done here, however, the velocity in girdle fabric is considered as invariant under

the rotation as well. Then, only the c-axes velocity is changing with rotation[1]. For an easier assessment of the amount of change with rotation of the plane only the change from $v_{\mathrm{p}}^{\mathrm{cx}}(\psi)$ to $v_{\mathrm{p}}^{\mathrm{cx},\vartheta_{\mathrm{s}}=0}(\psi)$ is shown in Fig. 6.8, for $\vartheta_{\mathrm{s}} > 0$. The thickness of the horizontal color bands is dependent on the layer thickness for each sample depth, as derived before for the fabric class shading, i.e. reflects the sampling interval only.

Seismic P-wave velocities are underestimated by the eigenvalue framework by max. $131\,\mathrm{m/s}$ and overestimated by max. $84\,\mathrm{m/s}$. For small angles the observation from comparing the zero-offset velocity profiles persists when rotating the seismic plane, i.e. white and light shades
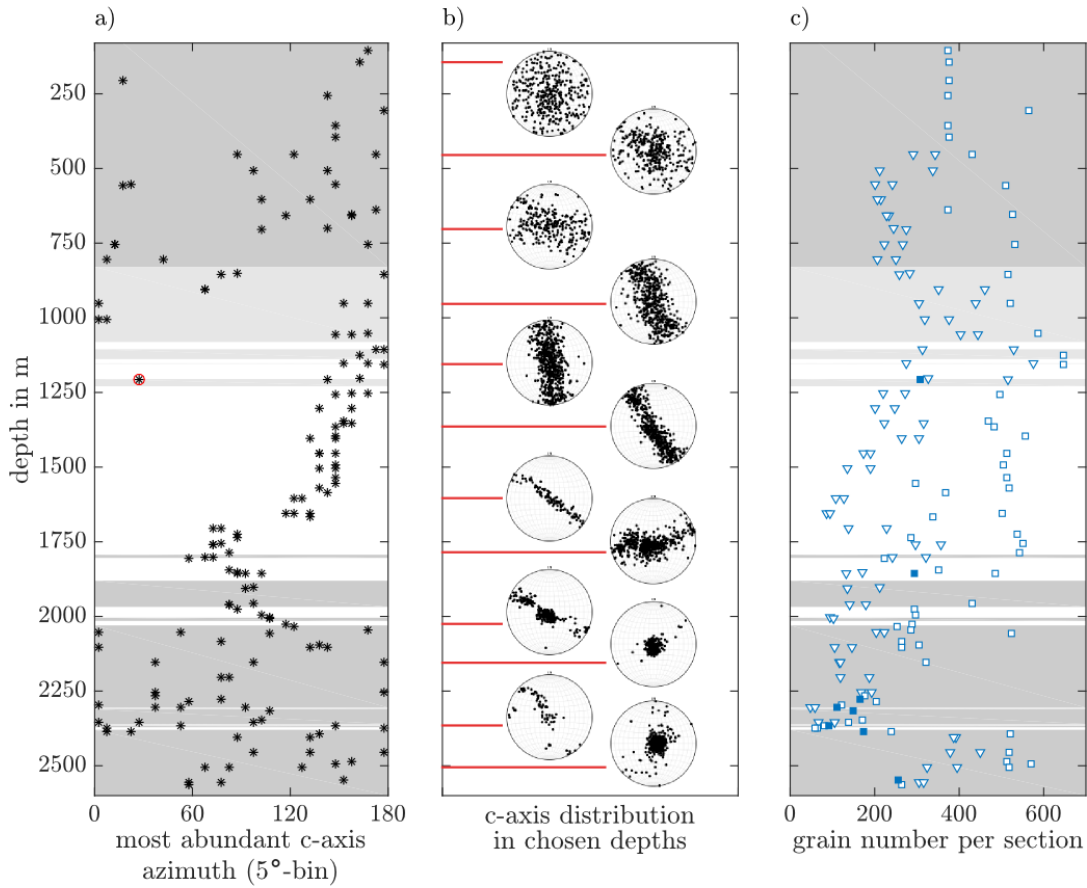
Fig. 6.7: Additional information on EDML's c-axes distributions. Shading as in Fig. 6.5. **a)** From the c-axis azimuth angle distribution of each sample the approximate direction of the girdle is found (5° angle interval). One data point appearing as outlier (red circle) could not be corrected. **b)** Examples of stereographic projections for different depths illustrate the development from isotropic/cone to girdle and back to cone fabric. **c)** shows the number of grains in each thin section sample with symbols as in Fig. 6.6. The total area of vertical thin sections is generally larger and contains more grains.

---

[1]"Difference" refers to the comparison of differently calculated velocities, while "change" is used for the azimuth-dependent observations.
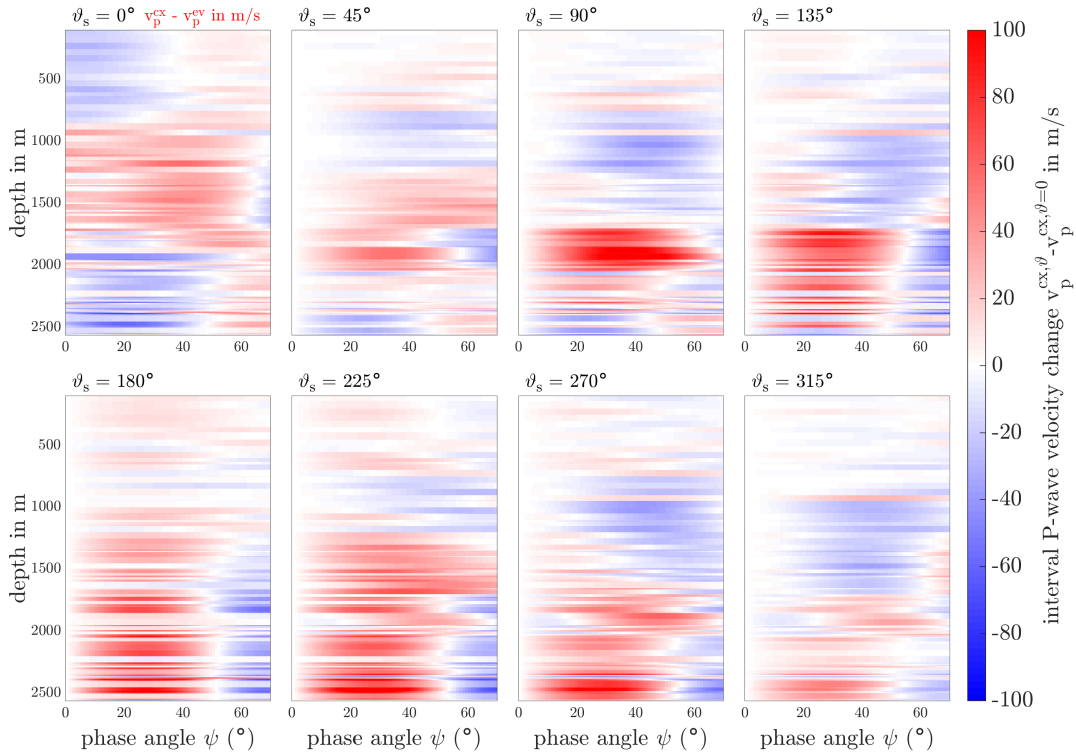
Fig. 6.8: Top left: Difference of EDML seismic P-wave velocity between c-axes and eigenvalue framework for incidence angles up to 70°. Blue colour indicates overestimation of velocity by eigenvalue framework, red shades show the opposite. The other panels show the change in P-wave velocity, as calculated with c-axes framework for different seismic plane azimuth angles ϑ_s, compared to $\vartheta_s = 0°$.

close to 0°. While for cone fabric in the upper part the difference is only small ($\pm 20 \, \text{m/s}$), the highest sensitivity to seismic azimuth is apparent for the lower part of the girdle fabric, below the earlier mentioned sudden rotation of the dominant azimuth direction that was not corrected, and cone fabric in the deep part of the core with up to more than $100 \, \text{m/s}$ change in interval velocity for some seismic azimuth planes as compared to the defined 0°–plane.

See Fig. D.1 (p. 191) for the absolute seismic P-wave velocities calculated with the c-axes framework for inclined incidence. The highest absolute velocities are found in the lower part of the ice core, where the fabric anisotropy is strong, for phase angles below 20–30°. The lowest velocities are found for higher incidence angles (Fig. 6.1).

Seismic S-wave velocity

The results for the seismic S-wave velocities for inclined incidence and several seismic plane azimuth angles are compared between the frameworks and between SH- and SV-wave of the c-axes framework. The figures for the absolute c-axes velocities for SH- and SV-wave (Fig. D.3, D.4, p. 192) as well as the comparison between the frameworks (Fig. D.5, D.6, p. 193) and the difference between the c-axes S-wave modes (Fig. D.7, p. 194) are appended.
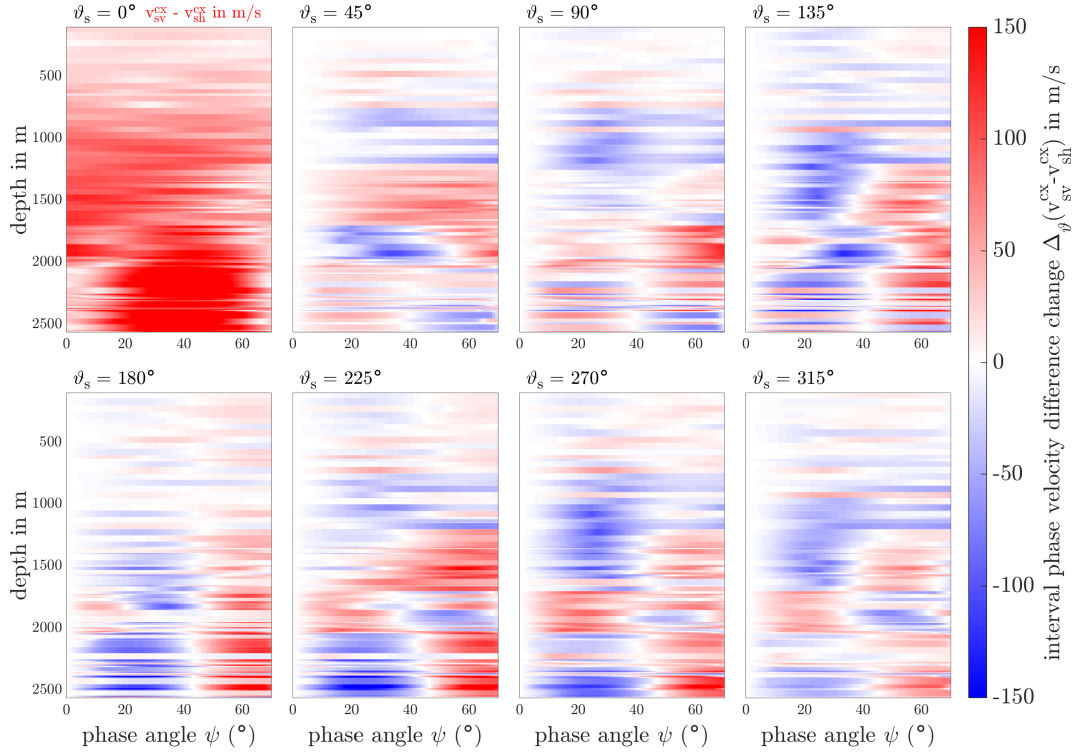
Fig. 6.9: Top left: Difference of EDML seismic velocities between SH- and SV-wave as calculated with c-axes framework for incidence angles up to 70°. The other seven panels give the change of the S-wave difference for different seismic plane azimuth angles ϑ_s.

For vertical incidence, the SH-wave velocity $v_\mathrm{sh0}^\mathrm{cx}$ is mostly overestimated by the eigenvalue framework in many depths by up to $200\,\mathrm{m/s}$ (Fig. D.5). The SV-wave velocity is underestimated by up to $150\,\mathrm{m/s}$ for phase angles below 20° and overestimated for larger angles in the girdle section (Fig. D.6). The change of this assessment when considering the rotation of the seismic plane is moderate, i.e. mostly around or below $\pm 50\,\mathrm{m/s}$ for SH-wave but somewhat more pronounced for the deeper part of the core below $1750\,\mathrm{m}$, when looking at SV-velocities.

Fig. 6.9 shows how the difference between SV- and SH-wave velocities (Fig. D.7) changes when rotating the seismic plane ($\vartheta_\mathrm{s} > 0°$) in comparison to the difference for $\vartheta_\mathrm{s} = 0°$ (top left panel). For small phase angles this difference is intermediate around $100\,\mathrm{m/s}$ in the girdle part and becomes maximal for medium phase angles in the deep cone fabric with up to $280\,\mathrm{m/s}$ as is to be expected for a near-VSM medium (Fig. 6.1). The azimuth sensitivity is in this case rather limited with low to moderate change in velocity for most depths when rotating the seismic plane.

6.3.2 Alpine ice core KCC

Diez (2013) and Diez et al. (2014) use the fabric data of the ice core KCI, drilled on Colle Gnifetti in 2005 in about $100\,\mathrm{m}$ distance to ice core KCC (Fig. 3.1, p. 14), to model anisotropic velocities. They are able to offer an explanation for the discrepancy in depth-conversion from P- and SH-waves from reflection seismic data collected around the borehole and processed under isotropic assumptions (Polom et al., 2014). The fabric data were obtained in 2012, after

99

storage of the core at -30 °C. The data consist of single thin section samples in ~ 3 m intervals in the lower half of the core, i.e. in the ice part from 30 down to 62 m depth. The derived phase velocities are corrected for firn density and borehole temperature. Diez et al. (2014) show that the calculated RMS velocities for zero-offset and normal moveout are different. This difference indicates how sensitive seismic velocities are to an anisotropic crystal-orientation fabric. It is found that the P-wave is clearly influenced by anisotropy with a difference of 7 % (228 m/s) between the velocity usually picked from seismic data and used for depth-conversion and the velocity that should be used for depth-conversion to account for crystal-orientation fabric.

For this case study, as for EDML, the estimate of the velocities using the eigenvalue framework is tested against the c-axes framework. The fabric data from KCC collected in this study and extensively described in sections 3.1, 3.3, 3.4 and 4 (p. 37) are used for the comparison of the eigenvalue and c-axes frameworks for the calculation of seismic phase velocities, as an example for an Alpine site. An overview of all KCC thin section samples used in this thesis can be found in appendix B.2 (p. 146). The seismic velocities were calculated with both frameworks following the instructions of Diez and Eisen (2015) and section 6.2, respectively. However, the threshold values for classifying the fabric are chosen such that only cone fabric is recognised by the algorithm, i.e. the threshold for girdle fabric is set to $\lambda_2 \geq 0.4$ and $\lambda_1 \leq 0.1$; cone fabric is identified elsewhere. This is done as it is evident from the evaluation of stereographic projections (section 4.2) that cone fabric is dominant in all samples, although some tendencies towards girdle can be made out in deeper samples, and artificial discontinuities are prevented. Area-weighting is applicable for both frameworks as grain size information is available from automatic image processing. The velocities are not corrected for density or temperature effects for the purpose of comparing the calculation approaches.

Seismic P-wave velocity for vertical incidence

Fig. 6.10 shows the results of the velocity calculations for vertical incidence:

- The cone angle calculated from the eigenvalues varies in a 10–30° interval for each depth range (Fig. 6.10a), discussed in section 4.2.

- The velocities calculated with both frameworks increase with depth as a stronger anisotropic crystal-orientation fabric evolves and are very variable between adjacent 10 cm samples for which the core orientation is always exactly the same (Fig. 6.10b). The dashed lines indicate the average velocity for a continuously measured depth range.

- The variability within the depth ranges for the different calculations expressed as standard deviation $s(v_{p0})$ increases up to almost 35 m/s for smaller cone angles with high short-scale variability in cone angle (Fig. 6.10c).

- The difference between the averages of the Voigt bounds of both frameworks is shown in Fig. 6.10d. The eigenvalue framework overestimates the P-wave velocity for the cone fabric classification, here by 41 m/s (without considering the bottom layer where the difference exceeds 90 m/s) and by 46 m/s respectively (including the bottom layer). Hence, differences between the frameworks are similar for the KCC ice core as for the cone fabric regions of the EDML ice core.

- In the bottom layer the largest difference is 135 m/s, which is due to the strong single maximum that is inclined to the vertical. In Fig. 6.10f the change in c-axes velocity δv_{p0}^{cx}

of each $10\,\mathrm{cm}$ sample to the previous is plotted. Changes of more than $40\,\mathrm{m/s}$ occur regularly within $10\,\mathrm{cm}$.

- For the estimate of RMS velocities the layer boundaries are chosen such that the measured ranges are centered within the layer as indicated in Fig. 6.10e by the alternating shading. Neither temperature nor density corrections are applied. The difference between the framework velocities at bedrock amounts to $-40\,\mathrm{m/s}$.

- The mean deviation $\Delta v_{\mathrm{p0}}^{\mathrm{cx}}$ of the Reuss bound velocity $v_{\mathrm{p0}}^{\mathrm{cx,R}}$ from the Voigt bound velocity $v_{\mathrm{p0}}^{\mathrm{cx}}$ (Fig. 6.10b) for the KCC data set is:

$$\Delta v_{\mathrm{p0}}^{\mathrm{cx}} = -21.9 \pm 6.0\,\mathrm{m/s} \tag{6.26}$$

The Reuss-Voigt bounds lie within $1\,\%$ of each other for the seismic P-wave zero-offset interval velocity of the considered KCC data set.
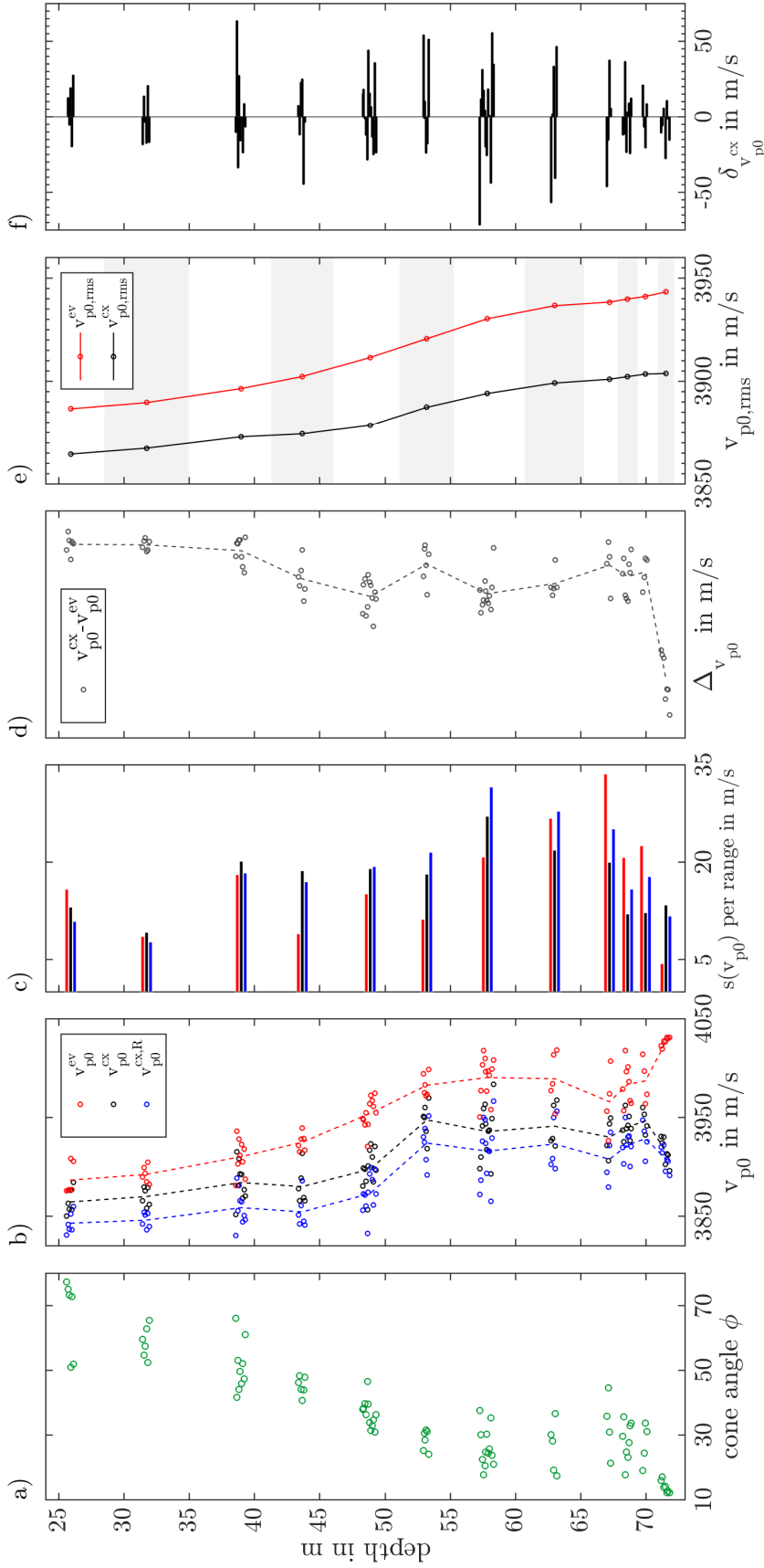
Fig. 6.10: Comparison of zero-offset P-wave velocities calculated from KCC fabric data via eigenvalue and c-axis approach. Panel **a)** shows cone angles derived from eigenvalues following Diez and Eisen (2015). **b)** presents the calculated P-wave velocities for the two frameworks for all thin sections (symbols) and the average velocities for each continuously sampled depth range (lines); red (ev) and black (cx) show the Voigt bound, blue the Reuss bound (cx). The standard deviation within a depth range is shown in **c)** using the same colors as in b). **d)** shows the difference $v_{p0}^{cx} - v_{p0}^{ev}$ per sample and per range average. In panel **e)** the RMS velocities resulting from the interval velocities were calculated from the layers centered around the measurements without taking into account temperature, density and the confining firn layer of 23 m. Panel **f)** illustrates the velocity change $\delta v_{p0}^{cx} = v_{p0}^{cx}(d_{i+1}) - v_{p0}^{cx}(d_i)$ between subsequent 10 cm sections at depths d_i.

Seismic P-wave velocity for inclined incidence

The change of the P-wave velocity with increasing phase angle and rotated seismic plane as calculated with the azimuth sensitive c-axes framework is displayed in Fig. 6.11. The thickness of the color bands is here constant for each sample and the dashed horizontal lines signify depth axis breaks to cut the intervals without measurements. The 12 depth ranges with continous thin section measurements consist of altogether 18 runs, i.e. ice core pieces. Five of these were presumably rotated relative to the majority of all ice core pieces during processing to optimise the aliquot cutting. The rotation was estimated and noted in hours i.e. in multiples of 30° (Tab. 3.1, p. 23). The data is corrected accordingly during the c-axes framework algorithm to allow the assessment of azimuth sensitivity, but no claim for completeness can be made.

The influence of the inherent asymmetry of the anisotropic fabric in the deeper part of KCC appears very clear. It is additionally illustrated with velocity profiles for an exemplary incidence angle of 10° in Fig. 6.12. The profiles show a spread of velocities for each layer of up to 120 m/s when considering different seismic plane azimuth angles. Analoguously to Fig. 6.8, the change in P-wave velocity v_p^{cx} with increasing phase angle is shown in Fig. 6.13. The difference in P-wave velocity when comparing the calculation frameworks reaches up to ± 190 m/s for the bottom layer and ± 50–100 m/s for most depths below the firn-ice-transition for various incidence angles and seismic plane azimuth angles (Fig. D.8, p. 194).
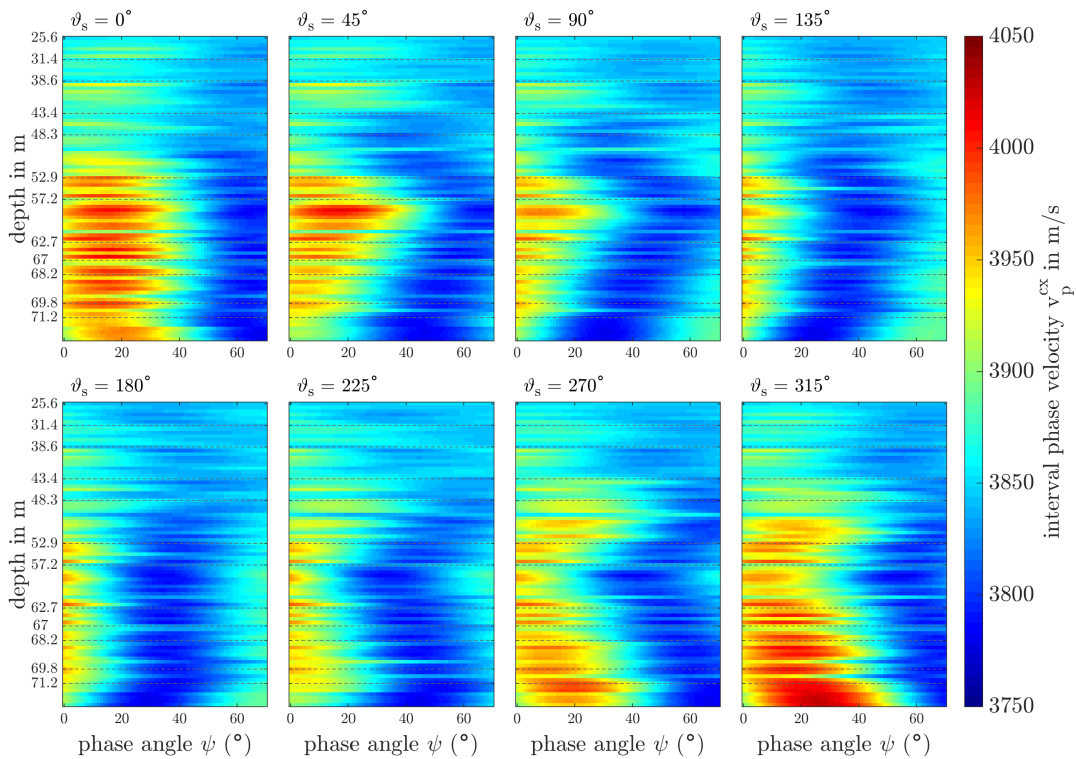
Fig. 6.11: Seismic P-wave velocities for KCC calculated with c-axes framework for incidence angles up to 70° and eight seismic plane azimuth angles ϑ_s. Note the breaks of the depth axis (dashed lines), where noted depth values refer to the top of the downward extending depth range.

Fig. 6.12: Profiles of KCC seismic P-wave interval velocity for an incidence angle ψ of 10°. The rotation of the seismic plane is color coded. For clarity the data points are plotted not against depth but are equidistant along the y-axis. The spread of velocities for a full rotation of the core for each sample exceeds 50 m/s for a large part of the samples, with up to 120 m/s for the bottom samples.
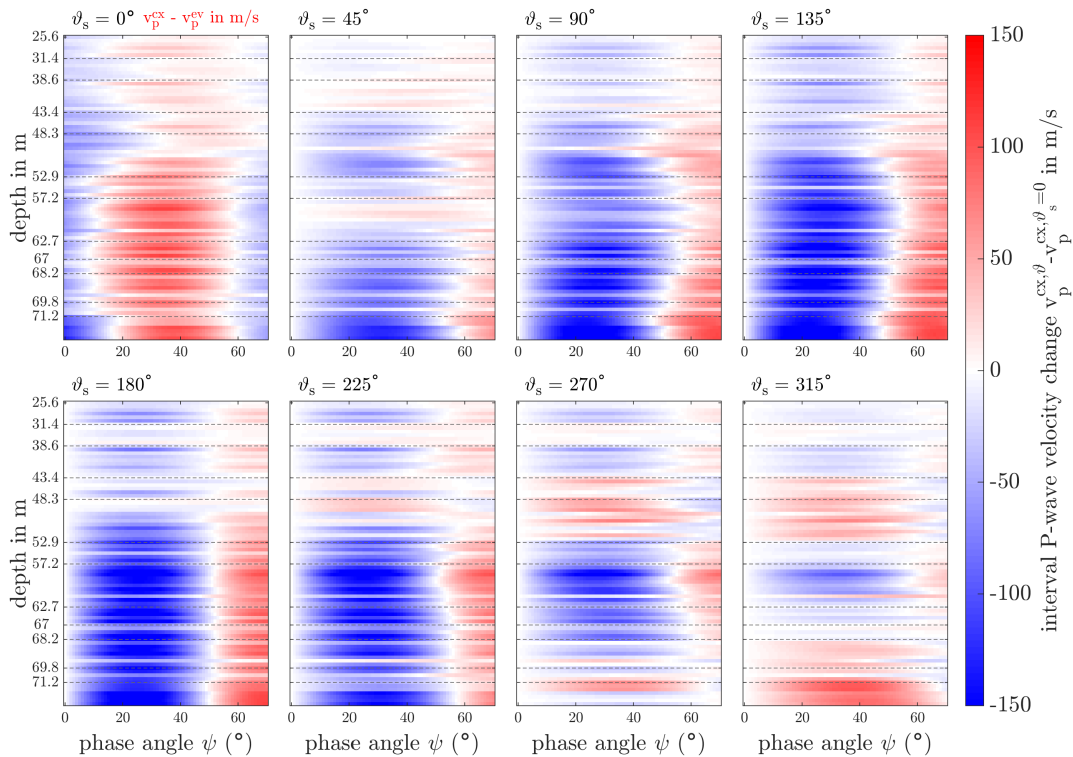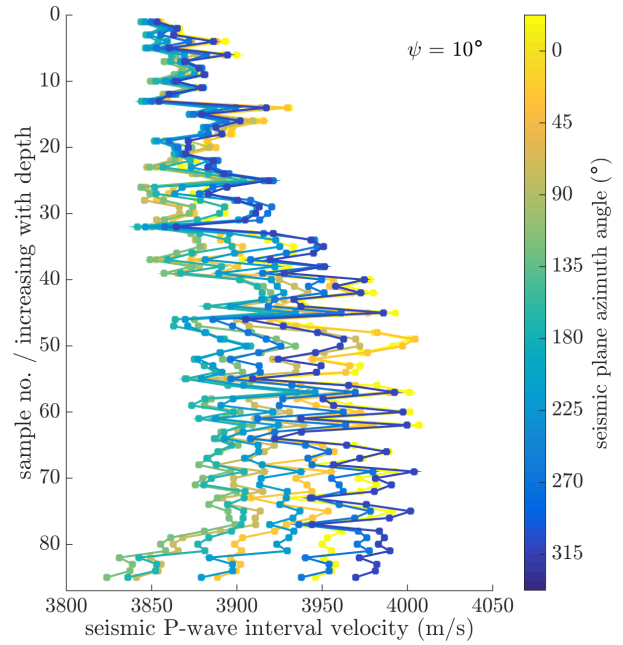
Fig. 6.13: Top left: Difference of KCC seismic P-wave velocity between c-axes and eigenvalue framework $(v_p^{cx} - v_p^{ev})$ for incidence angles up to 70°. The other panels show the change in P-wave velocity as calculated with c-axes framework for different seismic plane azimuth angles ϑ_s compared to $\vartheta_s = 0°$. Note the breaks of the depth axis where noted depth values refer to the top of the downward extending depth range.

Seismic S-wave velocity

Fig. 6.14 shows, analoguously to Fig. 6.9, the difference between SV- and SH-wave velocities for inclined incidence (top left panel and Fig. D.9, p. 195) and investigates how the difference between the S-wave modes changes when rotating the seismic plane. The initial difference ($\vartheta_\mathrm{s} = 0°$) is low for small angles but for the bottom samples. It reaches more than $200\,\mathrm{m/s}$ for angles $> 40°$. For KCC the change with rotation is much more sensitive to the seismic plane azimuth than is observed for EDML. For specific azimuth angles the change reaches about $200\,\mathrm{m/s}$ for many depths below the firn-ice-transition for incidence angles around $20°$. For angles above $40°$ the change in S-wave difference gets as low as -250 m/s. The major part of this large change under seismic plane rotation is caused by SV-wave variation (Fig. D.10, p. 195).
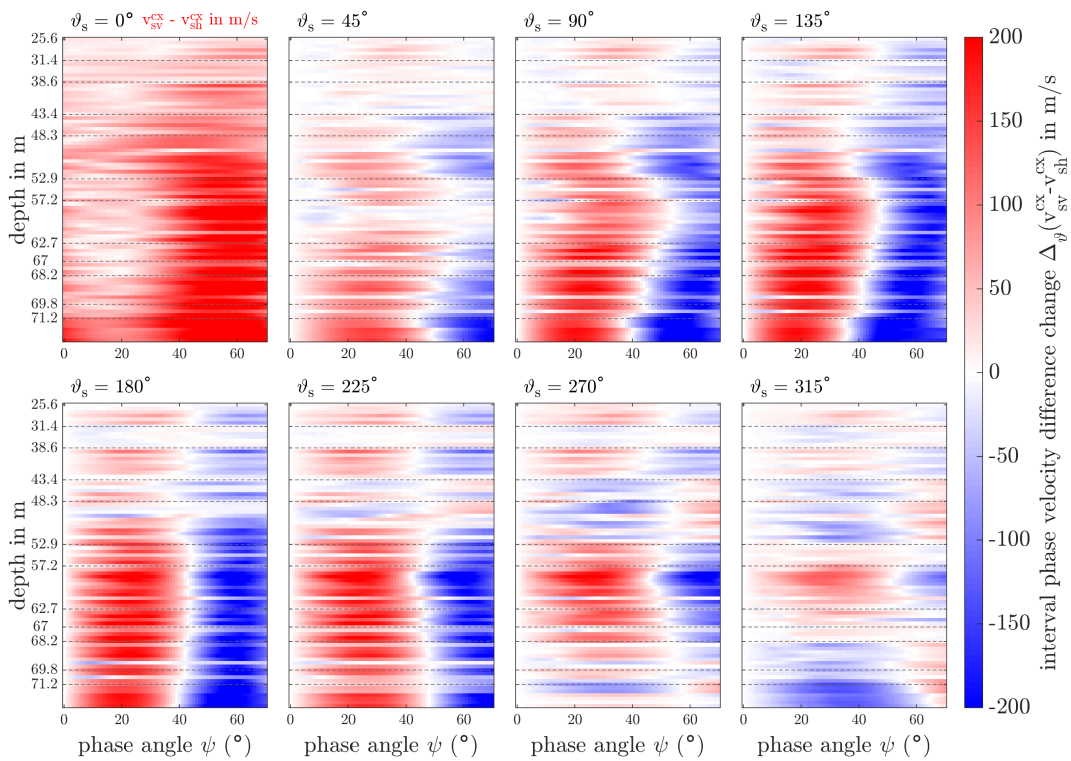
Fig. 6.14: Top left: Difference of KCC seismic velocities between SH- and SV-wave as calculated with c-axes framework for incidence angles up to 70°. The other seven panels give the change of the S-wave difference for different seismic plane azimuth angles ϑ_s. Note the breaks of the depth axis where noted depth values refer to the top of the downward extending depth range.

6.4 Discussion of implications of seismic velocities calculated from fabric data

Results of the comparison between two approaches (Diez and Eisen, 2015, and the present study) for the calculation of theoretical seismic velocities from fabric data were presented for two case studies on an Alpine (KCC) and a polar ice core (EDML). Differences between the frameworks were assessed for vertical and inclined incidence angles. The change in velocity for the c-axes framework in dependence of the seismic plane azimuth was investigated. The velocity differences between the frameworks for the two case studies are summarised in Tab. 6.2.

The main findings are:

- Short-scale variability in anisotropic fabric causes a high short-scale variability in seismic velocities in polar and Alpine ice. This variability exceeds the Voigt-Reuss bound difference.

- The difference between the frameworks is larger for the Alpine than for the polar core. This suggests that the eigenvalue framework provides a good enough approximation for the polar site for the current degree of resolution and interpretation of physical properties, not considering the artificial discontinuities, but is not adequate for the Alpine site.

- The fabric classification scheme in the eigenvalue framework can mask the true velocity variability by producing artificially enhanced peaks in the velocity profile.

- The Reuss and Voigt bounds are within 1% of each other for the c-axes framework, as for the eigenvalue framework (Diez and Eisen, 2015).

- The orientation of the fabric distribution should be considered for the calculation of seismic velocities from fabric data as the azimuthal change in P-wave velocity and shear-wave splitting can be larger than $100\,\mathrm{m/s}$.

- While the depth scale of KCC differs from that of EDML by a factor of 1/35, the presented case studies are another example of the importance of mid-latitude high-altitude glaciers as in situ laboratories to study fundamental processes in glaciers.

Evaluation of the c-axes framework

The c-axes framework, developed in this study, takes the asymmetry of anisotropic fabric, with respect to the vertical, into account. This is especially relevant for ice cores from dynamic flow regimes, e.g. flank flow, as becomes evident from the KCC case study, where the azimuthal change in fabric and the resulting velocities is not negligible. For such sites the approximation of the fabric by opening angles centered around the vertical deviates much more from the reality than for sites that are located in the vicinity of an ice divide. The main disadvantage of the framework is the dependency on accurate azimuthal information, i.e. the orientation of the fabric distribution in the equatorial plane has to be known for the consecutive fabric samples. To this date, the oriented drilling of ice cores remains a challenge. The reconstruction of the core pieces' orientation with respect to each other is feasible to a certain degree. Hence, the uncertainty for the seismic velocity calculation is much larger in vertical direction than under azimuthal rotation. A main advantage is the dispensation with the fabric classification, thus

eliminating artificial discontinuities. The example of high resolution sampling in the EDML ice core demonstrates the importance of this advance, allowing to separate the true high variability in seismic velocities from the artificially enhanced variability. This finding could, however, be used to tune the threshold values for the fabric classification in the eigenvalue framework. The eigenvalue framework could also be improved by considering the girdle azimuth, but this would also require the corresponding data.

Lateral extended crystal-orientation fabric

The analysis at inclined incidence is based on the major assumption of a laterally extended and coherent fabric layering. Although it is regularly observed in the KCC ice core and also in the continuously sampled depth regions in EDML, it is still unclear how representative these short-scale variations are for a larger region (e.g. Drews et al., 2012). Evidence has been presented for abrupt COF changes as a frequent cause of seismic reflectivity (Horgan et al., 2011). Other studies do not observe such a high reflectivity due to COF but identify a high degree of gradually evolving fabric anisotropy (Picotti et al., 2015) or single strong reflections associated with transition in fabric classes, e.g. from cone to girdle (e.g. Diez et al., 2015). The coherence of short-scale fabric changes will largely depend on the still unresolved question of how they evolve exactly. If the short-scale fabric stratigraphy is largely governed by local conditions and heterogenous small-scale deformation (possibly resulting in "layer roughness", Drews et al., 2009), no coherent structure is to be expected (Diez et al., 2015). In this case, it should be challenged, how representative the elastic properties derived from thin sections are, and the question arises, how non-coherent short-scale fabric changes alter the rheological properties of the bulk. It can be hypothesised that under the increasing influence of large-scale shear deformation in the deeper regions of the glacier coherent crystal-orientation fabric layers might develop, in an act of synchronisation (section 4.6, p. 62). Accordingly, more seismic reflectivity should be expected in depth and from more dynamic settings, as proposed from Horgan et al. (2011). Eisen et al. (2007) show that transitions in COF in the deep ice can be followed over long distances. Short-scale variations in seismic velocity cannot be resolved with conventional seismic techniques with large wavelengths of the order of 10 m, depending on the source of the seismic waves and the sounding depth. However, Hofstede et al. (2013) obtain numerous laterally continous reflections at Halvfarryggen, Antarctica. They suggest that closely spaced layers ("stacks") of varying fabric, as has been observed in this study, are the major cause for the reflections. Far more fabric data than is currently sampled in ice core studies, is required to investigate how a typical succession of short-scale fabric layers could induce such reflections.

Ultrasonic methods can be applied in ice core boreholes (Anandakrishnan et al., 1994; Gusmeroli et al., 2012) to infer crystal-orientation fabric in situ. Although the interpretation of these data is not straightforward (e.g. Maurel et al., 2015), it is currently the only technique that is capable of a continuous fabric measurement. However, a sonic pulse samples the volume around the borehole ($\sim 2\,\mathrm{m}^3$, Gusmeroli et al., 2012), i.e. the method is not azimuth-sensitive. While it cannot provide the two-dimensional structure nor exact fabric information, it is a trade-off that could help to bridge the gap between laboratory-based interval fabric measurements and large-scale seismic data. The presented c-axes framework contributes to the understanding of seismic velocities based on real anisotropic fabric.

Perspectives for future work

Several aspects for future work, which are beyond the scope of the present study, are identified:

- Diez et al. (2014) calculate a difference in RMS velocity at bedrock for the KCI core of $228\,\mathrm{m/s}$ as a result of anisotropic fabric. The difference of $40\,\mathrm{m/s}$ between framework RMS velocities would mean a $18\,\%$ reduction of this value, i.e. to $188\,\mathrm{m/s}$. However, the RMS velocities calculated in this study were not corrected for density and temperature. This should be considered for a more reliable analysis.

Tab. 6.2: Summary of the results from the seismic velocity comparison between frameworks. Values are estimates of observed extreme or average velocity differences. Negative values indicate smaller c-axes velocities relative to eigenvalue velocities.

Description	Notation	EDML	KCC
V-R bounds for c-axes framework	$\Delta v_{\mathrm{p0}}^{\mathrm{cx}} = v_{\mathrm{p0}}^{\mathrm{cx}} - v_{\mathrm{p0}}^{\mathrm{cx,R}}$	$-22.3 \pm 4.5\,\mathrm{m/s}$	$-21.9 \pm 6.0\,\mathrm{m/s}$
Difference between framework velocities at vertical incidence	Δv_{p0}	$\pm 17\,\mathrm{m/s}$, max. $\pm 90\,\mathrm{m/s}$	$-46\,\mathrm{m/s}$, max. $-135\,\mathrm{m/s}$
	Δv_{sh0}	$-200\,\mathrm{m/s}$	
	Δv_{sv0}	$+150\,\mathrm{m/s}$	$\sim 150\,\mathrm{m/s}$
Difference between the framework velocities at inclined incidence	$v_{\mathrm{p}}^{cx}(\psi) - v_{\mathrm{p}}^{ev}(\psi)$	$-84/+131\,\mathrm{m/s}$	$\pm 190\,\mathrm{m/s}$
Change of c-axes velocity with azimuth ϑ_{s}	$v_{\mathrm{p}}^{\mathrm{cx}}(\psi) - v_{\mathrm{p}}^{\mathrm{cx},\vartheta_{\mathrm{s}}=0}(\psi)$	$\sim 100\,\mathrm{m/s}$	$\sim 150\,\mathrm{m/s}$
	$v_{\mathrm{s}}^{\mathrm{cx}}(\psi) - v_{\mathrm{s}}^{\mathrm{cx},\vartheta_{\mathrm{s}}=0}(\psi)$	$\sim \pm 50\,\mathrm{m/s}$	
Change of S-wave velocity difference for c-axes framework with azimuth ϑ_{s}	$\Delta_{\vartheta}\left(v_{\mathrm{sv}}^{\mathrm{cx}} - v_{\mathrm{sh}}^{\mathrm{cx}}\right)$	$\sim \pm 50\,\mathrm{m/s}$	$-250/+200\,\mathrm{m/s}$
Variability (std. dev.) of eigenvalue framework velocity	$s(v_{\mathrm{p0}}^{\mathrm{ev}})$	$10\text{–}49\,\mathrm{m/s}$	$\sim 34\,\mathrm{m/s}$
Variability (std. dev.) of c-axes framework velocity	$s(v_{\mathrm{p0}}^{\mathrm{cx}})$	$20\text{–}37\,\mathrm{m/s}$	$\sim 33\,\mathrm{m/s}$
Vertical change in c-axes velocity	$\delta v_{\mathrm{p0}}^{\mathrm{cx}}$	$> \pm 50\,\mathrm{m/s}$	$\pm 50\,\mathrm{m/s}$
Difference between RMS velocities at bedrock	$v_{\mathrm{p0,rms}}^{\mathrm{cx}} - v_{\mathrm{p0,rms}}^{\mathrm{ev}}$	~ 0	$\sim -40\,\mathrm{m/s}$

- The possible influence of grain size and grain shape for the seismic wave propagation in polycrystalline ice is currently not considered for theoretical calculations. Following the perceptions of the present study, not only crystal-orientation fabric but also grain topology exhibits a strong variability on a short scale. Especially for polar ice cores, where the grain size variability is additionally influenced by climatic transitions and higher temperature and ages close to bedrock, grain boundary effects on the propagation of seismic waves should be revisited.

- The results demonstrate the high sensitivity of shear-wave splitting to asymmetric anisotropic fabric. This was earlier observed by Anandakrishnan et al. (1994). The seismic data from Colle Gnifetti (Polom et al., 2014; Diez et al., 2013) could be reanalysed, under consideration of the seismic velocities calculated from asymmetric fabric.

- As for the hypothesis that seismic reflections originating from COF changes could be a means to infer the impurity load (e.g. Horgan et al., 2008), it is an unresolved issue. While for climatic transitions this hypothesis appears likely, following observations from fabric studies on polar ice cores, the origin of short-scale fabric variations remains unclear. The findings presented in this study indicate, however, that fabric on the short-scale cannot be exploited to infer short-term climatic changes.

7 Conclusion and Outlook

The main objective of this work was to investigate the short-scale variability of anisotropic crystal-orientation fabric in a cold Alpine ice core and to examine a possible causal relationship with the paleo-climate proxies in the core. An improved understanding of the fabric evolution is crucial for the understanding of the flow of ice masses because the ice crystal properties on the short scale determine the rheological behaviour of the glacier bulk. The influence and interaction of the ice crystal properties with the impurity content in the ice, which is governed by the climate system on every time scale, is poorly understood, especially on a short scale, and needs to be investigated to determine the extent to which the rheological behaviour of ice is dependent on the climatic influences during the ice formation. The limitations in the determination of crystal-orientation fabric are due to the measurement options: (1) Time-consuming laboratory preparation of thin section samples from an ice core provide exact fabric information but only for the specific depth of the sample at the location of the ice core (2) Geophysical methods, like surface-based seismics, can be used to infer crystal-orientation fabric on a larger scale but with a very limited resolution far below the crystal scale. To further the interpretation of seismic measurements concerning the identification and quantification of anisotropic crystal-orientation fabric, the fabric data from thin section measurements can be used to model the seismic velocities that should be expected in the area of the ice core drilling site. By implication, a distant goal is the ability to deduce climatic changes from surface-based measurements.

In this work, the first comprehensive study of fabric and microstructure on a cold Alpine ice core was accomplished. Continuous thin section measurements of crystal-orientation fabric and ice microstructure were conducted for several intervals along the ice core, covering more than $10\,\%$ of the entire core length. The collected data comprise crystal-orientation fabric, grain topology and pore space parameters, which were evaluated on a scale of decimetre to metres as well as on a centimetre-scale and under consideration of additional physical properties available from the ice core (density and line scan). The variability of anisotropic crystal-orientation fabric on these scales was assessed and described. The larger-scale fabric and microstructure data was interpreted for the characterisation of the deformation regime at the southern flank of the Alpine drilling site Colle Gnifetti. The short-scale results were evaluated regarding the links between fabric and microstructural parameters and the fabric data were compared with impurity data from melt analysis. The likelihood of impurities to be the cause for short-scale variations in anisotropic fabric was investigated. A pilot study on the applicability of laser ablation for the investigation of the spatial distribution of impurities with respect to the ice fabric and microstructure was implemented. The obtained data on short-scale fabric anisotropy were used in the development of a new framework for the calculation of seismic velocities based on the exact crystal-orientation fabric information from thin section measurements. The modelled velocities were evaluated in two case studies of an Alpine and a polar ice core, with respect to an earlier calculation framework.

7. Conclusion and Outlook

The most important findings can be summarised as follows:

The fabric of the KCC ice core is highly anisotropic, already starting in the firn. A single maximum develops quickly under vertical compression and simple shear deformation and becomes inclined in the deepest 20 m of the ice core. An extensional flow component in the deeper part is suggested. The comparison with the neighbouring ice core KCI lead to the conclusion that the fabric evolution on the metre-scale is comparable over the lateral distance of a few hundred metres.

Short-scale fabric and grain size layering were frequently observed in the KCC ice core. The strength of the fabric is varying on the decimetre-scale between adjacent thin sections with an average variability (standard deviation) of 0.14 ± 0.02. The average variability (difference between extreme values) on a centimetre-scale within a range of adjacent thin sections reaches 0.28 ± 0.12. It is concluded that a single thin section cannot provide a fabric estimate that is representative for the typical vertical sampling intervals of ice core fabric studies. It is unclear whether the reported variability is representative for a larger horizontal region or restricted to the vicinity of the borehole.

Abundant evidence for dynamic recrystallisation was found from firn to bedrock by the evaluation of the grain topology and grain boundary network. This includes the formation of different types of subgrain boundaries, the occurrence of island grains, the development of tortuous and kinking grain boundaries resulting in a variety of grain shapes, and the redistribution of bubbles.

The results regarding the influence of the impurities on the short-scale anisotropic fabric variations could not unambiguously be resolved. A clear negative correlation between the mean grain size and the impurity content could be confirmed. A weaker anticorrelation between mean grain size and fabric, and by implication between fabric and impurities, was found, leading to the conclusing that the influence of impurities on short-scale fabric variations is exerted via the grain size in combination with the local deformation regime.

The potential of laser ablation measurements of the spatial distribution of impurities with respect to the ice microstructure was established. The preliminary results of the pilot study do not indicate that the spatial impurity distribution is dependent on a different microstructure or fabric. However, evidence for the accumulation of sodium in grain boundaries relative to the grain interiors was found for all samples. At the same time, no such pattern emerged for the distribution of iron in the ice.

A new framework for the calculation of the elasticity tensor of the polycrystal and the calculation of seismic interval velocities from the polycrystal elasticity tensor was implemented. It is based on the exact crystal orientation information of the constituent monocrystals and refrains from making use of approximations assuming a fabric symmetry. The algorithm provides the seismic P- and S-wave velocities in dependence of the seismic incidence angle and the horizontal azimuth angle of the seismic incidence with respect to the azimuthal orientation of the fabric, which is the input for the calculation. By using anisotropic fabric data from the Alpine KCC ice core and the polar EDML ice core the resulting vertical variability and azimuthal change in seismic velocities was demonstrated and compared with an earlier framework, which provides estimates of the seismic velocities under the assumption of vertically symmetric fabric. The

P-wave velocity differences between the two frameworks were found to be as large as $\pm 131\,\mathrm{m/s}$ for EDML and $\pm 190\,\mathrm{m/s}$ for KCC. The azimuth-sensitive S-wave splitting reaches values of more than $\pm 200\,\mathrm{m/s}$ for the asymmetric fabric of KCC.

The information density in this short Alpine ice core is extensive and provides enough material for various studies focussing on the interaction of physical properties and impurities in firn and ice. The potential of Colle Gnifetti as an in situ laboratory for glaciological studies was affirmed.

Several open questions and opportunities for follow-up studies remain at this point:

1. A detailed analysis of the microstructure image data set with the aim to identify the active recrystallisation processes at all depths, especially with regard to current microstructure modelling focussing on the role of bubbles for strain localisation (Steinbach et al., in review).

2. The correlation analysis between fabric and impurities should be expanded to all physical properties parameters in order to investigate, for example, the dependency of dust and bubble number density (Bendel et al., 2013) or density and calcium in firn (Hörhold et al., 2012). Also, the absolute concentrations of the CFA data have been neglected so far (Thorsteinsson, 1996) and should be included for the aim of unveiling the impurity-fabric cause-effect relationship.

3. Considering the relatively short length of KCC, continued fabric measurements could be an option with the aim to obtain the first full thin section fabric record of a closed glacier system.

4. 3D scans (μCT) of the ice core's archive pieces to obtain the full pore space information would allow for, e.g. the development of bubbles as deformation markers, favored by the glacio-dynamic setting at Colle Gnifetti.

5. A borehole deformation measurement in the KCC borehole could provide important information on the dominating influence on deformation at this specific site, where short-scale fabric anisotropy variations are a common feature but dust load is higher than, e.g. the polar NEEM ice core where borehole closure is closely connected to dust content (pers. comm. Ilka Weikusat, 2016).

6. The results from the laser ablation pilot study need further evaluation. Most importantly, the measured sodium concentrations in grain boundaries should be compared with the annual-layer signal to infer if the interpretation of the climate signal could be affected. Also, repeated measurements with an improved surface preparation is envisaged.

7. The seismic data from Colle Gnifetti should be revisited, now having gained detailed crystal-orientation fabric data and with the ability to provide azimuth-sensitive estimates of seismic velocities. Especially for the furthering of shear-wave analysis additional azimuthal seismic data could be collected on CG. Similarly, the calculated velocities can be used for the calculation of reflection coefficients to assess the likelihood of seismic reflections by abrupt short-scale fabric changes.

8. On the methodological side, the matching of LASM and FA images for a combined fabric and grain topology analysis (Binder, 2014) should be pursued and facilitated. The estab-

lishment of an automatic layer classification based on the eigenvalue gradient or extrema could be a resulting challenge for future short-scale fabric analysis.

For future studies of (short-scale) fabric variations following recommendations are made:

- For polar cores and conventional fabric measurements in large intervals, it is highly recommended to always sample several adjacent thin sections, i.e. continuous bags, accompagnied with horizontal sections to better constrain azimuth uncertainties while oriented drilling is not yet feasible. This is absolutely necessary in order to obtain a more representative grain and fabric statistic for each depth. Also, more thin section data should be acquired from ice core archives that are available to revisit earlier analyses.

- The oriented drilling of an ice core would be an important step to reduce uncertainties in the interpretation of ice fabric measurements.

- The borehole deformation measurements are likely to provide solid evidence on mechanical weak layers and should be considered as complementary to fabric studies.

- For future laser ablation measurements, the surface should be (i) mirrored to the thin section surface (ii) microtomed before the laser ablation measurement to remove possible surface effects that could have developed during storage.

- The relevance of short-scale anisotropic fabric variations for the rheology of the glacier is substantially determined by the question whether these are localised features. The measurement of fabric from neighbouring cores, perhaps by applying borehole sonic logging, would provide new insights concerning the representativeness of fabric from ice cores for a larger region, possibly allowing for the identification and differentiation of regional and local components (hypothesis) in the fabric record of individual cores.

- Short-scale variations in fabric anisotropy should be implemented in anisotropic flow models under the two assumptions that (i) they are very localised (ii) they are laterally coherent in order to evaluate if a short-scale fabric implementation is changing the result as compared to a larger scale fabric description.

Last but not least, the perceptions of the present work highlight the absolute necessity to differentiate the scale of observations in crystal-orientation fabric variability.

Bibliography

Adams, E. E. and D. A. Miller (2003). "Ice crystals grown from vapor onto an orientated substrate: application to snow depth-hoar development and gas inclusions in lake ice". *J. Glaciol.* **49**(164), 8–12. DOI: 10.3189/172756503781830953 (cit. on p. 7).

Aki, K. and P. G. Richards (2002). *Quantitative seismology* (cit. on p. 84).

Alean, J., W. Haeberli, and B. Schädler (1983). "Snow accumulation, firn temperature and solar radiation in the area of the Colle Gnifetti core drilling site (Monte Rosa, Swiss Alps): distribution patterns and interrelationships". *Z. Gletscherkd. Glazialgeol.* **19**(2), 131–147 (cit. on p. 13).

Allen, C. et al. (1960). "Structure of the lower Blue glacier, Washington". *Journal of Geology*, 601–625 (cit. on p. 2).

Alley, R. B. and C. R. Bentley (1988). "Ice-core analysis on the Siple Coast of West Antarctica". *Ann. Glaciol.* **11**, 1–7 (cit. on p. 45).

Alley, R. B., J. H. Perepezko, and C. R. Bentley (1986). "Grain growth in polar ice". *J. Glaciol.* **32**(112), 415–424 (cit. on pp. 8, 75).

Alley, R. and J. Fitzpatrick (1999). "Conditions for bubble elongation in cold ice-sheet ice". *J. Glaciol.* **45**(149), 147–153 (cit. on p. 66).

Alley, R. and G. Woods (1996). "Impurity influence on normal grain growth in the GISP2 ice core, Greenland". *J. Glaciol.* **42**(141), 255–260. DOI: 10.3198/1996JoG42-141-255-260 (cit. on p. 9).

Alley, R. B. (1992). "Flow-law hypotheses for ice-sheet modeling". *J. Glaciol.* **38**(129), 245–256 (cit. on pp. 1, 6).

Anandakrishnan, S. et al. (1994). "Shear-wave detection of asymmetric c-axis fabrics in the GISP2 ice core, Greenland". *J. Glaciol.* **40**(136), 491–496. DOI: 10.3198/1994JoG40-136-491-496 (cit. on pp. 107, 109).

Azuma, N. and A. Higashi (1985). "Formation processes of ice fabric pattern in ice sheets". *Ann. Glaciol.* **6**, 130–134 (cit. on p. 1).

Azuma, N. et al. (1999). "Textures and fabrics in the Dome F (Antarctica) ice core". *Ann. Glaciol.* **29**(1), 163–168. DOI: 10.3189/172756499781821148 (cit. on pp. 2, 6).

Azuma, N. (1994). "A flow law for anisotropic ice and its application to ice sheets". *Earth Planet. Sci. Lett.* **128**, 601–614. DOI: 10.1016/0012-821X(94)90173-2 (cit. on pp. 1, 62).

Azuma, N. et al. (2012). "Impeding effect of air bubbles on normal grain growth of ice". *J. Struct. Geol.* **42**, 184–193. DOI: 10.1016/j.jsg.2012.05.005 (cit. on pp. 47, 65).

Bibliography

Baker, I., D. Cullen, and D. Iliescu (2003). "The microstructural location of impurities in ice". *Can. J. Phys.* **81**, 1–9. DOI: `10.1139/p03-030` (cit. on p. 9).

Barnes, P. and E. Wolff (2004). "Distribution of soluble impurities in cold glacial ice". *J. Glaciol.* **50**(170), 311–324. DOI: `10.3189/172756504781829918` (cit. on pp. 9, 33, 81).

Barnes, P. R. et al. (2002). "Observations of polar ice from the Holocene and the glacial period using the scanning electron microscope". *Ann. Glaciol.* **35**(1), 559–566 (cit. on p. 9).

Bendel, V. et al. (2013). "High-resolution variations in size, number and arrangement of air bubbles in the EPICA DML (Antarctica) ice core". *J. Glaciol.* **59**(217), 972–980. DOI: `10.3189/2013JoG12J245` (cit. on pp. 66, 113).

Bennett, H. F. (1968). "An investigation into velocity anisotropy through measurements of ultrasonica wave velocities in snow and ice cores from Greenland and Antarctica". PhD thesis. University of Wisconsin-Madison (cit. on pp. 2, 84).

Binder, T. et al. (2013). "Extraction and parametrization of grain boundary networks in glacier ice, using a dedicated method of automatic image analysis". *J. Microsc.* **250**, 130–141. DOI: `10.1111/jmi.12029` (cit. on p. 21).

Binder, T. (2014). "Measurements of grain boundary networks in deep polar ice cores – A digital image processing approach". PhD thesis. Universität Heidelberg. URL: `http://epic.awi.de/35578/` (cit. on pp. 20, 26, 113).

Blankenship, D. D. and C. R. Bentley (1987). "The crystalline fabric of polar ice sheets inferred from seismic anisotropy". *IAHS Publ.* **170**, 17–28 (cit. on p. 2).

Bohleber, P. (2008). "Age distribution and δ18O variability in a low accumulation Alpine ice core: perspective for paleoclimate studies". Diploma thesis. Heidelberg University (cit. on p. 3).

Bohleber, P. (2011). "Ground-penetrating radar assisted ice core research: The challenge of Alpine glaciers and dielectric ice properties". PhD thesis. Universität Heidelberg. URL: `http://epic.awi.de/25535/` (cit. on pp. 13, 15, 64).

Bohleber, P. et al. (2013). "To what extent do water isotope records from low accumulation Alpine ice cores reproduce instrumental temperature series?" *Tellus B* **65**, 1–17. DOI: `10.3402/tellusb.v65i0.20148` (cit. on pp. 13, 41, 69 sq.).

Burt, J. and G. Barber (1996). *Elementary statistics for geographers.* Guilford Press, New York (cit. on p. 30).

Church, J. et al. (2013). "Climate Change 2013: The Physical Science Basis. Contribution of Working Group I to the Fifth Assessment Report of the Intergovernmental Panel on Climate Change". Ed. by T. Stocker et al. Cambridge University Press, Cambridge, United Kingdom and New York, NY, USA. Chap. Sea Level Change (cit. on p. 1).

Cuffey, K. and W. Paterson (2010). *The Physics of Glaciers.* 4th edition. Academic Press (cit. on pp. 5–8).

Cullen, D. and I. Baker (2000). "The chemistry of grain boundaries in Greenland ice". *J. Glaciol.* **46**, 703–706 (cit. on p. 9).

Daley, P. and E. Krebes (2004). "Alternative linearized expressions for qP, qS1 and qS2 phase velocities in a weakly anisotropic orthorhombic medium". *CREWES Annual Report* **21**(21.19) (cit. on p. 88).

Dash, J. G., H. Fu, and J. S. Wettlaufer (1995). "The premelting of ice and its environmental consequences". *Rep. Prog. Phys.* **58**(115), 115–167. DOI: `10.1088/0034-4885/58/1/003` (cit. on p. 82).

Della Lunga, D. et al. (2014). "Location of cation impurities in NGRIP deep ice revealed by cryo-cell UV-laser-ablation ICPMS". *J. Glaciol.* **60**(223), 970–988. DOI: `10.3189/2014JoG13J199` (cit. on pp. 33, 81).

DiPrinzio, C. L. et al. (2005). "Fabric and texture at Siple Dome, Antarctica". *J. Glaciol.* **51**(173), 281–290. DOI: `10.3189/172756505781829359` (cit. on pp. 2, 6, 65, 80).

Diez, A. and O. Eisen (2015). "Seismic wave propagation in anisotropic ice – Part 1: Elasticity tensor and derived quantities from ice-core properties". *The Cryosphere* **9**, 367–384. DOI: `10.5194/tc-9-367-2015` (cit. on pp. 2, 4, 84 sq., 88, 92 sq., 100, 102, 106, 184).

Diez, A. et al. (2014). "Influence of ice crystal anisotropy on seismic velocity analysis". *Ann. Glaciol.* **55**(67), 97–106. DOI: `10.3189/2014AoG67A002` (cit. on pp. 3, 62, 87, 90, 94, 99 sq., 108).

Diez, A. et al. (2015). "Seismic wave propagation in anisotropic ice – Part 2: Effects of crystal anisotropy in geophysical data". *The Cryosphere* **9**, 385–398. DOI: `10.5194/tc-9-385-2015` (cit. on pp. 2, 84, 92, 107).

Diez, A. (2013). "Effects of cold glacier ice crystal anisotropy on seismic data". PhD thesis. Karlsruher Institut für Technologie. URL: `http://digbib.ubka.uni-karlsruhe.de/volltexte/1000037984` (cit. on pp. 88, 92, 99).

Diez, A. et al. (2013). "Joint interpretation of explosive- and vibro-seismic surveys on cold firn for the investigation of ice properties". *Ann. Glaciol.* **54**(64), 201–210. DOI: `10.3189/2013AoG64A200` (cit. on pp. 2, 109).

Drews, R. et al. (2009). "Layer disturbances and the radio-echo free zone in ice sheets". *The Cryosphere* **3**(2), 195–203 (cit. on p. 107).

Drews, R. et al. (2012). "Potential mechanisms for anisotropy in ice-penetrating radar data". *J. Glaciol.* **58**(209), 613–624. DOI: `10.3189/2012JoG11J114` (cit. on pp. 2, 107).

Durand, G. et al. (2006a). "Effect of impurities on grain growth in cold ice sheets". *J. Geophys. Res.* **111**, 1–18. DOI: `10.1029/2005JF000320` (cit. on pp. 9, 80).

Durand, G. et al. (2007). "Change in ice rheology during climate variations – implications for ice flow modelling and dating of the EPICA Dome C core". *Clim. Past* **3**, 155–167 (cit. on pp. 2, 69).

Durand, G. et al. (2009). "Evolution of the Texture along the EPICA Dome C Ice Core". *Low Temperature Science* **68**, 91–105 (cit. on p. 2).

Durand, G. et al. (2006b). "Ice microstructure and fabric: an up-to-date approach for measuring textures". *J. Glaciol.* **52**(179), 619–630. DOI: `10.3189/172756506781828377` (cit. on pp. 9, 11).

Duval, P., M. Ashby, and I. Anderman (1983). "Rate-controlling processes in the creep of polycrystalline ice". *J. Phys. Chem.* **87**(21), 4066–4074. DOI: `10.1021/j100244a014` (cit. on pp. 5, 7).

Eichler, J. (2013). "C-Axis analysis of the NEEM ice core – An approach based on digital image processing". Diploma thesis. Freie Universität Berlin and Alfred-Wegener-Institut Bremerhaven (cit. on pp. 9, 19 sq., 24 sq.).

Eisen, O. et al. (2003). "Alpine ice cores and ground penetrating radar: combined investigations for glaciological and climatic interpretations of a cold Alpine ice body". *Tellus B* **55**(5), 1007–1017 (cit. on pp. 15, 64).

Eisen, O. et al. (2007). "Direct evidence for continuous radar reflector originating from changes in crystal-orientation fabric". *The Cryosphere* **1**, 1–10 (cit. on pp. 2, 107).

Elvin, A. A. (1996). "Number of grains required to homogenize elastic properties of polycrystalline ice". *Mechanics of Materials* **22**, 51–64. DOI: `10.1016/0167-6636(95)00024-0` (cit. on p. 85).

Faria, S. H., D. Ktitarev, and K. Hutter (2002). "Modelling evolution of anisotropy in fabric and texture of polar ice". *Ann. Glaciol.* **35**(1), 545–551. DOI: `10.3189/172756402781817040` (cit. on p. 1).

Faria, S. H., J. Freitag, and S. Kipfstuhl (2010). "Polar ice structure and the integrity of ice-core paleoclimate records". *Quat. Sci. Rev.* **29**(1), 338–351. DOI: `10.1016/j.quascirev.2009.10.016` (cit. on pp. 9, 75, 82).

Faria, S. H., I. Weikusat, and N. Azuma (2014). "The microstructure of polar ice. Part II: State of the art". *J. Struct. Geol.* **61**. Microdynamics of Ice, 21–49. DOI: `10.1016/j.jsg.2013.11.003`. URL: `http://www.sciencedirect.com/science/article/pii/S0191814113002009` (cit. on pp. 1, 6–8, 41, 62).

Fischer, H. et al. (2007). "Glacial/interglacial changes in mineral dust and sea-salt records in polar ice cores: Sources, transport, and deposition". *Rev. Geophys.* **45**(1). DOI: `10.1029/2005RG000192` (cit. on pp. 33, 69).

Fitzpatrick, J. J. et al. (2014). "Physical properties of the WAIS Divide ice core". *J. Glaciol.* **60**(224), 1181–1198. DOI: `10.3189/2014JoG14J100` (cit. on pp. 2, 6, 80 sq.).

Freitag, J. et al. (2013). "Impurity-controlled densification: a new model for stratified polar firn". *J. Glaciol.* **59**(218), 1163–1169. DOI: `10.3189/2013JoG13J042` (cit. on p. 6).

Freitag, J., F. Wilhelms, and S. Kipfstuhl (2004). "Microstructure-dependent densification of polar firn derived from X-ray microtomography". *J. Glaciol.* **50**(169), 243–250. DOI: `10.3189/172756504781830123` (cit. on p. 16).

Fujita, S. et al. (2009). "Metamorphism of stratified firn at Dome Fuji, Antarctica: A mechanism for local insolation modulation of gas transport conditions during bubble close off". *J. Geophys. Res.* **114**(F3). F03023. DOI: 10.1029/2008JF001143 (cit. on p. 7).

Gagliardini, O., G. Durand, and Y. Wang (2004). "Grain area as a statistical weight for polycrystal constituents". *J. Glaciol.* **50**(168), 87–95. DOI: 10.3189/172756504781830349 (cit. on p. 10).

Gagliardini, O. and J. Meyssonnier (1996). "Flow simulation of a firn-covered cold glacier". *Ann. Glaciol.* **24**, 242–248 (cit. on p. 62).

Gagliardini, O., F. Gillel-Chaulet, and M. Montagnat (2009). "A review of anisotropic polar ice models: from crystal to ice-sheet flow models". *Low Temperature Science* **68**(Supplement), 149–166 (cit. on p. 1).

Gammon, P. et al. (1983). "Elastic constants of artificial and natural ice samples by Brillouin spectroscopy". *J. Glaciol.* **29**, 433–460 (cit. on pp. 84, 86).

Gillet-Chaulet, F. et al. (2005). "A user-friendly anisotropic flow law for ice-sheet modelling". *J. Glaciol.* **51**(172), 3–14. DOI: 10.3189/172756505781829584 (cit. on pp. 1, 62).

Gkinis, V. et al. (2011). "Water isotopic ratios from a continuously melted ice core sample". *Atmos. Meas. Tech.* **4**(11), 2531–2542. DOI: 10.5194/amt-4-2531-2011 (cit. on p. 32).

Glen, J. W. (1955). "The Creep of Polycrystalline Ice". *Proc. Phys. Soc. London, Sect. A: Mathematical, Physical and Engineering Sciences* **228**(1175), 519–538. DOI: 10.1098/rspa.1955.0066 (cit. on p. 7).

Gold, L. W. (1958). "Some observations on the dependence of strain on stress for ice". *Can. J. Phys.* **36**(10), 1265–1275. DOI: 10.1139/p58-131 (cit. on p. 85).

Goldsby, D. and D. Kohlstedt (2001). "Superplastic deformation of ice: Experimental observations". *J. Geophys. Res.* **106**(B6), 11017–11030. DOI: 10.1029/2000JB900336 (cit. on p. 7).

Gow, A. J. and D. A. Meese (2007). "Physical properties, crystalline textures and c-axis fabrics of the Siple Dome (Antarctica) ice core". *J. Glaciol.* **53**(183), 573–584. DOI: 10.3189/002214307784409252 (cit. on pp. 2, 62, 80).

Gow, A. J. and T. Williamson (1976). "Rheological implications of the internal structure and crystal fabrics of the West Antarctic ice sheet as revealed by deep core drilling at Byrd Station". *Geol. Soc. Am. Bull.* **87**(12), 1665–1677 (cit. on pp. 1 sq., 6, 80).

Gusmeroli, A. et al. (2012). "The crystal fabric of ice from full-waveform borehole sonic logging". *J. Geophys. Res.* **117**, 1–13. DOI: 10.1029/2012JF002343 (cit. on pp. 2, 107).

Haeberli, W. and J. Alean (1985). "Temperature and accumulation of high altitude firn in the Alps". *Ann. Glaciol.* **6**, 161–163 (cit. on p. 13).

Haeberli, W. and M. Funk (1991). "Borehole temperatures at the Colle Gnifetti core-drilling site (Monte Rosa, Swiss Alps)". *J. Glaciol.* **37**(125), 37–46. DOI: 10.3198/1991JoG37-125-37-46 (cit. on p. 13).

Bibliography

Hambrey, M. J., A. G. Milnes, and H. Siegenthaler (1980). "Dynamics and structure of Griesgletscher, Switzerland". *J. Glaciol.* **25**(92), 215–228. DOI: 10.3198/1980JoG25-92-215-228 (cit. on p. 2).

Hambrey, M. and F. Müller (1978). "Structures and ice deformation in the white glacier, Axel Heiberg Island, Northwest Territories, Canada". *J. Glaciol.* **20**(82), 41–66 (cit. on p. 2).

Helgerud, M. B. et al. (2009). "Elastic wave speeds and moduli in polycrystalline ice Ih, sI methane hydrate, and sII methane-ethane hydrate". *J. Geophys. Res.* **114**(B2). B02212. DOI: 10.1029/2008JB006132 (cit. on p. 85).

Hill, R. (1952). "The Elastic Behaviour of a Crystalline Aggregate". *Proc. Phys. Soc. London, Sect. A* **65**(5), 349. DOI: 10.1088/0370-1298/65/5/307 (cit. on p. 85).

Hoelzle, M. et al. (2011). "Evidence of accelerated englacial warming in the Monte Rosa area, Switzerland/Italy". *The Cryosphere* **5**(1), 231–243. DOI: 10.5194/tc-5-231-2011 (cit. on p. 13).

Hoffmann, H. (2016). "Micro radiocarbon dating of the particulate organic carbon fraction in Alpine glacier ice: method refinement, critical evaluation and dating applications". PhD thesis. Universität Heidelberg (cit. on p. 3).

Hofstede, C. et al. (2013). "Investigating englacial reflections with vibro- and explosive-seismics surveys at Halvfarryggen ice dome, Antarctica". *Ann. Glaciol.* **54**, 189–200. DOI: 10.3189/2013AoG64A064 (cit. on p. 107).

Hondoh, T. (2000). "Physics of ice core records". Ed. by T. Hondoh. Hokkaido University Press. Chap. Nature and behavior of dislocations in ice, 3–24 (cit. on p. 7).

Horgan, H. J. et al. (2008). "Complex fabric development revealed by englacial seismic reflectivity: Jakobshavn Isbræ, Greenland". *Geophys. Res. Lett.* **35**, 1–6. DOI: 10.1029/2008GL033712 (cit. on pp. 2, 109).

Horgan, H. J. et al. (2011). "Englacial seismic reflectivity: imaging crystal-orientation fabric in West Antarctica". *J. Glaciol.* **57**(204), 639–650. DOI: 10.3189/002214311797409686 (cit. on pp. 2, 107).

Horn, M. (2010). "Ein Linescanner zur Erfassung von Korngrößenparametern: Entwicklung, Aufbau und Anwendung". Diploma thesis. Universität Bremen (cit. on pp. 19 sq., 45).

Hörhold, M. et al. (2012). "On the impact of impurities on the densification of polar firn". *Earth Planet. Sci. Lett.* **325–326**, 93–99. DOI: 10.1016/j.epsl.2011.12.022 (cit. on p. 113).

Iliescu, D. and I. Baker (2008). "Effects of impurities and their redistribution during recrystallization of ice crystals". *J. Glaciol.* **54**(185), 362–370 (cit. on pp. 9, 75).

Jacka, T. H. (1984). "Laboratory studies on relationships between ice crystal size and flow rate". *Cold Reg. Sci. Technol.* **10**(1), 31–42. DOI: 10.1016/0165-232X(84)90031-4 (cit. on p. 1).

Jacka, T. H. and L. Jun (2000). "Physics of Ice Core Records". Ed. by T. Hondoh. Hokkaido University Press. Chap. Flow rates and crystal orientation fabrics in compression of polycrystalline ice at low temperature and stresses, 83–102 (cit. on p. 1).

Jansen, D. et al. (2016). "Small-scale disturbances in the stratigraphy of the NEEM ice core: observations and numerical model simulations". *The Cryosphere* **10**, 359–370. DOI: 10.5194/tc-10-359-2016 (cit. on p. 66).

Jenk, T. M. et al. (2009). "A novel radiocarbon dating technique applied to an ice core from the Alps indicating late Pleistocene ages". *J. Geophys. Res.* **114**(D14) (cit. on p. 3).

Jona, V. F. and P. Scherrer (1952). "Die elastischen Konstanten von Eis-Einkristallen". *Helvetica Physica Acta* **25**(1–2), 33–54 (cit. on p. 84).

Kaufmann, P. R. et al. (2008). "An Improved Continuous Flow Analysis System for High-Resolution Field Measurements on Ice Cores". *Environ. Sci. Technol.* **42**, 8044–8040. DOI: 10.1021/es8007722 (cit. on p. 32).

Kennedy, J. H., E. C. Pettit, and C. L. DiPrinzio (2013). "The evolution of crystal fabric in ice sheets and its link to climate history". *J. Glaciol.* **59**(214), 357–373. DOI: 10.3189/2013JoG12J159 (cit. on p. 7).

Kipfstuhl, S. et al. (2006). "Microstructure mapping: a new method for imaging deformation-induced microstructural features of ice on the grain scale." *J. Glaciol.* **52**(178), 398–406. DOI: 10.3189/172756506781828647 (cit. on p. 20).

Kipfstuhl, S. et al. (2009). "Evidence of dynamic recrystallization in polar firn". *J. Geophys. Res.* **114**, 1–10. DOI: 10.1029/2008JB005583 (cit. on pp. 8, 21, 47, 63).

Kleitz, I. (2013). "Physikalische Eigenschaften und Spurenstoffe im grönländischen Eis – Korrelationsberechnungen zwischen Korngröße bzw. Eigenwert und Spurenstoffkonzentrationen an ausgewählten Stücken des NEEM-Eiskerns". Bachelor thesis. Universität Greifswald and Alfred-Wegener-Institut Bremerhaven (cit. on pp. 62, 80).

Kleitz, I. (2015). "Analysis of physical properties and impurities in Greenland ice using optical and Raman microscopy". Master thesis. Martin-Luther Universität Halle-Wittenberg, Alfred-Wegener-Institut Helmholtz-Zentrum für Polar- und Meeresforschung (cit. on pp. 30, 62).

Kohnen, H. (1972). "Über die Beziehung zwischen seismischen Geschwindigkeiten und der Dichte in Firn und Eis". *Z. Geophys.* **38**(5), 925–935 (cit. on p. 86).

Kohnen, H. (1974). "The temperature dependence of seismic waves in ice". *J. Glaciol.* **13**(67), 144–147 (cit. on p. 86).

Konrad, H. et al. (2013). "Determining the age distribution of Colle Gnifetti, Monte Rosa, Swiss Alps, by combining ice cores, ground-penetrating radar and a simple flow model". *J. Glaciol.* **59**(213), 179–189. DOI: 10.3189/2013JoG12J072 (cit. on pp. 15, 64).

Lipenkov, V. Y. (2000). "Physics of Ice Core Records". Ed. by T. Hondoh. Hokkaido University Press. Chap. Air bubbles and air-hydrate crystals in the Vostok ice core, 327–358 (cit. on pp. 51, 66).

Llorens, M.-G. et al. (2016a). "Dynamic recrystallisation of ice aggregates during co-axial viscoplastic deformation: a numerical approach". *J. Glaciol.* **62**(232), 359–377. DOI: 10.1017/jog.2016.28 (cit. on pp. 7 sq., 47, 63).

Bibliography

Llorens, M.-G. et al. (2016b). "Full-field predictions of ice dynamic recrystallisation under simple shear conditions". *Earth Planet. Sci. Lett.* **450**, 233 –242. DOI: 10.1016/j.epsl.2016.06.045 (cit. on pp. 1, 7 sq., 64).

Lüthi, M. and M. Funk (2000). "Dating ice cores from a high Alpine glacier with a flow model for cold firn". *Ann. Glaciol.* **31**, 69–79. DOI: 10.3189/172756400781820381 (cit. on p. 13).

Mainprice, D., R. Hielscher, and H. Schaeben (2011). "Calculating anisotropic physical properties from texture data using the MTEX open-source package". *Geological Society, London, Special Publications* **360**, 175–192. DOI: 10.1144/SP360.10 (cit. on p. 85).

Martin, C. et al. (2009). "On the effects of anisotropic rheology on ice flow, internal structure, and the age-depth relationship at ice divides". *J. Geophys. Res.* **114**, 1–18. DOI: 10.1029/2008JF001204 (cit. on p. 1).

Maurel, A., F. Lund, and M. Montagnat (2015). "Propagation of elastic waves through textured polycrystals: application to ice". *Proc. Roy. Soc. London, Ser. A* **471**(2177). DOI: 10.1098/rspa.2014.0988 (cit. on pp. 85, 89, 107, 184).

Montagnat, M. et al. (2012). "Measurements and numerical simulation of fabric evolution along the Talos Dome ice core, Antarctica". *Earth Planet. Sci. Lett.* **357**, 168–178. DOI: 10.1016/j.epsl.2012.09.025 (cit. on p. 2).

Montagnat, M. et al. (2013). "Multiscale modeling of ice deformation behavior". *J. Struct. Geol.* **61**, 78–108. DOI: 10.1016/j.jsg.2013.05.002 (cit. on p. 1).

Montagnat, M. et al. (2014). "Fabric along the NEEM ice core, Greenland, and its comparison with GRIP and NGRIP ice cores". *The Cryosphere* **8**(4), 1129–1138. DOI: 10.5194/tc-8-1129-2014 (cit. on p. 2).

Mudelsee, M. (2003). "Estimating Pearson's Correlation Coefficient with Bootstrap Confidence Interval from Serially Dependent Time Series". *Mathematical Geology* **35**(6), 651–665. DOI: 10.1023/B:MATG.0000002982.52104.02 (cit. on p. 31).

Mulvaney, R., E. W. Wolff, and K. Oates (1988). "Sulphuric acid at grain boundaries in Antarctic ice". *Nature* **331**(6153), 247–249 (cit. on p. 9).

Müller, W., J. M. G. Shelley, and S. O. Rasmussen (2011). "Direct chemical analysis of frozen ice cores by UV-laser ablation ICPMS". *J. Anal. At. Spectrom.* **26**, 2391–2395. DOI: 10.1039/c1ja10242g (cit. on p. 33).

Nanthikesan, S. and S. S. Sunder (1994). "Anisotropic elasticity of polycrystalline ice Ih". *Cold Reg. Sci. Technol.* **22**(2), 149–169. DOI: 10.1016/0165-232X(94)90026-4 (cit. on p. 85).

Ohno, H., M. Igarashi, and T. Hondoh (2005). "Salt inclusions in polar ice core: Location and chemical form of water-soluble impurities". *Earth Planet. Sci. Lett.* **232**, 171–178. DOI: 10.1016/j.epsl.2005.01.001 (cit. on p. 81).

Paterson, W. S. B. (1991). "Why ice-age ice is sometimes soft". *Cold Reg. Sci. Technol.* **20**, 75–98. DOI: 10.1016/0165-232X(91)90058-O (cit. on pp. 2, 9).

Peternell, M. et al. (2009). "A new approach to crystallographic orientation measurement for apatite fission track analysis: Effects of crystal morphology and implications for automation". *Chem. Geol.* **265**, 527–539. DOI: `10.1016/j.chemgeo.2009.05.021` (cit. on pp. 6, 19).

Petrenko, V. F. and R. W. Whitworth (1999). *Physics of ice.* Oxford University Press (cit. on pp. 5–7).

Pettit, E. C. et al. (2007). "The role of crystal fabric in flow near an ice divide". *J. Glaciol.* **53**(181), 277–288. DOI: `10.3189/172756507782202766` (cit. on p. 1).

Picotti, S. et al. (2015). "Anisotropy and crystalline fabric of Whillans Ice Stream (West Antarctica) inferred from multicomponent seismic data". *J. Geophys. Res.* **120**(6), 4237–4262. DOI: `10.1002/2014JB011591` (cit. on p. 107).

Pinzer, B. R., M. Schneebeli, and T. U. Kaempfer (2012). "Vapor flux and recrystallization during dry snow metamorphism under a steady temperature gradient as observed by time-lapse micro-tomography". *The Cryosphere* **6**, 1141–1155. DOI: `10.5194/tc-6-1141-2012` (cit. on p. 7).

Polom, U. et al. (2014). "First glacier-vibroseismic experiment – results from cold firn of Colle Gnifetti". *Near Surf. Geophys.* **12**, 493–504. DOI: `10.3997/1873-0604.2013059` (cit. on pp. 3, 99, 109).

Rau, S. (2008). "Stratigraphische Untersuchungen an einem tiefen Eisbohrkern der alpinen Miniatureiskappe Vadret dal Corvatsch". Diploma thesis. Universität Heidelberg (cit. on p. 39).

Rempel, A. W. et al. (2001). "Possible displacement of the climate signal in ancient ice by premelting and anomalous diffusion". *Nature* **411**, 568–571. DOI: `10.1038/35079043` (cit. on p. 82).

Reuss, A. (1929). "Berechnung der Fließgrenze von Mischkristallen auf Grund der Plastizitätsbedingung für Einkristalle". *Z. Angew. Math. Mech.* **9** (cit. on p. 85).

Riche, F., M. Montagnat, and M. Schneebeli (2013). "Evolution of crystal Orientation in snow during temperature gradient metamorphism". *J. Glaciol.* **59**(213), 47–55. DOI: `10.3189/2013JoG12J116` (cit. on p. 7).

Röthlisberger, R. (2000). "Technique for continuous high-resolution analysis of trace substances in firn and ice cores". *Environ. Sci. Technol.* **34**, 338–342. DOI: `10.1021/es9907055` (cit. on p. 32).

Samyn, D. et al. (2005). "Ice crystal properties of amber ice and strain enhancement at the base of cold Antarctic glaciers". *Ann. Glaciol.* **40**, 185–190 (cit. on pp. 2, 66).

Schulson, E. M. and P. Duval (2009). *Creep and fracture of ice.* Cambridge University Press Cambridge (cit. on pp. 1, 7, 9).

Seddik, H. et al. (2008). "Application of a continuum-mechanical model for the flow of anisotropic polar ice to the EDML core, Antarctica". *J. Glaciol.* **54**(187), 631–642. DOI: `10.3189/002214308786570755` (cit. on p. 1).

Sneed, S. B. et al. (2015). "New LA-ICP-MS cryocell and calibration technique for sub-millimeter analysis of ice cores". *J. Glaciol.* **61**(226), 233–242. DOI: 10.3189/2015JoG14J139 (cit. on pp. 33, 82).

Song, M., I. Baker, and D. M. Cole (2008). "The effect of particles on creep rate and microstructures of granular ice". *J. Glaciol.* **54**(186), 533–537. DOI: 10.3189/002214308785836959 (cit. on pp. 2, 9).

Steinbach, F. et al. (in review). "Strain localisation and dynamic recrystallisation in the ice-air aggregate: A numerical study". *The Cryosphere Discuss.* DOI: 10.5194/tc-2016-167 (cit. on pp. 8, 113).

Sunder, S. S. and M. S. Wu (1990). "Crack nucleation due to elastic anisotropy in polycrystalline ice". *Cold Reg. Sci. Technol.* **18**, 29–47. DOI: 10.1016/0165-232X(90)90036-V (cit. on p. 184).

Svensson, A. et al. (2003). "Properties of ice crystals in NorthGRIP late- to middle-Holocene ice". *Ann. Glaciol.* **37**, 113–118 (cit. on p. 2).

Svensson, A. et al. (2005). "Visual stratigraphy of the North Greenland Ice Core Project (North-GRIP) ice core during the last glacial period". *J. Geophys. Res.* **110**(D2). DOI: 10.1029/2004JD005134 (cit. on p. 21).

Thorsteinsson, T. (1996). "Textures and fabric in the GRIP ice core, in relation to climate history and ice deformation". PhD thesis. Universität Bremen (cit. on pp. 2, 80, 113).

Thorsteinsson, T., J. Kipfstuhl, and H. Miller (1997). "Textures and fabrics in the GRIP ice core". *J. Geophys. Res.* **102**(C12), 26583–26599. DOI: 10.1029/97JC00161 (cit. on p. 2).

Thorsteinsson, T. (2002). "Fabric development with nearest-neighbor interaction and dynamic recrystallization". *J. Geophys. Res.* **107**(B1). DOI: 10.1029/2001JB000244 (cit. on p. 1).

Tison, J.-L. and B. Hubbard (2000). "Ice crystallographic evolution at a temperate glacier: Glacier de Tsanfleuron, Switzerland". *Geological Society, London, Special Publications* **176**, 23–38. DOI: 10.1144/GSL.SP.2000.176.01.03 (cit. on p. 2).

Tomadin, L., D. Wagenbach, and V. Landuzzi (1996). "Mineralogy and source of high altitude glacial deposits in the western Alps: clay minerals as Saharan dust tracers". *The Impact of Desert Dust Across the Mediterranean.* Springer, 223–232 (cit. on p. 33).

Treverrow, A. et al. (2012). "The tertiary creep of polycrystalline ice: experimental evidence for stress-dependent levels of strain-rate enhancement". *J. Glaciol.* **58**(208), 301–314. DOI: 10.3189/2012JoG11J149 (cit. on p. 1).

Treverrow, A. et al. (2015). "Modelled stress distributions at the Dome Summit South borehole, Law Dome, East Antarctica: a comparison of anisotropic ice flow relations". *J. Glaciol.* **61**(229), 987–1004. DOI: doi:10.3189/2015JoG14J198 (cit. on p. 1).

Treverrow, A., L. Jun, and T. H. Jacka (2016). "Ice crystal c-axis orientation and mean grain size measurements from the Dome Summit South ice core, Law Dome, East Antarctica". *Earth Syst. Sci. Data* **8**(1), 253–263. DOI: 10.5194/essd-8-253-2016 (cit. on p. 2).

Tsvankin, I. (2001). *Seismic signatures and analysis of reflection data in anisotropic media.* Ed. by K. Helbig and S. Treitel. Pergamon (cit. on pp. 83, 87 sq., 90).

Vallon, M., J. Petit, and B. Fabre (1976). "Study of an ice core to the bedrock in the accumulation zone of an alpine glacier". *J. Glaciol.* **17**, 13–28 (cit. on p. 2).

Voigt, W (1910). *Lehrbuch der Kristallphysik: mit Ausschluss der Kristalloptik* (cit. on pp. 84 sq.).

Von Mises, R. (1928). "Mechanik der plastischen Formänderung von Kristallen". *ZAMM – Journal of Applied Mathematics and Mechanics/Zeitschrift für Angewandte Mathematik und Mechanik* **8**(3), 161–185. DOI: 10.1002/zamm.19280080302 (cit. on p. 7).

Wagenbach, D. and K. Geis (1989). "The Mineral Dust Record in a High Altitude Alpine Glacier (Colle Gnifetti, Swiss Alps)". *Paleoclimatology and Paleometeorology: Modern and Past Patterns of Global Atmospheric Transport.* Ed. by M. Leinen and M. Sarnthein. Springer Netherlands, 543–564. DOI: 10.1007/978-94-009-0995-3_23 (cit. on pp. 3, 13).

Wagenbach, D., P. Bohleber, and S. Preunkert (2012). "Cold, Alpine ice bodies revisited: What may we learn from their impurity and isotope content?" *Geografiska Annaler: Series A, Physical Geography* **94**(2), 245–263. DOI: 10.1111/j.1468-0459.2012.00461.x (cit. on pp. 3, 13, 64, 66).

Wang, Y. et al. (2003). "Ice-fabrics study in the upper 1500 m of the Dome C (East Antarctica) deep ice core". *Ann. Glaciol.* **37**(1), 97–104. DOI: 10.3189/172756403781816031 (cit. on p. 2).

Weikusat, I., S. Kipfstuhl, and A. Lambrecht (2013a). *Crystal c-axes (fabric G20) of ice core samples collected from the EDML ice core with links to raw data files.* Alfred Wegener Institute, Helmholtz Center for Polar and Marine Research, Bremerhaven. DOI: 10.1594/PANGAEA.807207 (cit. on p. 18).

Weikusat, I., S. Kipfstuhl, and A. Lambrecht (2013b). *Crystal c-axes (fabric G50) of ice core samples collected from the EDML ice core with links to raw data files.* Alfred Wegener Institute, Helmholtz Center for Polar and Marine Research, Bremerhaven. DOI: 10.1594/PANGAEA.807206 (cit. on p. 18).

Weikusat, I. et al. (in press). "From Microdynamics towards Macrodynamics of polar ice – A deformation analysis of an Antarctic ice core (EDML)". *Phil. Trans. R. Soc. A - Special Theme Issue MicroDICE (invited)* (cit. on pp. 2, 18 sq., 75, 94 sq.).

Weikusat, I. et al. (2009). "Subgrain boundaries and related microstructural features in EDML (Antarctica) deep ice core". *J. Glaciol.* **55**(191), 461–472. DOI: doi:10.3189/002214309788816614 (cit. on pp. 8, 63, 65).

Weikusat, I., A. Lambrecht, and S. Kipfstuhl (2013c). *Eigenvalues of crystal orientation tensors for c-axes distributions of horizontal thin sections from the EDML ice core.* DOI: 10.1594/PANGAEA.807141 (cit. on p. 92).

Weikusat, I., A. Lambrecht, and S. Kipfstuhl (2013d). *Eigenvalues of crystal orientation tensors for c-axes distributions of vertical thin sections from the EDML ice core.* DOI: 10.1594/PANGAEA.807142 (cit. on p. 92).

Weiss, J. et al. (2002). "Dome Concordia ice microstructure: impurities effect on grain growth". *Ann. Glaciol.* **35**(1), 552–558. DOI: 10.3189/172756402781816573 (cit. on pp. 2, 9).

Wilson, C. J. L., D. S. Russell-Head, and H. M. Sim (2003). "The application of an automated fabric analyzer system to the textural evolution of folded ice layers in shear zones". *Ann. Glaciol.* **37**, 7–17. DOI: 10.3189/172756403781815401 (cit. on pp. 6, 18).

Woodcock, N. H. (1977). "Specification of fabric shapes using an eigenvalue method". *Geol. Soc. Am. Bull.* **88**, 1231–1236 (cit. on p. 11).

List of Symbols

α	FA tile rotation angle
γ	Misorientation
κ	Woodcock parameter
$\lambda_{1,2,3}$	2nd-order orientation tensor eigenvalues (with $\lambda_1 \leq \lambda_2 \leq \lambda_3$)
ϕ	cone angle
ψ	phase angle (incidence angle of a seismic wave in the seismic plane), counted from vertical
φ	c-axis colatitude angle (counted from vertical to horizontal)
$\rho_{(\text{ice})}$	density (of ice)
σ_{mn}	stress tensor
Γ	temperature
Γ_{m}	measured temperature
τ_{op}	strain tensor
ϑ	c-axis azimuth angle (counted counterclockwise from east)
ϑ_{s}	azimuth angle of seismic plane (relative to oriented ice core)
$\bar{A}$	mean grain size (area)
$\tilde{A}$	median grain size (area)
A	grain size (area)
A_{B}	bubble area
a_{ij}	2nd-order orientation tensor
AR	bubble aspect ratio
$\mathbf{C}^{\text{t}}_{\text{m},n}$	elasticity tensor of n-th grain after coordinate transformation to global reference frame $\{x, y, z\}$
$\mathbf{C}^{\text{V,R}}$	elasticity tensor calculated following Voigt or Reuss assumption (Voigt if not indicated)
$\mathbf{C}_{\text{m}}$	elasticity tensor of monocrystal
$\mathbf{C}_{\text{p}}$	elasticity tensor of polycrystal
$\boldsymbol{c}$	c-axis orientation vector
C_{B}	bubble circularity
C_{ij}	elasticity tensor in Voigt notation (2nd-order tensor)
c_{mnop}	elasticity tensor (4th-order tensor)
d	depth
ℓ	Grain boundary linearity
$\boldsymbol{n}$	wave vector
n	grain number index per sample
N_{b}	number of air bubbles
N_{g}	number of grains
S_{ij}	compliance tensor in Voigt notation

s_{mnop}	compliance tensor
T_0	zero-offset TWT for multiple layers
t_0	zero-offset interval TWT
v, v^{cx}	seismic interval velocity calculated via c-axes method
v^{ev}	seismic interval velocity calculated via eigenvalue method
$v^{\mathrm{V,R}}$	seismic interval velocity calculated from $C^{\mathrm{V,R}}$ (Voigt if not indicated)
$v^{\vartheta_{\mathrm{s}}}$	seismic interval velocity for seismic plane azimuth angle ϑ_{s}
v_0	seismic zero-offset interval velocity
$v_{\mathrm{p,sh,sv}}$	seismic interval phase velocity for P-, SH-, SV-wave
v_{rms}	seismic root mean square velocity
v_{ψ}	seismic interval velocity for phase angle ψ
p, q, r	local cartesian coordinate system of single crystal with $r \parallel \boldsymbol{c}$
x, y, z	global cartesian coordinate system (x: east, y: north, z: up)

AWI	Alfred-Wegener-Institut Helmholtz-Zentrum für Meeres- und Polarforschung
CCI	Climate Change Institute (University of Maine)
CFA	Continuous-Flow Analysis
CG	Colle Gnifetti
COF	Crystal-Orientation Fabric
CPO	Crystal-Preferred Orientation (cf. COF)
DRX	Dynamic Recrystallisation
EDML	EPICA Dronning Maud Land ice core
EPICA	European Project for Ice Coring in Antarctica
FA	Fabric Analyser G50
FIT	Firn-Ice-Transition
GB	grain Boundary
GBS	Grain Boundary Sliding
GPR	Ground-Penetrating Radar
IUP	Institute of Environmental Physics (University of Heidelberg)
KUP	Institute of Physics, Climate and Environmental Physics (University of Bern)
LA-ICP-MS	Laser Ablation-Inductively Coupled Plasma-Mass Spectrometry (LA)
LASM	Large Area Scan Macroscope
LPO	Lattice-Preferred Orientation
LS	Line Scan
P-wave	compressional wave
PP	Physical Properties
RMS	Root Mean Square
S-wave	shear wave
SH-wave	horizontal shear wave
subGB	Subgrain Boundary
SV-wave	vertical shear wave
TWT	Two-Way Traveltime
VSM	Vertical Single Maximum
VTI	Vertical Transversely Isotropic
X2D	2D images from microtomography (μCT)

List of Figures

List of Tables

Appendix

A. Glossary

Tab. A.1: Short glossary with recurring terms as used in this thesis (see also p. 128 for symbol definitions and abbreviations).

Term	Explanation	Synonyms/ Abbrev.
Crystal-orientation fabric	orientation distribution of a grain ensemble providing anisotropy information of the polycrystal; the terms crystal-preferred and lattice-preferred orientation are preferentially used by other authors	fabric, COF
Microstructure	Grain boundary network, grain topology and enclosed bubbles	μS
Thin section (max. 10 cm)	prepared ice sample for fabric analysis, either horizontal or vertical cut	section, sample, cut
Run	Piece of ice core drilled as a whole (number independent of depth), used for KCC	
Range	Ice core interval made up of one or more consecutive runs, used for KCC	
Bag	One metre of drilled ice core, number matches depth (+ 1), used for EDML	
Marker depth scale	Depth scale based on markers on each aliquot at the last full 10 cm	
Thin section top depth scale	Depth scale for the alignment of thin section data based on marker depth scale	
New top depth scale	Depth scale for the alignment of whole runs, derived from ^{14}C markers and ^{14}C aliquot length (new compared to initial top depth scale from the core processing), used for X2D and line scan	

B. Fabric and microstructure

B.1 Fabric analyser and LASM measurement routine

The laboratory routine that was applied for this study is described in form of a tutorial, documenting the procedure step by step.

Tutorial for the preparation of thick and thin sections for physical properties measurements

Read each paragraph entirely before starting to follow the instructions!
Some instructions are based on individually developed techniques that can be altered.

Preparation and safety remarks

For preparing thin sections it is necessary to spend several hours in the ice laboratory at about -18° C. Bring your own scarf or fleece buff, wool or fleece hats and two pairs of gloves (thin and thick, both preferentially without the tendency to easily lose fluffs), warm jumper and socks. Down trousers and coats as well as boots are provided. If you have to stand still for a longer period, stand on a piece of styrofoam to insulate your boots from the metal floor. Keep the second pair of gloves in the warm notebook cabinet and you can change gloves once your finger tips start going numb.
Don't spend time in the lab alone or without having someone knowing you're in the lab who is checking on you regularly!
If you start to lose the feeling in finger tips, toes, nose – leave the lab and take a warming up break! The longer you wait the longer it takes to recover!

Logging and cutting

Physical properties ice core pieces must be measured and lengths/irregularities carefully logged (use protocol template sheet if offered) – once the ice is cut there's no other way to reconstruct the structure.
Don't change the work flow, i.e. always have the top point in the same direction (here: top to the right before cutting).
In the example total length is measured, cut positions determined and marked with pencil and difference from chalk marker on the ice to next cut position is noted.
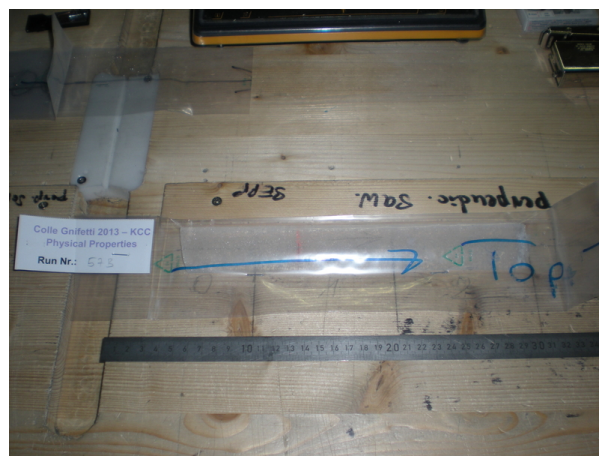
Samples shouldn't exceed 10 cm. Every section must be marked with a top arrow and the number of the section before cutting!

Usually counting starts at zero for there are 10 sections in each 1 m bag or run. For a straight cut and for minimizing the risk of injuries the ice is pushed towards the saw with a rectangular wooden board.

Beforehand polythene bags sealed on one side should be prepared with top arrow, run and section number for the storage of the left over ice. Top usually points towards the seal. Once the sections are cut, the bag is taken with the sample to each station in the preparation process.
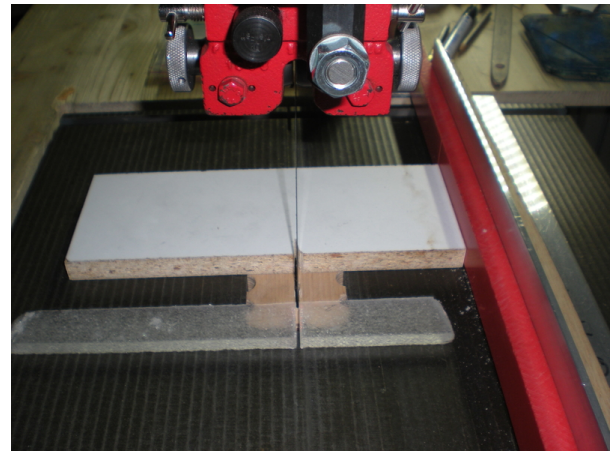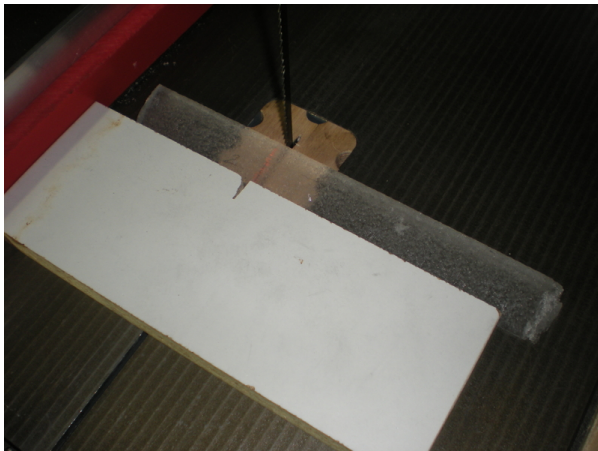
Microtoming the thick section

The microtom consists of a sledge with a glass stage on which the sample is fixed. The sledge is pushed to the back beneath an extremly sharp and delicate blade. With each successive push the stage is raised by turning a micrometer dial. When the sledge is pulled to the front, lower the stage again a tiny bit to avoid damage to the blade.

The blades are easily damaged and need to be first displaced and then replaced regularly (new ones are kept in the warm notebook cabinet) with the help of two pencil stumps – observe at least once before doing it yourself!

First a glass slide needs to be fixed at the stage by means of waterdrops. The small dropper bottles need to be kept from freezing, i.e. in the cabinet, and, while in use, in one of the down coat pockets. The opening should be very small and the water is best used when it's cooled down a bit, i.e. with higher viscosity. Push the slide from the side onto the stage, so that there's no space between them. Align the slide to the side of the stage. Have a drop run from the corner of the slide to the stage and, after a moment, suck the remaining water back into the bottle. Fix the diagonally opposite corner of the slide.
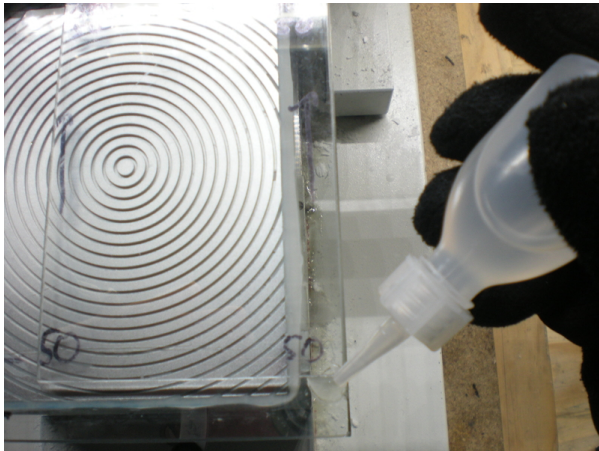
For the LASM recording a black background is needed which is provided by pieces of black cloth. Find or prepare a piece that fits the length of the sample, it should be just as long or a tiny bit longer. Align the sample on top of the cloth parallel to the stage border and with top arrow pointing to the back.

As the sample rarely consists of a parallelly cut slap of ice but is curved on the outside, you need to level the surface before fixing the sample with waterdrops. To this end lift the stage carefully by means of the lever until the sample surface is horizontal under the blade. Don't push to hard or the blade will be notchy from the start! Hold the lever without letting it lock in place and fix the sample with a waterdrop running along the vertical face onto the glass slide as described before. Once it's frozen you can lower the stage and fix the rear end.
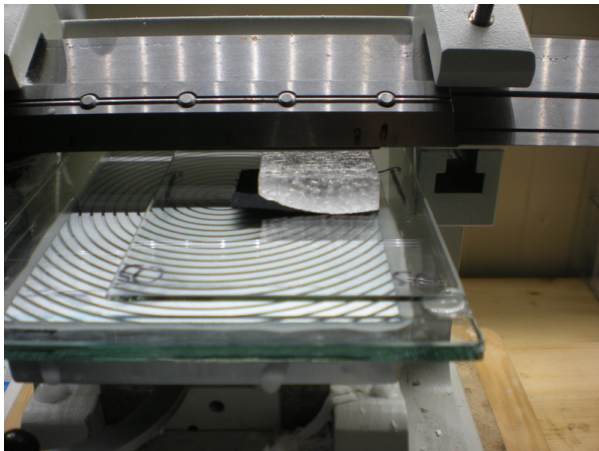
Before you start with microtoming make sure the wheel scale on the side of the sledge is set to zero – otherwise the stage will be raised automatically each time the sledge reaches the front! One turn of the dial corresponds to $250\,\mu$m.

For preparing the thick section it is advised to cut of about $1\,$mm of the surface – to be sure that the physical properties are not affected. Lock the stage so that the sample surface is shortly beneath the blade and raise the stage in steps of about $20-50\,\mu$m while pushing the

sledge until you see the first ice flaking on the blade. Use the brush and the cup to clean the blade from the ice waste, before it becomes too much and drops back on the surface. Continue in those steps until the surface is even.
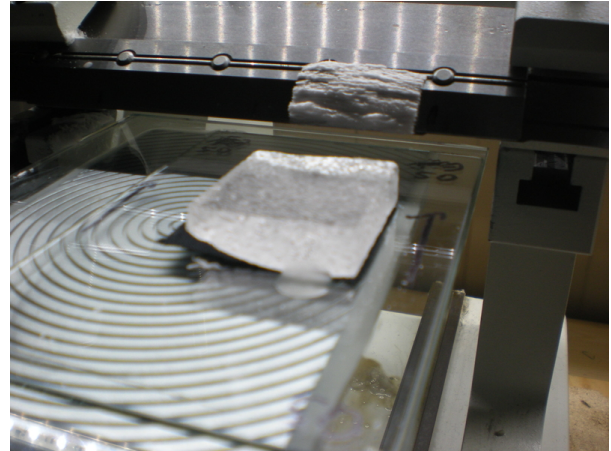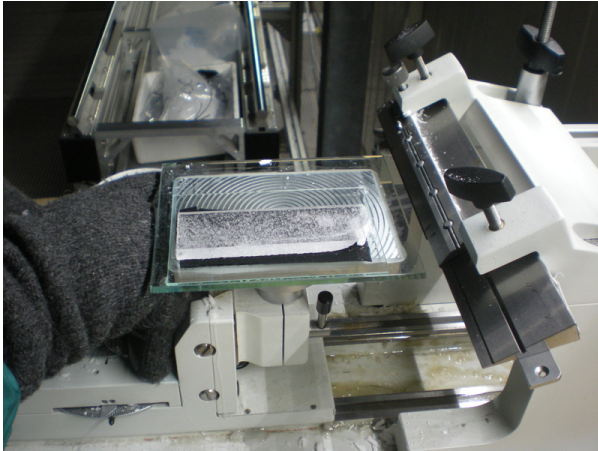
Then use the caliper gauge to measure the total thickness of ice sample and cloth on the slide. Take off 1 mm, i.e. 4 turns of the dial. Push the sledge quickly and steadily – ideally the ice waste looks like chocolate shavings or little rolls (if the blade is new). Decrease the steps towards the end, i.e. $10\,\mu$m steps and a few polishing steps, i.e. 5 - $2\,\mu$m. Make sure that there is a little ice waste as possible on your gloves and the blade before the polishing steps.
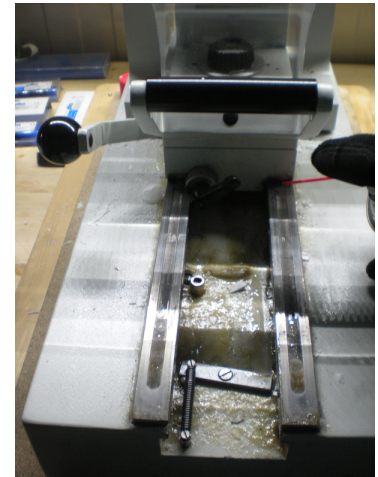
In this example all samples are supposed to have a thickness of 1 cm after polishing, so that the focus of the LASM doesn't need to be adjusted each time. Use the scraper to carefully break the drops that hold the slide on the stage and with your other hand prevent the slide to glide from the stage after the little jerk. Use the scraper to clean the stage.

Large Area Scanning Macroscope
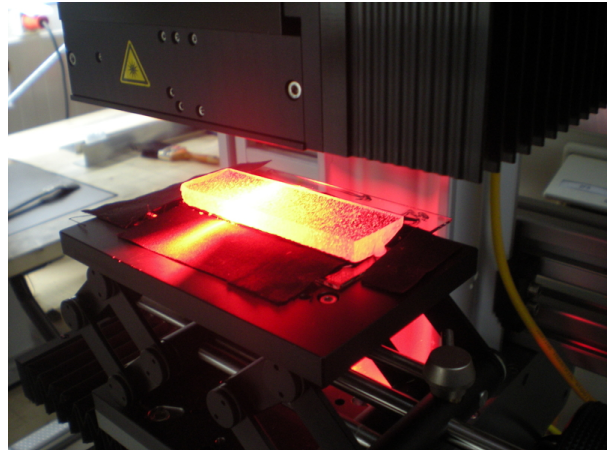
The glass slide with cloth and sample is aligned on the LASM stage with top pointing to the right, so that in the scan picture top corresponds to the ice top. The scan immediately shows if the surface has been affected e.g. scratched by the blade or accidentally touched with a glove or the brush.

Sublimation

After the immediate LASM image is recorded, the surface needs to sublimate, i.e. form sublimation grooves at the grain boundaries, before the actual scan is taken. Also smaller image disturbances from microtoming will diminish during sublimation. To this end the slide is put underneath a box with an opening to shield the polished surface from particles – put it down carefully so the frozen drops do not break! It takes up to several hours before the grooves are sufficiently developed. For the first sample of a run it makes sense to leave the sample on the LASM stage and regularly scan the surface to follow the sublimation process to determine the necessary sublimation duration. Meanwhile the next samples can be microtomed.

Fixing of thick section onto thin section glass slide

After the LASM scan comes the trickiest part: The installation of the polished surface of the thick section onto a glass slide for the thin section. Have clean glass slides (they come in plastic bags) marked with direction of top and the exact name of the sample beforehand. To avoid tedious adjusting of the scan window of the fabric analyzer for each sample it's helpful to use a template for the sample position on the glass slide.
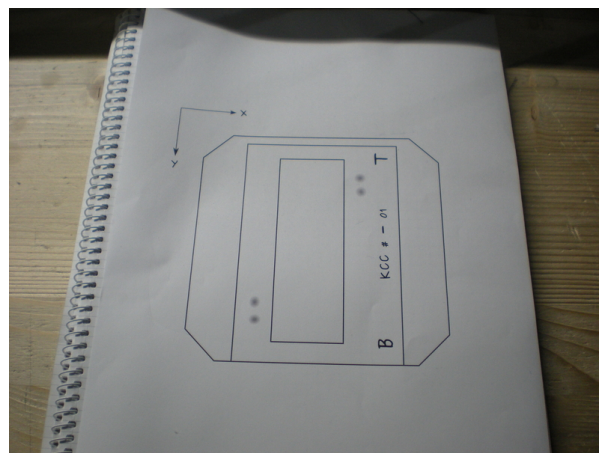
To avoid particles, e.g. glove fluffs, to cause a gap between ice and slide and disrupt the recording you need to wear additional plastic or latex gloves, which will also give you better grip – but your finger tips will immediately get colder!

First, clean the glass slide from both sides with some tissue paper, then adjust it to the template. Carefully break the drops that hold the thick section with the help of the scraper. Touch the thick section as little as possible e.g. once with two fingers of your left hand, on the long sides, and then with two fingers of your right hand, on the short sides, to gently lower it onto the designated position on the prepared glass slide – avoid gliding of the polished surface on the slide which can cause scratches! Shorter samples should be aligned with the template top line. After having picked up the section check the surface against the light for particles and if that's the case gently try to shake them off or use the brush if necessary. With your left hand press down the thick section and with the other hand fix all four corners by means of the dropper bottle as described before. When the drops are fully frozen continue with the water glueing on all four sides – quickly move the tip of the bottle over the water seam back and forth (the idea is that the thus created smaller crystals exert a smaller stress on the sample than larger crystals). Add two drops in cm-distance on both sides of the sample for height measurements of the thin section.
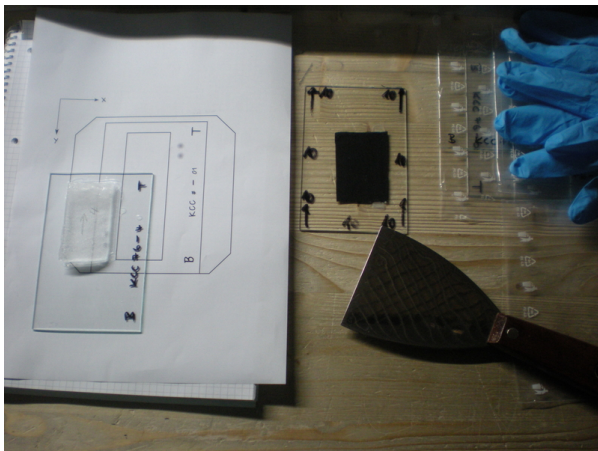
Sawing and packing

To get from thick to thin section you need the cut off most of the thick section. If you try to cut the ice thinner than $0.7 - 1\,\text{mm}$ it is very likely to be destroyed from the saw. So the gap between saw and metal needs to be adjusted accordingly (consider the thickness of the glass slide).

Start the saw and push the slide continuously with the help of styrofoam pieces or thick brushes slowly towards the back and slightly towards the metal boundary. A fixed piece of styrofoam can help preventing the break of the cut off thick section. Observe and practice the sawing on some waste ice first!

Pack the rest of the thick section in the earlier prepared plastic bags. The thin sections of each bag/run will be wrapped in bubble wrap for storage after the fabric analyzer measurements. The saw wheels regularly need to be scratched free of ice.

Microtoming the thin section

As in paragraph B.1 the glass slide will be fixed on the microtom stage. For the thin section new or very little damaged blades need to be used and the steps in raising the stage shouldn't exceed $20\,\mu$m at the beginning and $10\,\mu$m towards the finish. If the steps are too big, the thin section can't stand the pressure of the blade and will likely break! Start with levelling the surface, then measure the thickness with the caliper gauge on the drops. Calculate the steps for a final thickness of $300-400\,\mu$m which is ideal for a good fabric analyzer recording. Polish the surface with several $5-1\,\mu$m steps.
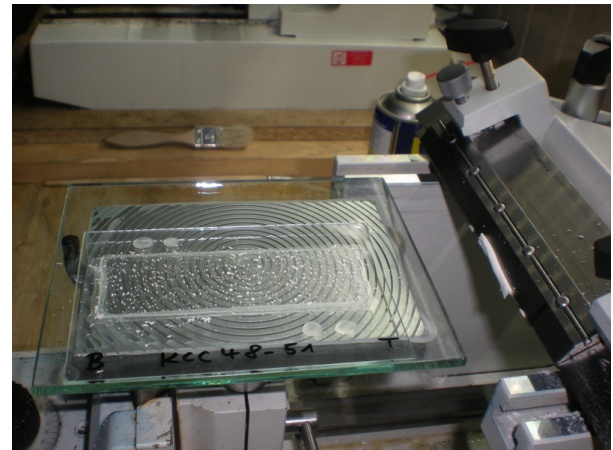
Fabric Analyzer

Use the plexiglass dummies to adjust the glass slide beneath the fabric analyzer. Top of the ice points towards the closed side so that ice top corresponds to the image top. Adjust the focus with the dial above the slide if necessary but if the samples have the same thickness this is usually evitable. For the first sample use a prescan to determine the horizontal position of the measuring grid. For shorter samples only the length needs to be adapted.

For 4×10 cm the measurement takes about $30 - 40$ minutes. Try not to trample on the floor to avoid trembling of the instrument.
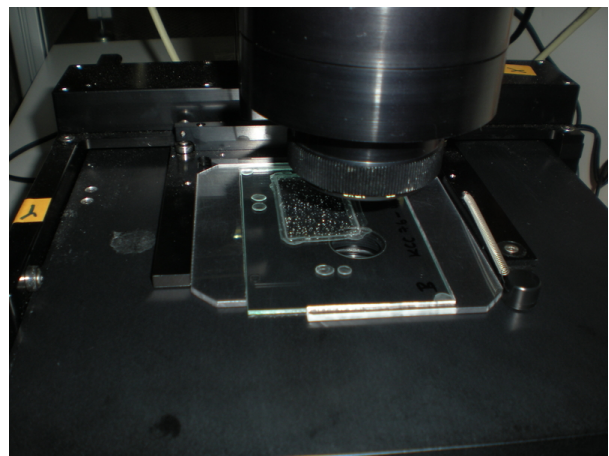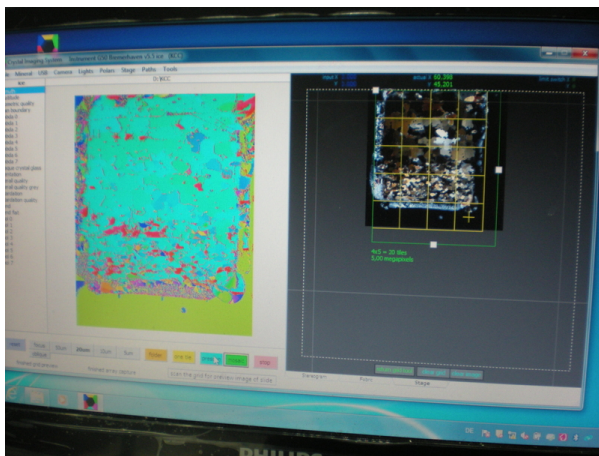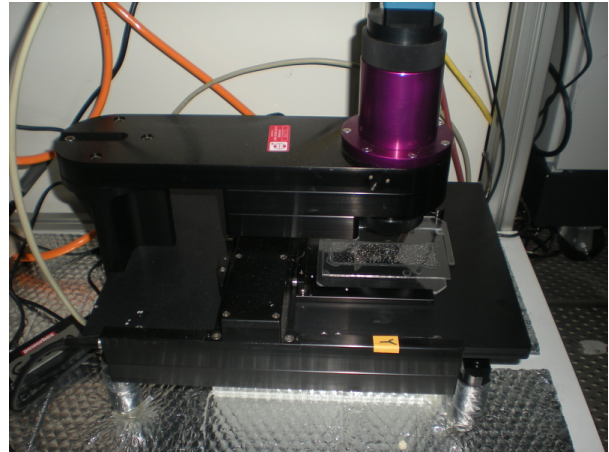
B.2 Information on the fabric data from thin sections

Tab. B.1: KCC thin section parameters: Top depth, area-weighted eigenvalues, and mean and maximum grain size.

Sample	Depth (m)	(m w.e.)	(%)	Eigenvalues λ_1	λ_2	λ_3	Grain size $\bar{A}$	$A_{\max}$
26-31	2561	1442	26.8	0.233	0.317	0.450	1.4	9.0
26-41	2571	1449	26.9	0.241	0.295	0.464	1.22	7.2
26-51	2581.5	1456.3	27.1	0.238	0.286	0.476	1.45	5.8
26-61	2590	1462.2	27.2	0.145	0.202	0.652	1.42	6.1
26-71	2600	1469.2	27.3	0.240	0.281	0.479	1.31	6.2
26-81	2610	1476.2	27.5	0.158	0.200	0.642	1.21	6.8
32-21	3143.3	1870.4	34.8	0.166	0.258	0.576	1.79	15.6
32-31	3153.2	1878	34.9	0.159	0.224	0.617	1.44	18.6
32-41	3163.2	1885.6	35.1	0.184	0.223	0.593	1.46	11.5
32-51	3173	1893.1	35.2	0.207	0.243	0.551	1.86	14.9
32-61	3183	1900.7	35.3	0.151	0.211	0.638	1.6	20.1
32-71	3193	1908.4	35.5	0.217	0.252	0.531	1.08	12.9
40-02	3857.7	2442.1	45.4	0.167	0.307	0.526	3.28	31.2
40-11	3866.3	2449.4	45.6	0.106	0.142	0.752	2.17	35.4
40-21	3875.3	2457.1	45.7	0.174	0.195	0.631	1.5	12.6
40-31	3882.1	2462.9	45.8	0.115	0.161	0.724	2.32	33.5
40-41	3891.7	2471.1	46	0.150	0.185	0.665	1.91	16.2
40-51	3901.7	2479.7	46.1	0.129	0.166	0.705	1.52	15.6
40-61	3911.7	2488.2	46.3	0.153	0.207	0.640	2.62	51.3
40-71	3921.7	2496.8	46.4	0.135	0.177	0.688	2.96	35.8
40-81	3930.5	2504.3	46.6	0.169	0.267	0.565	2.88	24.7
48-01	4337.3	2853.7	53.1	0.142	0.156	0.701	2.63	47.1
48-11	4347.3	2862.4	53.2	0.129	0.192	0.678	4.59	77.7
48-21	4357.3	2871.2	53.4	0.117	0.157	0.725	1.61	36.9
48-31	4367.3	2879.9	53.6	0.075	0.164	0.762	1.36	34.3
48-41	4377.4	2888.7	53.7	0.121	0.153	0.726	4.16	103.5
48-51	4387.6	2897.6	53.9	0.131	0.185	0.684	3.68	207.2
57a-01	4829.5	3287.6	61.1	0.076	0.135	0.789	2.99	92.9
57a-11	4833	3290.7	61.2	0.088	0.127	0.786	1.95	51.2
57a-21	4843	3299.5	61.4	0.085	0.144	0.771	2.54	46.5
57a-31	4853	3308.4	61.5	0.092	0.103	0.805	4.31	85.5

Sample	Depth (m)	(m w.e.)	(%)	Eigenvalues λ_1	λ_2	λ_3	Grain size $\bar{A}$	$A_{\max}$
57b-01	4863.1	3317.3	61.7	0.087	0.216	0.697	6.38	281.4
57b-11	4870	3323.4	61.8	0.079	0.148	0.773	3.48	64.3
57b-21	4880	3332.2	62	0.068	0.104	0.828	4.45	120.4
58-01	4890.2	3341.2	62.1	0.040	0.110	0.850	2.48	35.1
58-11	4900	3349.8	62.3	0.073	0.090	0.837	3.24	176.7
58-21	4910	3358.5	62.5	0.066	0.114	0.821	5.36	198.0
58-31	4920	3367.3	62.6	0.053	0.092	0.855	4.02	79.2
58-41	4930	3376.1	62.8	0.080	0.114	0.805	3.76	34.9
66-02	5294.2	3698.7	68.8	0.033	0.062	0.905	1.93	25.1
66-14	5299	3703.1	68.9	0.031	0.112	0.857	1.05	6.7
66-21	5303.1	3706.8	68.9	0.035	0.088	0.877	2.05	65.9
66-31	5313.1	3715.8	69.1	0.054	0.097	0.849	5.51	415.3
66-41	5323.1	3724.8	69.3	0.064	0.082	0.853	5.93	123.3
66-51	5333.1	3733.9	69.4	0.025	0.060	0.915	1.42	74.1
75a-01	5724.2	4079.6	75.9	0.063	0.144	0.793	6.01	175.6
75a-12	5735	4089.2	76.1	0.049	0.088	0.862	6.8	390.1
75a-21	5744.7	4097.9	76.2	0.031	0.042	0.926	4.79	221.1
75a-32	5754.5	4106.6	76.4	0.017	0.030	0.954	5.78	254.2
75b-01	5765	4115.8	76.5	0.021	0.040	0.939	1.95	87.9
75b-11	5769	4119.3	76.6	0.027	0.063	0.910	3.99	211.2
75b-21	5779	4128.2	76.8	0.057	0.082	0.861	7.81	229.5
76-01	5789	4137.2	76.9	0.032	0.056	0.912	4.44	106.9
76-11	5800	4147.1	77.1	0.043	0.055	0.902	2.61	60.3
76-22	5810	4156.2	77.3	0.075	0.111	0.814	16.95	346.8
76-31	5820	4165.2	77.5	0.038	0.044	0.917	1.55	52.4
76-42	5830.8	4174.8	77.6	0.025	0.039	0.936	0.75	5.7
85-03	6272.7	4567.8	85	0.057	0.081	0.862	5.3	224.0
85-12	6283	4577.1	85.1	0.042	0.078	0.880	4.11	174.2
85-24	6293	4586.1	85.3	0.016	0.038	0.946	1.57	45.6
85-33	6303	4595.1	85.5	0.052	0.146	0.802	3.22	123.0
85-44	6314.2	4605.3	85.6	0.015	0.030	0.955	2.75	70.3
92a-11	6700	4948.6	92	0.069	0.122	0.809	8.02	299.6
92a-22	6710.5	4958.3	92.2	0.050	0.230	0.720	9.79	148.1
92a-32	6720	4966.9	92.4	0.043	0.103	0.854	4.58	140.9

Sample	Depth (m)	(m w.e.)	(%)	Eigenvalues			Grain size	
				λ_1	λ_2	λ_3	$\bar{A}$	$A_{\max}$
92a-41	6730	4976.1	92.5	0.019	0.047	0.934	3.43	55.1
94-01	6823	5058.9	94.1	0.037	0.097	0.866	2.81	63.8
94-11	6830	5065	94.2	0.059	0.130	0.811	4.19	63.7
94-21	6840	5073.8	94.4	0.020	0.026	0.954	3.81	85.6
94-32	6850	5082.6	94.5	0.022	0.068	0.910	2.91	52.1
94-41	6860	5091.4	94.7	0.017	0.061	0.922	3.23	107.0
94-52	6870	5100.2	94.9	0.031	0.084	0.885	4.12	106.8
95-01	6877.8	5107	95	0.054	0.109	0.837	5.18	162.0
95-11	6885.9	5114.3	95.1	0.031	0.139	0.830	3.31	76.4
97b-11	6976	5195	96.6	0.017	0.036	0.947	4.77	76.6
97b-21	6986	5204.1	96.8	0.031	0.057	0.912	2.88	46.0
97b-31	6996	5213.1	97	0.046	0.125	0.829	5.12	195.6
97b-41	7006	5222.1	97.1	0.023	0.124	0.853	3.24	76.4
100-22	7116	5320.4	98.9	0.015	0.023	0.962	1.39	45.9
100-31	7126	5329.4	99.1	0.017	0.026	0.957	0.91	16.2
100-41	7136	5338.3	99.3	0.014	0.016	0.970	1.22	33.1
101-11	7150	5350.4	99.5	0.015	0.017	0.969	1.67	35.2
101-21	7160	5359	99.7	0.010	0.014	0.976	1.24	19.2
101-31	7170	5367.7	99.8	0.011	0.015	0.974	1.87	51.8
101-41	7180	5376.3	100	0.010	0.014	0.976	2.11	49.7

EDML

Tab. B.2: EDML thin section information: Depth, vertical/horizontal section, Fabric Analyser model.

Depth (m)	ver./hor. section	FA type	Depth (m)	ver./hor. section	FA type	Depth (m)	ver./hor. section	FA type
104.05	verS	G20	1494.25	verS	G20	2354.00	horS	G20
144.05	verS	G20	1505.00	horS	G20	2354.90	horS	G20
205.15	verS	G20	1505.90	horS	G20	2355.05	verS	G20
255.15	verS	G20	1534.15	verS	G20	2359.05	verS	G50
304.35	verS	G20	1553.96	verS	G20	2359.15	verS	G50
355.15	verS	G20	1568.05	verS	G20	2359.25	verS	G50
395.15	verS	G20	1585.05	verS	G20	2359.35	verS	G50
454.00	horS	G20	1603.00	horS	G20	2359.45	verS	G50

Depth (m)	ver./hor. section	FA type	Depth (m)	ver./hor. section	FA type	Depth (m)	ver./hor. section	FA type
454.25	verS	G20	1603.90	horS	G20	2359.55	verS	G50
454.90	horS	G20	1655.00	horS	G20	2359.65	verS	G50
506.00	horS	G20	1655.05	verS	G20	2359.75	verS	G50
506.90	horS	G20	1655.90	horS	G20	2359.85	verS	G50
553.00	horS	G20	1665.05	verS	G20	2359.95	verS	G50
553.90	horS	G20	1704.00	horS	G20	2365.05	verS	G20
555.45	verS	G20	1704.90	horS	G20	2366.85	verS	G50
604.00	horS	G20	1725.05	verS	G20	2372.05	verS	G50
604.90	horS	G20	1735.05	verS	G20	2372.15	verS	G50
636.85	verS	G20	1755.05	verS	G20	2372.25	verS	G50
655.45	verS	G20	1758.00	horS	G20	2372.35	verS	G50
657.00	horS	G20	1758.90	horS	G20	2372.45	verS	G50
657.90	horS	G20	1785.05	verS	G20	2372.55	verS	G50
702.00	horS	G20	1802.00	horS	G20	2372.65	verS	G50
702.90	horS	G20	1802.90	horS	G20	2372.75	verS	G50
754.00	horS	G20	1805.05	verS	G20	2372.85	verS	G50
754.90	horS	G20	1845.05	verS	G20	2372.95	verS	G50
755.95	verS	G20	1854.00	horS	G20	2373.05	verS	G50
805.00	horS	G20	1854.90	horS	G20	2373.15	verS	G50
805.90	horS	G20	1855.25	verS	G20	2373.25	verS	G50
853.00	horS	G20	1856.95	verS	G50	2373.35	verS	G50
853.90	horS	G20	1904.00	horS	G20	2373.45	verS	G50
854.75	verS	G20	1904.90	horS	G20	2373.55	verS	G50
906.00	horS	G20	1955.05	verS	G20	2373.65	verS	G50
906.90	horS	G20	1960.00	horS	G20	2373.75	verS	G50
952.00	horS	G20	1960.90	horS	G20	2373.85	verS	G50
952.90	horS	G20	1975.05	verS	G20	2373.95	verS	G50
953.45	verS	G20	1995.05	verS	G20	2375.05	verS	G20
1004.00	horS	G20	2004.00	horS	G20	2375.25	verS	G20
1004.90	horS	G20	2004.90	horS	G20	2379.05	verS	G50
1053.15	verS	G20	2025.05	verS	G20	2379.15	verS	G50
1056.00	horS	G20	2035.05	verS	G20	2379.25	verS	G50
1056.90	horS	G20	2045.05	verS	G20	2379.35	verS	G50
1105.00	horS	G20	2052.00	horS	G20	2379.45	verS	G50

Appendix

Depth (m)	ver./hor. section	FA type	Depth (m)	ver./hor. section	FA type	Depth (m)	ver./hor. section	FA type
1105.90	horS	G20	2052.90	horS	G20	2379.55	verS	G50
1124.15	verS	G20	2055.05	verS	G20	2379.65	verS	G50
1152.00	horS	G20	2085.05	verS	G20	2379.75	verS	G50
1152.90	horS	G20	2095.05	verS	G20	2379.85	verS	G50
1155.15	verS	G20	2104.00	horS	G20	2379.95	verS	G50
1204.00	horS	G20	2104.90	horS	G20	2383.95	verS	G50
1204.90	horS	G20	2105.05	verS	G20	2385.05	verS	G20
1205.15	verS	G50	2154.00	horS	G20	2395.05	verS	G20
1253.00	horS	G20	2154.90	horS	G20	2404.00	horS	G20
1253.90	horS	G20	2155.05	verS	G20	2404.90	horS	G20
1255.15	verS	G20	2204.00	horS	G20	2454.00	horS	G20
1304.00	horS	G20	2204.90	horS	G20	2454.90	horS	G20
1304.90	horS	G20	2254.00	horS	G20	2455.05	verS	G20
1345.15	verS	G20	2254.90	horS	G20	2485.05	verS	G20
1354.00	horS	G20	2265.05	verS	G20	2495.05	verS	G20
1354.90	horS	G20	2276.05	verS	G50	2504.00	horS	G20
1364.15	verS	G20	2285.05	verS	G20	2504.90	horS	G20
1395.85	verS	G20	2295.05	verS	G20	2505.05	verS	G20
1404.00	horS	G20	2304.00	horS	G20	2546.95	verS	G50
1404.90	horS	G20	2304.90	horS	G20	2554.00	horS	G20
1454.00	horS	G20	2306.05	verS	G50	2554.90	horS	G20
1454.15	verS	G20	2316.25	verS	G50	2563.05	verS	G20
1454.90	horS	G20	2345.05	verS	G20			

B.3 Thin section pole figures
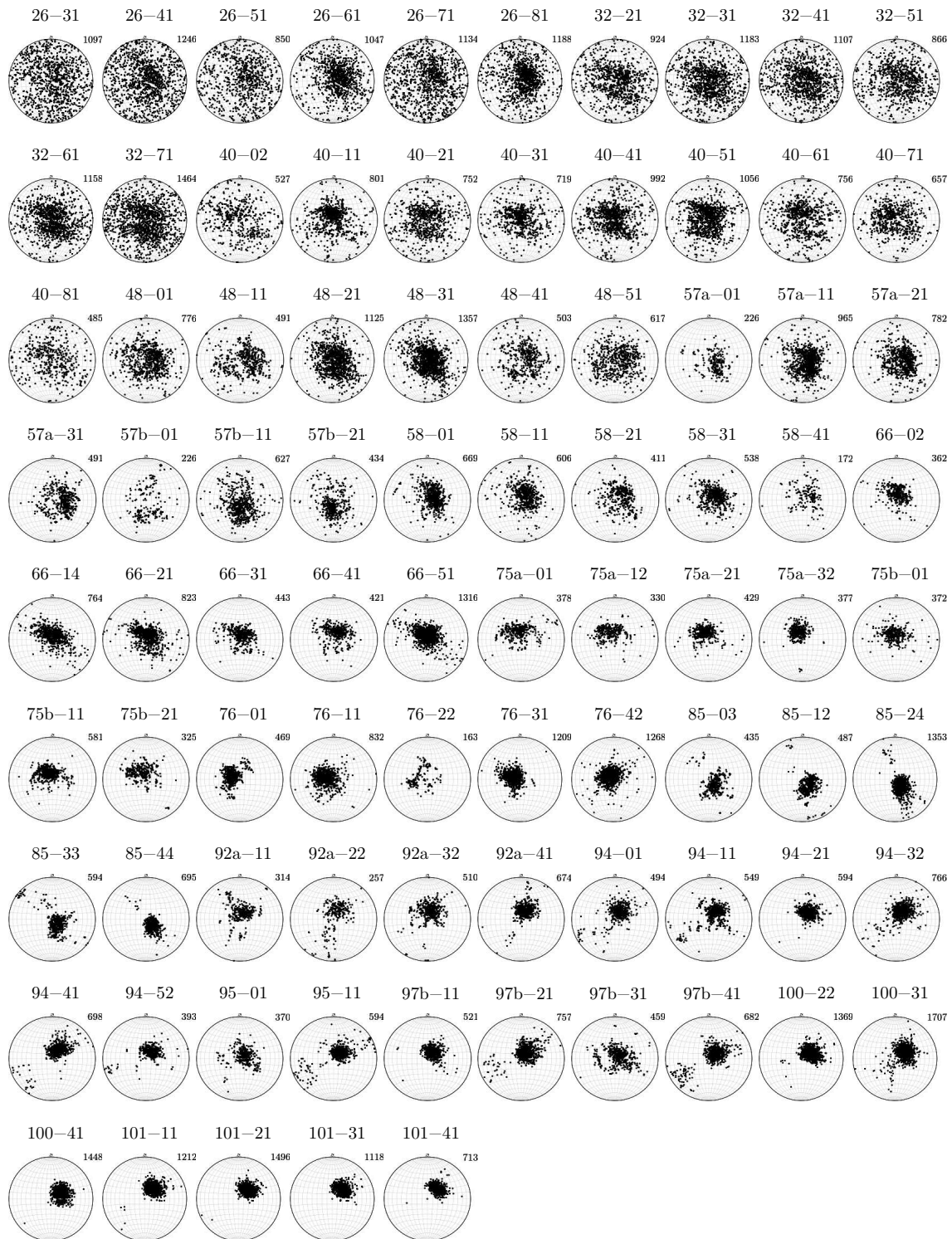
Fig. B.1: Schmidt diagrams for all KCC thin sections. Each dot represents one c-axis. Number of axes is indicated on the top right of each pole figure.
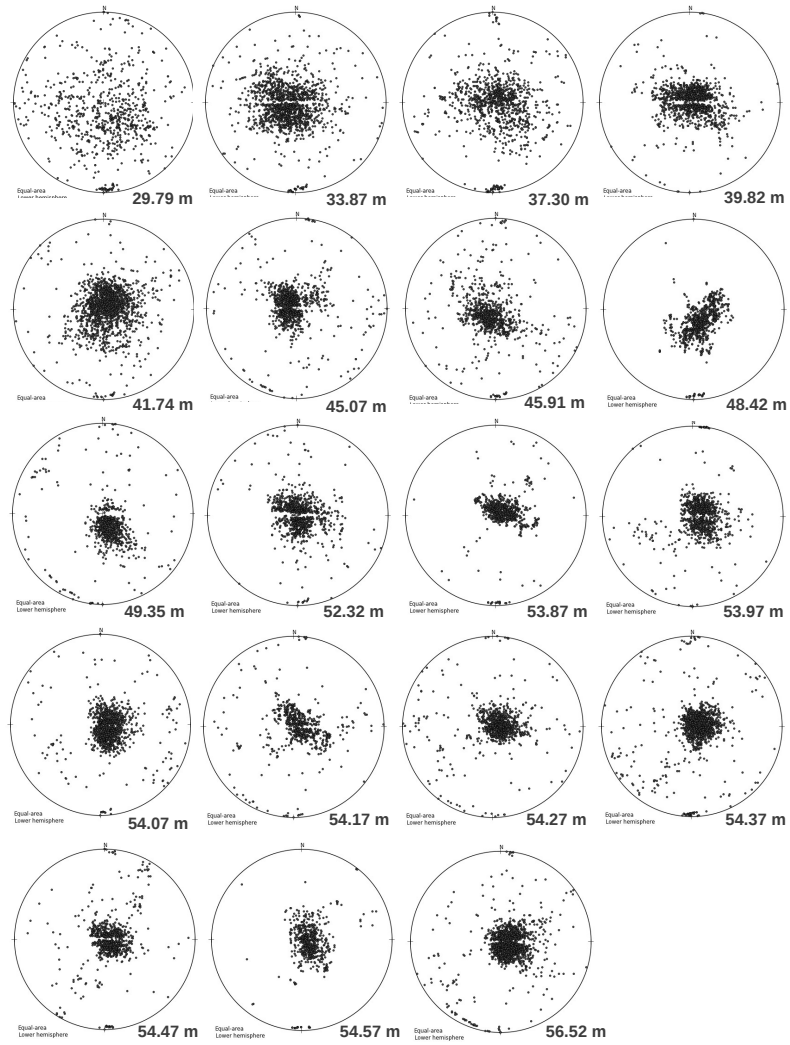
Fig. B.2: Schmidt diagrams for KCI thin sections (pers. comm. Jan Eichler, 2013). Each dot represents one c-axis. Depth is indicated on the bottom right. The interval is approx. 2–3 m with continous thin section measurements between 53.87 and 54.57 m.
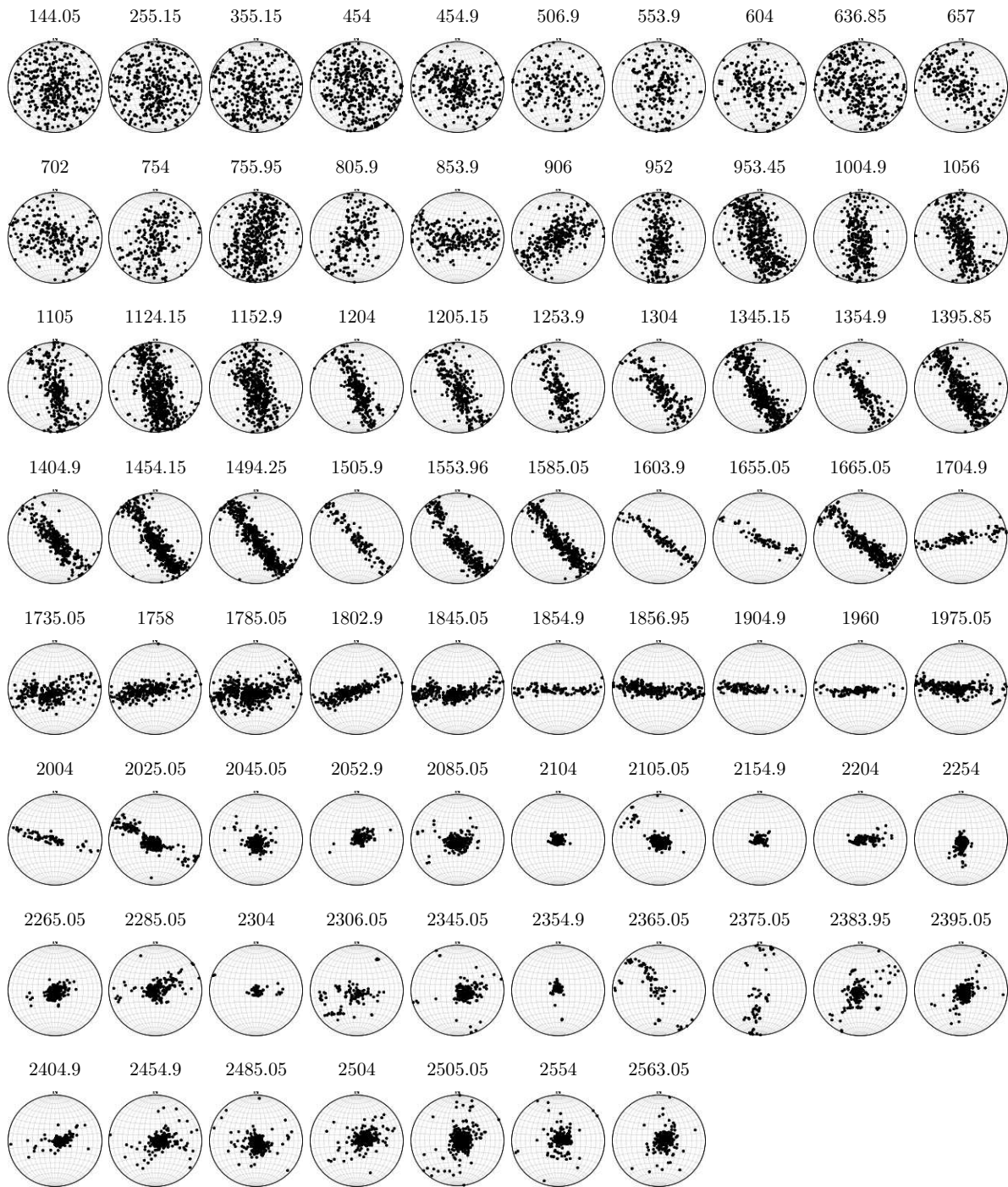
Fig. B.3: Schmidt diagrams for every second EDML thin sections used in this study. Each dot represents one c-axis.

B.4 Data from continuous flow analysis
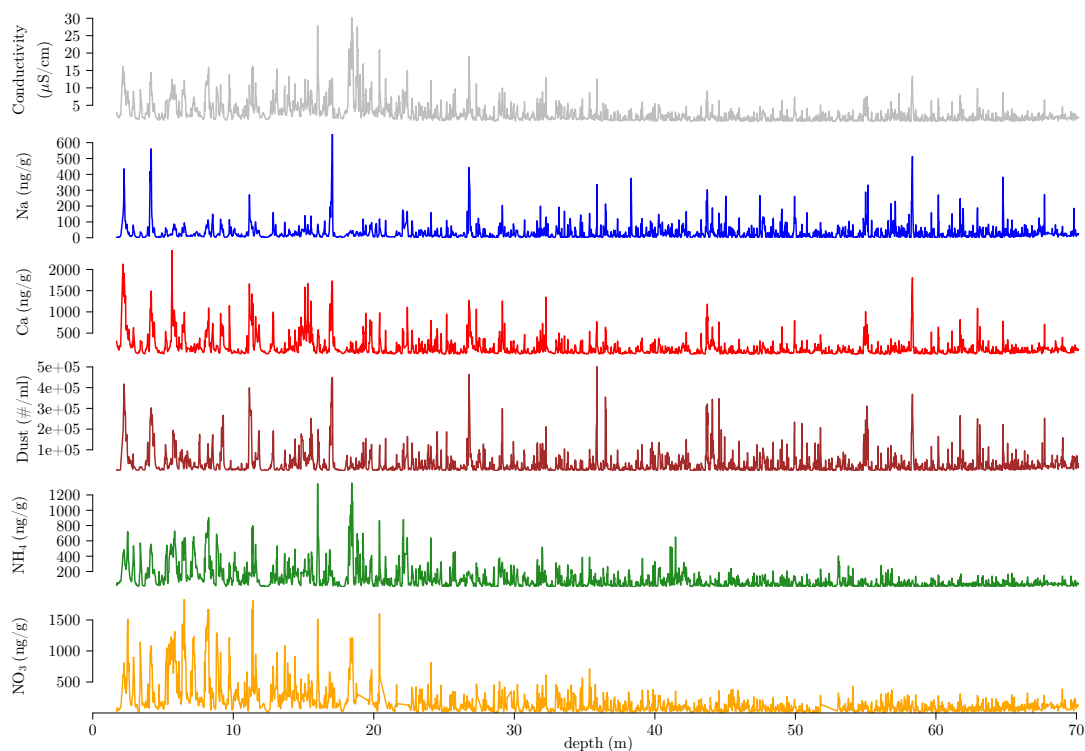
Fig. B.4: CFA data from KCC ice core (pers. comm. H. Fischer/T. Erhardt, University of Bern, 2014). Conductivity, calcium (Ca^{2+}), sodium (Na^+), particulate dust content, ammonium (NH_4^+) and nitrate (NO_3^-) were measured and are shown here smoothed with $2\,cm$ bandwidth.
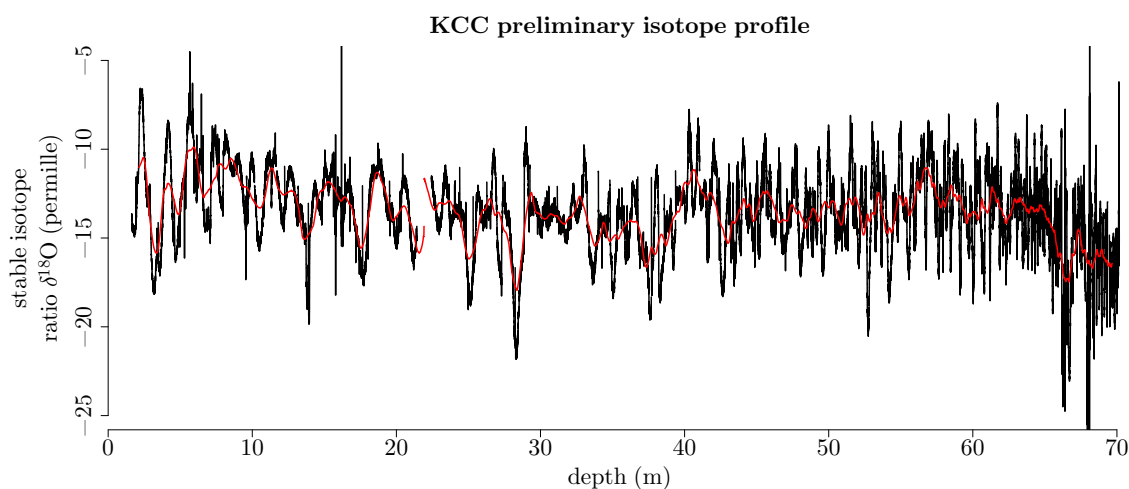
Fig. B.5: Stable oxygen isotope ratio $\delta^{18}O$ (‰) of KCC ice core as measured online during CFA (pers. comm. H. Fischer/G. van der Wel, University of Bern, 2014).

B.5 Density from X2D
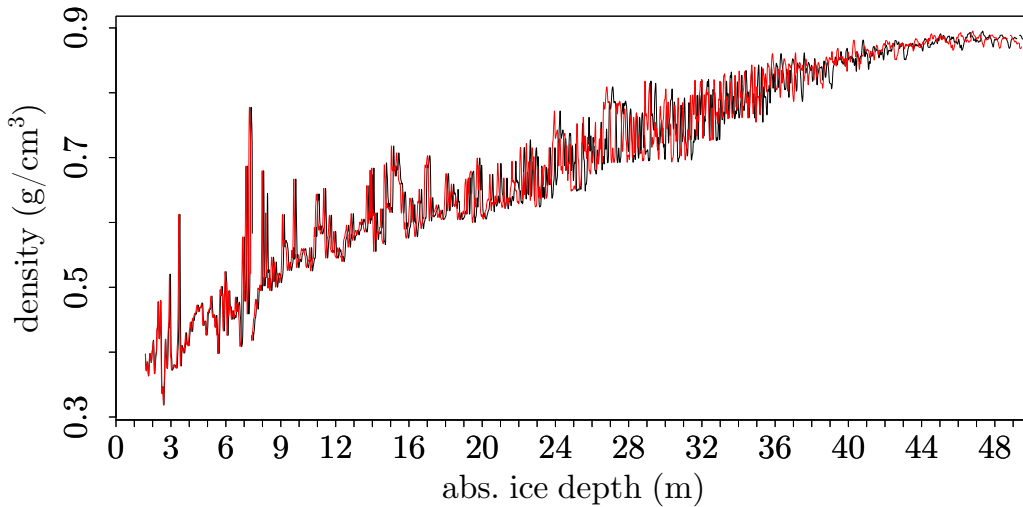
Fig. B.6: Illustration of the depth scale correction for X2D density. Smoothed (with a bandwidth of 0.05 m) high resolution density for the upper 50 m of the KCC ice core with old (black) and corrected (red) depth scale. The cumulative shift at the bedrock amounts to 55 cm.

B.6 ImageJ macro for bubble analysis

This macro is saved as `.ijm` and the batch process for a stack of images is started in `ImageJ` via `Process/Batch/Macro`.

```
file = getTitle()
sample = replace(file,".bmp","")
path = "../LASM_cropped_margins/ImageJ_bubble_analysis_batch_input/output/"
run("8-bit");
setAutoThreshold("Default");
run("Threshold...");
setThreshold(0, xx);
setOption("BlackBackground", false);
run("Convert to Mask");
run("Analyze Particles...",
"size=50-Infinity circularity=0.1-1.00 show=[Overlay Masks] exclude clear include");
saveAs("PNG", path+sample+"_mask");
run("Set Measurements...", "area center fit shape add redirect=None decimal=3");
run("Analyze Particles...", "size=30-Infinity circularity=0.1-1.00 show=Ellipses display exclude clear");
saveAs("PNG", path+sample+"_ell");
saveAs("Results", path+sample+".dat");
run("Close");
run("Close");
```

with *xx:* threshold value between 40 and 60 for different runs.

B.7 Line scan description

Tab. B.3: Stratigraphic description of all KCC runs including layer inclination estimates. Core azimuth was estimated during aliquoting in hours, i.e. in multiples of 30°, with 15 (o'clock) referring to 0°.

KCC run number	Stratigraphic description	Estimated layer inclination (°)	Estimated core azimuth
KCC001	weakly visible layers 5-10 cm	yes	
KCC002	several thin melt layers	–(7–10)	15
KCC003	thick melt layer (2 cm)		15
KCC004a	some ice lenses		23
KCC004b	weakly visible layers 2–5 cm		14
KCC005a	weakly visible thick layers 20–25 cm		15
KCC005b	coarse grained, layers 5–10 cm		23
KCC006b	many thin melt layers and ice lenses, layers with coarse grains 3–5 cm	–(6–12)	15
KCC007	several thick melt layers 1–4 cm, transition fine to coarser layers 20 cm, coarser grains closer to melt layers		24
KCC008	thin melt layers, a thick melt layer 3 cm, ice lenses and coarser grains, thick bands with coarser grains 10 cm	8–15	13
KCC009a	melt layer and ice lenses, coarser grains	14	13
KCC009b	ice lense		15
KCC010b	melt layers 1 cm and ice lenses		15
KCC010c	weakly visibly layers 10–20 cm		16
KCC011b	several thin and thick melt layers 1–2 cm, change in inclination	–(6–22)	20
KCC012a	uniform		21
KCC012b	uniform		21
KCC013a	uniform		15
KCC013b	thin melt layers and ice lenses, coarser grains closeby, thick melt layer 1 cm, weakly visibly layered 5-10 cm	–9	15
KCC014b	thick melt layer (2 cm), thin melt layers, layering of finer and coarser grains 5-10 cm		15
KCC015	many ice lenses, thin melt layers, transitions of finer and coarser grains (resp. higher and lower density layers)	–16	15
KCC016b	transition lighter/darker, thin ice lense		15

KCC run number	Stratigraphic description	Estimated layer inclination (°)	Estimated core azimuth
KCC016c	ice lense, lighter/darker layering 2-10 cm	−(3–6)	21
KCC017b	lighter/darker transitions	10–16	15
KCC018b	thin melt layer and coarser grained layer	10	14
KCC019c	thin melt layers, ice lenses, lighter/darker transitions	11	15
KCC020a	ice lenses, clear lighter/darker banding 2-10 cm	5–7	15
KCC020b	fairly uniform, one darker layer 3 cm, few ice lenses		19
KCC021	thin melt layers and coarser grains, lighter/darker transitions 3-15 cm	11	17
KCC022	lighter/darker banding 2-20 cm, few ice lenses		14
KCC023a	lighter/darker banding 2-15 cm	−11	23
KCC023b	lighter/darker banding, ice lenses		15
KCC024	banding, thick melt layer 1 cm, large ice lenses/percolation features in darker bands	−5	23
KCC025	banding, irregular thickness, some ice lenses		23
KCC026	banding, lighter bands 2-5 cm, thicker darker bands, break at the end	−6	22
KCC027a	blurred banding, some thin melt layers	9	15
KCC027b	blurred banding, thick melt layer 1 cm, ice lense	13	15
KCC028	banding 1-15 cm, thin melt layer	10	15
KCC029a	banding 4-10 cm	12	15
KCC029b	blurred banding, massive melt layer 3 cm, several ice lenses/percolation features	11	15
KCC030a	banding 5 cm, melt layer	10	15
KCC030b	banding (min. 16 layers) 2-12 cm		23
KCC031a	banding, melt layer	8	15
KCC031b	uniform (short)		15
KCC032	banding (min. 19 layers) 2-10 cm, break in the middle	8	15
KCC033a	banding		15
KCC033b	regular banding 2-5 cm	yes	15
KCC034	irregular banding		18
KCC035a	banding, ice lense	10	15
KCC035b	banding	−5	23
KCC036a	banding	−5	15
KCC036b	blurred banding	10	15
KCC037	blurred banding	10	15

Appendix

KCC run number	Stratigraphic description	Estimated layer inclination (°)	Estimated core azimuth
KCC038	weakly visible banding, melt layers, break	10	15
KCC039	weakly discernible lighter/darker layers a few cm, melt layer 1 cm, break	−(6–12)	21
KCC040	lighter/darker transitions, break	5–10	15
KCC041	lighter/darker transitions, 2 breaks		15
KCC042	lighter/darker transitions, break		15
KCC043	lighter/darker transitions, break		22
KCC045	rather uniform, layers are faintly indicated	−10	22
KCC046	rather uniform, layers are faintly indicated		15
KCC047	some layers apparent, melt layer	−7	14
KCC048	weakly discernible lighter/darker banding 20-25 cm		15
KCC049a	rather uniform		15
KCC049b	weakly discernible lighter/darker banding		15
KCC050	weakly discernible lighter/darker banding		21
KCC051	weakly discernible lighter/darker banding 1-2 cm		15
KCC052	weakly discernible lighter/darker banding		21
KCC053	weakly discernible lighter/darker banding		22
KCC054	weakly discernible lighter/darker banding 5-10 cm		15
KCC055	weakly discernible lighter/darker banding 5-15 cm		15
KCC056	weakly discernible lighter/darker banding a few cm, break		15
KCC057a	weak banding		15
KCC057b	rather uniform		23
KCC058	lighter/darker transitions		15
KCC059	blurred, weakly discernible layers		15
KCC060	lighter/darker banding discernible		15
KCC061	lighter/darker banding discernible, break		21
KCC062	lighter/darker transitions, rather uniform		15
KCC063	blurred, lighter/darker transitions, a darker layer 3cm	11	15
KCC064	noisy, weakly discernible lighter/darker banding, a lighter layer 2 cm, break and rotated pieces	8	13/23
KCC065	noisy, weakly discernible lighter/darker transitions, break		24/15
KCC066	blurred, weakly discernible lighter/darker banding	12	15
KCC067	noisy, weakly discernible banding, break		23 / 14

KCC run number	Stratigraphic description	Estimated layer inclination (°)	Estimated core azimuth
KCC068	weak transitions, lighter bands, break	10	13
KCC069	banding 1-10 cm, break	−9	23
KCC070	banding a few cm	−10	21
KCC071	weak banding	5	15
KCC072	blurred banding	−12	21
KCC073	rather uniform (short)		18
KCC074	bands/transitions		24
KCC075a	blurred banding, one steep dark band feature	12	15
KCC075b	blurred banding	12	15
KCC076	blurred transitions, two transitions to lighter band then a very dark/clear band and break	6–12	14
KCC077a	blurred banding	13	15
KCC077b	rather uniform		14
KCC078	blurred banding	10–15	15
KCC079	blurred banding, break at a clear layer	10	15
KCC080	blurred banding	−13	21
KCC081	transitions, break		17
KCC082a	weak banding	−5	22
KCC082b	noisy, weak banding	15	15
KCC083	blurred banding, break at a clear layer	6	17
KCC084	noisy, blurred banding, break at a clear layer	10–15	13
KCC085	noisy, blurred banding, break at a clear layer		23
KCC086	noisy, blurred banding/layers, break at a clear layer		18
KCC087a	weak blurred banding	15–20	23
KCC087b	banding, blurred layers 1-2 cm, contrast increasing	15–20	15
KCC088	many blurred layers 1 cm, some bands, break at dark/clear layer after light band, impression of steep features	15–20	15
KCC089	many blurred layers 1 cm, some bands	12–20	15
KCC090	many layers/bands, partially noisy, break at a dark/clear layer	15–20	15
KCC091	noisy, blurred banding, double break at a clear layer	6–14	15
KCC092a	noisy, blurred banding, impression of steep features, layer curved	18–30	15
KCC092b093	blurred layers/bands, several breaks and rotated pieces	15–18	18 above BR, 16 below

KCC run number	Stratigraphic description	Estimated layer incli- nation (°)	Estimated core azimuth
KCC094	noisy, blurred banding, steep features, dark layers seem disturbed	20–30	15
KCC095	blurred banding	10	15
KCC096	noisy, no laminar banding, rather lighter/darker regions, break at a dark/clear band		17.5
KCC097a	noisy, lighter/darker regions		24
KCC097b	transition, noisy blurred banding, layer boundaries appear not only blurred but disturbed	10–15	15
KCC098	blurred banding, overlayed with lighter/darker regions/patches, break		13
KCC099	noisy (short)		19
KCC100	rather uniform, some darker layers	20–30	15
KCC101	uniform		21

B.8 Correlation computation sample sizes

Tab. B.4: Sample size n, i.e. number of pairs of bivariate data, for correlation computation. The second column refers to Fig. 4.23, columns 3–9 refer to Fig. 5.4, p. 74.

	Eigenvalue λ_3	Eigenvalue λ_3 / Mean grain size $\bar{A}$ / Grain number N_g						
Range	μS	Na^+	Ca^{2+}	Dust	NH_4^+	NO_3^-	Cond.	$\delta^{18}O$
26	27/28	22	25	25	25	25	25	27
32	28	28	27	28	28	28	28	28
40	38	32	32	31	32	31	31	36
48	29	26	26	26	26	25	26	28
57/58	50/51	43	43	43	43	43	43	49
66	23	17	17	17	17	17	17	22
75/76	55	45	45	45	45	45	45	53
85	24	14	16	15	15	15	15	23
92a	19	14	14	14	14	13	14	19
94/95	35	25	23	22	21	22	22	33
97b	19	18	18	18	18	13	18	19
100/101	32							

B.9 Autocorrelation graphs
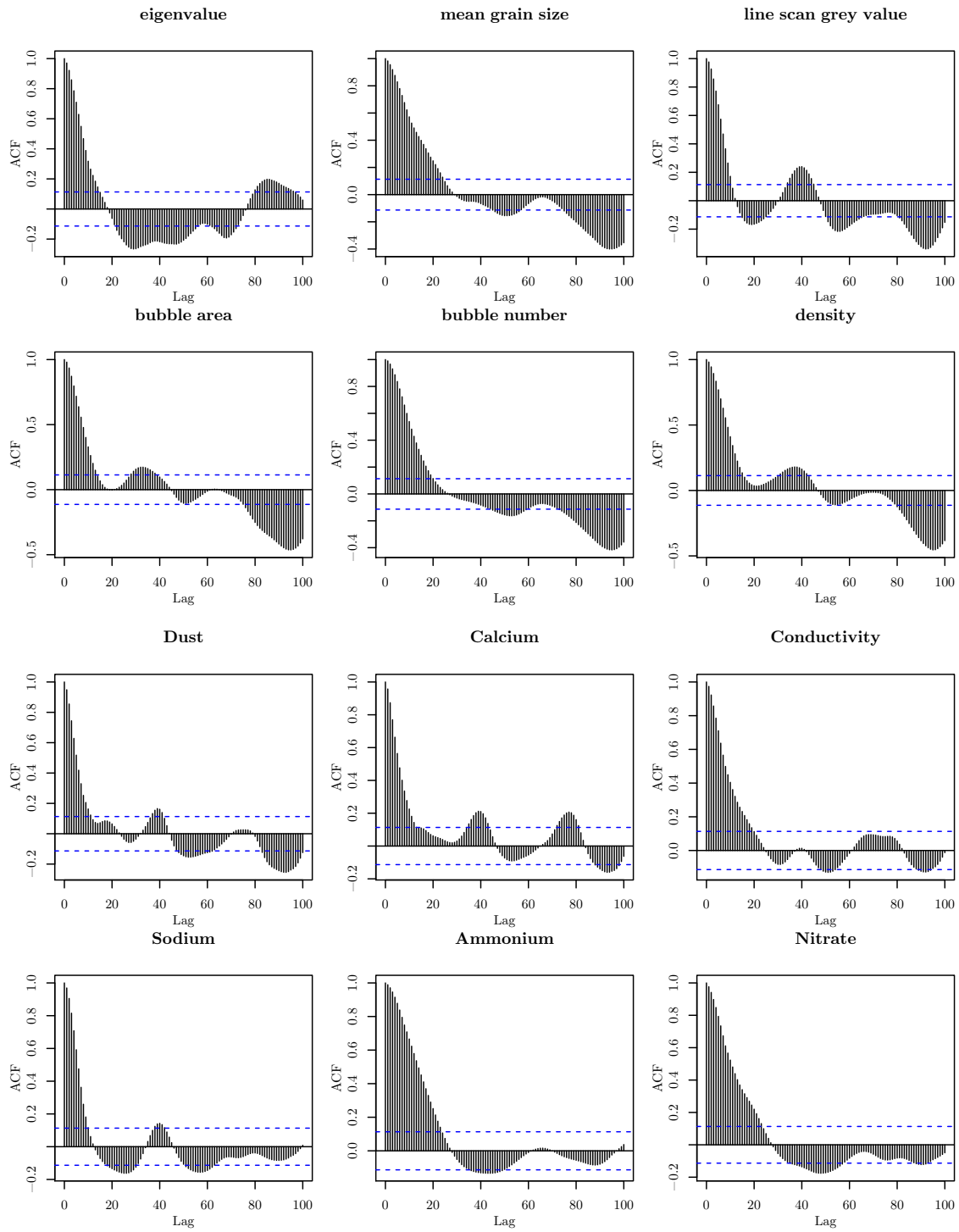
Fig. B.7: Autocorrelation for fabric, microstructure and impurity data of range 32 is shown exemplarily. The lag is given in 2 mm steps, max. lag 20 cm.

B.10 Cm-scale fabric and microstructure graphs
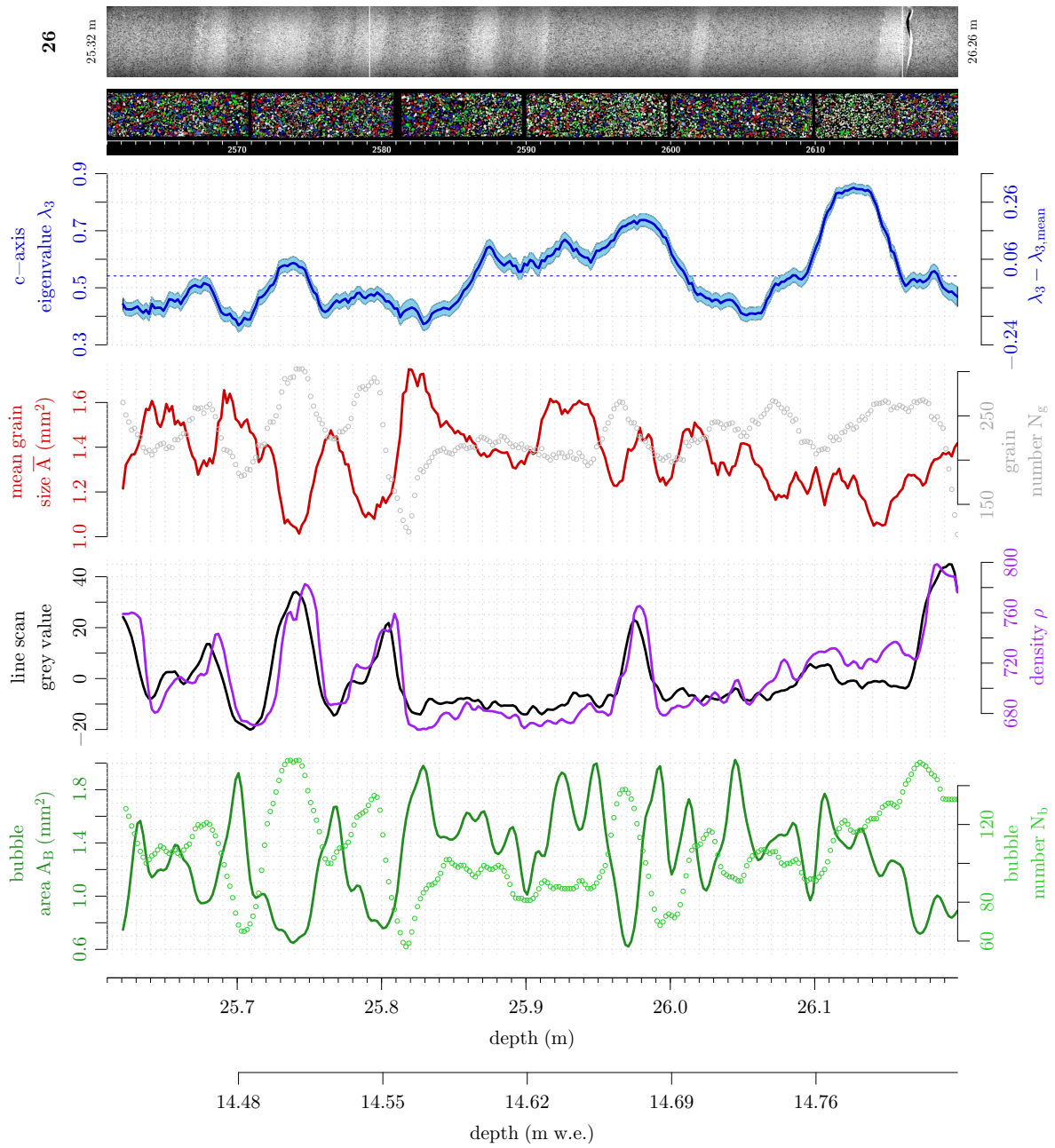
Fig. B.8: Fabric and microstructure in cm-resolution for KCC run 26. The eigenvalue appears largely independent of the other microstructural parameters which relate to each other to a certain degree. Strongest eigenvalue variability of all ranges. Only the middle part (between white lines) of the line scan corresponds to the parameter records.
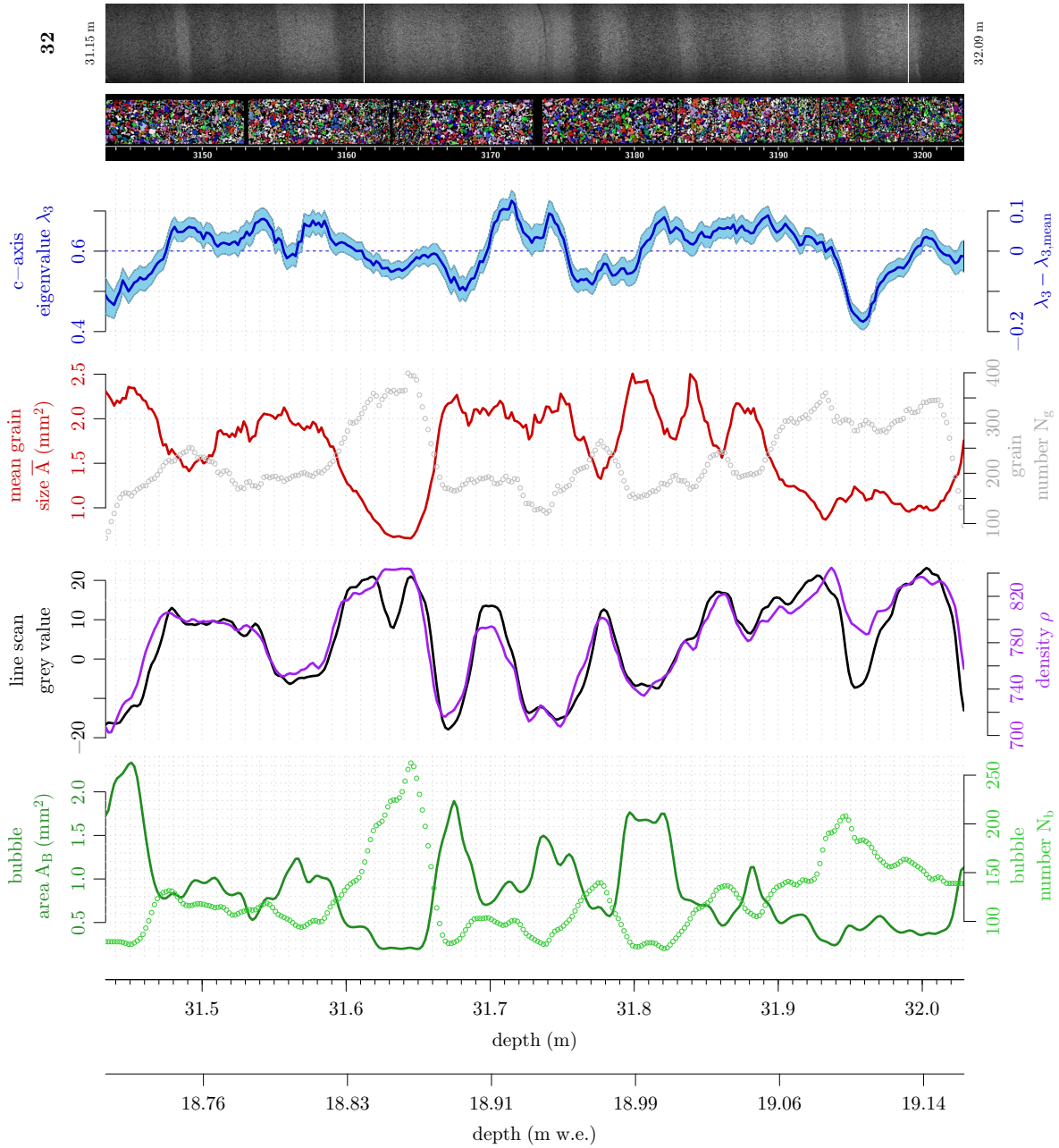
Fig. B.9: Fabric and microstructure in cm-resolution for KCC run 32. Line scan grey value and density showed a systematic offset of 2 cm for the line scan values, based on the comparison with the mean grain size, which can be a likely result from erroneous depth assignment. This offset was corrected for plotting and correlation computation. Line scan and eigenvalue record exhibit some common features.
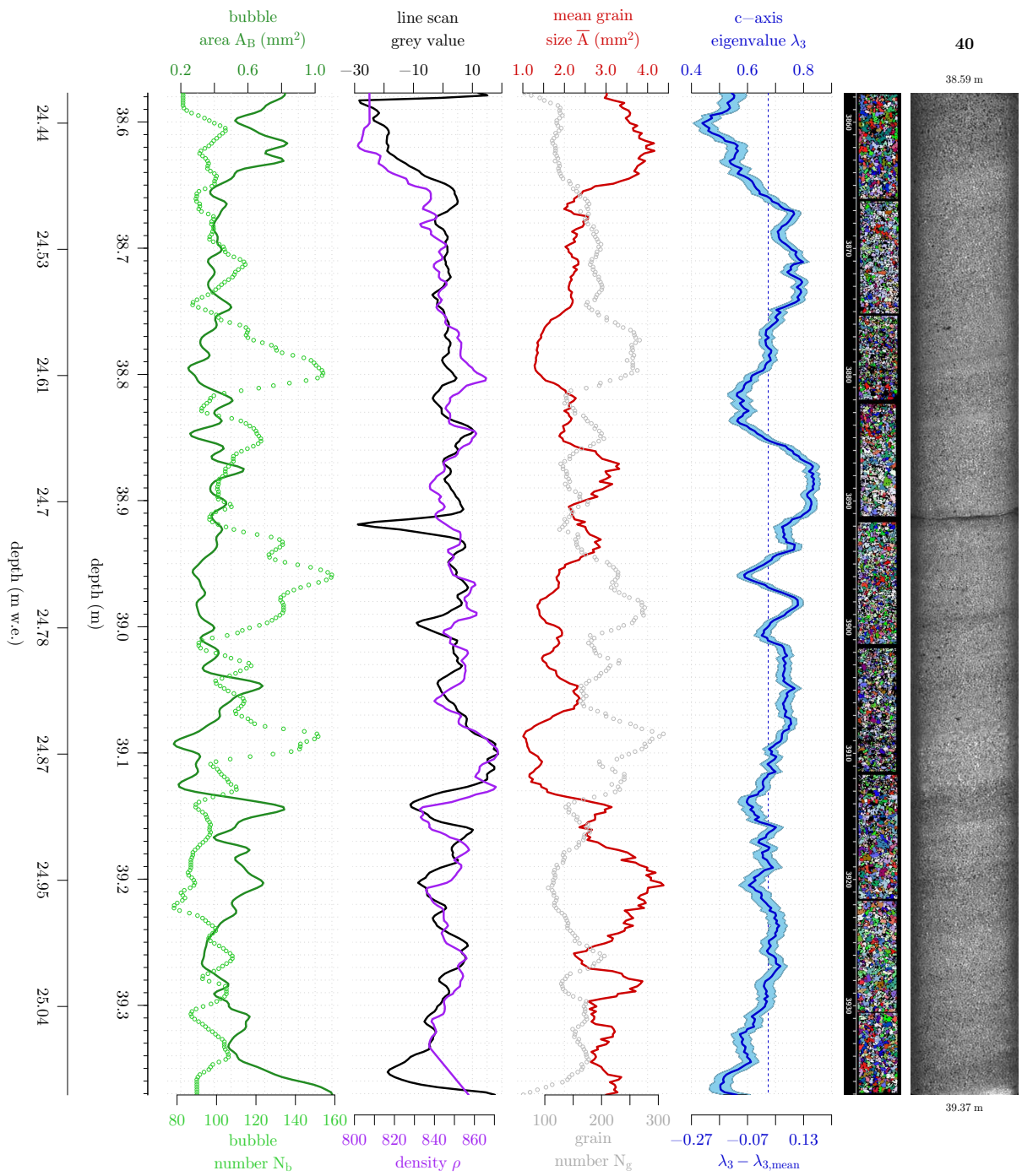
Fig. B.10: Fabric and microstructure in cm-resolution for KCC run 40. The line scan grey value peak at $38.92\,\mathrm{m}$ is due to a break. While line scan and eigenvalue have a common tendency in some places, the inverse relation between grain size and eigenvalue is barely apparent. Third strongest short-scale variability in eigenvalue.
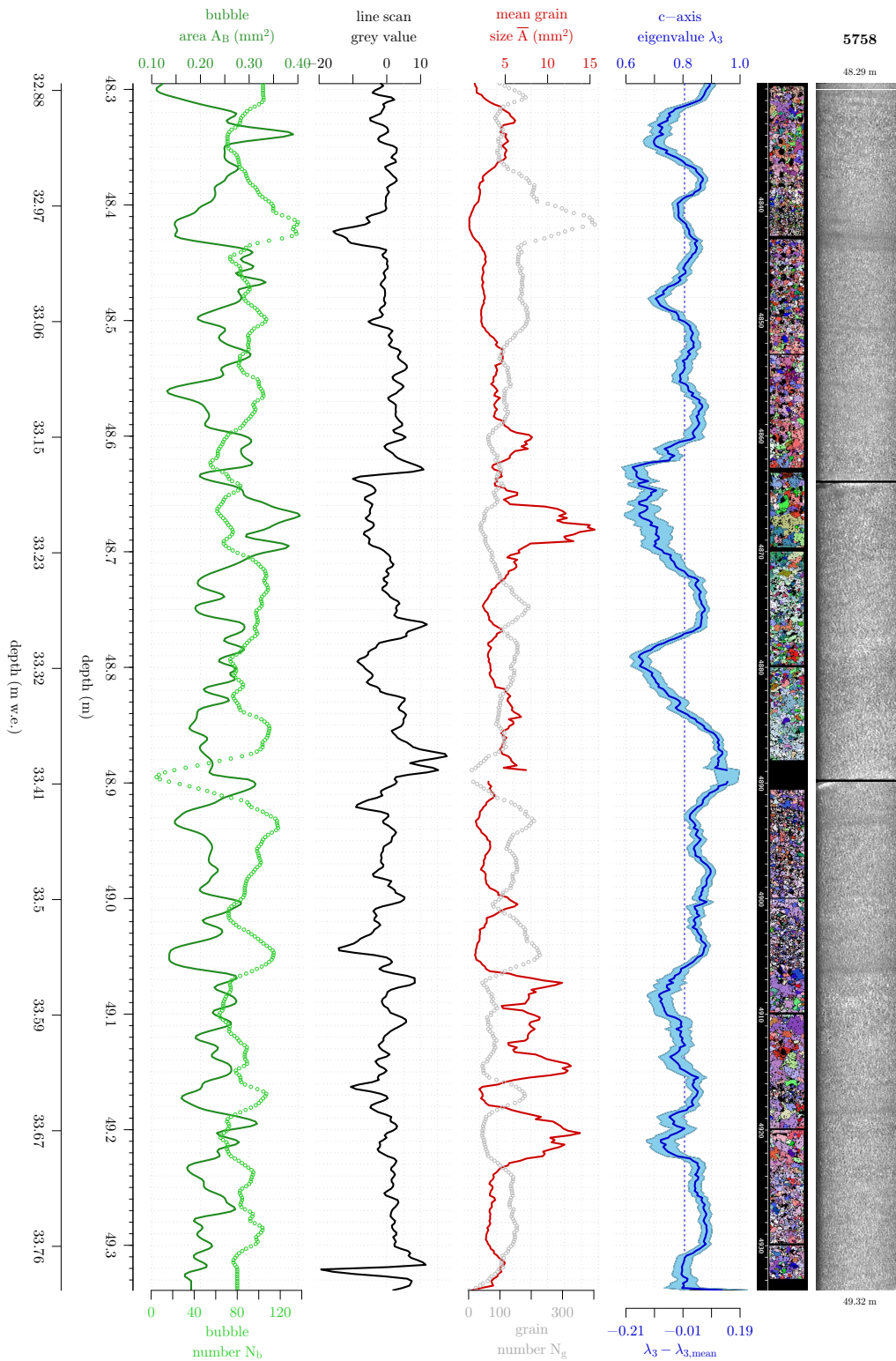
Fig. B.11: Fabric and microstructure in cm-resolution for KCC range 57/58. Some layers with fairly large grains have low eigenvalues. Transitions in the line scan stratigraphy appear to coincide with fabric layer transitions when comparing both the records and the images.
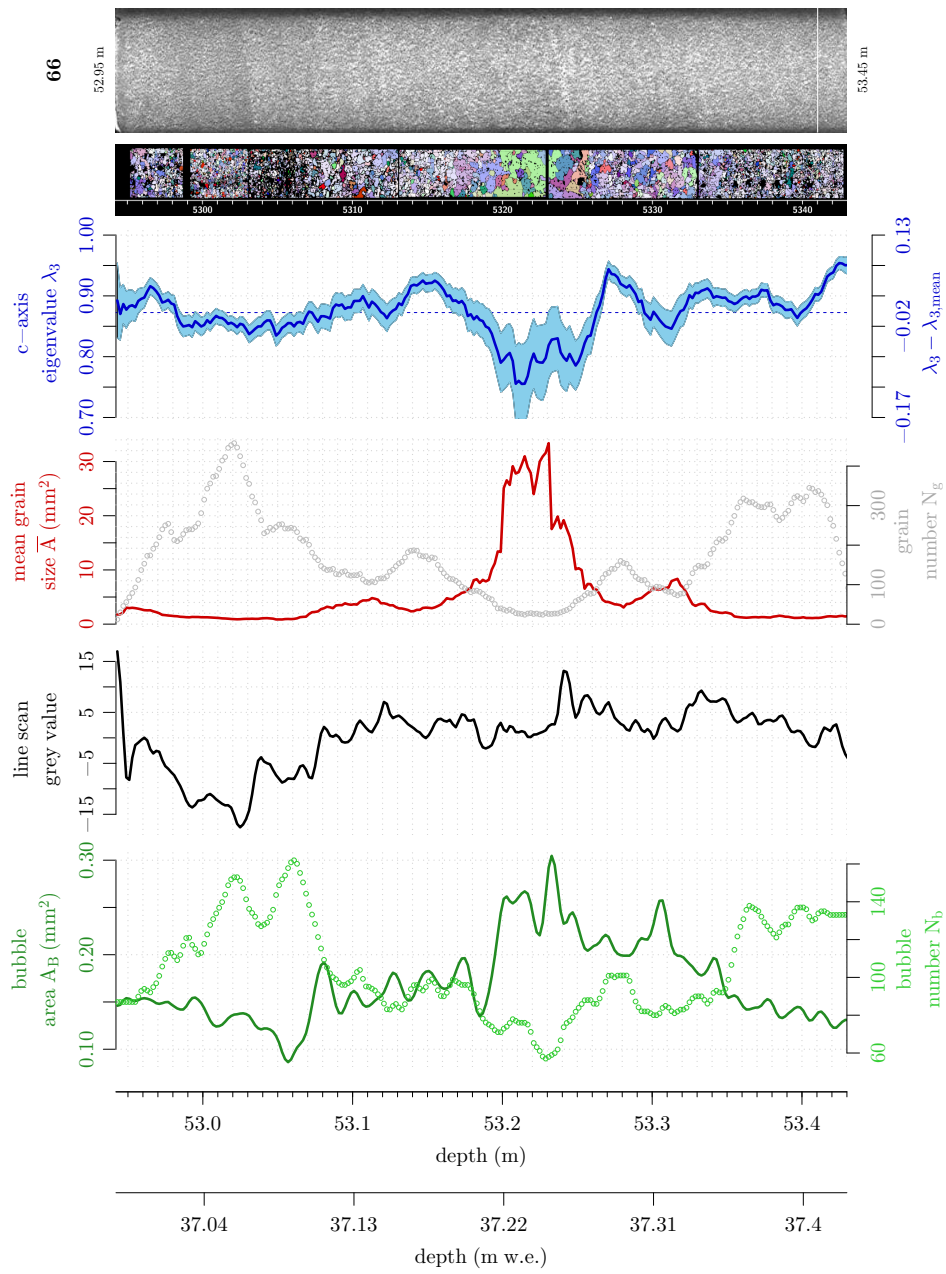
Fig. B.12: Fabric and microstructure in cm-resolution for KCC run 66. A thick layer of less oriented large grains with few large bubbles stands out.
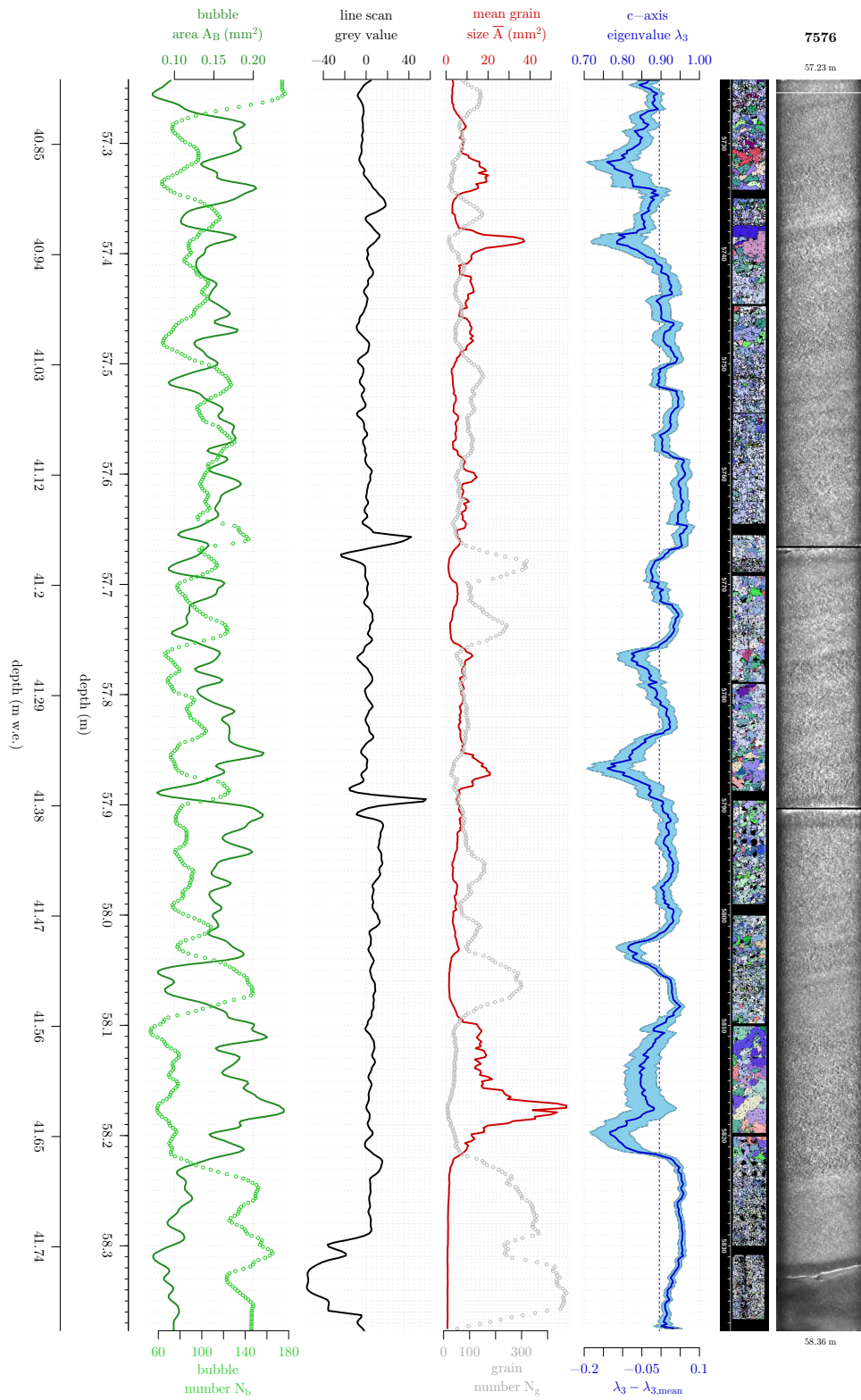
Fig. B.13: Fabric and microstructure in cm-resolution for KCC range 75/76. Several less oriented large-grain layers can be observed, including some strong grain size gradients. Only for a more than 10 cm long section with enormous grains fewer and larger bubbles can be found. At the bottom of this range a stark change in the line scan coincides with a break. The peaks in line scan grey value at 57.65 and 57.89 m depth are artificial.
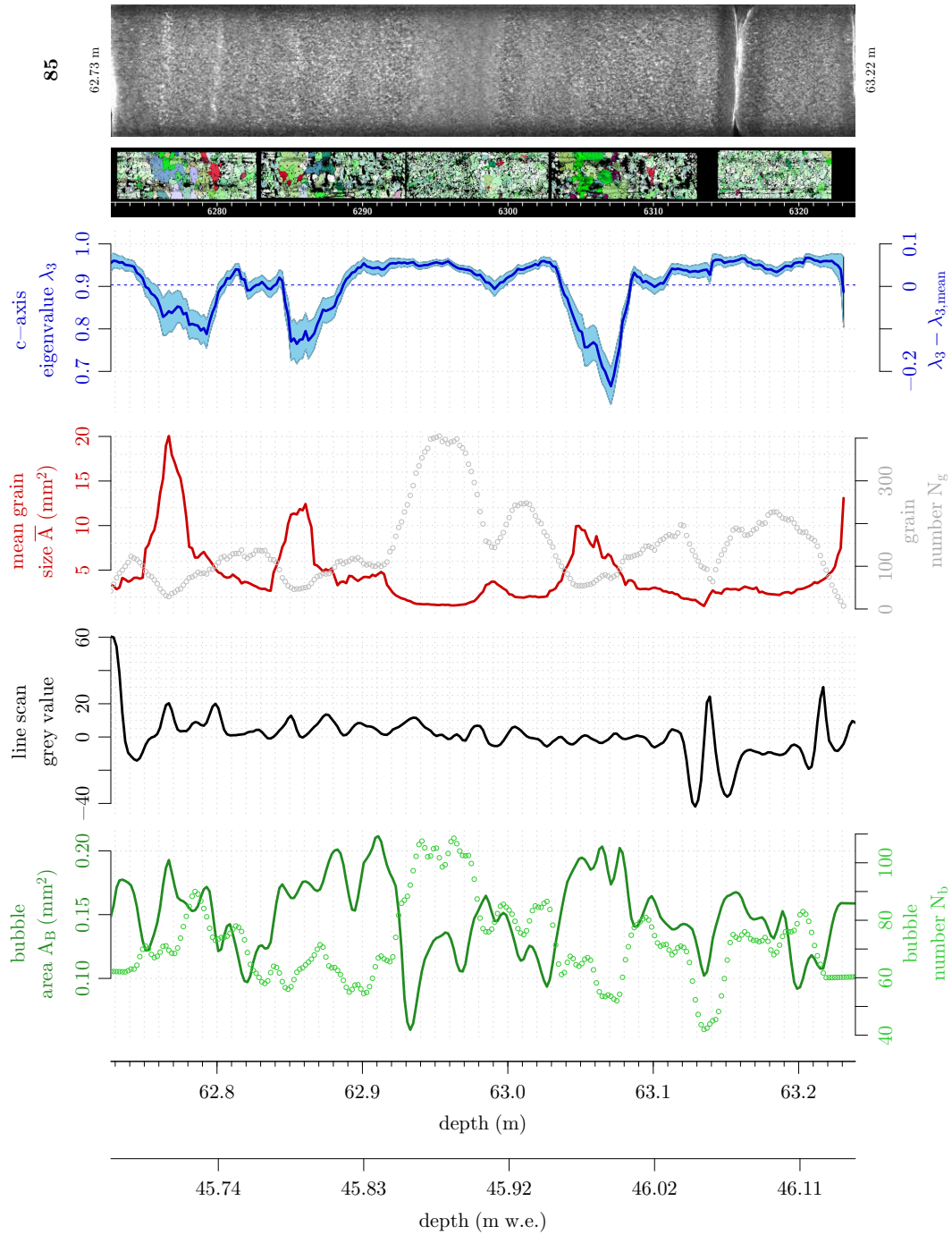
Fig. B.14: Fabric and microstructure in cm-resolution for KCC run 85. Three less oriented large grain layers with a tendency of larger bubbles are apparent. Line scan grey value peaks are again artificially induced from breaks and gaps, otherwise nondescript. The greenish shades of the grain images is due to the different core azimuth of this run as compared to most other runs with shades of purple.
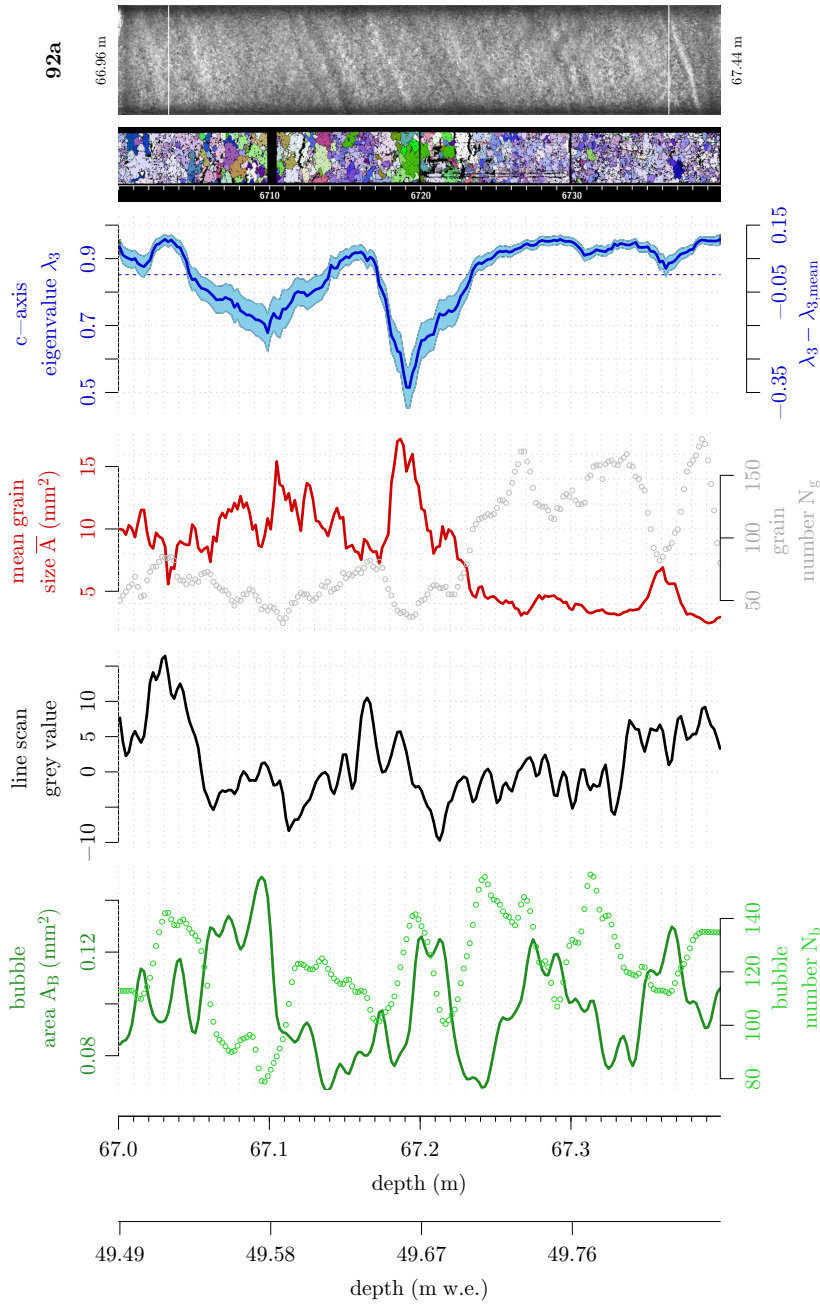
Fig. B.15: Fabric and microstructure in cm-resolution for KCC run 92a. This run is marked by a 20 cm long large-grain section that can be subdivided in three layers of alternating fabric strength. The strongest change in fabric strength in the entire data set is found at 67.2 m depth. The finer stratigraphy of inclined layers visible in the linescan is not represented in the fabric variations. For the upper part of the long section larger and fewer bubbles are observed.
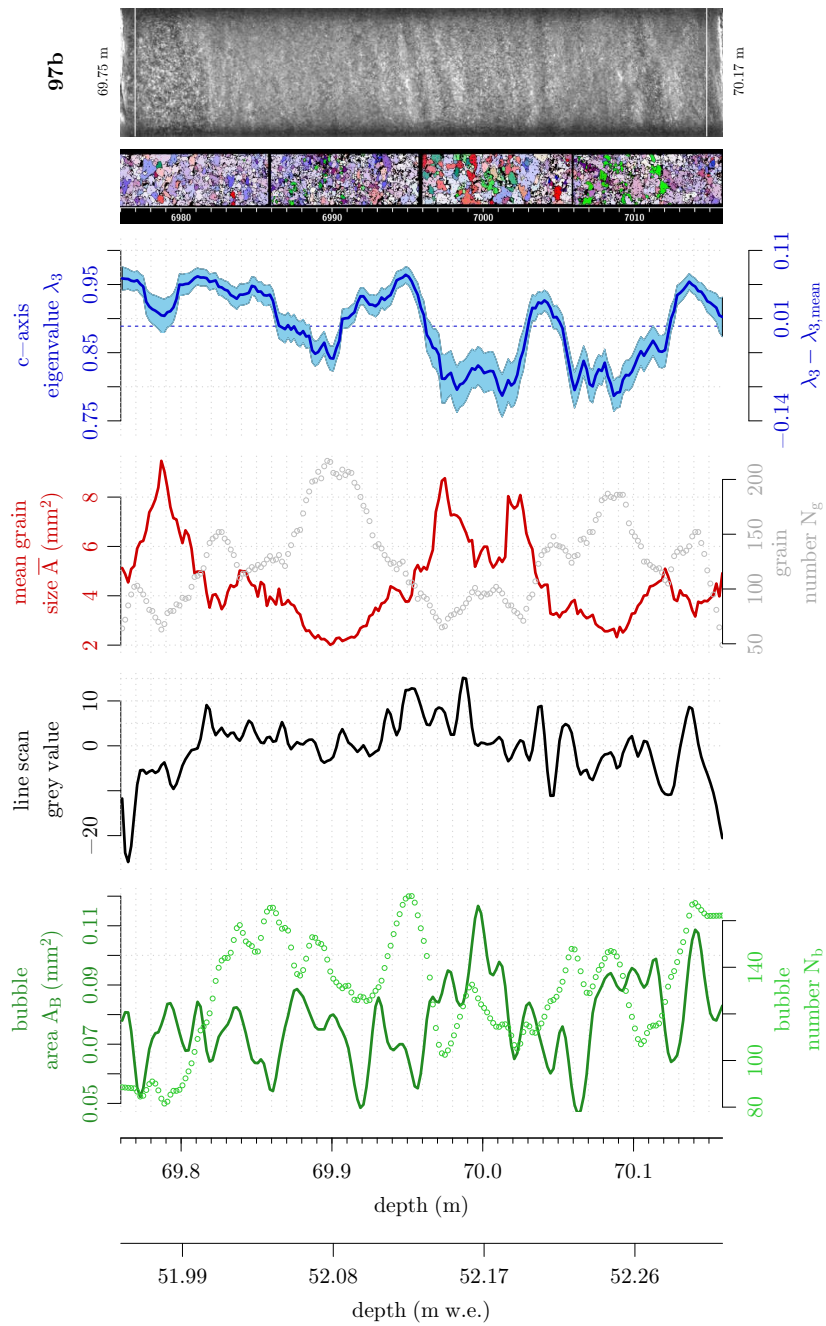
Fig. B.16: Fabric and microstructure in cm-resolution for KCC run 97b. Next to a large-grain section with less oriented grains the fabric is weakened in some sections by several scattered grains with a c-axis orientation almost perpendicular to the cone orientation. These grains contribute to the faint girdle apparent in Fig. 4.9 and B.1.
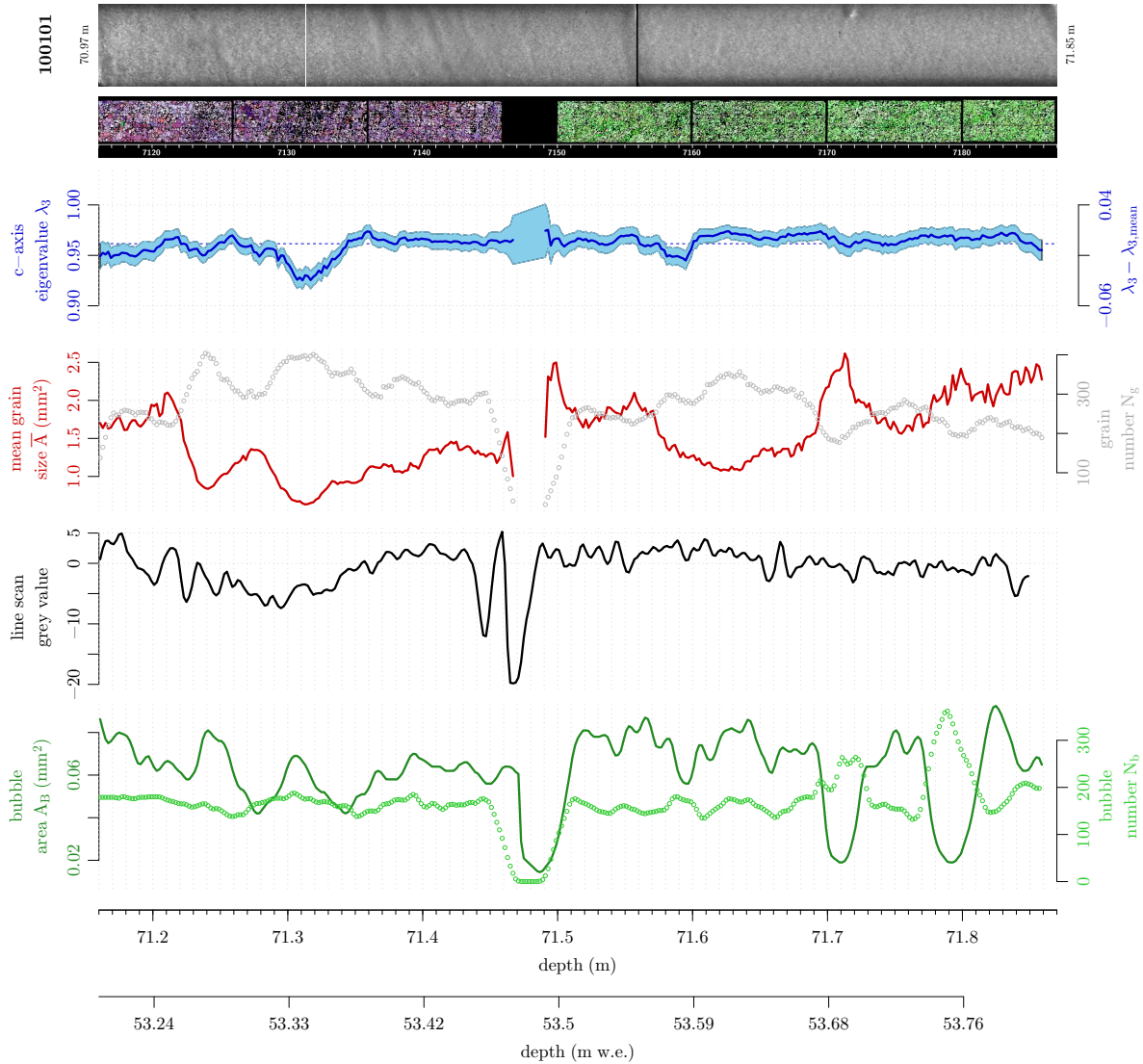
Fig. B.17: Fabric and microstructure in cm-resolution for KCC range 100/101. The basal microstructure is fairly homogeneous. The grain images are differently shaded due to different core azimuth. The lowermost run (green shades) exhibits very faintly steeply inclined structures marked by a slightly different c-axis orientation (Fig. 4.18).

B.11 Cm-scale fabric and impurities graphs
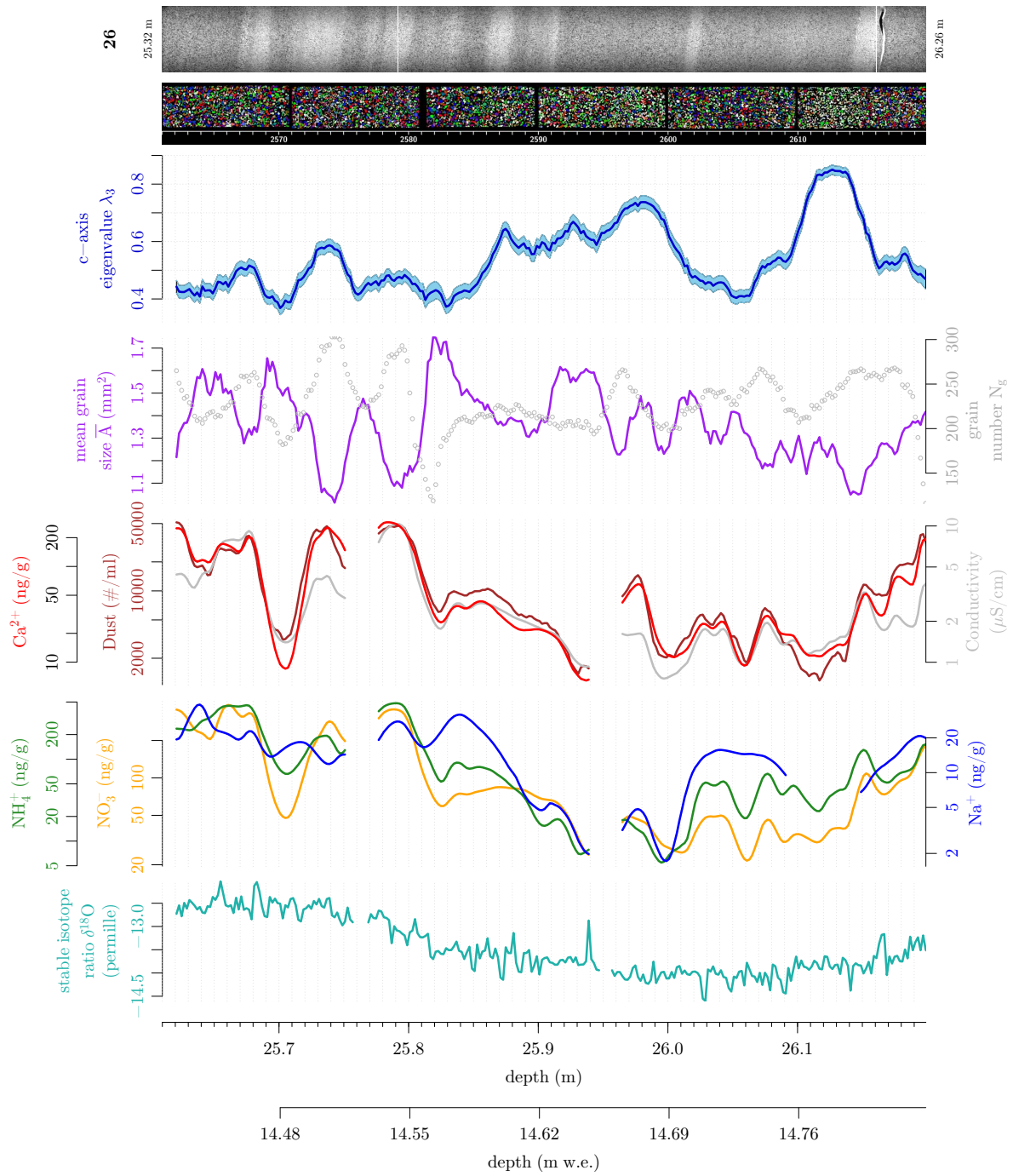
Fig. B.18: Fabric and microstructure parameters in cm-resolution in comparison with CFA data for KCC range 26.
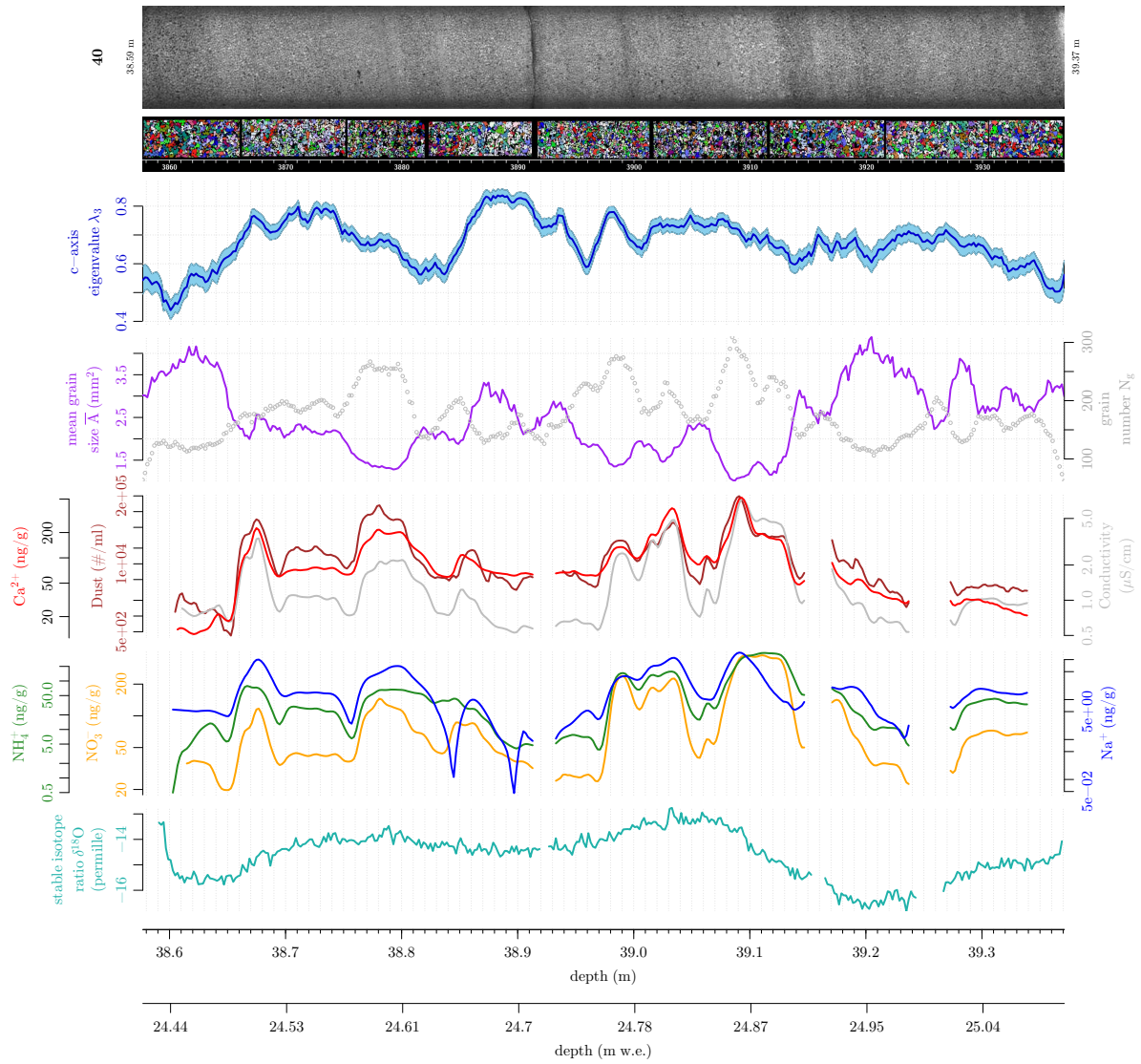
Fig. B.19: Fabric and microstructure parameters in cm-resolution in comparison with CFA data for KCC range 40.
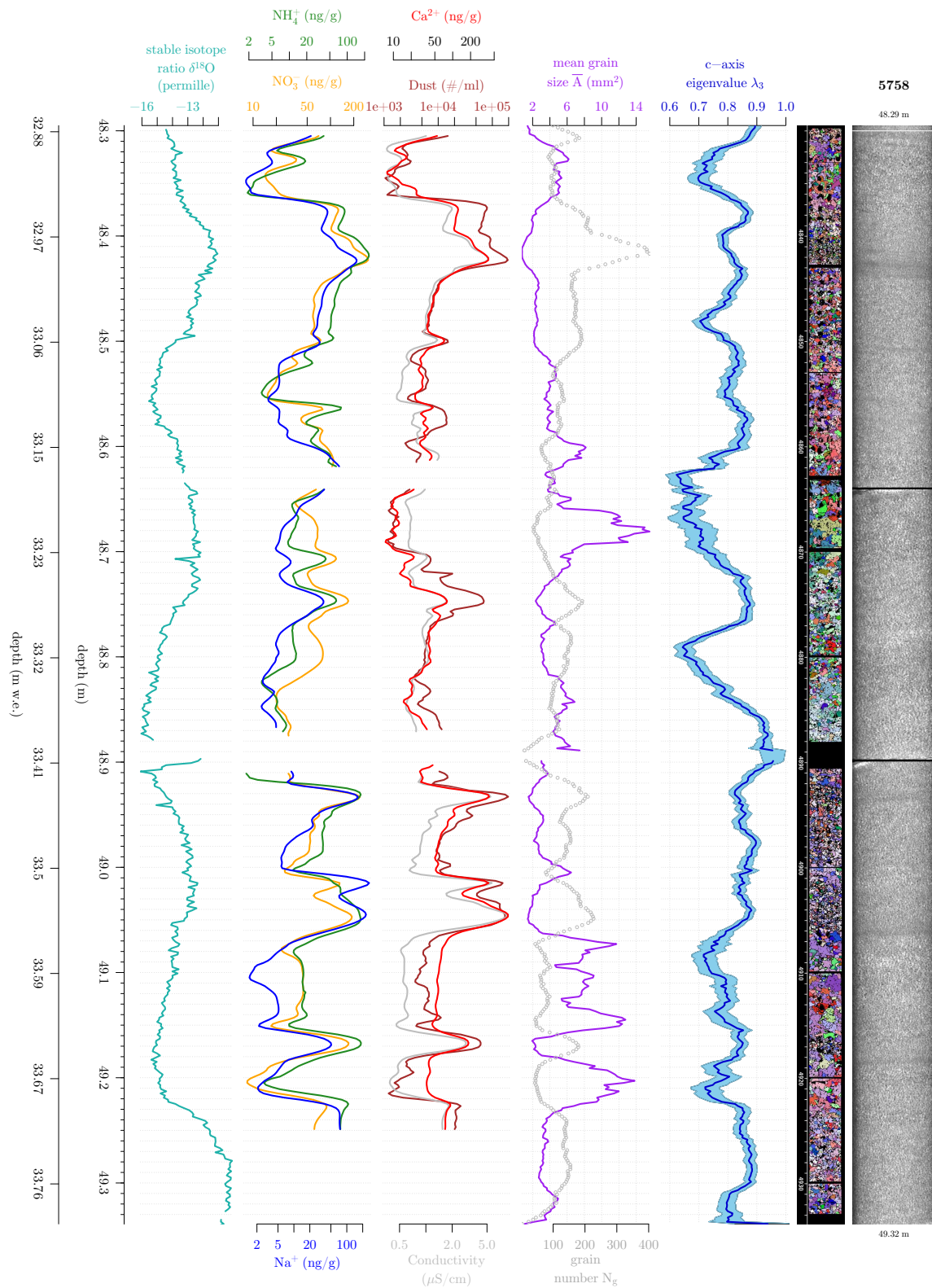
Fig. B.20: Fabric and microstructure parameters in cm-resolution in comparison with CFA data for KCC range 57/58.
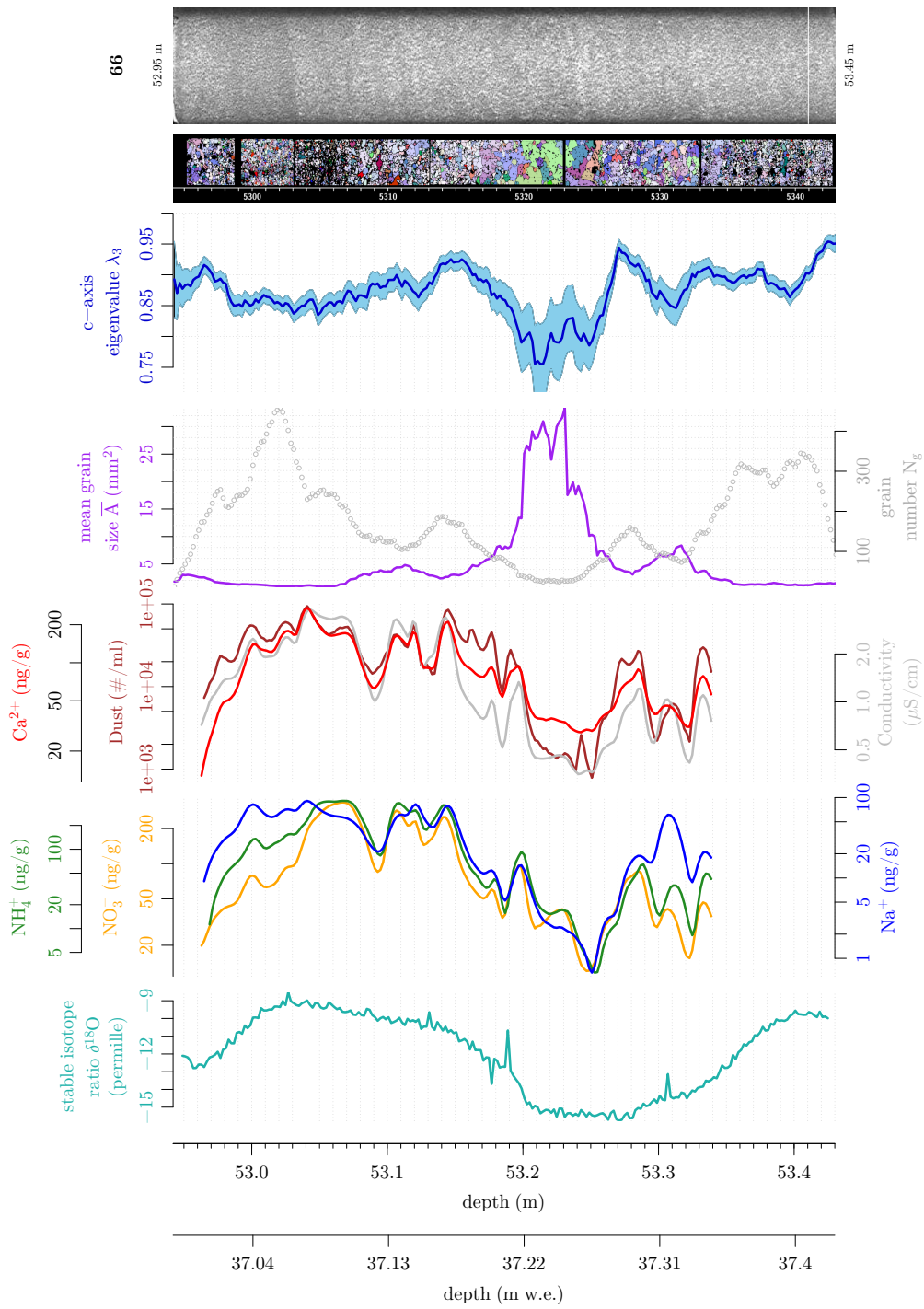
Fig. B.21: Fabric and microstructure parameters in cm-resolution in comparison with CFA data for KCC range 66.
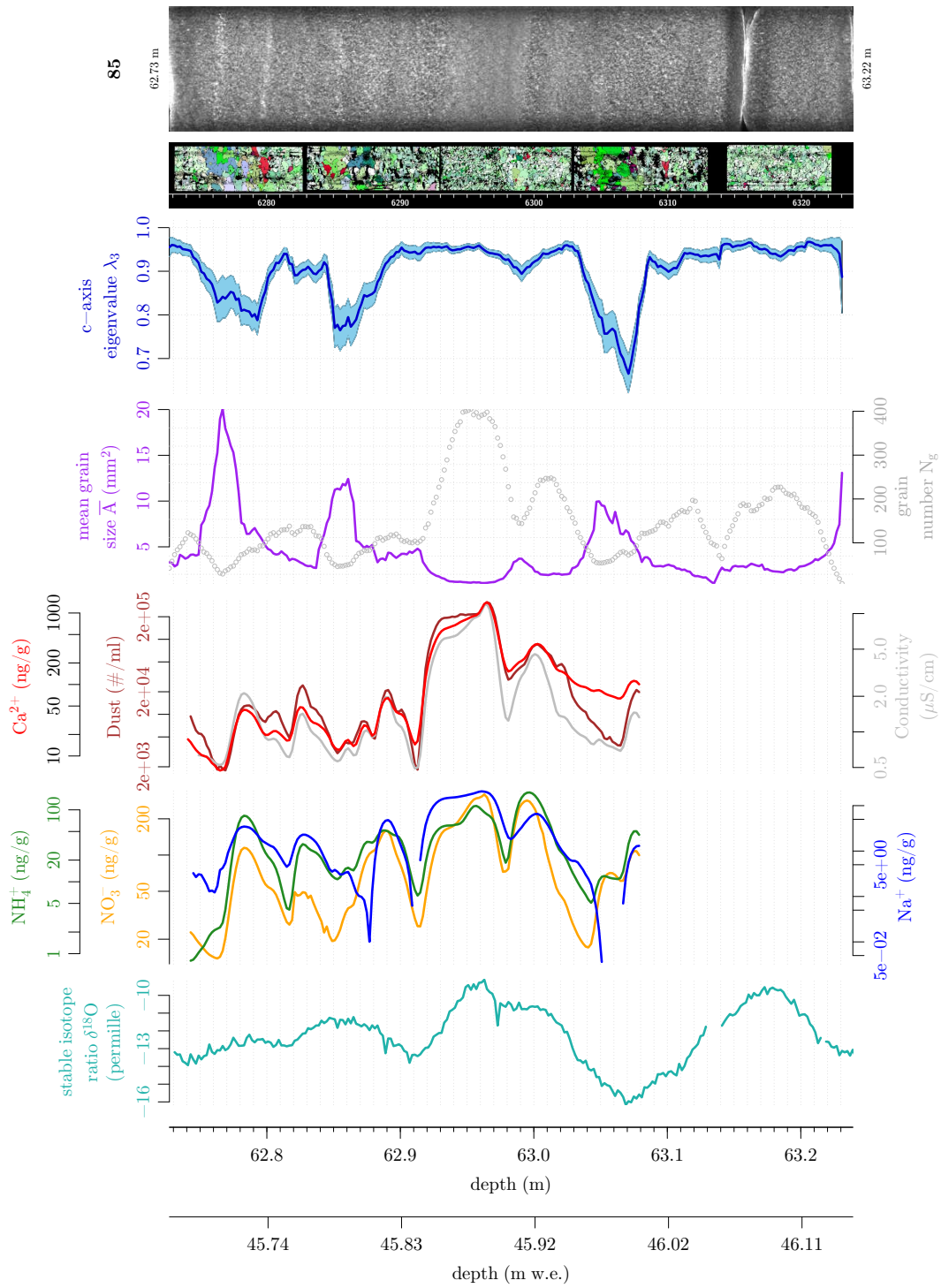
Fig. B.22: Fabric and microstructure parameters in cm-resolution in comparison with CFA data for KCC range 85.
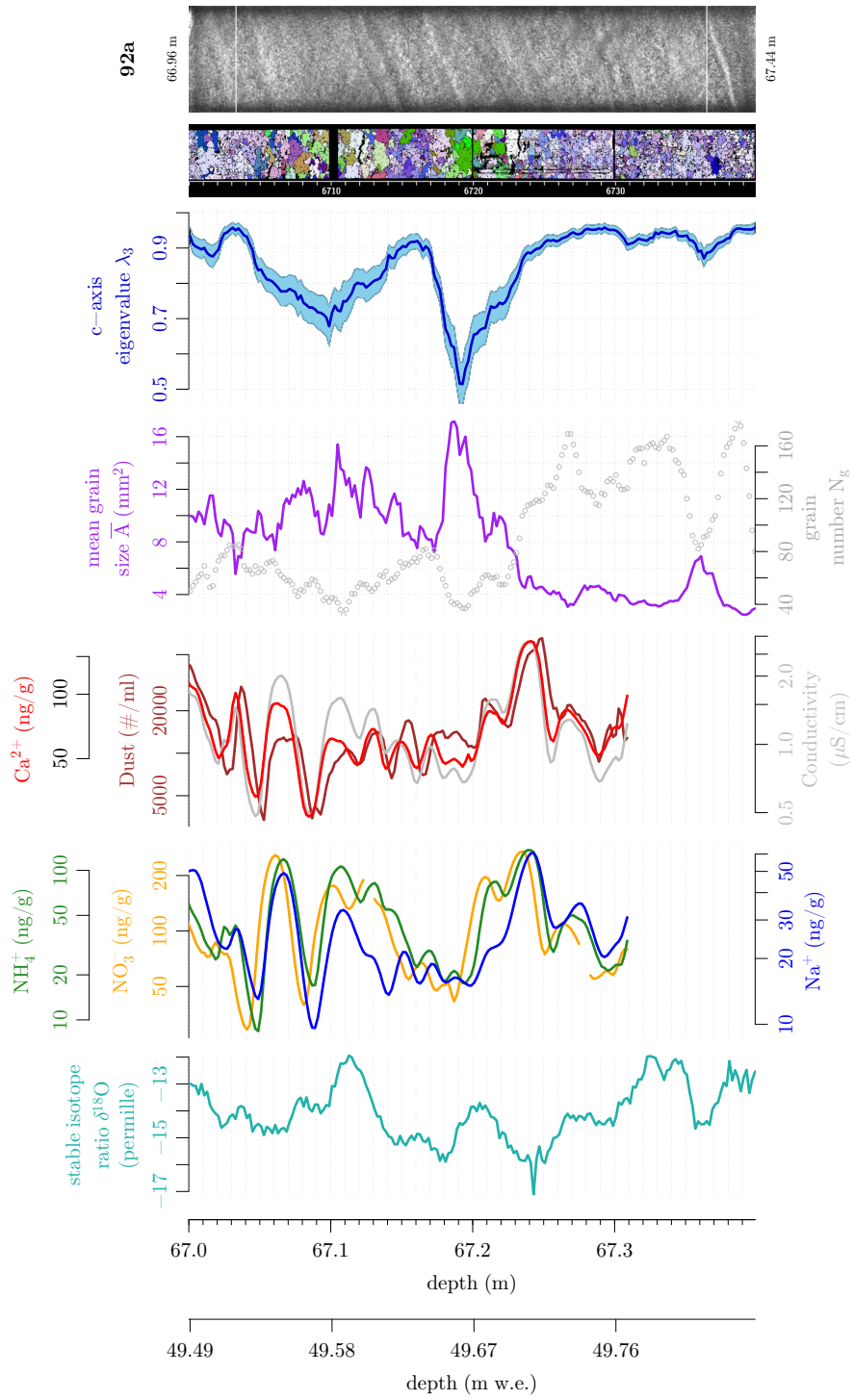
Fig. B.23: Fabric and microstructure parameters in cm-resolution in comparison with CFA data for KCC range 92a.
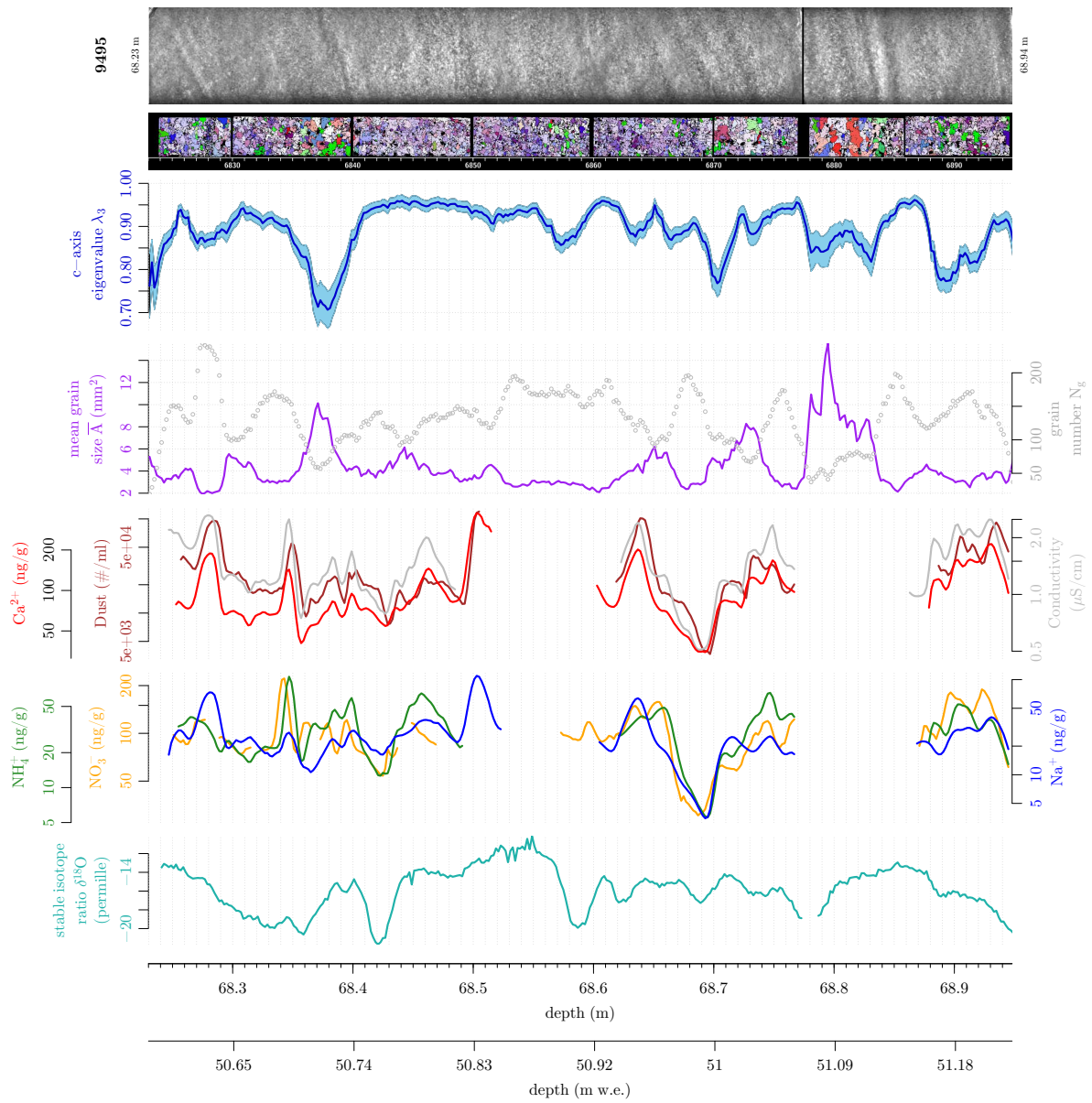
Fig. B.24: Fabric and microstructure parameters in cm-resolution in comparison with CFA data for KCC range 94/95.
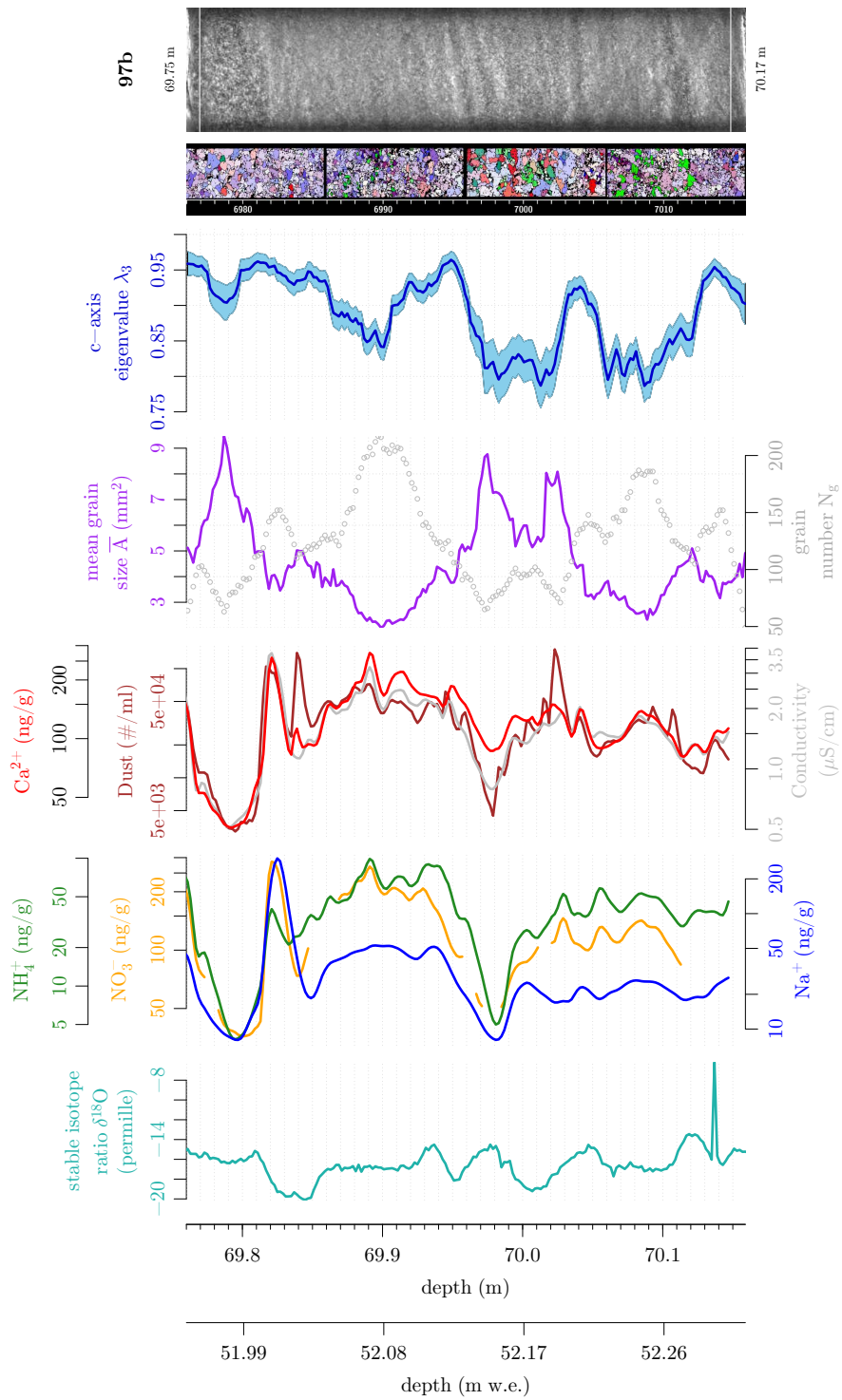
Fig. B.25: Fabric and microstructure parameters in cm-resolution in comparison with CFA data for KCC range 97b.

C. Laser ablation on microstructure

Data from LA-ICP-MS for sodium and iron are shown for individual grains of two exemplary sections out of seven (Tab. 3.4, p. 33). Concentration in grain boundaries is indicated in red, parallel lines in blue. The logarithmic scale is fixed to 25000/15000 counts/sec for better comparison. Dashed lines show the calculated background level for each measurement.

Sodium
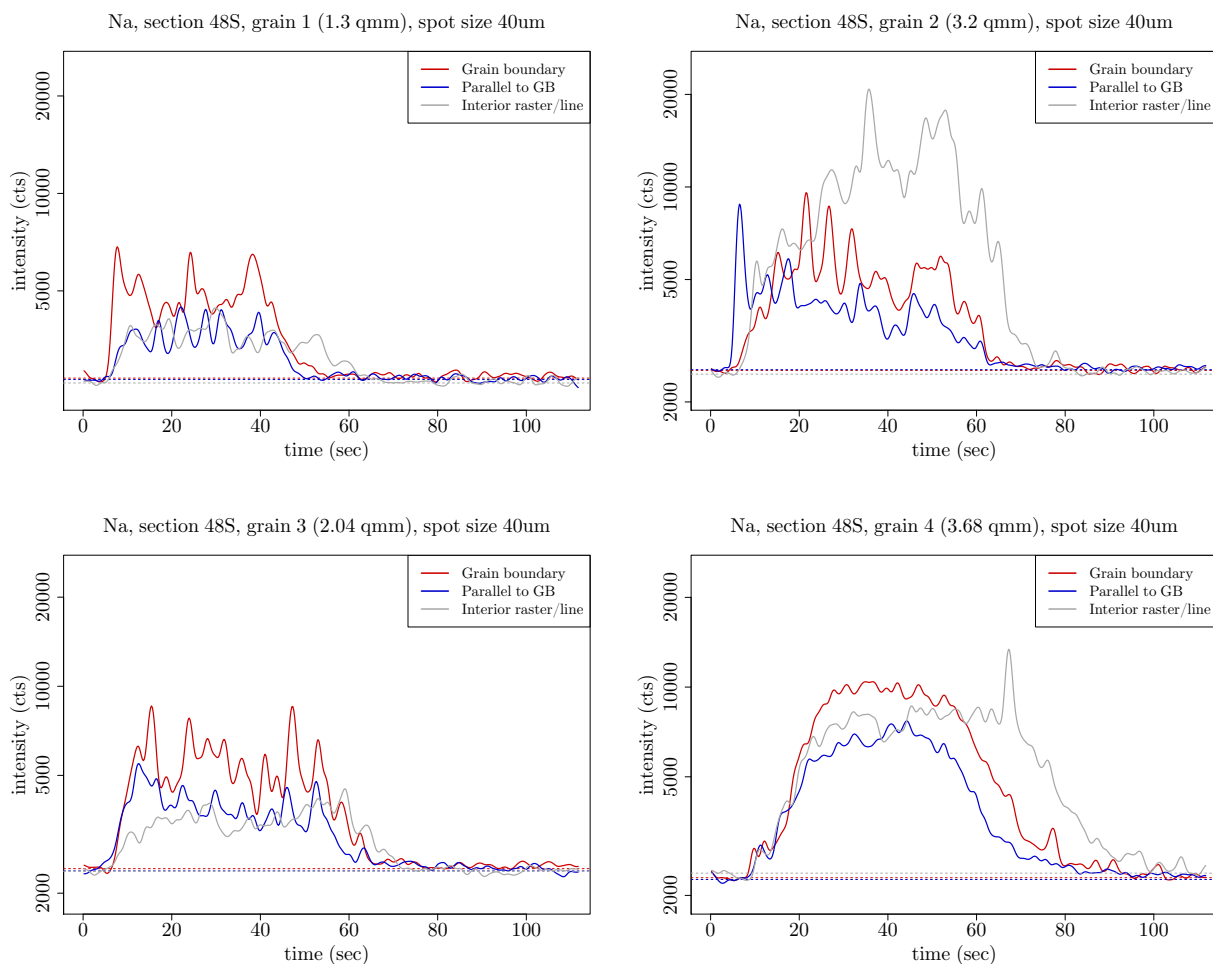
Fig. C.1: Small-grain section 48S: Grain boundaries show mostly higher sodium content than grain interiors. Grain 2 is an exception/outlier to that observation, grain 4 is not clear either – both grains are larger than the others. Grain 5 is shown in Fig. 5.7, p. 77.

Na, section 48L, grain 1 (NA qmm), spot size 40um

Na, section 48L, grain 2 (NA qmm), spot size 40um

Na, section 48L, grain 3 (NA qmm), spot size 40um

Na, section 48L, grain 4 (NA qmm), spot size 40um

Na, section 48L, grain 5 (NA qmm), spot size 40um

Fig. C.2: Larger-grain section 48L: An even larger difference in sodium concent between grain boundary and grain interior can be observed in grains in this section, other than grain 1. For this section no grain size estimates are available.

181

Iron

Fe, section 48S, grain 2 (3.2 qmm), spot size 40um

Fe, section 48S, grain 3 (2.04 qmm), spot size 40um

Fe, section 48S, grain 4 (3.68 qmm), spot size 40um

Fe, section 48S, grain 6 (1.9 qmm), spot size 40um

Fe, section 48S, grain 7 (2.07 qmm), spot size 40um
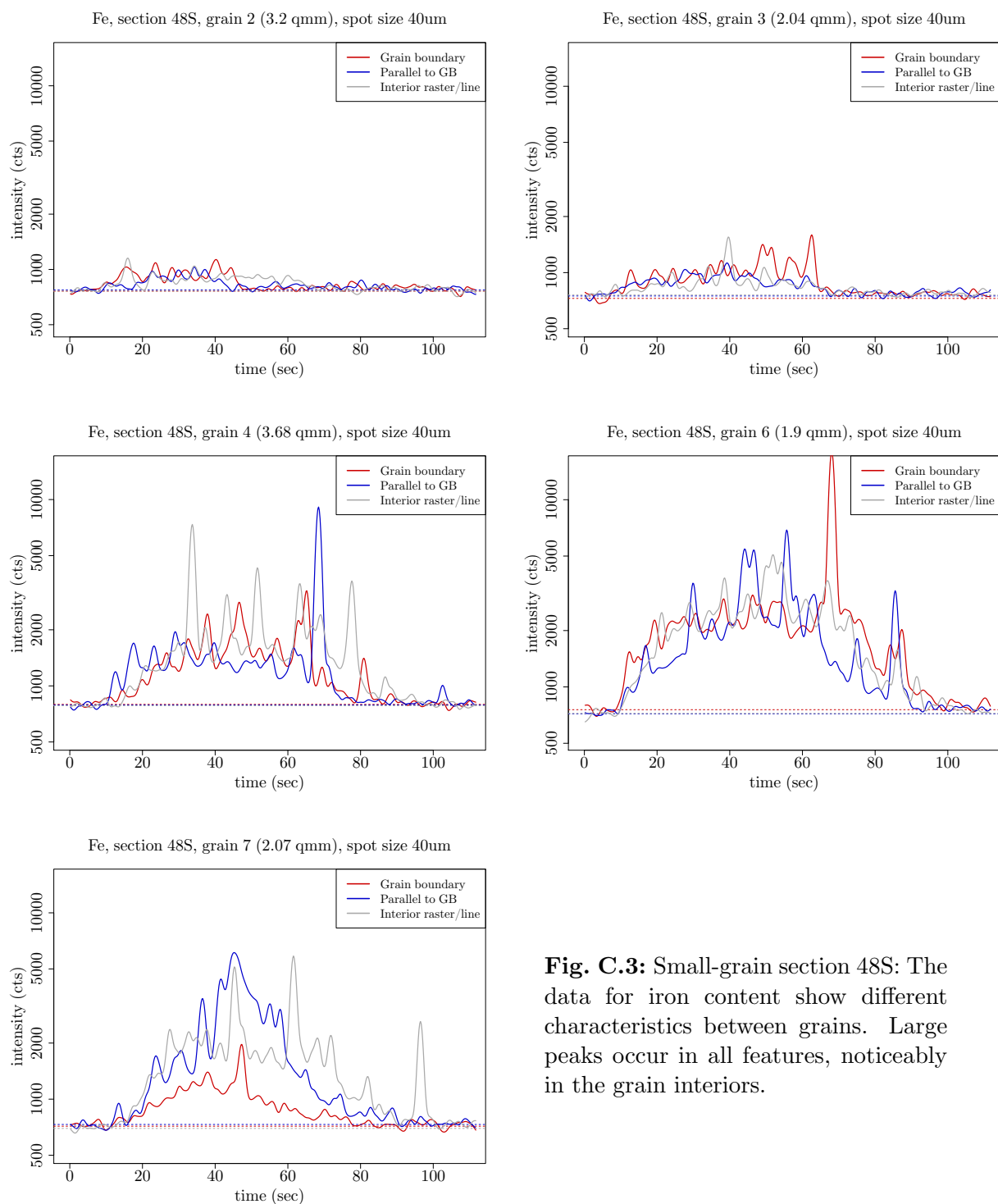
Fig. C.3: Small-grain section 48S: The data for iron content show different characteristics between grains. Large peaks occur in all features, noticeably in the grain interiors.

Fe, section 48L, grain 3 (NA qmm), spot size 40um

Fe, section 48L, grain 4 (NA qmm), spot size 40um

Fe, section 48L, grain 5 (NA qmm), spot size 40um

Fe, section 48L, grain 6 (NA qmm), spot size 40um

Fe, section 48L, grain 7 (NA qmm), spot size 40um
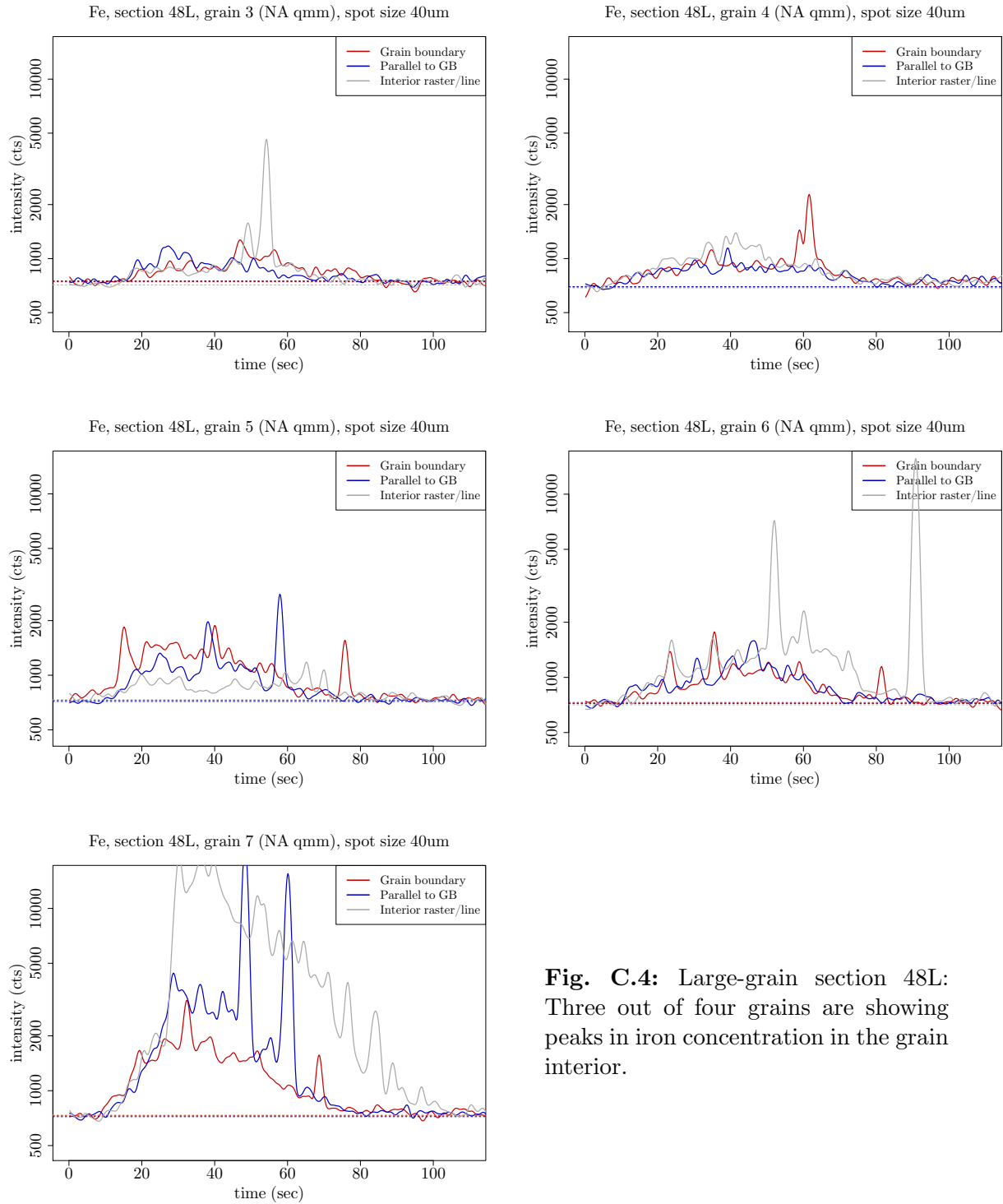
Fig. C.4: Large-grain section 48L: Three out of four grains are showing peaks in iron concentration in the grain interior.

D. Seismic velocities from fabric

D.1 Tensor transformation

A fourth-order tensor rotation is expressed as:

$$c^{\text{rot}}_{mnop} = R_{mi}R_{nj}R_{ok}R_{pl}c_{ijkl} \qquad \text{or} \qquad \mathbf{C}^{\text{rot}} = \mathbf{R} \cdot \mathbf{R} \cdot \mathbf{C} \cdot \mathbf{R}^{\top} \cdot \mathbf{R}^{\top} \tag{D.1}$$

The general rotation matrix in three dimensions is given by the cosines between the axes of local $\{p, q, r\}$ and global $\{x, y, z\}$ coordinate frame:

$$\mathbf{R} = \begin{pmatrix} \cos(x,p) & \cos(x,q) & \cos(x,r) \\ \cos(y,p) & \cos(y,q) & \cos(y,r) \\ \cos(z,p) & \cos(z,q) & \cos(z,r) \end{pmatrix} = \begin{pmatrix} l_1 & l_2 & l_3 \\ m_1 & m_2 & m_3 \\ n_1 & n_2 & n_3 \end{pmatrix} \tag{D.2}$$

For a coordinate transformation of the monocrystal elasticity tensor $\mathbf{C}_{\text{m}}$ from crystal to global frame two basic rotations are needed, one around the y-axis given by the colatitude angle φ and another around the z-axis with azimuth ϑ.

$$\mathbf{R}_y = \begin{pmatrix} \cos(\varphi) & 0 & \sin(\varphi) \\ 0 & 1 & 0 \\ -\sin(\varphi) & 0 & \cos(\varphi) \end{pmatrix} \qquad \text{and} \qquad \mathbf{R}_z = \begin{pmatrix} \cos(\vartheta) & -\sin(\vartheta) & 0 \\ \sin(\vartheta) & \cos(\vartheta) & 0 \\ 0 & 0 & 1 \end{pmatrix} \tag{D.3}$$

It is possible to express both rotations in a single rotation matrix (as done by Maurel et al. (2015, section 3).

By using Voigt notation (section 6.1), which mathematically implies a change of base, the rotation matrix $\mathbf{R}_{\text{C}}$ for the elasticity tensor is constructed following Sunder and Wu (1990, see appendix) using the parameterisation in eq. (D.2) and eq. (D.3) for the respective rotation:

$$\mathbf{R}_{\text{C}} = \begin{pmatrix} l_1^2 & m_1^2 & n_1^2 & m_1 n_1 & n_1 l_1 & l_1 m_1 \\ l_2^2 & m_2^2 & n_2^2 & m_2 n_2 & n_2 l_2 & l_2 m_2 \\ l_3^2 & m_3^2 & n_3^2 & m_3 n_3 & n_3 l_3 & l_3 m_3 \\ 2l_2 l_3 & 2m_2 m_3 & 2n_2 n_3 & m_2 n_3 + m_3 n_2 & n_2 l_3 + n_3 l_2 & l_2 m_3 + l_3 m_2 \\ 2l_3 l_1 & 2m_3 m_1 & 2n_3 n_1 & m_3 n_1 + m_1 n_3 & n_3 l_1 + n_1 l_3 & l_3 m_1 + l_1 m_3 \\ 2l_1 l_2 & 2m_1 m_2 & 2n_1 n_2 & m_1 n_2 + m_2 n_1 & n_1 l_2 + n_2 l_1 & l_1 m_2 + l_2 m_1 \end{pmatrix} \tag{D.4}$$

The rotation matrix $\mathbf{R}_{\text{S}}$ for the compliance tensor is given by:

$$\mathbf{R}_{\text{S}} = \begin{pmatrix} l_1^2 & m_1^2 & n_1^2 & 2m_1 n_1 & 2n_1 l_1 & 2l_1 m_1 \\ l_2^2 & m_2^2 & n_2^2 & 2m_2 n_2 & 2n_2 l_2 & 2l_2 m_2 \\ l_3^2 & m_3^2 & n_3^2 & 2m_3 n_3 & 2n_3 l_3 & 2l_3 m_3 \\ l_2 l_3 & m_2 m_3 & n_2 n_3 & m_2 n_3 + m_3 n_2 & n_2 l_3 + n_3 l_2 & l_2 m_3 + l_3 m_2 \\ l_3 l_1 & m_3 m_1 & n_3 n_1 & m_3 n_1 + m_1 n_3 & n_3 l_1 + n_1 l_3 & l_3 m_1 + l_1 m_3 \\ l_1 l_2 & m_1 m_2 & n_1 n_2 & m_1 n_2 + m_2 n_1 & n_1 l_2 + n_2 l_1 & l_1 m_2 + l_2 m_1 \end{pmatrix} \tag{D.5}$$

The expressions for $\mathbf{R}_{\text{C}}$ and $\mathbf{R}_{\text{S}}$ as given in Diez and Eisen (2015, eq. (A.6) and (A.7)) are reversed by mistake.

D.2 Zero-offset velocities

Tab. D.1: KCC P-wave zero-offset velocities for eigenvalue (only Voigt bound) and c-axes framework (Voigt/Reuss bound).

Depth (m)	v_{p0}^{ev}	v_{p0}^{cx}	$v_{p0}^{cx,R}$	Depth (m)	v_{p0}^{ev}	v_{p0}^{cx}	$v_{p0}^{cx,R}$
25.61	3875.82	3850.08	3830.87	53.23	3973.62	3918.39	3891.84
25.71	3876.19	3862.74	3841.62	53.33	3998.40	3969.82	3951.39
25.82	3876.74	3857.20	3836.99	57.24	3950.29	3898.14	3872.31
25.90	3908.39	3876.45	3852.45	57.35	3977.16	3910.01	3886.37
26.00	3876.91	3856.59	3836.34	57.45	4003.32	3941.39	3925.76
26.10	3905.76	3884.23	3859.58	57.55	4017.84	3958.99	3950.27
31.43	3889.83	3865.78	3842.22	57.65	4009.67	3963.32	3948.06
31.53	3899.32	3879.51	3854.08	57.69	3996.27	3943.37	3923.87
31.63	3893.55	3875.75	3851.32	57.79	3976.77	3917.63	3893.31
31.73	3885.11	3858.18	3836.08	57.89	3997.12	3936.09	3916.18
31.83	3904.71	3878.89	3853.06	58.00	3992.96	3937.00	3915.71
31.93	3882.03	3861.89	3839.48	58.10	3958.25	3892.96	3865.11
38.58	3881.36	3851.53	3830.64	58.20	3999.27	3948.72	3929.05
38.66	3936.26	3915.12	3888.81	58.31	4008.14	3983.57	3966.72
38.75	3902.89	3881.28	3855.37	62.73	3977.16	3926.67	3902.74
38.82	3927.88	3908.61	3880.89	62.83	3984.21	3928.59	3908.40
38.92	3911.84	3892.70	3865.89	62.93	4013.36	3962.10	3950.23
39.02	3922.57	3892.31	3864.72	63.03	3953.65	3921.26	3898.19
39.12	3905.23	3868.44	3844.50	63.14	4018.42	3967.88	3956.65
39.22	3917.97	3877.11	3850.94	67.00	3956.32	3921.55	3894.74
39.30	3887.64	3870.33	3846.48	67.11	3926.74	3906.07	3879.60
43.37	3921.48	3877.83	3851.35	67.20	3974.01	3943.61	3921.58
43.47	3915.30	3865.84	3842.12	67.30	4007.15	3949.31	3935.05
43.57	3928.16	3888.69	3861.03	68.23	3978.73	3937.31	3919.74
43.67	3939.48	3913.73	3885.70	68.30	3957.09	3925.56	3903.25
43.77	3928.45	3869.01	3845.09	68.40	4017.84	3962.21	3950.17
43.88	3916.90	3865.44	3841.09	68.50	3996.27	3938.58	3922.21
48.30	3948.83	3880.74	3856.01	68.60	4001.49	3941.91	3930.18
48.33	3947.74	3899.01	3872.49	68.70	3986.17	3951.06	3931.21
48.43	3942.49	3897.67	3871.30	68.78	3967.29	3926.61	3900.47
48.53	3954.79	3885.48	3860.26	68.86	3964.52	3939.02	3920.92
48.63	3920.39	3856.84	3832.73	69.76	4013.91	3960.10	3947.29

Depth (m)	P-wave zero-offset velocities			Depth (m)	P-wave zero-offset velocities		
	$v_{\text{p0}}^{\text{ev}}$	$v_{\text{p0}}^{\text{cx}}$	$v_{\text{p0}}^{\text{cx,R}}$		$v_{\text{p0}}^{\text{ev}}$	$v_{\text{p0}}^{\text{cx}}$	$v_{\text{p0}}^{\text{cx,R}}$
48.70	3943.17	3901.03	3874.44	69.86	3997.12	3953.21	3936.20
48.80	3963.73	3916.66	3893.08	69.96	3964.12	3932.60	3905.48
48.90	3972.43	3923.42	3899.46	70.06	3973.62	3941.27	3925.56
49.00	3967.29	3909.92	3887.01	71.16	4022.55	3930.55	3920.13
49.10	3960.98	3884.80	3861.28	71.26	4019.58	3924.62	3914.48
49.20	3974.40	3920.66	3897.66	71.36	4027.41	3930.37	3922.01
49.30	3954.79	3896.76	3872.66	71.50	4026.80	3902.62	3895.58
52.94	3994.19	3950.98	3930.36	71.60	4031.05	3913.41	3907.36
52.99	3975.19	3949.96	3925.18	71.70	4029.84	3911.93	3905.88
53.03	3983.04	3960.35	3938.94	71.80	4031.05	3896.33	3891.25
53.13	3972.04	3936.28	3907.37				

Tab. D.2: KCC S-wave zero-offset velocities for eigenvalue ($v_{\text{sh}}^{\text{ev}} = v_{\text{sv}}^{\text{ev}}$) and c-axes framework (only Voigt bound velocities).

Depth (m)	S-wave zero-offset velocities			Depth (m)	S-wave zero-offset velocities		
	$v_{\text{s0}}^{\text{ev}}$	$v_{\text{sh0}}^{\text{cx}}$	$v_{\text{sv0}}^{\text{cx}}$		$v_{\text{s0}}^{\text{ev}}$	$v_{\text{sh0}}^{\text{cx}}$	$v_{\text{sv0}}^{\text{cx}}$
25.61	1947.73	1950.08	1969.77	53.23	1878.81	1909.77	1945.13
25.71	1948.86	1941.88	1957.01	53.33	1855.88	1865.68	1894.84
25.82	1949.56	1945.78	1963.45	57.24	1899.50	1911.12	1972.02
25.90	1933.58	1942.44	1956.69	57.35	1875.58	1922.75	1942.38
26.00	1949.69	1948.21	1963.02	57.45	1851.23	1869.25	1944.01
26.10	1935.51	1930.23	1955.23	57.55	1837.32	1841.12	1939.62
31.43	1946.03	1945.94	1967.92	57.65	1845.18	1852.10	1921.58
31.53	1940.04	1932.84	1961.18	57.69	1857.89	1878.20	1931.74
31.63	1943.82	1942.12	1953.49	57.79	1875.94	1902.07	1950.77
31.73	1948.47	1955.65	1967.38	57.89	1857.09	1888.18	1934.73
31.83	1936.27	1932.17	1966.73	58.00	1860.99	1871.94	1948.77
31.93	1949.67	1947.50	1966.04	58.10	1892.55	1925.49	1971.88
38.58	1949.87	1943.04	1989.34	58.20	1855.06	1871.46	1929.22
38.66	1911.46	1904.68	1941.67	58.31	1846.64	1857.40	1879.81
38.75	1937.57	1937.60	1956.52	62.73	1875.58	1905.24	1932.08
38.82	1918.37	1906.89	1948.48	62.83	1869.11	1894.76	1936.79
38.92	1931.01	1918.20	1958.56	62.93	1841.63	1847.89	1925.94
39.02	1922.65	1927.11	1958.12	63.03	1896.58	1895.08	1933.34
39.12	1935.89	1933.93	1984.24	63.14	1836.76	1843.01	1921.08

Depth (m)	S-wave zero-offset velocities			Depth (m)	S-wave zero-offset velocities		
	$v_{\text{s0}}^{\text{ev}}$	$v_{\text{sh0}}^{\text{cx}}$	$v_{\text{sv0}}^{\text{cx}}$		$v_{\text{s0}}^{\text{ev}}$	$v_{\text{sh0}}^{\text{cx}}$	$v_{\text{sv0}}^{\text{cx}}$
39.22	1926.28	1934.65	1976.96	67.00	1894.24	1891.91	1950.64
39.30	1947.23	1934.46	1968.52	67.11	1919.30	1891.22	1967.68
43.37	1923.52	1953.82	1959.97	67.20	1878.45	1880.38	1921.45
43.47	1928.36	1928.13	2001.50	67.30	1847.59	1850.05	1946.11
43.57	1918.14	1941.86	1952.80	68.23	1874.15	1867.45	1943.79
43.67	1908.75	1911.21	1940.19	68.30	1893.57	1893.91	1937.38
43.77	1917.91	1940.27	1988.58	68.40	1837.32	1853.20	1923.06
43.88	1927.12	1937.01	1995.49	68.50	1857.89	1854.79	1959.41
48.30	1900.77	1939.13	1976.38	68.60	1852.96	1849.47	1956.64
48.33	1901.70	1933.43	1948.68	68.70	1867.30	1867.40	1924.67
48.43	1906.20	1932.76	1948.25	68.78	1884.51	1896.75	1940.19
48.53	1895.59	1930.05	1977.00	68.86	1886.99	1865.22	1937.03
48.63	1924.38	1940.11	2010.95	69.76	1841.11	1859.15	1920.62
48.70	1905.62	1901.40	1975.01	69.86	1857.09	1860.28	1928.90
48.80	1887.69	1883.38	1967.53	69.96	1887.34	1889.96	1935.97
48.90	1879.88	1912.08	1930.17	70.06	1878.81	1857.92	1945.03
49.00	1884.51	1896.84	1966.23	71.16	1832.74	1852.63	1978.14
49.10	1890.14	1907.56	2001.39	71.26	1835.63	1852.90	1987.39
49.20	1878.09	1901.71	1944.09	71.36	1828.00	1848.52	1982.63
49.30	1895.59	1915.72	1966.80	71.50	1828.60	1853.16	2023.78
52.94	1859.84	1876.21	1918.84	71.60	1824.42	1849.13	2010.49
52.99	1877.38	1878.07	1915.92	71.70	1825.61	1849.28	2012.69
53.03	1870.20	1874.83	1900.33	71.80	1824.42	1850.92	2036.58
53.13	1880.24	1885.09	1938.73				

Tab. D.3: EDML P-wave zero-offset velocities for eigenvalue (only Voigt bound) and c-axes framework (Voigt/Reuss bound).

Depth (m)	P-wave zero-offset velocities			Depth (m)	P-wave zero-offset velocities		
	$v_{\text{p0}}^{\text{ev}}$	$v_{\text{p0}}^{\text{cx}}$	$v_{\text{p0}}^{\text{cx,R}}$		$v_{\text{p0}}^{\text{ev}}$	$v_{\text{p0}}^{\text{cx}}$	$v_{\text{p0}}^{\text{cx,R}}$
104.05	3876.60	3857.88	3837.16	1960.00	3959.14	3949.21	3923.31
144.05	3877.50	3860.92	3839.40	1960.90	3960.74	3963.07	3940.73
205.15	3875.95	3846.66	3827.63	1975.05	3896.26	3920.48	3893.49
255.15	3876.01	3858.22	3837.63	1995.05	3905.42	3917.72	3892.33
304.35	3875.74	3850.60	3831.45	2004.00	3911.93	3937.29	3911.24
355.15	3875.94	3856.17	3836.04	2004.90	3965.98	3972.79	3950.56

Appendix

Depth (m)	P-wave zero-offset velocities			Depth (m)	P-wave zero-offset velocities		
	$v_{\mathrm{p0}}^{\mathrm{ev}}$	$v_{\mathrm{p0}}^{\mathrm{cx}}$	$v_{\mathrm{p0}}^{\mathrm{cx,R}}$		$v_{\mathrm{p0}}^{\mathrm{ev}}$	$v_{\mathrm{p0}}^{\mathrm{cx}}$	$v_{\mathrm{p0}}^{\mathrm{cx,R}}$
395.15	3875.73	3859.37	3838.99	2025.05	3901.81	3934.79	3909.73
454.00	3877.68	3861.07	3839.76	2035.05	3961.29	3954.64	3931.05
454.25	3876.02	3852.53	3832.62	2045.05	4013.31	3998.87	3983.87
454.90	3892.26	3879.79	3854.71	2052.00	4010.81	4006.08	3991.05
506.00	3886.36	3883.44	3858.73	2052.90	4024.12	4010.94	3999.71
506.90	3882.39	3863.63	3841.00	2055.05	4003.51	3988.81	3969.71
553.00	3879.68	3863.71	3841.39	2085.05	3998.92	3988.19	3968.43
553.90	3883.40	3873.11	3849.54	2095.05	3993.45	3984.67	3964.20
555.45	3877.08	3850.11	3830.24	2104.00	4034.63	4028.05	4020.69
604.00	3882.25	3868.56	3845.46	2104.90	4027.90	4022.60	4014.63
604.90	3890.78	3875.90	3851.27	2105.05	3998.53	4001.63	3986.43
636.85	3875.75	3854.10	3834.39	2154.00	4024.72	4018.35	4008.26
655.45	3876.18	3854.21	3834.18	2154.90	4034.29	4027.88	4020.34
657.00	3885.21	3877.47	3853.74	2155.05	4014.46	4007.55	3994.21
657.90	3888.36	3865.23	3841.73	2204.00	3998.62	3986.60	3965.44
702.00	3884.09	3875.01	3851.04	2204.90	3997.71	3999.45	3982.13
702.90	3885.56	3871.78	3847.97	2254.00	4020.64	4002.88	3989.20
754.00	3886.09	3866.36	3843.05	2254.90	3988.31	3986.00	3968.06
754.90	3892.80	3875.03	3850.36	2265.05	4010.03	3997.32	3979.64
755.95	3880.33	3860.07	3838.01	2276.05	3975.67	3972.26	3949.08
805.00	3894.01	3876.91	3852.04	2285.05	3965.90	3956.89	3930.60
805.90	3890.63	3876.95	3852.18	2295.05	3992.51	3962.43	3941.70
853.00	3860.49	3892.49	3866.56	2304.00	3988.38	3991.11	3972.15
853.90	3859.73	3882.44	3857.08	2304.90	4006.37	3992.87	3974.46
854.75	3856.32	3865.35	3842.84	2306.05	3860.19	3907.79	3881.02
906.00	3861.29	3898.64	3871.66	2316.25	3992.55	3981.17	3959.80
906.90	3863.18	3897.74	3870.55	2345.05	3975.19	3948.03	3927.63
952.00	3865.45	3895.61	3869.60	2354.00	4017.32	4003.76	3988.29
952.90	3862.46	3888.44	3862.45	2354.90	4013.85	4010.93	3998.34
953.45	3860.71	3866.27	3843.26	2355.05	3983.62	3975.24	3954.17
1004.00	3864.87	3898.04	3871.31	2359.05	3955.48	3968.86	3947.20
1004.90	3864.46	3882.25	3856.69	2359.15	3980.92	3955.06	3932.08
1053.15	3862.21	3868.84	3845.77	2359.25	3999.40	3970.60	3952.94
1056.00	3863.79	3900.68	3874.06	2359.35	3864.73	3927.36	3901.09
1056.90	3864.42	3898.23	3871.34	2359.45	3865.22	3900.11	3875.50

Depth (m)	P-wave zero-offset velocities			Depth (m)	P-wave zero-offset velocities		
	v_{p0}^{ev}	v_{p0}^{cx}	$v_{p0}^{cx,R}$		v_{p0}^{ev}	v_{p0}^{cx}	$v_{p0}^{cx,R}$
1105.00	3877.37	3906.58	3880.29	2359.55	3946.56	3952.38	3927.39
1105.90	3864.30	3905.24	3877.71	2359.65	3987.71	3998.86	3982.95
1124.15	3862.54	3874.08	3850.65	2359.75	3985.31	3979.33	3958.32
1152.00	3879.91	3901.94	3875.28	2359.85	3969.58	3964.41	3941.11
1152.90	3864.54	3902.58	3875.14	2359.95	3944.87	3941.77	3916.56
1155.15	3875.75	3885.88	3860.54	2365.05	3863.18	3890.00	3866.41
1204.00	3888.84	3913.52	3886.41	2366.85	3991.90	3988.66	3970.94
1204.90	3877.91	3897.05	3870.44	2372.05	3877.19	3895.50	3873.82
1205.15	3865.36	3900.80	3874.51	2372.15	3880.75	3912.17	3887.90
1253.00	3881.19	3897.47	3870.95	2372.25	3894.68	3898.74	3875.07
1253.90	3881.44	3898.98	3872.47	2372.35	3861.61	3907.56	3886.43
1255.15	3876.20	3874.79	3851.69	2372.45	3860.77	3861.30	3840.77
1304.00	3880.62	3902.11	3875.27	2372.55	3945.04	3883.40	3860.15
1304.90	3878.22	3897.44	3871.48	2372.65	3897.00	3934.13	3908.88
1345.15	3875.73	3878.26	3854.75	2372.75	3954.03	3879.94	3870.92
1354.00	3881.92	3907.07	3880.54	2372.85	3863.44	3864.81	3843.40
1354.90	3893.15	3921.40	3893.86	2372.95	3864.18	3887.92	3864.08
1364.15	3875.73	3878.50	3855.06	2373.05	3865.45	3911.48	3886.64
1395.85	3876.41	3886.15	3861.16	2373.15	3862.72	3851.63	3833.97
1404.00	3877.87	3890.20	3864.82	2373.25	3862.09	3906.18	3878.78
1404.90	3898.99	3925.17	3897.74	2373.35	3957.13	3935.85	3909.79
1454.00	3881.10	3903.20	3876.71	2373.45	3895.96	3888.37	3862.37
1454.15	3877.32	3880.96	3857.10	2373.55	3876.71	3889.87	3869.69
1454.90	3878.91	3898.43	3871.94	2373.65	3856.73	3897.46	3872.86
1494.25	3875.78	3878.52	3854.47	2373.75	3911.20	3868.59	3846.45
1505.00	3896.29	3912.68	3886.27	2373.85	3907.86	3863.19	3841.38
1505.90	3878.15	3909.44	3883.79	2373.95	3864.22	3880.29	3855.85
1534.15	3876.81	3903.60	3877.51	2375.05	3887.50	3866.29	3846.25
1553.96	3876.04	3873.86	3851.44	2375.25	3903.24	3860.62	3840.72
1568.05	3878.30	3902.56	3876.35	2379.05	3935.98	3937.65	3911.24
1585.05	3877.41	3886.31	3861.79	2379.15	3961.14	3976.92	3954.96
1603.00	3877.42	3908.71	3883.51	2379.25	3946.63	3925.24	3897.47
1603.90	3877.19	3901.38	3875.17	2379.35	3966.65	3970.03	3947.33
1655.00	3890.44	3916.30	3889.50	2379.45	3975.11	3969.08	3944.78
1655.05	3876.59	3892.90	3868.42	2379.55	3974.72	3965.08	3939.83

Depth (m)	P-wave zero-offset velocities			Depth (m)	P-wave zero-offset velocities		
	$v_{\mathrm{p0}}^{\mathrm{ev}}$	$v_{\mathrm{p0}}^{\mathrm{cx}}$	$v_{\mathrm{p0}}^{\mathrm{cx,R}}$		$v_{\mathrm{p0}}^{\mathrm{ev}}$	$v_{\mathrm{p0}}^{\mathrm{cx}}$	$v_{\mathrm{p0}}^{\mathrm{cx,R}}$
1655.90	3876.83	3890.81	3865.28	2379.65	3965.59	3966.14	3941.47
1665.05	3879.90	3884.99	3860.49	2379.75	4002.72	3986.46	3966.28
1704.00	3891.23	3917.91	3891.70	2379.85	3861.13	3953.57	3929.24
1704.90	3886.67	3930.69	3905.56	2379.95	4001.76	3996.00	3977.23
1725.05	3892.27	3892.51	3867.35	2383.95	3967.33	3962.34	3938.52
1735.05	3901.94	3898.10	3872.42	2385.05	4003.37	3973.90	3958.13
1755.05	3893.35	3897.45	3871.88	2395.05	4022.01	4009.10	3998.62
1758.00	3908.11	3921.85	3894.34	2404.00	4020.88	4012.09	4001.77
1758.90	3907.80	3925.54	3898.69	2404.90	4024.79	4010.29	4000.91
1785.05	3892.55	3898.25	3872.41	2454.00	4007.50	4008.75	3994.76
1802.00	3964.20	3943.76	3918.41	2454.90	4005.93	3997.42	3982.59
1802.90	3949.12	3927.69	3901.04	2455.05	4006.07	3977.28	3961.93
1805.05	3891.54	3899.72	3874.17	2485.05	4011.65	3994.87	3981.21
1845.05	3887.65	3903.59	3878.49	2495.05	3983.47	3967.85	3946.69
1854.00	3905.09	3918.26	3892.36	2504.00	4001.67	3962.67	3945.48
1854.90	3880.88	3896.85	3871.34	2504.90	3992.88	3985.03	3967.14
1855.25	3897.52	3902.14	3876.65	2505.05	3996.10	3984.38	3966.24
1856.95	3884.28	3890.21	3865.62	2546.95	3960.59	3942.36	3917.62
1904.00	3957.05	3948.36	3924.05	2554.00	4002.22	3996.47	3980.12
1904.90	3952.56	3910.73	3884.83	2554.90	4002.58	3996.96	3980.29
1955.05	3953.96	3933.17	3908.12	2563.05	3999.45	3977.05	3958.37

D.3 Additional seismic velocity figures
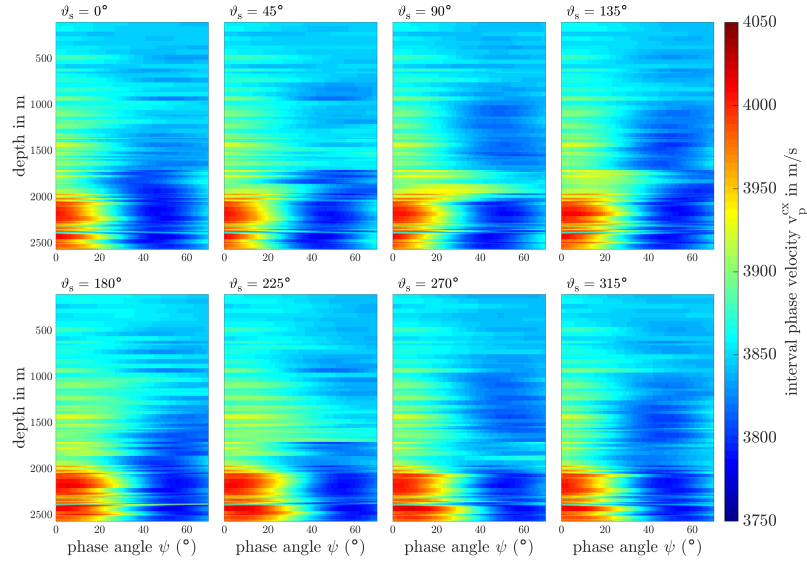
Fig. D.1: Seismic P-wave interval velocity for c-axes method for incidence angles up to 70° and eight seismic plane azimuth angles ϑ_s (EDML).
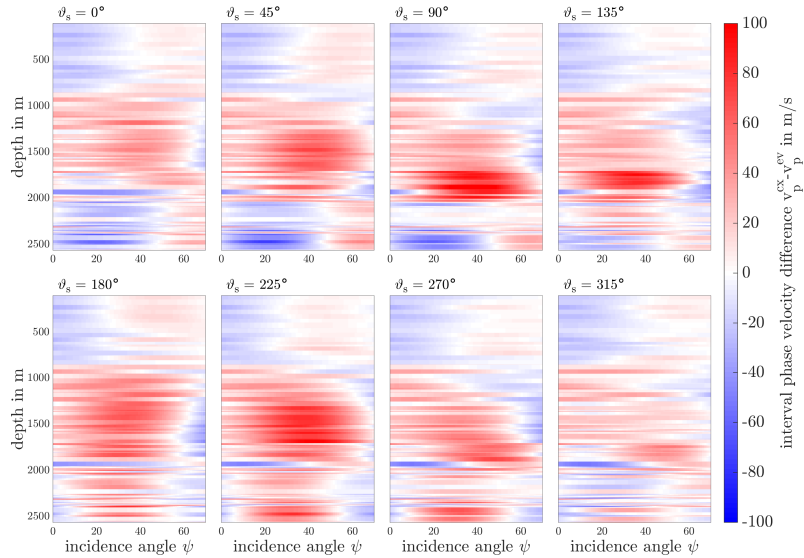
Fig. D.2: Difference of EDML seismic P-wave interval velocity between c-axes and eigenvalue method for incidence angles up to 70° and eight seismic plane azimuth angles ϑ_s. $v_\mathrm{p}^\mathrm{ev}(\psi)$ is independent of ϑ_s, so the change is only due to the c-axes method. Blue colour indicates overestimation of velocity by eigenvalue method, red shades show the opposite.
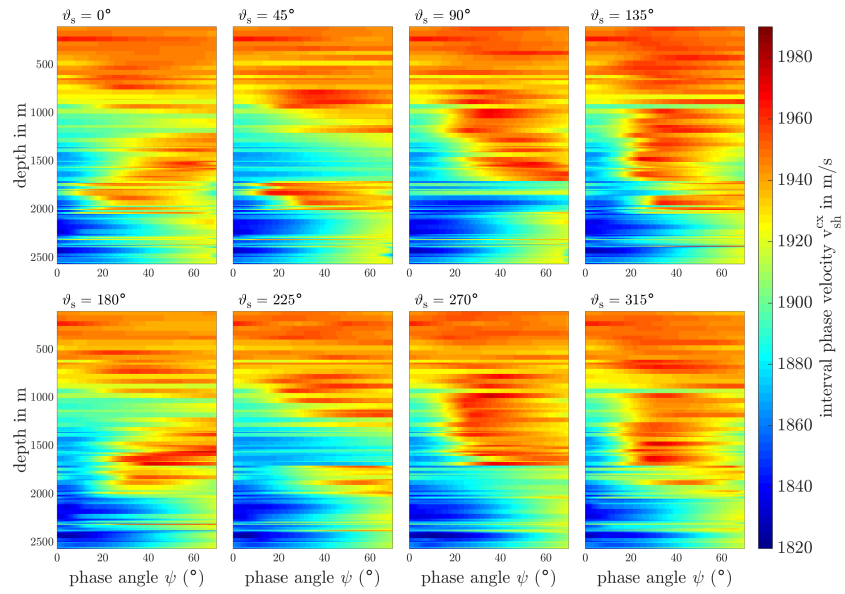
Fig. D.3: Seismic SH-wave interval velocity for c-axes method (EDML).
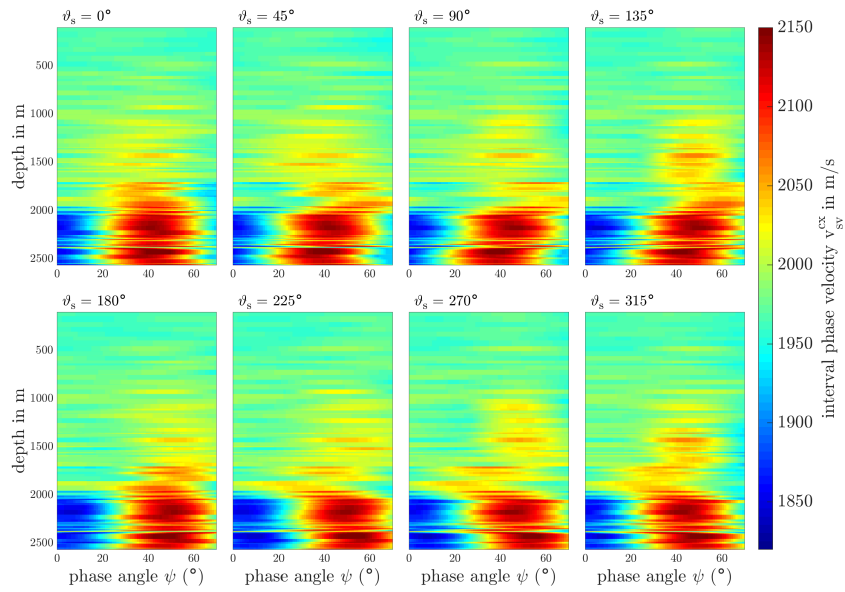
Fig. D.4: Seismic SV-wave interval velocity for c-axes method (EDML).
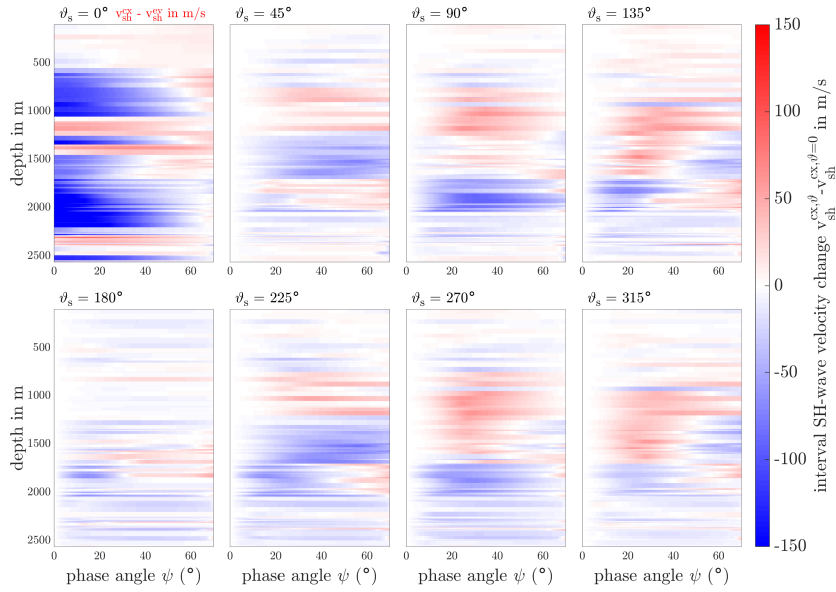
Fig. D.5: Top left: Difference in EDML seismic SH-wave interval velocity between c-axes and eigenvalue method. For $\vartheta_s > 0°$ the change in difference is shown as compared to $\vartheta_s = 0°$.
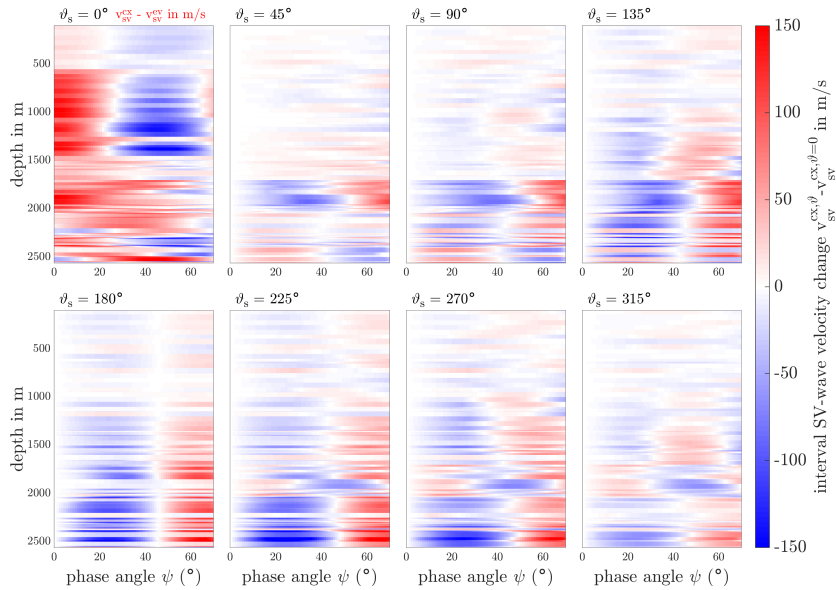
Fig. D.6: Top left: Difference in EDML seismic SV-wave interval velocity between c-axes and eigenvalue method. For $\vartheta_s > 0°$ the change in difference is shown as compared to $\vartheta_s = 0°$.
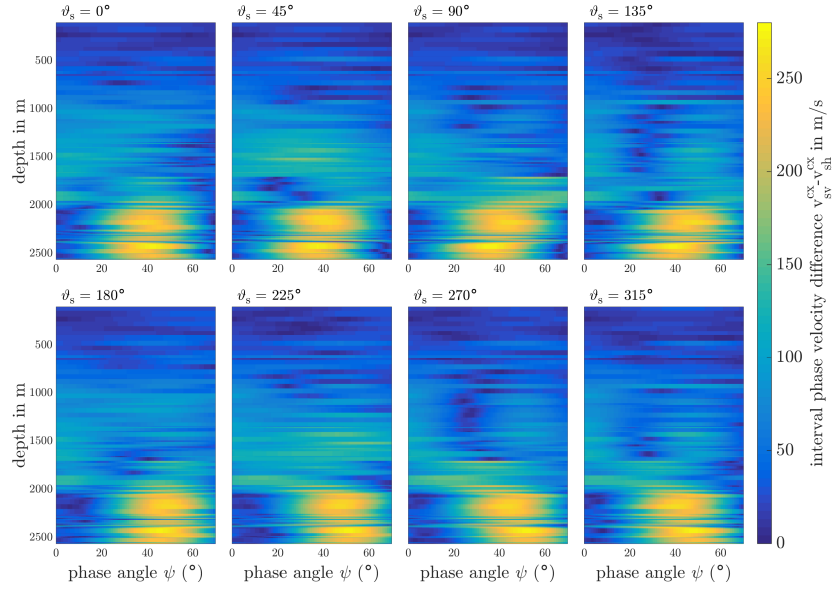
Fig. D.7: Difference in EDML seismic interval velocity between SV- and SH wave as calculated with c-axes method.
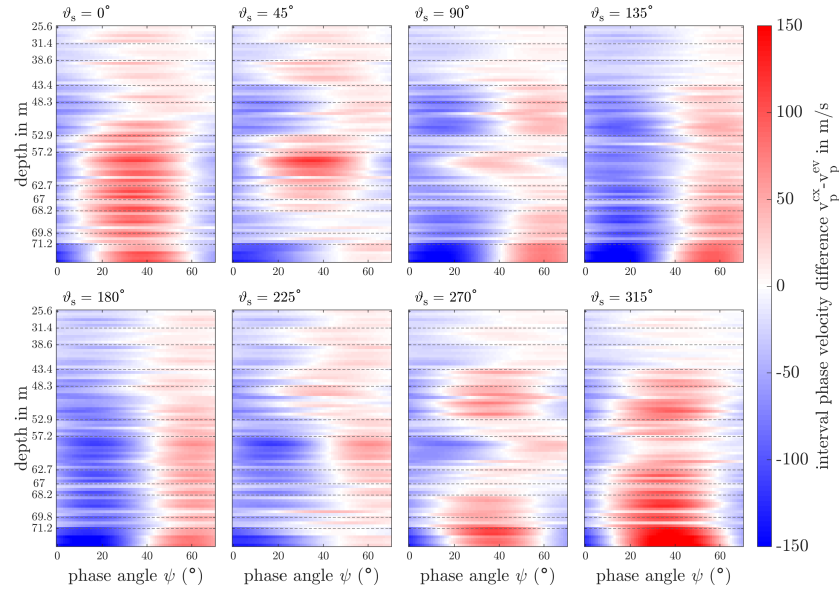
Fig. D.8: Difference of KCC seismic P-wave interval velocity between c-axes and eigenvalue method $(v_{\mathrm{p}}^{\mathrm{cx}} - v_{\mathrm{p}}^{\mathrm{ev}})$ for incidence angles up to 70° and eight seismic plane azimuth angles ϑ_{s}. $v_{\mathrm{p}}^{\mathrm{ev}}(\psi)$ is independent of ϑ_{s}, so the change is only due to the c-axes method. Blue colour indicates overestimation of velocity by eigenvalue method, red shades show the opposite. Note the breaks of the depth axis where noted depth values refer to the top of the downward extending depth range.
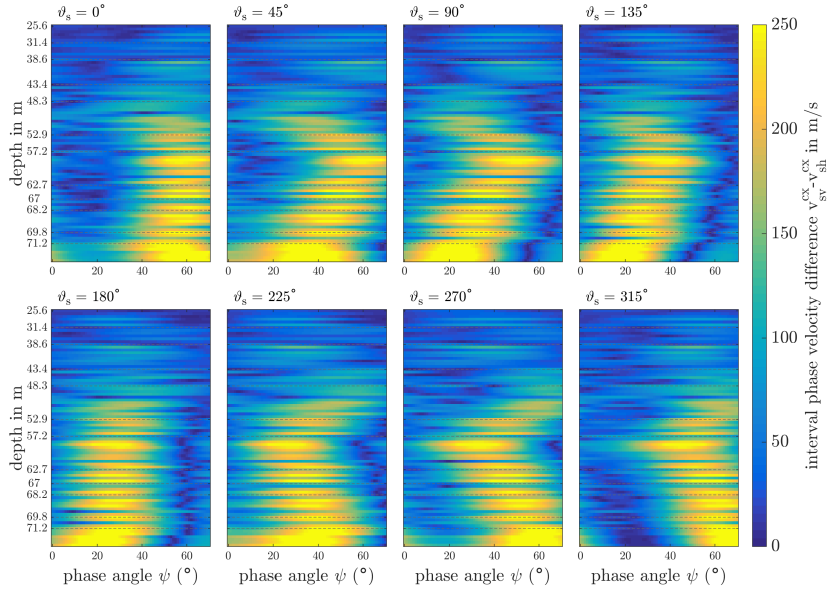
Fig. D.9: Difference in KCC seismic interval velocity between SV- and SH wave as calculated with c-axes method. Note the breaks of the depth axis where noted depth values refer to the top of the downward extending depth range.
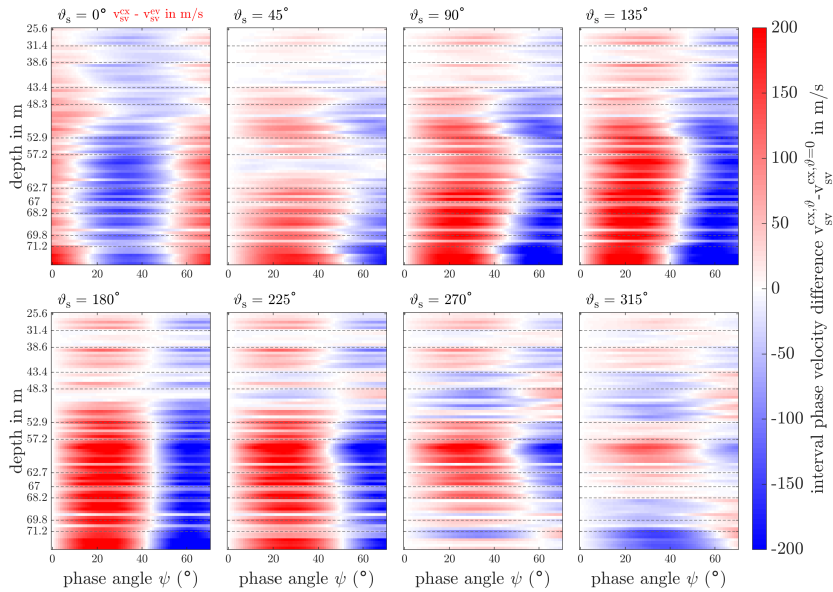
Fig. D.10: Top left: Difference in KCC seismic SV-wave interval velocity between c-axes and eigenvalue method. For $\vartheta_s > 0°$ the change in difference is shown as compared to $\vartheta_s = 0°$. Note the breaks of the depth axis where noted depth values refer to the top of the downward extending depth range.

It always seems impossible until it's done.
(Nelson Mandela)

I am deeply grateful to the wonderful and supportive people who made it possible for me to finish this work.

Thank you.

Olaf who shares my fascination for anisotropy and trusted me with this study. His calmness and steady guidance were invaluable.

Ilka who welcomed and accompanied me on this trip with many patient discussions and constantly reminded me not to take things to seriously.

Anja who always had time for long and complicated discussions, never losing her good humour, and for detailed comments to this thesis. I couldn't have conquered the elasticity tensor without her help.

Pascal who tried to teach me how to ski (it's not his fault it didn't work), initiated the opportunity for me to visit Maine, provided comments to this thesis and home-made pale ale for the final sprint.

Nicky for the cooperative work and her sincere communication.

Daniela who has supported me in the ice lab and beyond, with comments to this thesis and with a new knitting pattern.

Tobias and **Jan** who have advised me many times on image analysis issues.

Sepp and **Johannes** for their interest in my work, critical questions and unique advice.

Christian and **Tobias** for sharing their offices with me in Bremerhaven and **York**
and **Fernando** for searching and moving of ice core boxes.

Gema, Florian, Ernst, Jan and **Ina** for being in a virtual group with me and sharing their research experiences.

All who helped me in the ice lab preparing the measurements while freezing off their fingertips and toes – Gema, Florian, Maria, Sophie and Jonas...

Paul Bons for agreeing to evaluate this thesis.

Paul Mayewski for supporting the laser ablation pilot study at CCI.

Martin for contributing with his artistic talent.

Without the dedicated work of the **KCC drilling team of 2013**, the **CFA crew in Bern** and the **IUP administration** this thesis would be empty.

Lars, Carlo, Josef and **Helene** for holding the fort and carrying on.

Tilman for being my companion in this venture.

Ingeborg who has watched over us and for giving honest advice in all matters.

Feo and **Birte** who I can always rely on for unwavering encouragement.

Helene for being my best friend anytime, providing me with care packages and silliness.

Alexander who writes extraordinary poetry when faced with a devastated girlfriend and makes the world's best pizza.

Rita and **Jürgen** who have always been supporting me with all their heart.

I am deeply thankful to **Dietmar** who impressed me with his joy of life and who would have enjoyed the results of this work, I think.